Hannes Raggam

SATELLITE RADARGRAMMETRY

PHASE I

by
Franz W. Leberl
Johann Raggam
Technical University and
Graz Research Center

Principal Investigator

Franz W. Leberl
Institute for Applied Geodesy and Photogrammetry
Technical University, A-8010 Graz, Austria
and
Graz Research Center

Research Project
INTERNATIONAL COOPERATION IN SPACE
NASA - AUSTRIA
VENUS ORBITAL IMAGING RADAR
PHASE I

Final Report
31 March 1982

DIBAG - Bericht Nr. 4

ABSTRACT

This report summarizes results of work obtained during Phase I of a research project "International Cooperation In Space NASA-AUSTRIA - Venus Orbital Imaging Radar". Duration of this effort was from 1 May 1980 through 30 April 1982. It serves to generate basic understanding of radargrammetric concepts to ultimately map the planet Venus from an orbiting spacecraft carrying a side-looking radar sensor. Emphasis was on the radargrammetric evaluation of satellite radar imagery using single images and stereo pairs. New methods were developed on the basis of previous work. Results are mainly achieved with SEASAT terrestrial satellite radar. During this project the work concentrated on the analysis of hard-copy imagery on film, without resorting to digital imagery processing techniques. A thorough understanding was developed of the capabilities of stereo radar from satellites based on existing data : stereo viewability, vertical exaggeration and measuring accuracies in a three-dimensional model. As a by-product, work with single satellite images led to the evaluation of an application to study rapidly changing phenomena on Earth such as sea ice motion.

ZUSAMMENFASSUNG

Dieser Bericht fasst Ergebnisse der Arbeit zusammen, welche im Rahmen der Phase I eines Forschungsprojektes "Internationale Kooperationsforschung im Weltraum NASA-Oesterreich, Venus Orbital Imaging Radar" geleistet wurde. Diese Arbeit umfasst die Periode vom 1. Mai 1980 bis 31. April 1982. Sie dient der Erarbeitung grundsaetzlicher radargrammetrischer Konzepte fuer eine Venus-Mission zur Kartierung des Planeten aus einem Radarsatelliten. Betont wurde die radargrammetrische Beurteilung von Satellitenradar mit Einzelbildern und Stereobildpaaren. Neue Verfahren werden angegeben, welche schon bestehende erweitern. Tatsaechliche Ergebnisse wurden mit terrestrischen SEASAT-Satellitenradarbildern erhalten. Waehrend dieser ersten Projektphase konzentrierte sich die Arbeit auf die Analyse von Analog-Bildern auf Film ohne wesentliche Anstrengungen in der digitalen Bildverarbeitung. Ein tieferes Verstaendnis der Stereoradarproblematik wurde mittels bestehender Satellitendaten erworben : Stereobetrachtung, Ueberhoehung und Messgenauigkeit im dreidimensionalen Modell wurden untersucht. Als ein Nebenprodukt der Einzelbildauswertung wurde auch ein Verfahren entwickelt und beurteilt, um auf der Erdoberflaeche aus Satellitenbildern rasch veraenderliche Erscheinungen zu erfassen, wie dies etwa bei Meereseisbewegungen auftritt.

ACKNOWLEDGEMENTS

This work would not have been possible without the support received from the Austrian Ministry of Science and Research, Vienna, the staff of the Graz Research Center, and the counterparts at NASA's Jet Propulsion Laboratory. In particular we wish to express our gratitude to Min.-Rat Dipl.-Ing. O. Zellhofer, Vienna for financial and moral support, to Dr. Charles Elachi, Mr. Ben Holt, Dr. S. Saunders and Mr. Mike Kobrick of JPL, for data discussions, Dr. J. Boyce of NASA-Headquarters for having us actively participate in NASA's planetary radargrammetry activities, and - as a side-line in Venus radar research - to Dr. Bill Campbell of the US Geological Survey for his interest and data on terrestrial sea-ice motion.

We look forward to continued co-operation.

C O N T E N T S

C H A P T E R 1

VENUS RADAR MAPPING

1.1 INTRODUCTION

Among the terrestrial planets Venus is least well understood. This is caused by the perennial cloud cover hiding the surface from observation (see Figure 1.1).

Figure 1.1 Mariner 10 vidicon image of the Venusian cloud cover in UV-light

Radar imaging is the only means of mapping this surface. This has been done from the Pioneer Venus ortiter using large antennas of radio telescopes, and from the Pioneer Venus orbiter using a radar altimeter. However, geometrical resolution so far

was 10 to 30 km for Earth based methods, and 30 to 100 km for Pioneer Venus. This is far poorer than the resolutions at which all other terrestrial planets are known.

A Venus Orbital Radar Mapping Mission is thus currently planned by NASA to map the entire surface of the planet at a resolution at least comparable to that at which other planets have been imaged. A high resolution side-looking radar (SLR) system will be carried into an orbit around Venus. The essential purpose is a study of the Venusian surface; other experiments are being planned as well but are of secondary weight in mission design.

The Venus Orbital Imaging Radar Mission (VOIR) ist the result of numerous proposals to map the Venusian surface through the heavy layer of clouds. Early project studies were by BROWN et al.(1972), SAUNDERS et al.(1973), FRIEDMAN and ROSE (1973), MARTIN-MARIETTA (1974), WESTINGHOUSE (1974) and others. The engineering challenge of such an undertaking inspired numerous smaller preparatory projects, and it may have led to spin-offs in other areas, such as in the Apollo 17 Lunar Sounder Experiment (ALSE) in 1972 and Seasat in 1978, two projects for orbital mapping from radar images. These projects generated experiences that currently help greatly in planning a Venus Mapping Project and they are providing a capability to predict the expected quality of radar images.

In 1978 NASA formed a Venus Science Investigation Team with participation of an Austrian representative. Originally this was to prepare an approved VOIR-Mission. In the meantime the

thinking has drifted to a mission concept that is simpler as regards the spacecraft and orbit design, but more difficult regarding data analysis, essentially pointing towards an elliptical orbit whereas VOIR was with a circular orbit.

The administrative facts about VOIR, Austrian participation and future outlook are presented in a separate document (*).

This report presents the results of 2 years of work to develop satellite radargrammetry, so that a clearer understanding exists about possibilities and limitations and to support also the Venus Radar Mapping effort.

This chapter will describe the scientific environment in which the mission is developing, presenting a review of the current knowledge of the surface of Venus which resulted from Pioneer Venus and Earth based radar. It will then outline the operation of a synthetic aperture radar for Venus and present examples of images as they might be generated in this mission.

The subsequent chapters then separately address the single image and stereo pair, therety dealing first with the theory (chapters 2 and 3) then with practical experiences (chapters 4 and 5).

Due to various delays in the Venus mission, an opportunity developed to more fully study existing satellite radar data such

---

(*) [illegible] project no. [illegible]

as SEASAT images and to apply basic concepts to existing aircraft radar. It is expected that this will be helpful in the future intensification of preparations to actually fly a mapping mission to Venus. As a by - product also terrestrial satellite radar applications can benefit from the effort.

1.2 CURRENT KNOWLEDGE OF THE SURFACE OF VENUS

So far 14 spacecraft have successfully been sent to Venus. Surface images exist now from [illegible] missions: [illegible] 9 and 10 with one image each taken directly after landing (FLORENSKY et al.,1977), from Pioneer Venus orbiter data ([illegible] et al.,1979a, b, 1980; MASURSKY et al.,1980) and most recently from VENERA 13 and 14. Surface images also exist from Earth based radar employing either the radar telescope at Arecibo (RAGEORS and CAMPBELL, 1974; ROGERS et al.,1970; CAMPBELL et al.,1972, 1976, 1979, 1980) or the Deep Space Network (DSN) antenna at Goldstone in California (GOLDSTEIN, 1965; GOLDSTEIN et al.,1972, 1976, 1978; JURGENS, 1970 1980; RUMSEY et al.,1974).

1.2.1 Data from Pioneer Venus

The Pioneer Venus orbiter radar mapper provided the most extensive surface data available on Venus so far. It operated in two modes:

(a) as an altimeter;

(b) as a side-looking radar imaging system.

The results from this sensor were presented by MASURSKY et al.(1980) and by PETTENGILL et al.(1980).

Topographic relief was obtained from the altimeter measurements. This is shown in Figure 1.2 in the form of a shaded relief map, juxtaposed to a comparable presentation of the Earth for ease of comparison. Figure 1.3 is a contour map of Venus at a 1 km contour interval. It should be noted that the altimeter measurements after 16 months of data collection have a density of between 75 and 200 km. The accuracy of an individual height is estimated by PETTENGILL et al.(1980) to be about ± 200 m (standard deviation). Depending on the further duration of the Pioneer Venus mission a higher resolution topographic map can be accumulated.

The other main product from the orbiter radar mapper is a mosaic compiled from the data otained in the side-looking radar imaging mode. This coverage is less than that produced in the altimeter mode since the orbit was ellipitcal and imaging was only done when the spacecraft was at altitudes below 550 km. Altimeter data, however, were taken also at bihger spacecraft altitudes.

1.2.2 Data from Earth Based Radar

Mapping of segments of the Venusian surface began in the sixties with the reception of echoes from radar pulses sent to Venus. Early images were obtained with interferometric methods at 3.8 cm wavelength by ROGERS and INGALLS (1969). Currently

(Figure 1.2 (a))

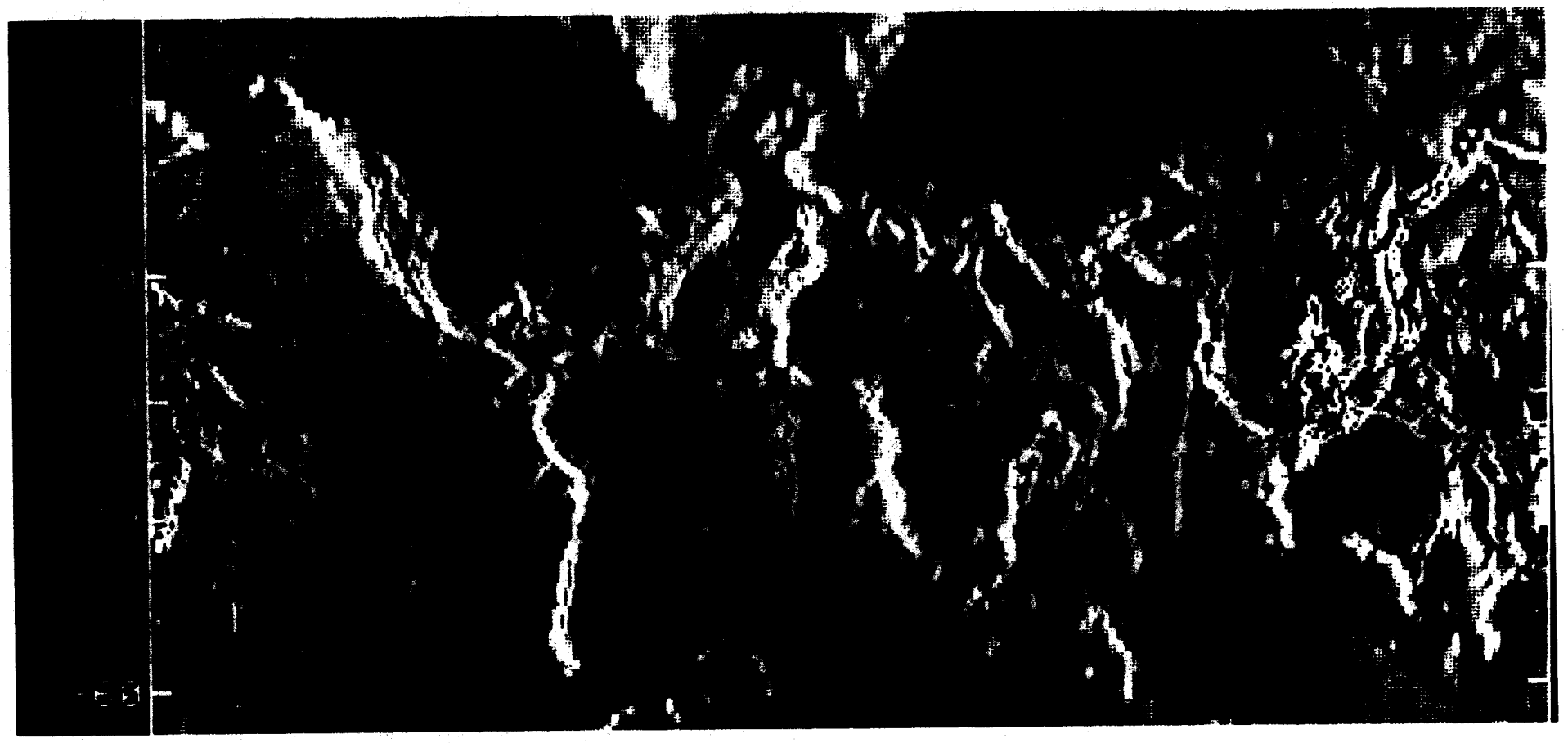

(Figure 1.2 (b))

Figure 1.2 Shaded relief maps of Venus and Earth. Venus data (a) are compiled from Pioneer Venus altimeter at a grid spacing of 75 to 200 km (from Masursky et al.,1980; Pettengill et al.,1980). Earth presentation (b) for comparision.

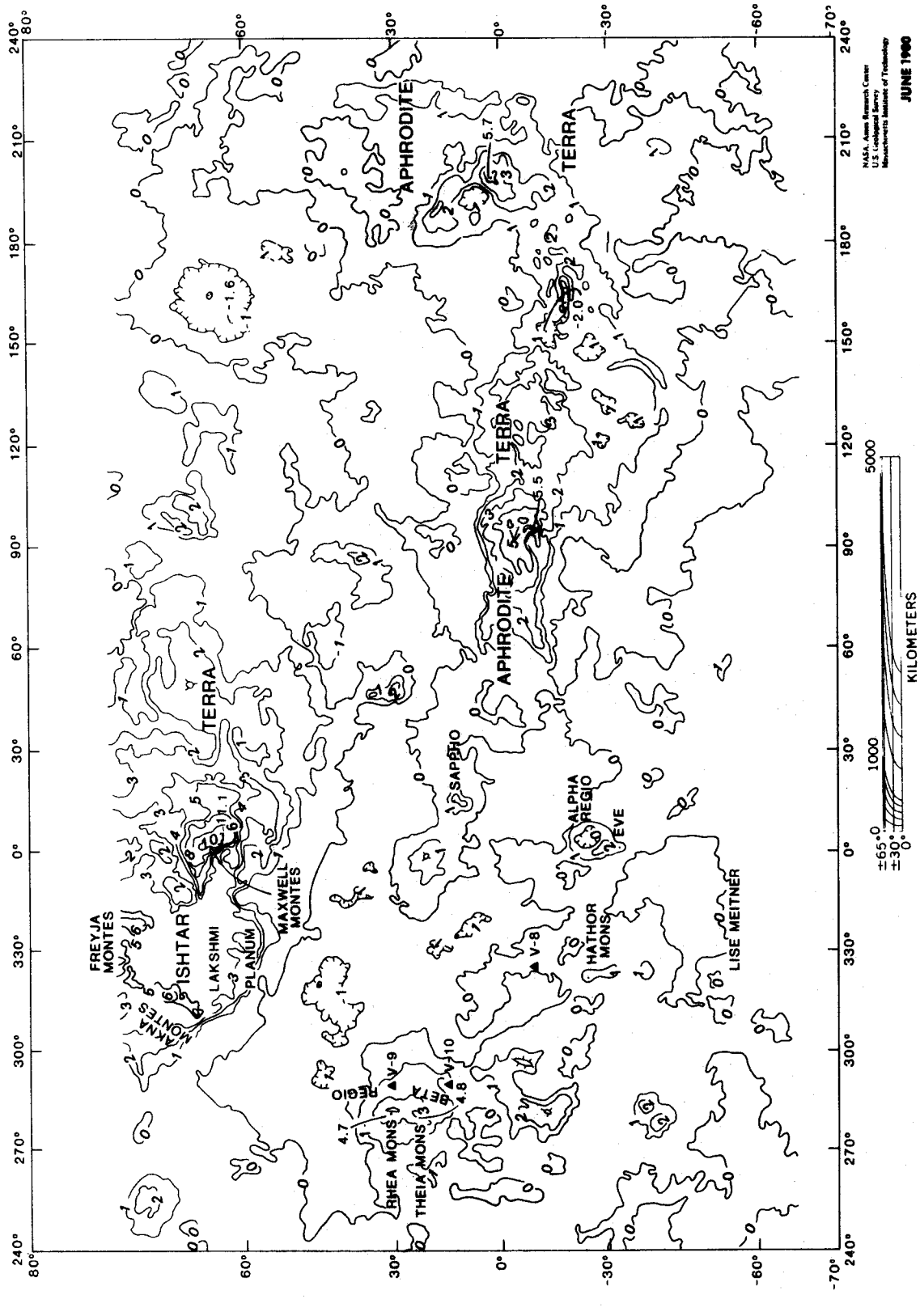

Figure 1.3 Contour map with 1 km equidistance, compiled from Pioneer Venus altimeter data with a grid spacing of 75 to 200 km (from Masursky et al.,1980)

these images are generated with the antenna in Arecibo, Puerto Rico (CAMPBELL et al.,1980) and with the Goldstone antenna in California (JURGENS et al,1980).

The technique employed is explained in Figure 1.4 : A transmitted, highly focussed radar pulse illuminates the surface of the planet. The echo is received on the Earth by the transmitting antenna. Echo time serves to resolve the illuminated area into parallel slices as shown in Figure 1.4, where the Doppler effect is created by the revolution of the planet.

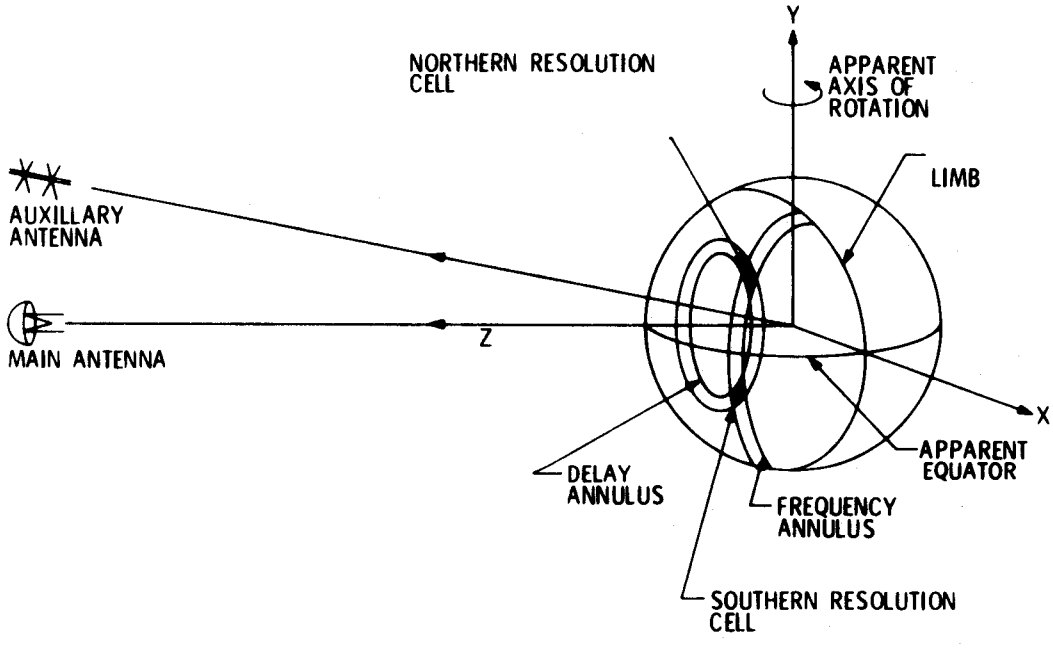

Figure 1.4 Concept of Earth based radar to map planetary surfaces

We can observe in Figure 1.4 that the received echo can be resolved into separate though ambiguous image points: each point corresponds to two object areas, one in the northern, one in the southern hemisphere. This ambiguity can be resolved if

the beam is sufficiently focussed to illuminate just one hemisphere, as is being done in comparable work on the Moon. If sufficient focussing is not feasible, such as is the case with Venus, then an interferometric method must be used to resolve the ambiguity. The radar echos are received at two antennas rather than one, and are summed up. This allows to measure phase differences at the two receiving antennas. Phases are different in the echos from the northern and southern hemisphere at the two antennas. GOLDSTEIN et al.(1978) carried the interferometric technique even further and employed three antennas: the large one for transmission and reception, and the two secondary antennas for reception only. This configuration not only allows for the separation of north/south signals, but also for the creation of a three-dimensional model of the topography. The technique has an analogy to stereo at very steep look angles and with small stereo bases. We know that this results in comparatively high accuracies of the vertical dimension, similar to an altimeter, but leaves a weak planimetric solution.

Earth based radar images of Venus have a resolution of 10 to 30 km (diameter of a pixel). CAMPBELL et al.(1980) report on images of selected areas at a resolution of 5 km, and in CAMPBELL et al.(1982), even a 3 km resolution is obtained of certain areas. Presentations are in one of two forms: (a) as normal radar images where image density is proportional to the radar backscatter; (b) as a relief presentation with coded gray tones for a digital height model, or other similar displays of height.

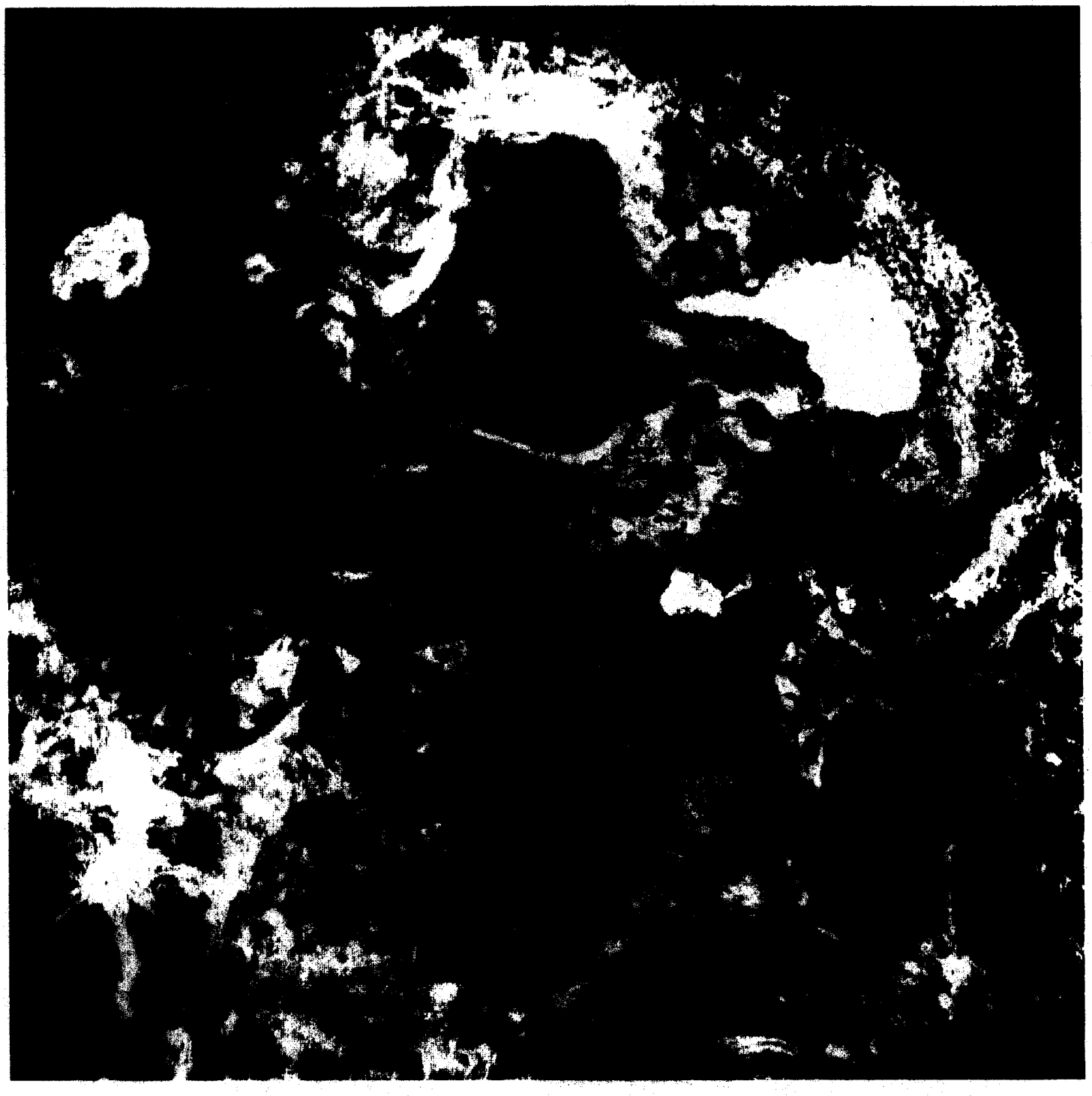

Figure 1.5 Mosaic of Earth-based radar images of Venus, obtained by Campbell et al.(1980) in Arecibo. Shown is the northern hemisphere.

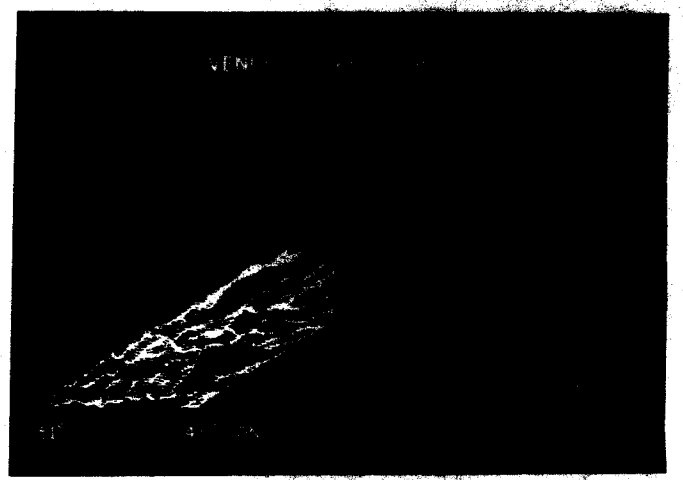

Figure 1.6 Earth based radar image and derived presentations;
(a) reflectivity image
(b) digital height model coded with gray tones
(c) digital height model of a section presented as a profile plot.
Illustrations obtained through the Goldstone antenna (Courtesy R. Jurgens).

Examples of Earth-based radar images are shown in Figures 1.5 and 1.6. Figure 1.5 is a mosaic presenting an overview of results from CAMPBELL et al.(1980) obtained at Arecibo. Figure 1.6 is a set of illustrations typical of the results obtained at Goldstone (JURGENS et al.,1980), presenting both a reflectivity map and a map of topographic heights.

These images all show a higher geometric resolution than those obtained from Pioneer Venus. This demonstrates the value of Earth based observations inspite of existing orbiting spacecraft. The essential advantage of the current coverage by Pioneer Venus over the Earth based radar is the more global coverage and the higher accuracy of individual topographic height measurements.

1.2.3 Interpretations of the Available Images

MALIN and SAUNDERS (1977) were the first to attempt a geological interpretation of the data received through Earth based radar. They described landforms, identified features with a tentative classification as volcanic and as impact craters. A more thorough analysis had to wait, however, for the more global, accurate, but less densely sampling Pioneer Venus mission. PETTENGILL et al.(1980) and MASURSKY et al.(1980) gave an exhaustive analysis from the currently available data, combining Earth-based with satellite measurements.

Maxwell Mons is the highest feature (compare Figure 1.3 for feature names), about 11.1 km above the reference radius of 6051.0 km. The lowest area seems to be Diana Chasma in

Aphrodite Regio . The entire relief seems to amount to about 2/3 of the Earth's (20 km). Venus topography is less accentuated than the Earth's (compare the shaded relief maps of Figure 1.2). The contours in Figure 1.3 show that highlands indeed are of a limited extent.

There is an abundance of evidence for craters of both volcanic and impact origin. An example of a volcanic feature probably is Rhea Mons at 30 degrees N, 80 degrees W, in Beta Regio. The early speculation of MALIN and SAUNDERS (1977), regarding plate tectonic activity seems probable, for example due to the existence of highlands and of deep trenches such as Diana Chasma. Early attempts have been made at crater counts to compare Venus to other terrestrial planets. The coarse resolution of current images impairs the success of such attempts.

Many questions remain unanswered, such as regarding plate tectonics, the history of the planets surface, the type and origin of craters, the interaction between atmosphere and surface etc. Such questions can only be tackled with improved imaging capabilities. Available data on Venus are limited when compared to Mars, where Mariner 9 imaged at a resolution of up to 250 m per pixel; Mercury was mapped with 1 km per pixel. Venus is mapped at 100 km resolution, and some small segments with 5 km per pixel.

An improved imaging capability comparable to that of Mariner 9 is required to achieve a similarly thorough understanding of Venus than that we have had after Mariner 9 from Mars. The

planned Radar Imaging effort is intended to provide this capability.

1.3 MISSION PLAN

1.3.1 VOIR

Early concepts for orbital side-looking radar exploration of Venus were studied in an extensive report by BROWN et al.(1972). Since then the parameters of the mission have been changed several times. The latest plan was that of the Venus Orbital Imaging Radar (VOIR) mission and is shown in Table 1.1.

Planned launch	November 1987
Launch vehicle	Space Shuttle, Centaur
Beginning of imaging	July 1988
Duration of science acquisition	126 days nominal mission
Orbit type	Circular
Circularization of orbit	Aerobraking
Orbit inclination	87
Orbit altitude	250 km + 25 km
Imaging sensor	Synthetic aperture radar
Sensor wavelength	L-Band (25 cm)
SAR antenna look angle	45 to 50 off-nadir
Pointable antenna	Still under discussion
Ground resolution, mapping	600 per line pair
Ground resolution, high	150 m per line pair
Swath width, mapping	30 km
Swath width, high resolution	12 km
Length of image strips	45 min. (time) per orbit
Multiple looks in imaging mode	16
Multiple looks in high resolution	4
Expected orbit accuracy, 1 sigma	Still under discussion
72 hrs after occurence, absolute	1 km radial, 10 km plan
72 hrs after occurence, relative	.3 km radial, 1 km plan
Other primary data acquisition	Altimetry
Secondary science experiments	Various (5 in total)
Altmeter accuracy	As SAR high resolution

Table 1.1 Proposed VOIR mission parameters (1981)

A spacecraft, launched from the Space Shuttle in November 1987, was to arrive at Venus four months later and enter into a highly

elliptical orbit. By a technique called "aerobraking",the orbit was to be circularized using atmospheric friction near periapsis (Figure 1.7).

From the circular orbit a radar coverage of nearly the entire planet would have had to be generated during 126 days. Multiple coverages in near-polar regions could serve to define the rotation axis and a coordinate grid. Radar coverage could be tied to this grid based on orbit data and on the use of overlapping coverages. Limitations on energy and data rates would result in a requirement to use an intricate imaging strategy to sequentially cover the entire surface in a patch work pattern.

Envisaged data rates were 1 Mbits per second for imaging and recording, and 1 Mbits per second for transmission to the Earth. Intermediate storage of the radar signals was planned on tape recorders for coverage of the planet's backside.

There were two geometric resolutions planned: the so called "mapping mode" at 600 m per line-pair and a "high-resolution mode" at 150 m per line-pair. The global coverage was only for the lower resolution. Higher resolution was to be used as the mission developed. Provisions were for a 1 % coverage at this high resolution during the nominal mission, of areas that would have had to be selected on the basis of the mapping mode data. This strategy was motivated by the experiences on Mars, where lower resolution images led to misinterpretations that became obvious with later higher

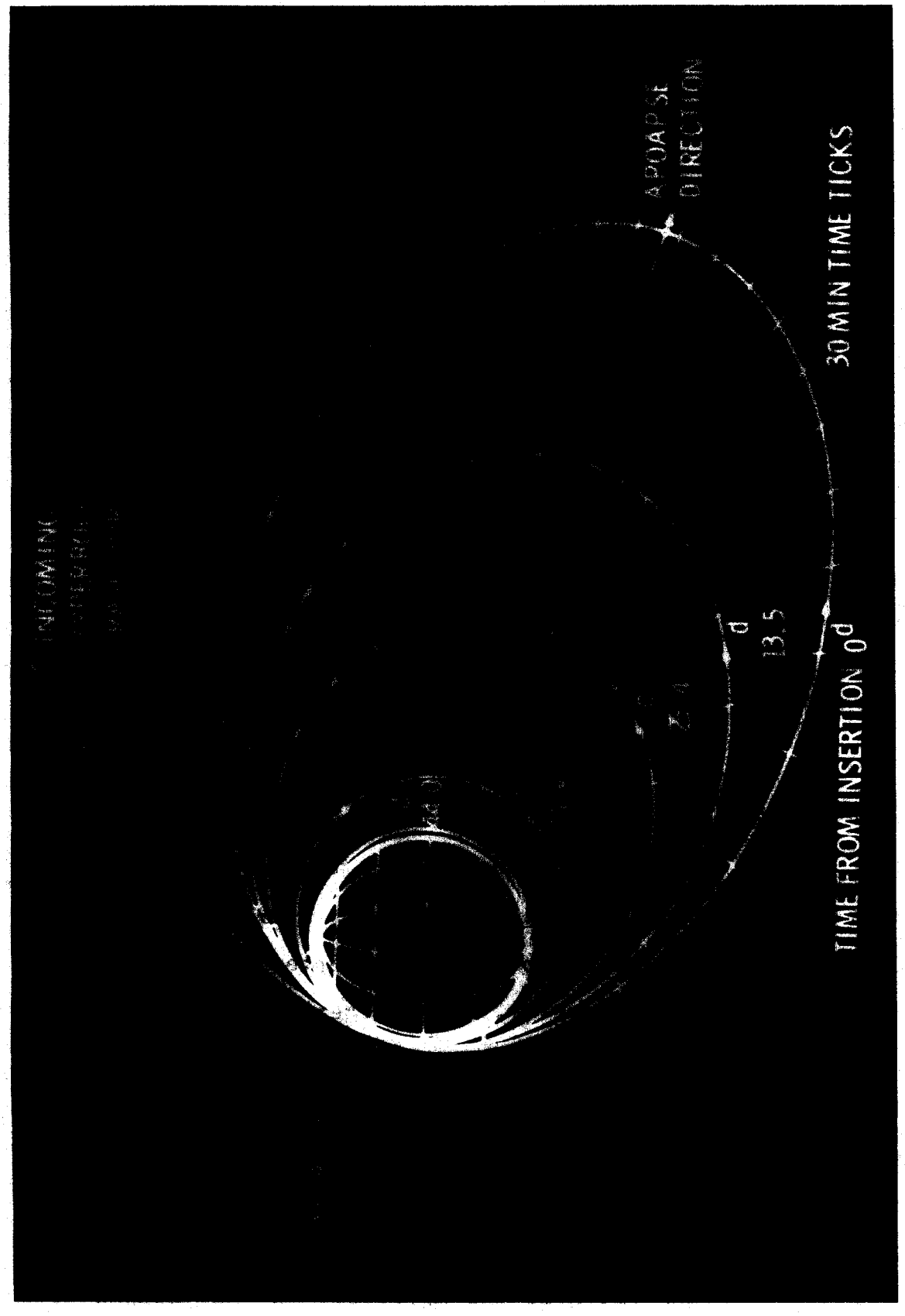

Figure 1.7 Aerobraking for the VOIR mission to circularize the elliptical orbit without fuel consumption

resolution images (Mariner 9).

The radar look angle was to be at about 50 degrees off the nadir. This is seen as a compromise between the accentuation of gentle relief with a simultaneous lack of lay-over distortion (obtainable with large look angles off-nadir) and the accentuation of backscatter differences of various materials and roughnesses with simultaneous lack of shadowing (obtainable with small look angles).

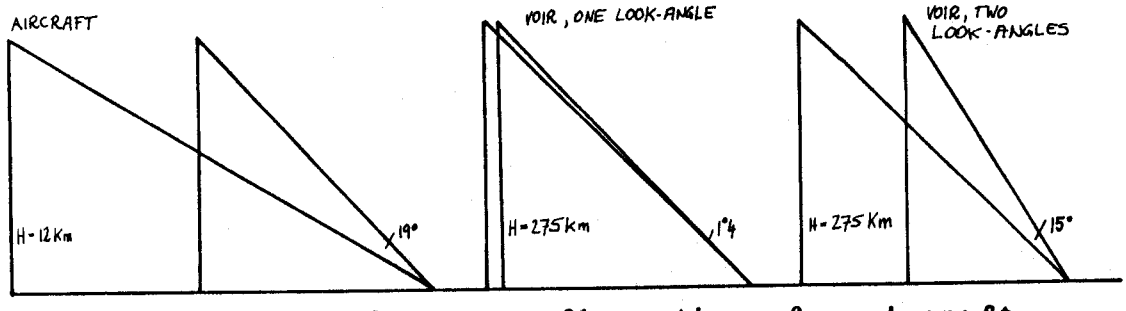

Figure 1.8 Stereo configurations for aircraft, VOIR without variable look angles, and with variable look angle

A discussion is ongoing concerning stereo (Figure 1.8). Clearly stereo intersection angles will be poor if look angles are kept constant throughout the mission. Stereo intersection angles of only 3 degrees or so must be accepted if no look angle variation is provided. However, much larger intersection angles are optimal. The current Venus science investigation group was pressing for the inclusion of a variable look angle in the design of the mission, not only for stereo, but also to be capable to illuminate the Venusian surface during the mission at whatever angle then appears to be the optimum. This may be guided by the surface features and materials to be encountered at the time of the mission.

The main argument against a variable look angle is the added complexity and resulting cost. A simple spacecraft roll, or the use of ascending and descending orbit passes could result in a "free" second look from the opposite side; however, one must expect this to produce image pairs that cannot be used for stereo analysis by planetologists nor for the measurements of topographic contours.

Besides imaging radar also altimetric data were planned to be acquired in VOIR. For this purpose the imaging radar system is to be used as an altimeter, imaging the nadir. These data were to help to improve the knowledge of surface topography and eventually were to be combined with the results from imaging into a composite product. Techniques for this task were not yet developed.

1.3.2 Current Status

A radar imaging mission is currently under consideration that is less costly than VOIR would have been. The main change is to work with a highly elliptical orbit. The decision to abandon the original VCIR-concept was taken only in January 1982 under the pressures of budget constraints. The new, reduced specifications still need to be generated by the Venus Radar Science Investigation Team.

1.4 CURRENT IMAGING RADAR

1.4.1 Imaging Side-Looking Radar (SLR) System

Extensive literature exists on imaging radar and applications to mapping and geoscience (see f.e.MATTHEWS, 1975; RADAR GEOLOGY, 1980). From orbital altitudes a reasonably high resolution can only be expected using a synthetic aperture technique. In real aperture radars imaging is achieved by illuminating a small segment (line) on the ground using an electro magnetic pulse, and by receiving and recording the reflected energy according to Figure 1.9. An areally extended image of terrain is generated by sequentially composing repeated pulses and lines while the sensor is transported past the terrain.

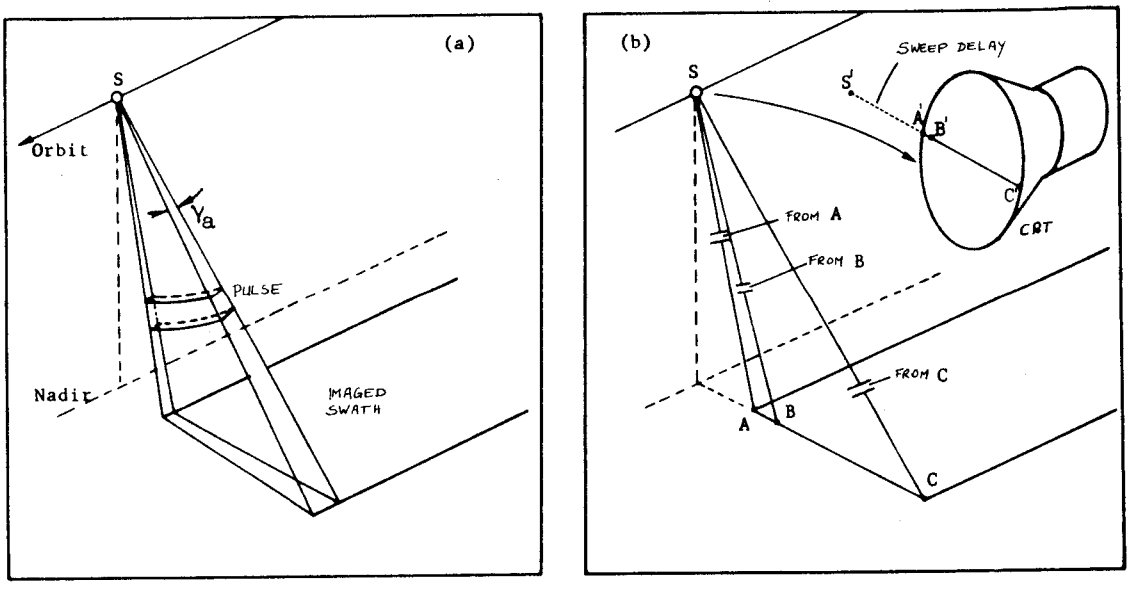

Figure 1.9 Principle of real aperture radar imaging system with the operation in object space, transmitting a pulse (a), and receiving echoes to be recorded on tape or on a cathode ray tube (b)

Synthetic aperture radars (SAR) do not record the received

echo directly but only after summing it up with a coherent reference frequency identical to that of the transmitted pulse. This creates a holographic record containing phase and Doppler frequency information about the received echo. A processing step is called "correlation". An example of a raw signal recording and correlated SAR image is shown as Figure 1.10.

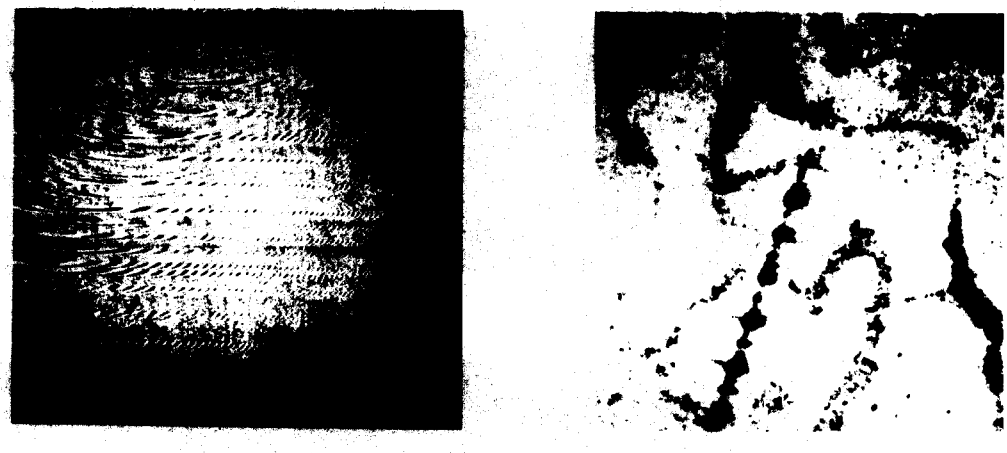

Figure 1.10 Example of a synthetic aperture radar image, (a) in its holographic raw form, (b) in its final image form after correlation. Shown are a series of transmission line towers (courtesy W. Brown)

Currently correlation of SAR signals is done optically with laser light; however, digital correlation techniques are quickly becoming operational and are the ones to be used for Venus exclusively, possibly requiring the establishment of optimal computer architectures.

1.4.2 Side-Looking Radar from Satellites

Side-looking radars are being used in civilian applications from aircraft since the early 1960's. Orbital SAR was employed for the first time in the Apollo 17 Lunar Sounder Experiment

(ALSE). Results were presented by PHILLIPS et al.(1973). Attempts at mapping segments of the lunar surface were undertaken by TIERNAN et al.(1976) using single radar images, and by LEBERL (1976) using both single and stereo images. An example of a lunar ALSE stereo pair is shown as Figure 1.11.

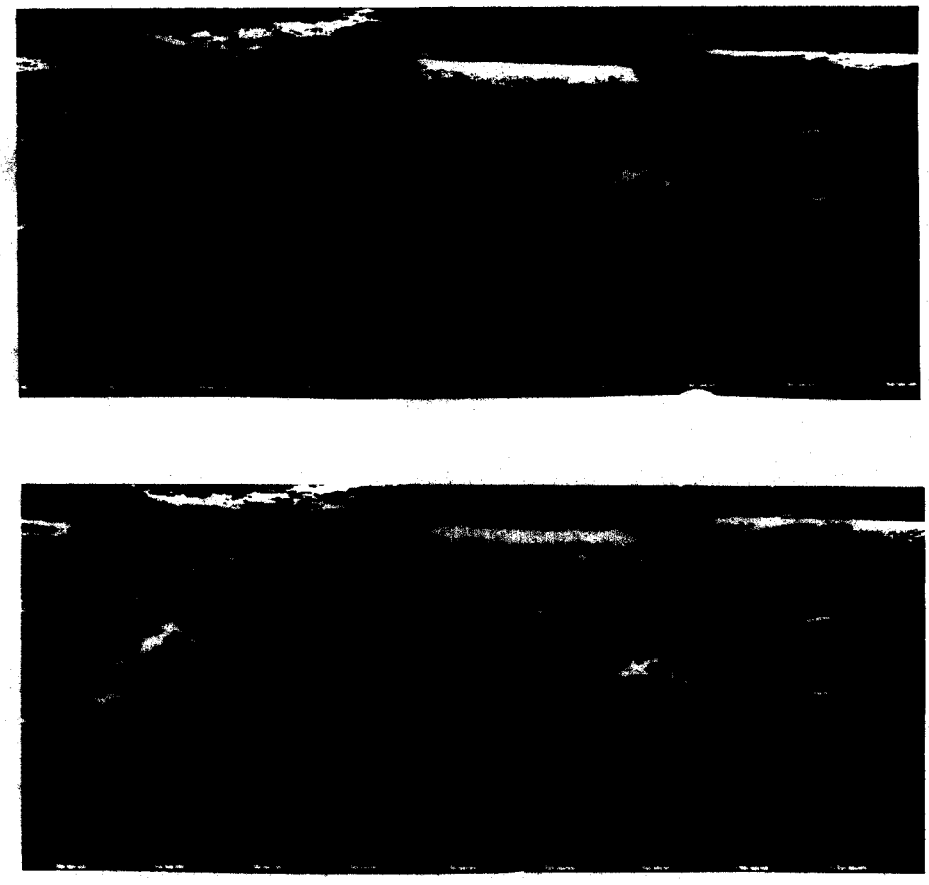

Figure 1.11 Apollo 17 Lunar Sounder Experiment (ALSE) radar stereo pair, VHF (2m) wavelength, taken over crater Maraldi

Orbital radar was also generated in the Seasat mission of 1978 to map the oceans and continents of the Earth (e.g. TELEKI and RAMSEIER, 1978). Results are going to be shown in chapters 4 and 5. The characteristic radar image projection leads to typical distortion of high relief.

1.4.3 Some Observations on Geometry

In order to correctly interpret a radar image it is necessary to understand the imaging geometry. Echo time imaging is the basis of SIR. Therefore all points on the planet's surface that are at the same distance from the antenna will project into the same image point. We have here a "range projection" as opposed to the central projection of camera imaging. A crater on the Moon was therefore imaged by the ALSE sytem as shown in Figure 1.12. The bottom of the crater is imaged, but the sidewall is laid over it in the projection.

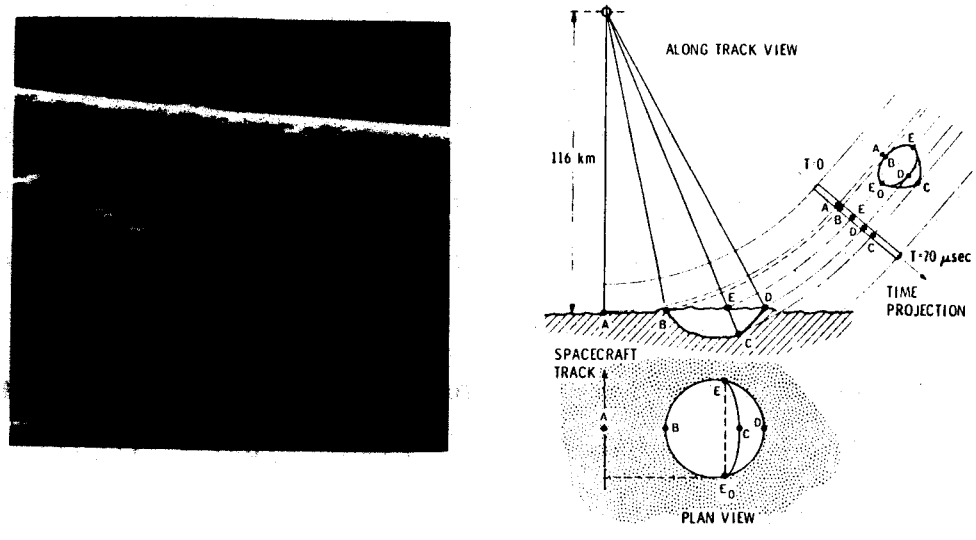

Figure 1.12 ALSE radar image of a lunar crater and geometrical sketch to explain imaging geometry for this crater using the range geometry

In Seasat and in ALSE, the surface was viewed under steep look angles, with the imaged area at about 20 degrees off-nadir in Seasat, and even near nadir in ALSE. Usually one has not with aircraft radar such steep look angles, but prefers to use much larger ones, anywhere between 45 degrees to 80 degrees, depending on the local circumstances and the purpose of the project. From orbital altitudes one cannot expect to achieve large look angles as with aircraft radar due to radar design

constraints.

Geometric resolution of SAR is not a function of the distance to the object, but entirely a design parameter. Resolution improves with increasing look angle off-nadir. This is another reason why one prefers larger look angles for imaging. Near nadir resolution is poor. Current aircraft high performance mapping radars resolve the ground with 3 m to 10 m. Seasat nominally provided a 25 m ground resolution.

1.4.4 Expected Results from a Venus Radar Mission

Seasat SAR images of land areas on the Earth can be used to simulate expected Venus images. Figure 1.13 shows a sequence of Seasat images with artificially degraded geometric resolution to approach that one expected for a Venus project, and from improved Earth based radar. There are thus images at 4 km, 600 m and 150 m per line pair resolutions. Visual inspection quickly reveals that a radar orbiter -if successful- will greatly improve our knowledge of the planet Venus over the state of knowledge available today or to be anticipated with even improved Earth based radar imaging.

(Figure 1.13 (d))

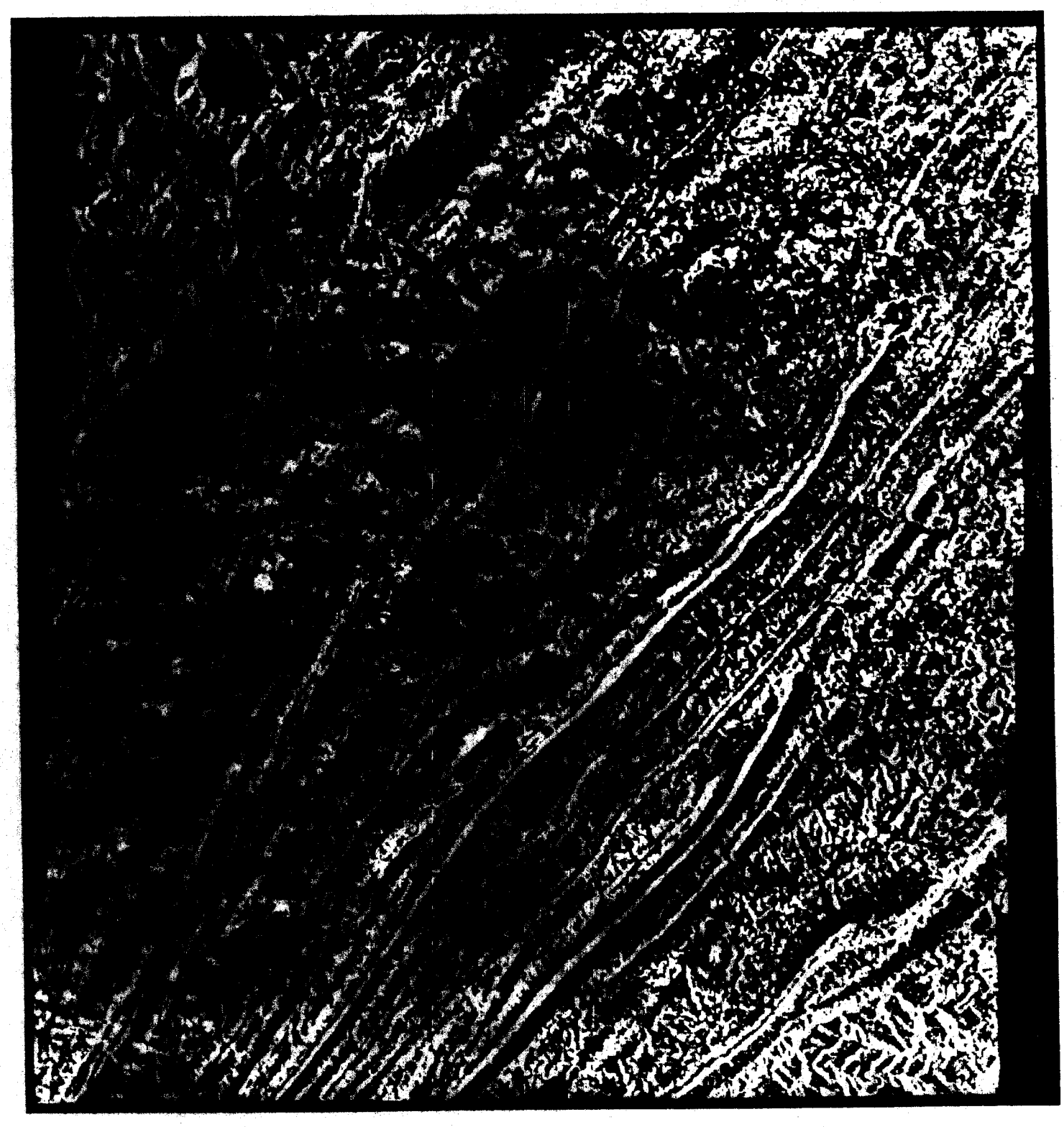

(Figure 1.13 (b))

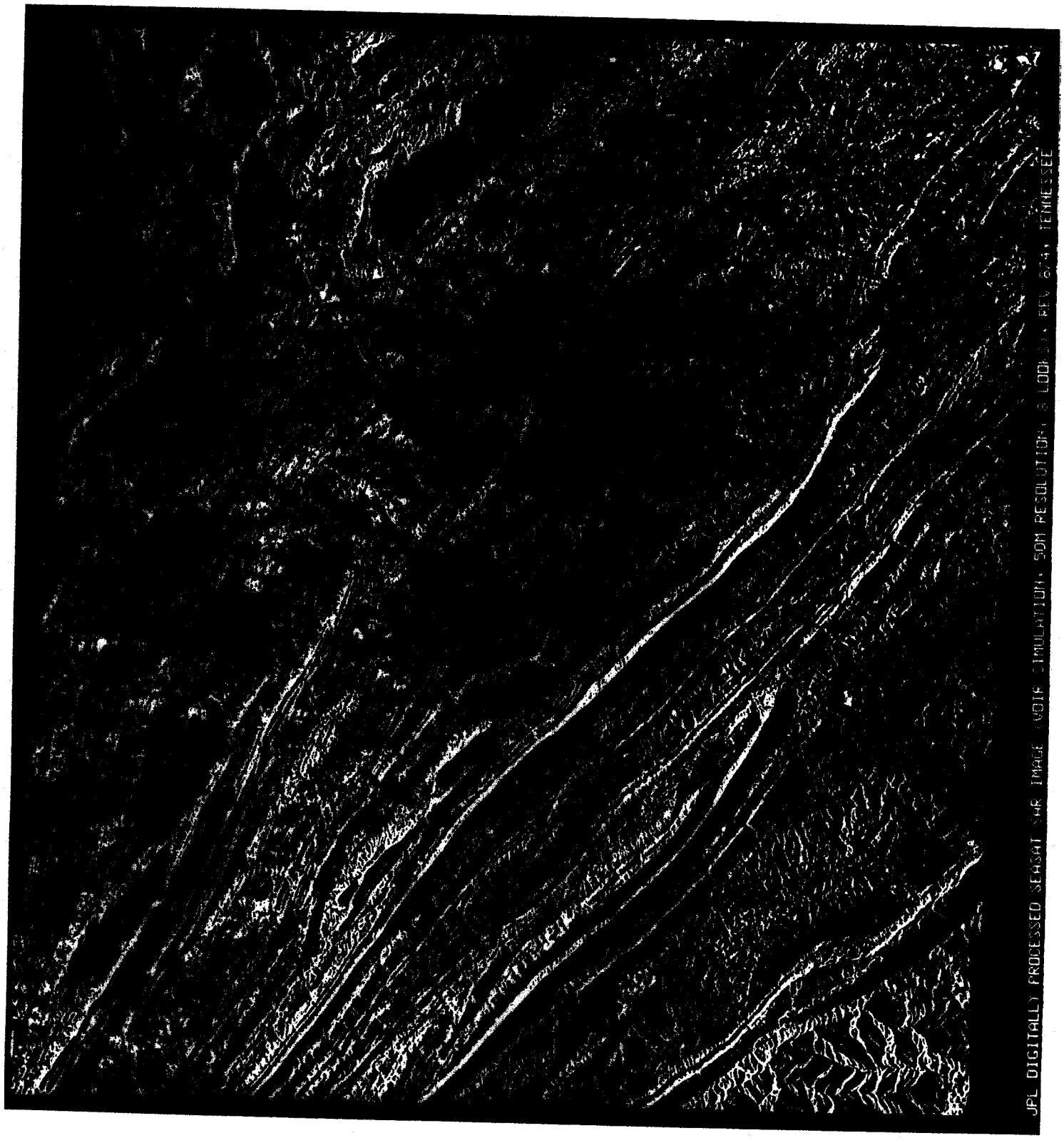

(Figure 1.13 (c))

Figure 1.13 Expected future Venus radar images, demonstrated and derived from SEASAT SAR of the Apalachian Fault Belt, Tennessee.
(a) 4 km resolution of the future Earth based imaging;
(b) 600 m per line pair;
(c) 150 m per line pair.

C H A P T E R 2

RIGOROUS MATHEMATICAL FORMULATIONS FOR SINGLE-IMAGE SYNTHETIC APERTURE RADAR MAPPING

We will need in this study a set of basic formulas to model the radar imaging process in a satellite sensor. Such formulas were presented for the first time by ROSENFIELD (1968), however for real aperture radar. Then GRACIE et al.(1970) and others successfully implemented similar equations in work with actual images. The specific requirements for synthetic aperture satellite radargrammetry were analysed by LEBERL (1978).

The following is, first of all, a review of these formulas so that they are then available for easy reference in subsequent parts of this study. We then address the various techniques for analytical (digital) single image radar mapping.

2.1 PROJECTION EQUATION OF SYNTHETIC APERTURE SIDE-LOOKING RADAR

In a synthetic aperture radar system the flight-line of the imaging sensor is defined with positions $\underline{s}$ of the radar sensor as a function of time:

$$\underline{s} = \underline{s}(t) = (x_s(t),\ y_s(t),\ z_s(t))^T$$

Furthermore the projection rays for a given sensor position $\underline{s}$ form a surface that might in general be a cone or, as a special case, a plane. The orientation of the surface in space

is defined by the velocity vector $\dot{\underline{s}}$ of the sensor, which is given as first derivative of $\underline{s}$:

$$\dot{\underline{s}}(t) = (\dot{x}_s(t),\ \dot{y}_s(t),\ \dot{z}_s(t))^T$$

The basic measurements of a single radar image are the slant range r_p, i. e. the distance between sensor locations and imaged ground point p, and the time t of imaging p.

According to Figure 2.1 the coordinates of ground point p in a geo- or planetocentric coordinate system $(\underline{x},\underline{y},\underline{z})$ are obtained by the following equations (2.1):

$$\begin{aligned} \underline{p} &= \underline{s} + \underline{r} \\ \text{with}\quad \underline{r} &= \underline{A}.\underline{p}^* \end{aligned} \qquad (2.1)$$

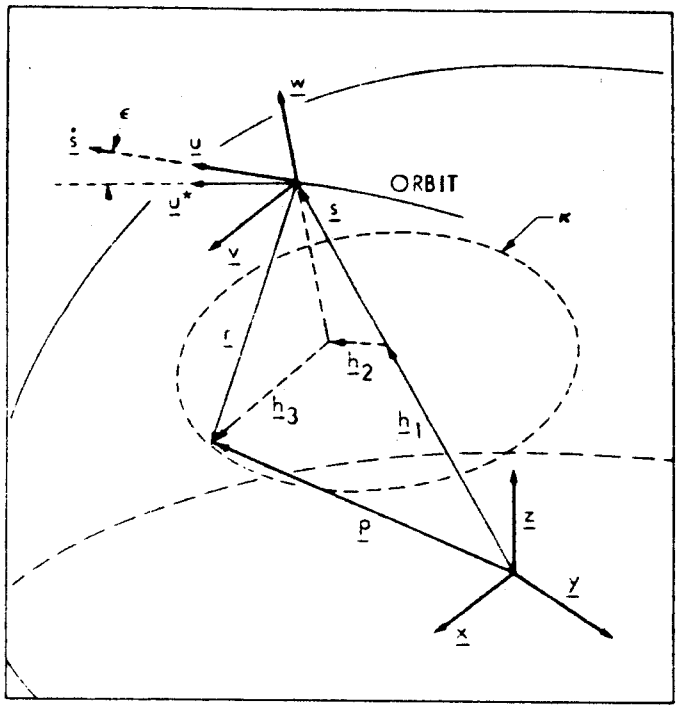

Figure 2.1 Definition of entities in a planetocentric coordinate system

Vector $\underline{p}^*$ describes the location of ground point p in an antenna coordinate system ($\underline{u}$,$\underline{v}$,$\underline{w}$) (see Figure 2.2) :

$$\underline{p}^* = r_p \cdot \begin{bmatrix} \sin\tau \\ (\sin^2\Omega - \sin^2\tau)^{1/2} \\ -\cos\Omega \end{bmatrix} = \begin{bmatrix} u_p \\ v_p \\ w_p \end{bmatrix} \qquad (2.2)$$

r_p .....slant range for p

Ω ......elevation angle of projection ray

τ ......'squint angle' or 'cone-complement angle' of the cone defined by the radar beam.

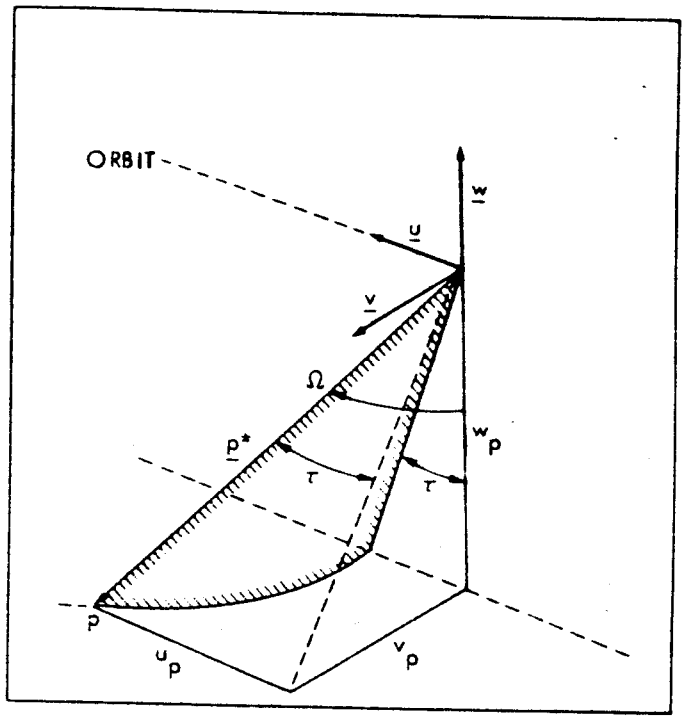

Figure 2.2 Definition of entities in the antenna coordinate system

The matrix $\underline{A}$ of equations (2.1) describes the rotation between antenna coordinate system $\underline{u}$, $\underline{v}$, $\underline{w}$ parallel to the system $\underline{x}$, $\underline{y}$, $\underline{z}$, which in turn defines the planetocentric coordinate system. Therefore $\underline{A}$ consists of the components of $\underline{u}$, $\underline{v}$ and $\underline{w}$:

$$\underline{A} = \begin{bmatrix} x_u & y_u & z_u \\ x_v & y_v & z_v \\ x_w & y_w & z_w \end{bmatrix} \qquad (2.3)$$

For real aperture radar (RAR) the antenna coordinate system is defined by the attitude of the real antenna. In this case the matrix $\underline{A}$ contains the orientation angles φ , ω , $\varkappa$ as known from traditional photogrammetry. For a synthetic aperture radar (SAR) system the antenna coordinate system is defined by the velocity vector of the real antenna and the vectors $\underline{u}$, $\underline{v}$ and $\underline{w}$ are functions of $\underline{s}$ and $\dot{\underline{s}}$:

$$\begin{aligned} \underline{u} &= \dot{\underline{s}} \;/\; |\dot{\underline{s}}| \\ \underline{v} &= (\underline{s} \times \dot{\underline{s}}) \;/\; |\underline{s} \times \dot{\underline{s}}| \\ \underline{w} &= (\underline{u} \times \underline{v}) \;/\; |\underline{u} \times \underline{v}| \end{aligned} \tag{2.4}$$

An alternative formulation of equations (2.1) and (2.2) is obtained if Ω is eliminated:

$$|\underline{p} - \underline{s}| = r \tag{2.5}$$

$$\underline{u}.(\underline{p} - \underline{s}) = \sin\tau \,.|\underline{u}|.|\underline{p} - \underline{s}| \tag{2.6}$$

Equations (2.5) and (2.6) define two surfaces of the location of an object point p. These are, on the one hand, a shere with its center at sensor position $\underline{s}$ and radius r_r ('range sphere') and, on the other hand, a cone with the axis along vector $\underline{u}$ and the 'cone-complement angle' τ . If $\tau = \emptyset$, the cone degenerates to a plane ('scanning plane'):

$$\underline{u}.(\underline{p} - \underline{s}) = \emptyset \tag{2.7}$$

2.2 RIGOROUS METHODS OF SINGLE-IMAGE RADAR

2.2.1 Inputs to Single-Image Radargrammetry:

The inputs of single-image radargrammetry consist of:

(a) Measurements of slant ranges r_p and so called 'sensor event times' t_p of imaging of a selected number of image points p . r_p and t_p are obtained of image coordinates x,y with equations 2.8, where f_r is a scale factor in across-track(y)-direction and f_t is a scale factor in x-direction (compare Figure 2.3)

$$\begin{aligned} r_p &= y_p . f_r + c \\ t_p &= t_o + f_t . (x_p - x_o) \end{aligned} \qquad (2.8)$$

(b) Measurements of sensor positions $\underline{s}(t)$ and the corresponding sensor velocity vector $\dot{\underline{s}}(t)$.

(c) Position vectors g of a number of ground control points.

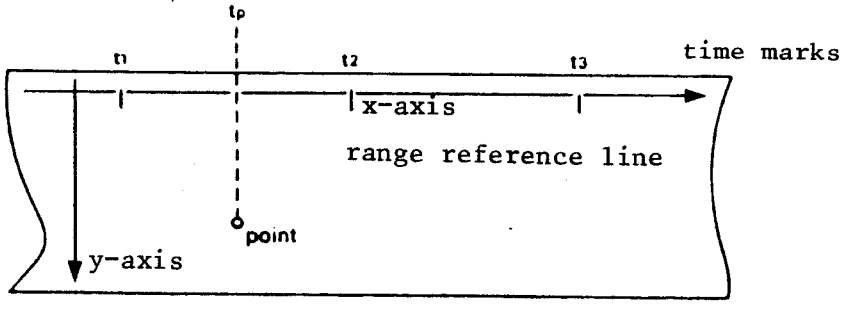

Figure 2.3 Definition of image coordinate system

The sensor positions $\underline{s}$ at times t_i and $t_i + \Delta t$ are correlated. Mathematically this can be expressed in one of several ways. Methods that have been discussed employ an

are assumed to be error-free constants, only the slant ranges (r' and r'') and the times of imaging (t' and t'') remain as measurements. The polynomial coefficients and approximate values for p are again evaluated from the single radar images. This algorithm was formulated by GRACIE (1970).

The most general formulation of a radar stereo model would require the assumption that both times of imaging and sensor positions $\underline{s}$ with velocity vector $\dot{\underline{s}}$ are introduced as measurements. $\underline{s}$ and $\dot{\underline{s}}$ again should be represented with one of the above mentioned methods, for example time polynomials.

The coefficients of these polynomials (for both images of the stereo pair) and the corrections to the measurements for slant ranges (r' ,r'') and times (t' ,t'') can be evaluated by a simultanous adjustment, following the rules of least squares. Also ground control points g can be introduced in this adjustment.

The equation systems for such a rigorous formulation are presented in the following section, taking once equations (3.1) as the basic equations for each point (Case A) and once equations 3.2 (Case B). For both formulations the sensor positions $\underline{s}'$,$\underline{s}''$ are defined as time polynomials of k-th order (compare equations 2.9) and the sensor velocity vectors $\dot{\underline{s}}'$, $\dot{\underline{s}}''$ therefore obviously are obtained as the first derivatives of these polynomials :

$$x_s(t) = a_o + a_1.t + a_2.t^2 + a_3.t^3 + \ldots$$
$$y_s(t) = b_o + b_1.t + b_2.t^2 + b_3.t^3 + \ldots \qquad (2.10)$$
$$z_s(t) = c_o + c_1.t + c_2.t^2 + c_3.t^3 + \ldots$$

A solution for the polynomial coefficients a_o ....c_i is again found with a least squares algorithm, so that a sensor position $\underline{s}$ can be computed for any given value of time t. The velocity vector $\dot{\underline{s}}$ of the sensor is given by the first derivatives of equations (2.10).

2.2.2 Computation of Coordinates of Imaged Points p

With a known sensor position and attitude the three equations (2.1) are insufficient to solve for the four unknowns x_p, y_p, z_p and Ω and therefore are underdetermined. Therefore one of the unknowns has to be given or to be measured externally to solve for the other three. In single-image radargrammetry it makes sense to assume a value for the height of an object; in many applications this can be zero, implying an image of the sea surface.

The coordinates of the ground point p in a planeto(geo-)centric coordinate system are then computed by the intersection of three geometrical surfaces :

(1) the geometrical shape of the object, namely the planetary surface : This can be a sphere with radius R, or more generally , an ellipsoid with a and b as the lengths of equatorial and polar semi-axes. Obviously the center of this figure should be the center of the planeto(geo-)centric system.

(2) a sphere with radius r_p (slant range) and center at

The solution for coordinate corrections Δp is found by a least squares algorithm:

$$\begin{aligned} \underline{Q}_{\Delta p} &= (\underline{D}^T.(\underline{C}.\underline{G}^{-1}.\underline{C}^T)^{-1}.\underline{D})^{-1} \\ \Delta \underline{p} &= -\underline{Q}_p.\underline{D}^T.(\underline{C}.\underline{G}^{-1}.\underline{C}^T)^{-1}.\underline{w} \\ \underline{p} &= \underline{p}_o + \Delta \underline{p} \end{aligned} \qquad (3.4)$$

ad (b):

Equations (3.2) can be written in the form of three conditions:

$$\underline{s}' + \underline{r}'.\underline{A}'.\underline{p}' - \underline{s}'' - \underline{r}''.\underline{A}''.\underline{p}'' = \underline{\emptyset} \qquad (3.5)$$

This is a system of three nonlinear equations for the two unknown elevation angles Ω' and Ω'' Linearization leads to the following correction equations (in matrix formulation):

$$\underline{v} + \underline{E}.\Delta\underline{\Omega} + \underline{w} = \underline{\emptyset} \qquad (3.6)$$

$\Delta\underline{\Omega} = (\Delta\Omega', \Delta\Omega'')$ ... vector of corrections to approximate values for Ω' and Ω''

$\underline{w}$ .....vector of contradictions of equations (3.5)

$\underline{v}$ .....differences between p' and p''.

$\underline{E}$ .....coefficient matrix of linearized system

If one could assume to have sufficiently accurate approximate values $\underline{p}_o$ for the imaged point, a Taylor-linearization would lead to better solutions of this non-linear problem:

$$\begin{aligned} f_1(\underline{p}_o) + f'_1(d\underline{p}) &= f_1(\underline{p}) = \emptyset \\ f_2(\underline{p}_o) + f'_2(d\underline{p}) &= f_2(\underline{p}) = \emptyset \\ f_3(\underline{p}_o) + f'_3(d\underline{p}) &= f_3(\underline{p}) = \emptyset \end{aligned} \qquad (2.13)$$

or

$$\begin{aligned} a_{11}.dx + a_{12}.dy + a_{13}.dz &= w_1 = -f_1(\underline{p}_o) \\ a_{21}.dx + a_{22}.dy + a_{23}.dz &= w_2 = -f_2(\underline{p}_o) \\ a_{31}.dx + a_{32}.dy + a_{33}.dz &= w_3 = -f_3(\underline{p}_o) \end{aligned} \qquad (2.14)$$

a_{ij} ...coefficients of linearization

$d\underline{p}$ ...vector of corrections for approximate values for $\underline{p}$.

$\underline{w}$ ...vector of contradictions of equations (2.12)

$$\begin{aligned} a_{11} &= 2x \,/\, a^2 \\ a_{12} &= 2y \,/\, a^2 \\ a_{13} &= 2z \,/\, b^2 \\ a_{21} &= 2.(x - x_s) \\ a_{22} &= 2.(y - y_s) \\ a_{23} &= 2.(z - z_s) \\ a_{31} &= x_s - \sin\tau\,(x - x_s).|\dot{\underline{s}}|/|\underline{p} - \underline{s}| \\ a_{32} &= y_s - \sin\tau\,(y - y_s).|\dot{\underline{s}}|/|\underline{p} - \underline{s}| \\ a_{33} &= z_s - \sin\tau\,(z - z_s).|\dot{\underline{s}}|/|\underline{p} - \underline{s}| \end{aligned} \qquad (2.15)$$

This can either be

(a) a pair of equations (2.5) and (2.6) (see chapter 2)

$$
\begin{aligned}
|\underline{P} - \underline{S}'| &= r' \\
|\underline{P} - \underline{S}''| &= r'' \\
\underline{u}'.(\underline{P} - \underline{S}') &= \sin\tau'.|\underline{u}'|.|\underline{P} - \underline{S}'| \\
\underline{u}''.(\underline{P} - \underline{S}'') &= \sin\tau''.|\underline{u}''|.|\underline{P} - \underline{S}''|
\end{aligned}
\tag{3.1}
$$

or

(b) a pair of equations (2.1) of chapter 2

$$
\begin{aligned}
\underline{P} &= \underline{S}' + r'.\underline{A}'.\underline{p}' \\
\underline{P} &= \underline{S}'' + r''.\underline{A}''.\underline{p}''
\end{aligned}
\tag{3.2}
$$

ad (a):

The four equations (3.1) are nonlinear and contain the three unknown coordinates (x_p, y_p, z_p) of ground point P. Their linearization leads to the following correction equations for every point (in matrix notation):

$$\underline{C}.\underline{v} + \underline{D}.\Delta\underline{p} + \underline{w} = \emptyset \tag{3.3}$$

$\Delta\underline{p} = (\Delta x_p, \Delta y_p, \Delta z_p)$... vector of corrections to approximate values for p $(p_o = (x_o, y_o, z_o)^T)$.

$\underline{v}$..... vector of the 16 observation corrections for s', s'', $\dot{s}'$, $\dot{s}''$, r', r'', τ', τ''

$\underline{w}$..... vector of contradictions of equations (3.1)

2.2.3 Use of Ground Control Points

The use of ground control points is mostly in one of three ways: either interpolatively or parametrically or in a mixed (hybrid) form:

(a) interpolatively: The interpolatively use of ground control points is based on imaging equations as follows :

$$\begin{bmatrix} x \\ y \\ z \end{bmatrix} = \underline{s} + \underline{A} \cdot \begin{bmatrix} u + \Delta u \\ v + \Delta v \\ w + \Delta w \end{bmatrix}$$

The differences between radargrammetrically computed position vectors p and corresponding ground points g are used to interpolate corrections in radargrammetric points with polynomials or other interpolation methods.

(b) parametric: In this case the basic imaging equations are

$$\begin{bmatrix} x \\ y \\ z \end{bmatrix} = \underline{s}(t) + \underline{A}(t) \cdot \begin{bmatrix} u \\ v \\ w \end{bmatrix}$$

The ground control points serve for the computation of corrections to measured or approximate values of the sensor positions $\underline{s}$, velocity vectors $\dot{\underline{s}}$ and elements of interior orientation.

(c) hybrid technigue: For the hybrid technique the imaging equations are given as follows :

$$\begin{bmatrix} x \\ y \\ z \end{bmatrix} = \underline{s}(t) + \underline{A}(t) \cdot \begin{bmatrix} u + \Delta u \\ v + \Delta v \\ w + \Delta w \end{bmatrix}$$

C H A P T E R 3

MATHEMATICAL METHODS OF STEREO RADAR MAPPING

We can work with mathematical stereo radar formulations of varying degrees of complexity. An original mathematical contribution was by ROSENFIELD (1968), and was used by GRACIE et al.(1970) with synthetic aperture radar images. LEBERL (1972) performed an error analysis, DBA (1974) and DOWIDEIT (1977) dealt with aircraft radar strips, whereas LEBERL (1978,1979) discussed satellite radar. Simplified models were used by DERENYI (1974,1975), by KOOPMANS (1974), LA PRADE (1963,1970) and by LEBERL (1979 a,b). An implementation on a photogrammetric stereo plotter was attempted by NORVELLE (1972) and by AUTOMETRIC (1981). In the following we will review the general formulations and discuss several special cases.

3.1 INTERIOR ORIENTATION

In the sense of photogrammetry the process of interior orientation refers to the determination of the principal point and the principal distance (focal length) of a photo. In a radar imaging system there are no such entities and the principal point as the origin of the image coordinate system theoretically can be placed anywhere on the radar image. However, according to Figure 2.3 it will be usually chosen at the near range edge of the image with the x-axis showing in flight direction. Interior orientation in radargrammetry is therefore based on determining the x-axis as the range reference

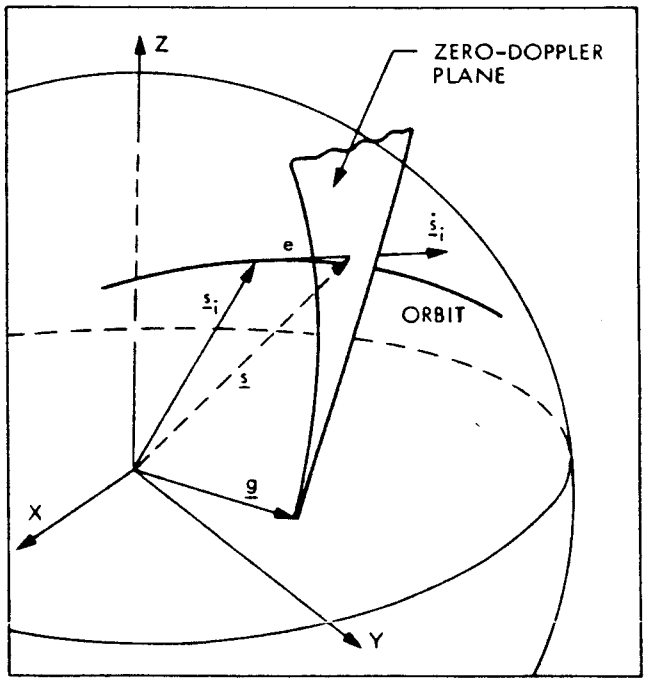

Figure 2.4 Intersection of imaging surface (plane) and orbit

If the flight line is represented as a time polynomial, $\underline{s}_g$ is computed with the condition (2.18a):

$$\dot{\underline{s}}.(\underline{g} - \underline{s}_g)/|\dot{\underline{s}}|.|\underline{g} - \underline{s}_g| = \sin\tau \qquad (2.18a)$$

or if the cone degenerates to a plane

$$\dot{\underline{s}}.(\underline{g} - \underline{s}_g) = 0 \qquad (2.18b)$$

In formulas (2.17a) and (2.18a) it is assumed, that the squint angle τ is counted positively in flight direction, that is defined by the directional vectors $\dot{\underline{s}}_i$ or $\dot{\underline{s}}$, respectively, and negative against flight direction, so that one can get unambiguous solutions for $\underline{s}_g$.

Calibration polynomials for slant range and time

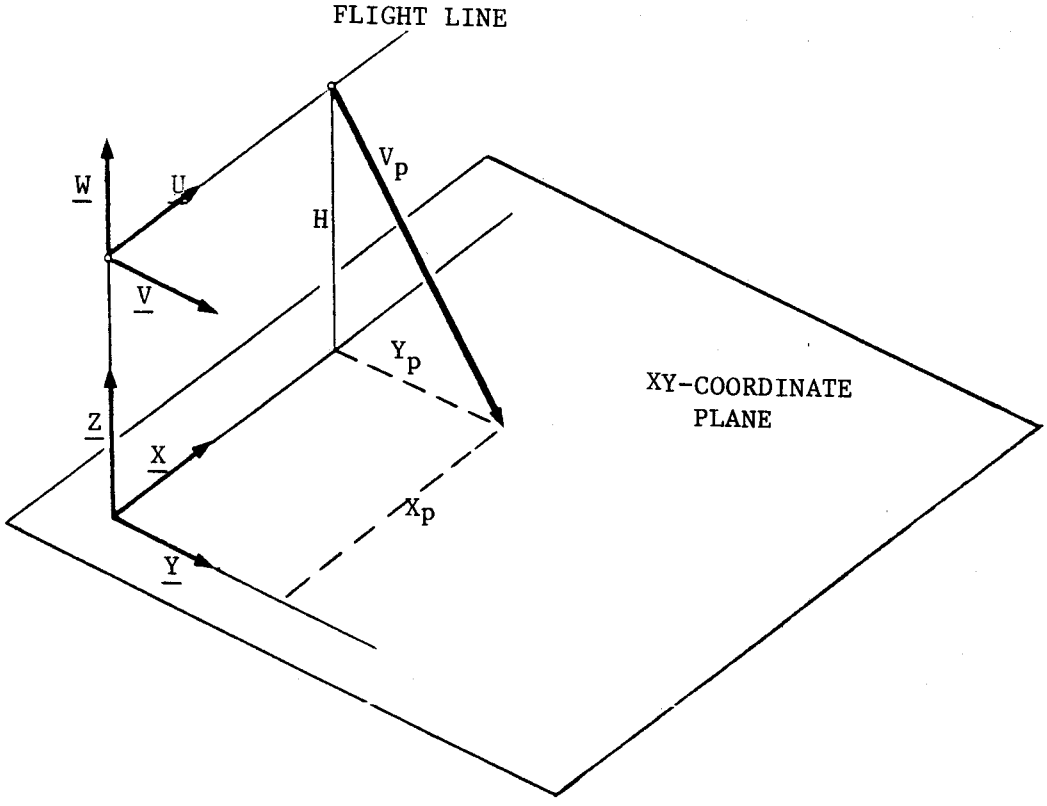

Figure 2.5 Arrangement of coordinate systems for simplified coordinate evaluations

This leads to three equations for the solution of four unknowns x , y , z and Ω :

$$\begin{bmatrix} x \\ y \\ z \end{bmatrix} = \begin{bmatrix} x_s \\ 0 \\ H \end{bmatrix} + r. \begin{bmatrix} 0 \\ \sin\Omega \\ -\cos\Omega \end{bmatrix} \qquad (2.19)$$

As for the rigorous solution one might assume the height z of the image point referenced to the x,y-plane to be zero.

Then the coordinates of the imaged point are computed after eliminating the elevation angle Ω as follows:

$$\begin{aligned} x &= x_s \\ y &= (r^2 - H^2)^{1/2} \\ z &= 0 \end{aligned} \qquad (2.20)$$

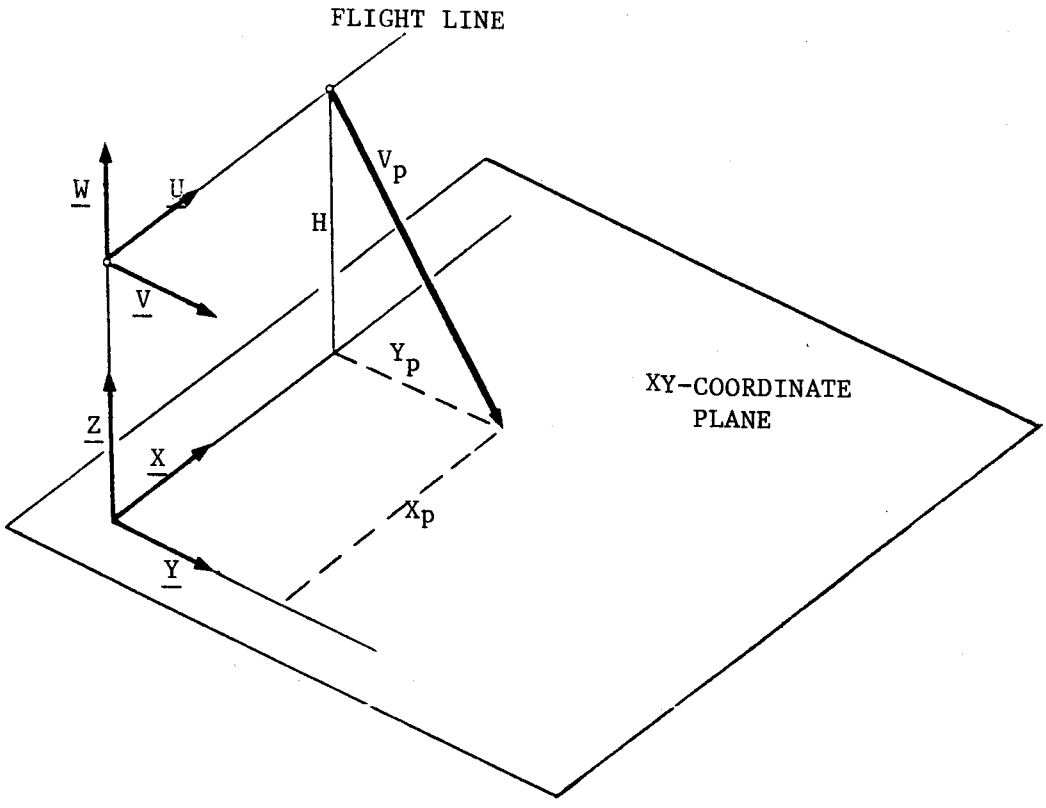

Figure 2.5 Arrangement of coordinate systems for simplified coordinate evaluations

This leads to three equations for the solution of four unknowns x , y , z and Ω :

$$\begin{bmatrix} x \\ y \\ z \end{bmatrix} = \begin{bmatrix} x_s \\ 0 \\ H \end{bmatrix} + r. \begin{bmatrix} 0 \\ \sin\Omega \\ -\cos\Omega \end{bmatrix} \qquad (2.19)$$

As for the rigorous solution one might assume the height z of the image point referenced to the x,y-plane to be zero.

Then the coordinates of the imaged point are computed after eliminating the elevation angle Ω as follows:

$$\begin{aligned} x &= x_s \\ y &= (r^2 - H^2)^{1/2} \\ z &= 0 \end{aligned} \qquad (2.20)$$

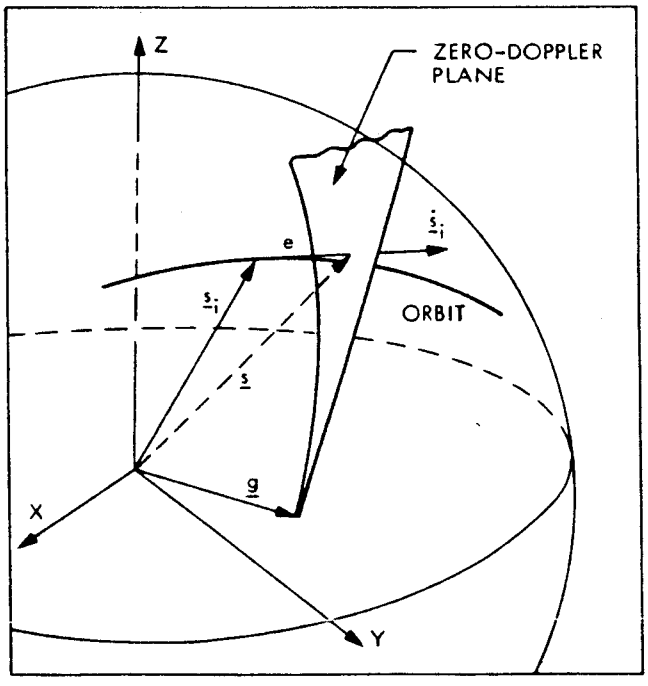

Figure 2.4 Intersection of imaging surface (plane) and orbit

If the flight line is represented as a time polynomial, $\underline{s}_g$ is computed with the condition (2.18a):

$$\dot{\underline{s}}.(\underline{g} - \underline{s}_g)/|\dot{\underline{s}}|.|\underline{g} - \underline{s}_g| = \sin\tau \qquad (2.18a)$$

or if the cone degenerates to a plane

$$\dot{\underline{s}}.(\underline{g} - \underline{s}_g) = 0 \qquad (2.18b)$$

In formulas (2.17a) and (2.18a) it is assumed, that the squint angle τ is counted positively in flight direction, that is defined by the directional vectors $\dot{\underline{s}}_i$ or $\dot{\underline{s}}$, respectively, and negative against flight direction, so that one can get unambiguous solutions for $\underline{s}_g$.

Calibration polynomials for slant range and time

C H A P T E R 3

MATHEMATICAL METHODS OF STEREO RADAR MAPPING

We can work with mathematical stereo radar formulations of varying degrees of complexity. An original mathematical contribution was by ROSENFIELD (1968), and was used by GRACIE et al.(1970) with synthetic aperture radar images. LEBERL (1972) performed an error analysis, DBA (1974) and DOWIDEIT (1977) dealt with aircraft radar strips, whereas LEBERL (1978,1979) discussed satellite radar. Simplified models were used by DERENYI (1974,1975), by KOOPMANS (1974), LA PRADE (1963,1970) and by LEBERL (1979 a,b). An implementation on a photogrammetric stereo plotter was attempted by NORVELLE (1972) and by AUTOMETRIC (1981). In the following we will review the general formulations and discuss several special cases.

3.1 INTERIOR ORIENTATION

In the sense of photogrammetry the process of interior orientation refers to the determination of the principal point and the principal distance (focal length) of a photo. In a radar imaging system there are no such entities and the principal point as the origin of the image coordinate system theoretically can be placed anywhere on the radar image. However, according to Figure 2.3 it will be usually chosen at the near range edge of the image with the x-axis showing in flight direction. Interior orientation in radargrammetry is therefore based on determining the x-axis as the range reference

2.2.3 Use of Ground Control Points

The use of ground control points is mostly in one of three ways: either interpolatively or parametrically or in a mixed (hybrid) form:

(a) interpolatively: The interpolatively use of ground control points is based on imaging equations as follows :

$$\begin{bmatrix} x \\ y \\ z \end{bmatrix} = \underline{s} + \underline{A} \cdot \begin{bmatrix} u + \Delta u \\ v + \Delta v \\ w + \Delta w \end{bmatrix}$$

The differences between radargrammetrically computed position vectors p and corresponding ground points g are used to interpolate corrections in radargrammetric points with polynomials or other interpolation methods.

(t) parametric: In this case the basic imaging equations are

$$\begin{bmatrix} x \\ y \\ z \end{bmatrix} = \underline{s}(t) + \underline{A}(t) \cdot \begin{bmatrix} u \\ v \\ w \end{bmatrix}$$

The ground control points serve for the computation of corrections to measured or approximate values of the sensor positions $\underline{s}$, velocity vectors $\dot{\underline{s}}$ and elements of interior orientation.

(c) hybrid technigue: For the hybrid technique the imaging equations are given as follows :

$$\begin{bmatrix} x \\ y \\ z \end{bmatrix} = \underline{s}(t) + \underline{A}(t) \cdot \begin{bmatrix} u + \Delta u \\ v + \Delta v \\ w + \Delta w \end{bmatrix}$$

This can either be

(a) a pair of equations (2.5) and (2.6) (see chapter 2)

$$\begin{aligned} |\underline{P} - \underline{S}'| &= r' \\ |\underline{P} - \underline{S}''| &= r'' \\ \underline{u}'.(\underline{p} - \underline{s}') &= \sin\tau'.|\underline{u}'|.|\underline{p} - \underline{s}'| \\ \underline{u}''.(\underline{p} - \underline{s}'') &= \sin\tau''.|\underline{u}''|.|\underline{p} - \underline{s}''| \end{aligned} \qquad (3.1)$$

or

(b) a pair of equations (2.1) of chapter 2

$$\begin{aligned} \underline{P} &= \underline{S}' + r'.\underline{A}'.\underline{p}' \\ \underline{P} &= \underline{S}'' + r''.\underline{A}''.\underline{p}'' \end{aligned} \qquad (3.2)$$

ad (a):

The four equations (3.1) are nonlinear and contain the three unknown coordinates (x_p, y_p, z_p) of ground point P. Their linearization leads to the following correction equations for every point (in matrix notation):

$$\underline{C}.\underline{v} + \underline{D}.\Delta\underline{p} + \underline{w} = \emptyset \qquad (3.3)$$

$\Delta\underline{P} = (\Delta x_p, \Delta y_p, \Delta z_p)$... vector of corrections to approximate values for p ($p_o = (x_o, y_o, z_o)^T$).

$\underline{v}$..... vector of the 16 observation corrections for s', s'', $\dot{s}'$, $\dot{s}''$, r', r'', τ', τ''

$\underline{w}$..... vector of contradictions of equations (3.1)

If one could assume to have sufficiently accurate approximate values $\underline{p}_o$ for the imaged point, a Taylor-linearization would lead to better solutions of this non-linear problem:

$$\begin{aligned} f_1(\underline{p}_o) + f'_1(d\underline{p}) &= f_1(\underline{p}) = \emptyset \\ f_2(\underline{p}_o) + f'_2(d\underline{p}) &= f_2(\underline{p}) = \emptyset \\ f_3(\underline{p}_o) + f'_3(d\underline{p}) &= f_3(\underline{p}) = \emptyset \end{aligned} \qquad (2.13)$$

or

$$\begin{aligned} a_{11}.dx + a_{12}.dy + a_{13}.dz &= w_1 = -f_1(\underline{p}_o) \\ a_{21}.dx + a_{22}.dy + a_{23}.dz &= w_2 = -f_2(\underline{p}_o) \\ a_{31}.dx + a_{32}.dy + a_{33}.dz &= w_3 = -f_3(\underline{p}_o) \end{aligned} \qquad (2.14)$$

a_{ij} ...coefficients of linearization

$d\underline{p}$ ...vector of corrections for approximate values for $\underline{p}$.

$\underline{w}$ ...vector of contradictions of equations (2.12)

$$\begin{aligned} a_{11} &= 2x \,/\, a^2 \\ a_{12} &= 2y \,/\, a^2 \\ a_{13} &= 2z \,/\, b^2 \\ a_{21} &= 2.(x - x_s) \\ a_{22} &= 2.(y - y_s) \\ a_{23} &= 2.(z - z_s) \\ a_{31} &= x_s - \sin\tau\,(x - x_s).|\dot{\underline{s}}|/|\underline{p} - \underline{s}| \\ a_{32} &= y_s - \sin\tau\,(y - y_s).|\dot{\underline{s}}|/|\underline{p} - \underline{s}| \\ a_{33} &= z_s - \sin\tau\,(z - z_s).|\dot{\underline{s}}|/|\underline{p} - \underline{s}| \end{aligned} \qquad (2.15)$$

The solution for coordinate corrections Δp is found by a least squares algorithm:

$$\begin{aligned} \underline{Q}_{\Delta p} &= (\underline{D}^T.(\underline{C}.\underline{G}^{-1}.\underline{C}^T)^{-1}.\underline{D})^{-1} \\ \Delta\underline{p} &= -\underline{Q}_p.\underline{D}^T.(\underline{C}.\underline{G}^{-1}.\underline{C}^T)^{-1}.\underline{w} \\ \underline{p} &= \underline{p}_o + \Delta\underline{p} \end{aligned} \qquad (3.4)$$

ad (b):

Equations (3.2) can be written in the form of three conditions:

$$\underline{s}' + r'.\underline{A}'.\underline{p}' - \underline{s}'' - r''.\underline{A}''.\underline{p}'' = \emptyset \qquad (3.5)$$

This is a system of three nonlinear equations for the two unknown elevation angles Ω' and Ω'' Linearization leads to the following correction equations (in matrix formulation):

$$\underline{v} + \underline{E}.\Delta\underline{\Omega} + \underline{w} = \emptyset \qquad (3.6)$$

$\Delta\underline{\Omega} = (\Delta\Omega', \Delta\Omega'')$ ... vector of corrections to approximate values for Ω' and Ω''

$\underline{w}$.....vector of contradictions of equations (3.5)

$\underline{v}$.....differences between p' and p''.

$\underline{E}$.....coefficient matrix of linearized system

$$x_s(t) = a_o + a_1.t + a_2.t^2 + a_3.t^3 + \ldots$$
$$y_s(t) = b_o + b_1.t + b_2.t^2 + b_3.t^3 + \ldots \qquad (2.10)$$
$$z_s(t) = c_o + c_1.t + c_2.t^2 + c_3.t^3 + \ldots$$

A solution for the polynomial coefficients a_o ....c_i is again found with a least squares algorithm, so that a sensor position $\underline{s}$ can be computed for any given value of time t. The velocity vector $\dot{\underline{s}}$ of the sensor is given by the first derivatives of equations (2.10).

2.2.2 Computation of Coordinates of Imaged Points p

With a known sensor position and attitude the three equations (2.1) are insufficient to solve for the four unknowns x_p, y_p, z_p and Ω and therefore are underdetermined. Therefore one of the unknowns has to be given or to be measured externally to solve for the other three. In single-image radargrammetry it makes sense to assume a value for the height of an object; in many applications this can be zero, implying an image of the sea surface.

The coordinates of the ground point p in a planeto(geo-)centric coordinate system are then computed by the intersection of three geometrical surfaces :

(1) the geometrical shape of the object, namely the planetary surface : This can be a sphere with radius R, or more generally , an ellipsoid with a and b as the lengths of equatorial and polar semi-axes. Obviously the center of this figure should be the center of the planeto(geo-)centric system.

(2) a sphere with radius r_p (slant range) and center at

are assumed to be error-free constants, only the slant ranges (r' and r'') and the times of imaging (t' and t'') remain as measurements. The polynomial coefficients and approximate values for p are again evaluated from the single radar images. This algorithm was formulated by GRACIE (1970).

The most general formulation of a radar stereo model would require the assumption that both times of imaging and sensor positions $\underline{s}$ with velocity vector $\dot{\underline{s}}$ are introduced as measurements. $\underline{s}$ and $\dot{\underline{s}}$ again should be represented with one of the above mentioned methods, for example time polynomials.

The coefficients of these polynomials (for both images of the stereo pair) and the corrections to the measurements for slant ranges (r', r'') and times (t', t'') can be evaluated by a simultanous adjustment, following the rules of least squares. Also ground control points g can be introduced in this adjustment.

The equation systems for such a rigorous formulation are presented in the following section, taking once equations (3.1) as the basic equations for each point (Case A) and once equations 3.2 (Case B). For both formulations the sensor positions $\underline{s}'$, $\underline{s}''$ are defined as time polynomials of k-th order (compare equations 2.9) and the sensor velocity vectors $\dot{\underline{s}}'$, $\dot{\underline{s}}''$ therefore obviously are obtained as the first derivatives of these polynomials :

2.2 RIGOROUS METHODS OF SINGLE-IMAGE RADAR

2.2.1 Inputs to Single-Image Radargrammetry:

The inputs of single-image radargrammetry consist of:

(a) Measurements of slant ranges r_p and so called 'sensor event times' t_p of imaging of a selected number of image points p . r_p and t_p are obtained of image coordinates x,y with equations 2.8, where f_r is a scale factor in across-track(y)-direction and f_t is a scale factor in x-direction (compare Figure 2.3)

$$\begin{aligned} r_p &= y_p . f_r + c \\ t_p &= t_o + f_t . (x_p - x_o) \end{aligned} \qquad (2.8)$$

(b) Measurements of sensor positions $\underline{s}(t)$ and the corresponding sensor velocity vector $\dot{\underline{s}}(t)$.

(c) Position vectors g of a number of ground control points.

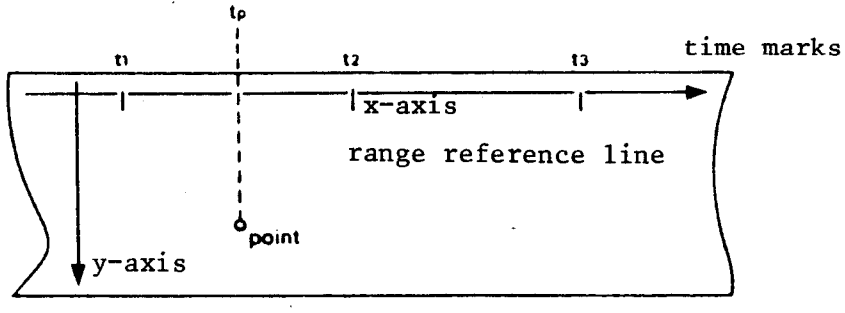

Figure 2.3 Definition of image coordinate system

The sensor positions $\underline{s}$ at times t_i and $t_i + \Delta t$ are correlated. Mathematically this can be expressed in one of several ways. Methods that have been discussed employ an

$$
\begin{aligned}
v_{x_s}' &= da_o' + t'da_1' + \ldots + t'^k da_k' - x_s' \\
v_{y_s}' &= db_o' + t'db_1' + \ldots + t'^k db_k' - y_s' \\
v_{z_s}' &= dc_o' + t'dc_1' + \ldots + t'^k dc_k' - z_s' \\
v_{x_s}'' &= da_o'' + t''da_1'' + \ldots + t''^k da_k'' - x_s'' \\
v_{y_s}'' &= db_o'' + t''db_1'' + \ldots + t''^k db_k'' - y_s'' \\
v_{z_s}'' &= dc_o'' + t_1''dc'' + \ldots + t''^k dc_k'' - z_s''
\end{aligned}
\qquad (3.11)
$$

or in matrix notation

$$
\begin{bmatrix} \underline{v}_x' \\ \underline{v}_y' \\ \underline{v}_z' \\ \underline{v}_x'' \\ \underline{v}_y'' \\ \underline{v}_z'' \end{bmatrix} = \begin{bmatrix} \underline{M}_x & . & . & 0 & 0 \\ . & \underline{M}_y & & . & . \\ . & & \underline{M}_z & . & . \\ . & & & \underline{M}_x & . \\ . & & & & \underline{M}_y \\ 0 & . & . & \underline{M}_z & 0 \end{bmatrix} \cdot \underbrace{\begin{bmatrix} d\underline{a}' \\ d\underline{b}' \\ d\underline{c}' \\ d\underline{a}'' \\ d\underline{b}'' \\ d\underline{c}'' \end{bmatrix}}_{d\underline{C}} - \begin{bmatrix} \underline{x}_s' \\ \underline{y}_s' \\ \underline{z}_s' \\ \underline{x}_s'' \\ \underline{y}_s'' \\ \underline{z}_s'' \end{bmatrix} \qquad (3.12)
$$

respectively

$$
\underline{v}_1 = \underline{M}_1 . \Delta\underline{u} - \underline{l}_1 \qquad (3.13)
$$

The vector $\Delta\underline{u}$ contains the increments for the unknown polynomial coefficients and squint angles. With $\underline{Q}$ as the inverse of the weight matrix $\underline{G}$ of the observations the normal equations would become

$$
(\underline{M}_1^T . \underline{Q}_1^{-1} . \underline{M}_1) . \Delta\underline{u} = \underline{M}_1^T . \underline{Q}_1^{-1} . \underline{l}_1 \qquad (3.14)
$$

(2) for ground control points :

In this case the equations (3.10) need to be linearized, where the values for the coordinates of the ground control points (x,y,z) can be assumed to be error-free. Since $\underline{s}$ respectively $\dot{\underline{s}}$ are expressed by equations (3.8) respectively (3.9), also their partial derivatives $d\underline{s}$ and $d\dot{\underline{s}}$ need to be replaced by the appropriate derivatives of equations (3.8) and (3.9). Then the observation equations contain the measurements r', r'', t', t'' and the unknown polynomial coefficients and squint angles and therefore their linearization leads to :

$$\underline{C}.\underline{v} + \underline{D}.\Delta\underline{u} = \underline{w} \qquad (3.15)$$

$\underline{C}$ and $\underline{D}$ are coefficient matrices, $\underline{v}$ contains the corrections for the measurements of times and slant ranges and $\underline{w}$ is the vector of contradictions of equations (3.10). Vector $\Delta\underline{u}$ is defined as in equation (3.13).

With the weight matrix $\underline{G}$ of the observations the following normal equations are obtained :

$$(\underline{D}^T.(\underline{C}.\underline{G}^{-1}.\underline{C}^T)^{-1}.\underline{D})^{-1}.\Delta\underline{u} = -\underline{D}^T.(\underline{C}.\underline{G}^{-1}.\underline{C}^T)^{-1}.\underline{w} \qquad (3.16)$$

or, in correspondence with equation (3.13)

$$(\underline{M}_2^T.\underline{G}_2^{-1}.\underline{M}_2).\Delta\underline{u} = \underline{M}_2^T.\underline{G}_2^{-1}.\underline{l}_2 \qquad (3.17)$$

(3) for image points :

In this case also the values x,y,z for the ground coordinates of each imaged point are only approximately known and therefore corrected by increments $\Delta\underline{p} = (dx,dy,dz)$. The linearized observational equations can be written as follows :

$$\underline{C}.\underline{v} + \underline{D}.\Delta\underline{u} + \underline{E}.\Delta\underline{p} = \underline{w} \tag{3.18}$$

A modification of this adjustment problem leads to

$$\underline{v}^* = \underline{D}.\Delta\underline{u} + \underline{E}.\Delta\underline{p} - \underline{w} \tag{3.19}$$

For a number of n image points this can be written as

$$\begin{bmatrix} \underline{v}^*_1 \\ \cdot \\ \cdot \\ \cdot \\ \underline{v}^*_n \end{bmatrix} = \begin{bmatrix} \underline{D}_1 & \underline{E}_1 & \cdot & \cdot & \cdot & \emptyset \\ \cdot & \cdot & \cdot & & & \cdot \\ \cdot & \cdot & & \cdot & & \cdot \\ \cdot & \cdot & & & \cdot & \cdot \\ \underline{D}_n & \emptyset & \cdot & \cdot & \cdot & \underline{E}_n \end{bmatrix} \cdot \begin{bmatrix} \Delta\underline{u} \\ \Delta\underline{p}_1 \\ \cdot \\ \cdot \\ \Delta\underline{p}_n \end{bmatrix} - \begin{bmatrix} \underline{w}_1 \\ \cdot \\ \cdot \\ \cdot \\ \underline{w}_n \end{bmatrix} \tag{3.20}$$

Now the equation system contains also the unknown increments Δp for each imaged ground point p. However, $\underline{E}$ is a band matrix, and for this reason the unknowns Δp easily can be eliminated separately for each image point with the following formulas, where $\underline{G}$ again is the weight matrix for appropriate observations :

$$\underline{F}_i = \underline{E}_i.(\underline{E}_i^T.(\underline{C}_i\underline{G}_i^{-1}.\underline{C}_i^T)^{-1}.\underline{E}_i)^{-1}.\underline{E}_i.(\underline{C}_i\underline{G}_i^{-1}.\underline{C}_i^T)^{-1}$$

$$\underline{M}_{3,i} = (\underline{I} - \underline{P}_i).\underline{D}_i \tag{3.21}$$

$$\underline{l}_{3,i} = (\underline{I} - \underline{P}_i).\underline{w}_i$$

The modified adjustment problem is

$$\underline{v}^* = \underline{M}_3\Delta\underline{u} - \underline{l}_3 \tag{3.22}$$

with the weight matrix $\underline{Q}_3^{-1} = (\underline{D}.\underline{G}^{-1}.\underline{D}^T)^{-1}$ and the normal equations now will become

$$(\underline{M}_3^T.\underline{Q}_3^{-1}.\underline{M}_3).\Delta\underline{u} = \underline{M}_3^T.\underline{Q}_3^{-1}.\underline{l}_3 \tag{3.23}$$

The three equations (3.14), (3.17) and (3.23) lead to solutions for the unknowns $\Delta\underline{u}$ as follows :

$$(\sum_{i=1}^{3} \underline{M}_i^T \cdot \underline{Q}_i^{-1} \cdot \underline{M}_i) \cdot \Delta u = \sum_{i=1}^{3} \underline{M}_i^T \cdot \underline{Q}_i^{-1} \cdot \underline{l}_i$$
$$\underline{Q}_{\Delta u} = (\sum_{i=1}^{3} \underline{M}_i^T \cdot \underline{Q}_i^{-1} \cdot \underline{M}_i) \qquad (3.24)$$

After evaluating the unknowns $\Delta\underline{u}$ also the increments $\Delta\underline{p}$ for the approximate values of the ground coordinates can be computed for each point

$$\Delta\underline{P}_i = (\underline{E}_i^T \cdot (\underline{C}_i \cdot \underline{G}_i^{-1} \cdot \underline{C}_i^T)^{-1} \cdot \underline{E}_i)^{-1} \cdot \underline{E}_i \cdot (\underline{C}_i \cdot \underline{G}_i^{-1} \cdot \underline{C}_i^T)^{-1} \cdot (\underline{w}_i - \underline{D}_i \cdot \Delta\underline{u}) \qquad (3.25)$$

Case B

If equations (3.2) are used as basic equations again three kinds of linearized observational equations are obtained :

(1) for orbit position measurements :

For this kind of observations there is no difference to case A and we get the following normal equations

$$(\underline{N}_1^T \cdot \underline{Q}_1^{-1} \cdot \underline{N}_1) \cdot \Delta\underline{u} = \underline{N}_1^T \cdot \underline{Q}_1^{-1} \cdot \underline{l}_1 \qquad (3.26)$$

(2) for ground control points :

In this case for each point six observation equations are obtained according to equations (3.2) :

$$\underline{s}' + \underline{r}' \cdot \underline{A}' \cdot \underline{p}' - \underline{p} = \underline{0}$$
$$\underline{s}'' + \underline{r}'' \cdot \underline{A}'' \cdot \underline{p}'' - \underline{p} = \underline{0} \qquad (3.27)$$

The orbit positions are again replaced by time polynomials . Therefore the observation equations are functions of the

observations r', r'', t', t'' and the unknown polynomial coefficients, squint angles τ', τ'' and elevation angles Ω', Ω''. Linearization leads to

$$\underline{C}.\underline{v} + \underline{D}.\Delta\underline{u} + \underline{E}.\Delta\underline{\Omega} = \underline{w} \qquad (3.28)$$

or, in a modified adjustment formulation

$$\underline{v}^* = \underline{D}.\Delta\underline{u} + \underline{E}.\Delta\underline{\Omega} - \underline{w} \qquad (3.29)$$

For a number of n ground control points the following linearized observation equations are obtained :

$$\begin{bmatrix} \underline{v}_1^* \\ \cdot \\ \cdot \\ \cdot \\ \underline{v}_n^* \end{bmatrix} = \begin{bmatrix} \underline{D}_1 & \underline{E}_1 & \cdot & \cdot & \cdot & 0 \\ \cdot & \cdot & \cdot & & & \cdot \\ \cdot & \cdot & & \cdot & & \cdot \\ \cdot & \cdot & & & \cdot & \cdot \\ \underline{D}_n & \underline{E}_n & \cdot & \cdot & \cdot & \ell \end{bmatrix} \cdot \begin{bmatrix} \Delta\underline{u} \\ \Delta\Omega_1 \\ \cdot \\ \cdot \\ \Delta\Omega_n \end{bmatrix} - \begin{bmatrix} \underline{w}_1 \\ \cdot \\ \cdot \\ \cdot \\ \underline{w}_n \end{bmatrix} \qquad (3.30)$$

Like in the discussion of case A the unknowns $\Delta\underline{\Omega}_i = (\Delta\Omega'_i, \Delta\Omega''_i)$ can be eliminated for each point with formulas according to equations (3.21), so that again normal equations with only the unknowns $\Delta\underline{u}$ are obtained :

$$\begin{aligned} \underline{v} &= \underline{N}_2.\Delta\underline{u} - \underline{l}_2 \\ \underline{Q}_2 &= \underline{D}.\underline{G}^{-1}.\underline{D}^T \\ (\underline{N}_2^T.\underline{Q}_2^{-1}.\underline{N}_2).\Delta\underline{u} &= \underline{N}_2^T.\underline{Q}_2^{-1}.\underline{l}_2 \end{aligned} \qquad (3.31)$$

(3) for image points :

For each imaged point three equations are obtained :

$$\underline{s}' + r'.\underline{A}'.\underline{p}' - \underline{s}'' - r''.\underline{A}''.\underline{p}'' = 0 \qquad (3.32)$$

$$\underline{C}.\underline{v} + \underline{D}.\Delta\underline{u} + \underline{E}.\Delta\underline{\Omega} = \underline{w}$$
$$\text{or} \quad \underline{v}^{*} = \underline{D}.\Delta\underline{u} + \underline{E}.\Delta\underline{\Omega} - \underline{w} \tag{3.33}$$

In this case also the unknowns $\Delta\underline{\Omega}$ are eliminated for each point as done for ground control points in section (2). The normal equation system is then again

$$(\underline{N}_3^{T}.\underline{Q}_3^{-1}.\underline{N}_3).\Delta\underline{u} = \underline{N}_3^{T}.\underline{Q}_3^{-1}.\underline{l}_3 \tag{3.34}$$

Like for case A the solution for the unknowns $\Delta\underline{u}$ is found by

$$(\sum_{i=1}^{3} \underline{N}_i^{T}.\underline{Q}_i^{-1}.\underline{N}_i).\Delta\underline{u} = \sum_{i=1}^{3} \underline{N}_i^{T}.\underline{Q}_i^{-1}\,\underline{l}_i \tag{3.35}$$

With the adjusted values for $\Delta\underline{u}$ the increments $\Delta\Omega_i'$, $\Delta\Omega_i''$ can be computed for each imaged point with equations (3.36) :

$$\Delta\underline{\Omega}_i = (\underline{E}_i^{T}.(\underline{C}_i.\underline{G}_i^{-1}.\underline{C}_i^{T})^{-1}.\underline{E}_i)^{-1}.\underline{E}_i^{T}.(\underline{C}_i.\underline{G}_i^{-1}.\underline{C}_i^{T})^{-1}.(\underline{w}_i - \underline{D}_i.\Delta\underline{u}) \tag{3.36}$$

The ground coordinates x,y,z of an imaged point then can be determined, when introducing the adjusted polynomial coefficients and elevation angles as well as the corrected measurements r', r", t', t" in equations (3.27).

3.3 SIMPLIFIED STEREO FORMULATIONS

3.3.1 With Measured Slant Ranges

Like for single image radargrammetry one might also choose a local coordinate system for radar stereo evaluations as shown in Figure 3.2.

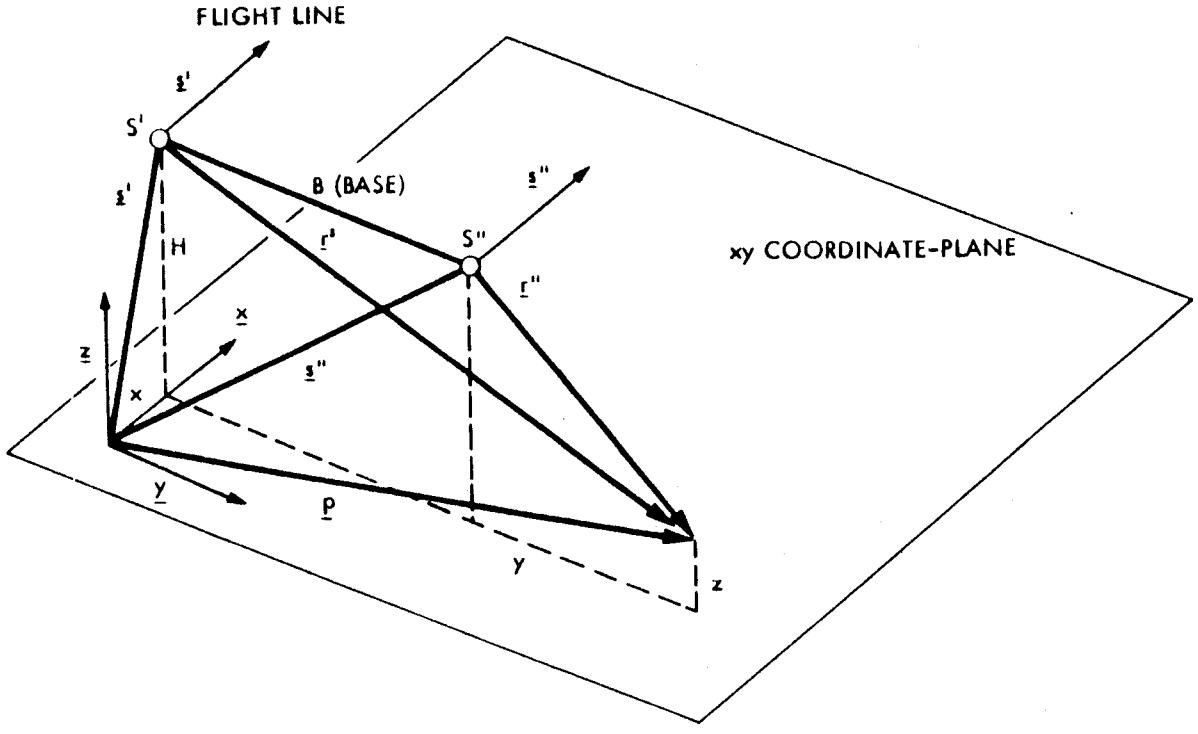

Figure 3.2 Arrangement of coordinate systems for simplified stereo evaluations

In this case the planetary surface is again assumed to be a plane and to be parallel to the flight paths, which are represented by straight lines. The x-axis of this local system is parallel to the flight lines and the y-axis parallel to the stereo base B and therefore the sensor positions $\underline{s}'$ and $\underline{s}''$ and the velocity vectors $\dot{\underline{s}}'$ and $\dot{\underline{s}}''$ are defined as follows:

$$\underline{s}' = (x'_s \,, 0 \,, H)$$
$$\dot{\underline{s}}' = (\dot{x}'_s \,, 0 \,, 0)$$
$$\underline{s}'' = (x''_s \,, B \,, H)$$
$$\dot{\underline{s}}'' = (\dot{x}''_s \,, 0 \,, 0)$$

If these vectors are introduced in equations (3.1) and the squint angle τ is assumed to be zero, one obtains the following equations for the computation of the coordinates of imaged point P:

$$\begin{aligned} x &= (x'_s + x''_s)/2 \\ y &= (-r''^2 + r'^2 + B^2)/2B \\ z &= H-[(r'^2 - y^2) + (r''^2 - (B - y)^2)^{1/2}]/2 \end{aligned} \qquad (3.37)$$

A slightly different approach to compute the height z above a reference datum is still with projection circles :

$$\begin{aligned} y &= \tan\Omega'.(H - z) \\ y &= \pm\tan\Omega''.(H - z) + B \\ z &= H - B/(\tan\Omega' \pm \tan\Omega'') \end{aligned} \qquad (3.38)$$

3.3.2 With Measured Parallaxes

Another simplified technique of stereo radargrammetry can be based on an assumption of rectilinear flight lines, where flight lines (') and (") are parallel. As in aerial photogrammetry the stereo radar images can be used to define height differences h between two points from their parallax differences, Δp. These may be measured for example using a stereoscope and a parallax bar. Because in photogrammetry the projection rays are straight lines (central projection) and in radargrammetry they are circles (range projection), the formulas to convert Δp into Δh are more complex, and they are different depending whether a ground range or a slant range presentation is used for the radar images.

KOOPMANS (1974), DERENYI (1975), LEBERL (1975) and others found

(a) for ground range presentation (see Figure 3.3)

$$p' = \Delta h.\cot \Omega'$$

$$p'' = \Delta h.\cot \Omega''$$

$$\Delta p = p'' - p' = \Delta h.(\cot \Omega'' - \cot \Omega')$$

$$\Delta h = \Delta p/(\cot \Omega'' - \cot \Omega') \qquad (3.39)$$

The plus sign is for opposite side, the minus sign for same side geometry.

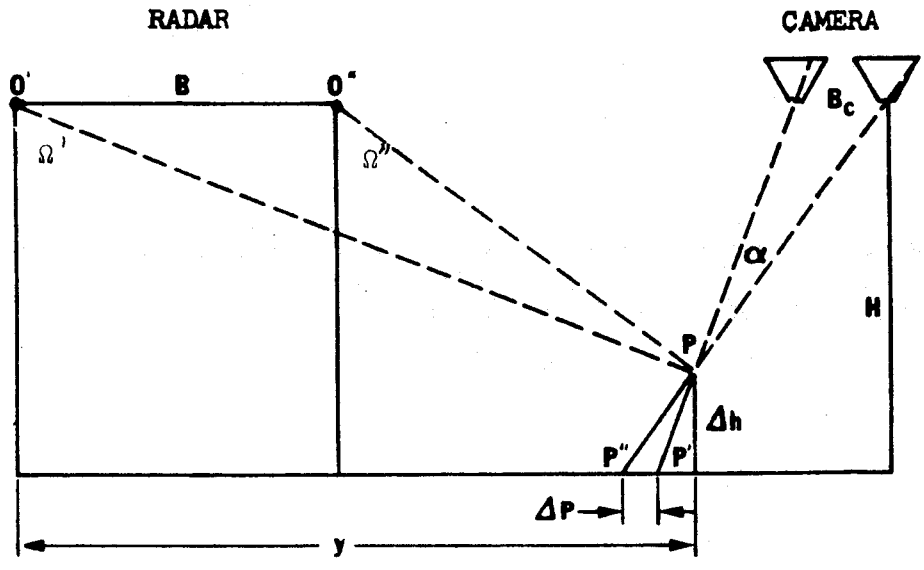

Figure 3.3 Definition of parallax differences Δp for ground range presentation

(b) for slant range presentation (see Figure 3.4)

$$p' = \Delta h.\cos \Omega'$$

$$p'' = \Delta h.\cos \Omega''$$

$$\Delta p = p'' - p' = \Delta h.(\cos \Omega'' - \cos \Omega')$$

$$\Delta h = \Delta p/(\cos \Omega'' - \cos \Omega') \qquad (3.40)$$

The plus sign is again for opposite side and the minus sign for same side stereo arrangements.

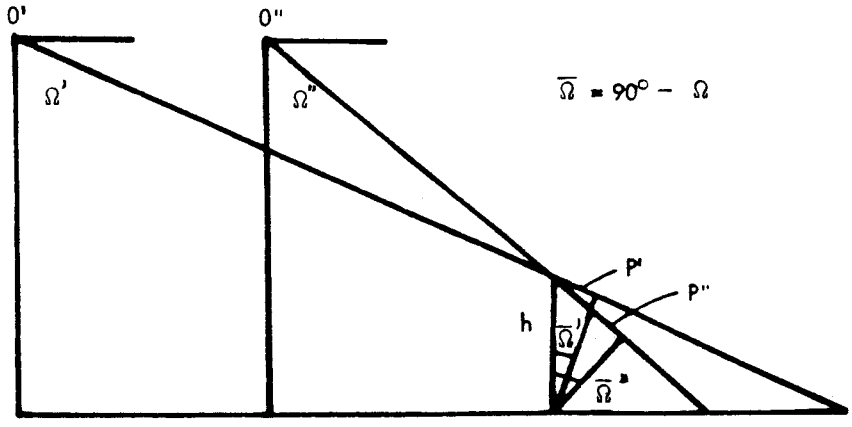

Figure 3.4 Definition of parallax differences Δp for slant range presentation

In the approximate equations (3.39) and (3.40) the projection circles are replaced by straight lines perpendicular to the connecting lines between sensor and object point. These approximations become increasingly coarse as look angles Ω', Ω'' reduce to smaller values. More correctly the parallax Δp is related to height Δh as follows :

$$p' = y - (r'^2 - H^2)^{1/2}$$
$$p'' = y - B - (r''^2 - H^2)^{1/2}$$
$$\Delta p = B + (r''^2 - H^2)^{1/2} - (r'^2 - H^2)^{1/2} \qquad (3.41)$$

This is a non-linear relationship between Δp and Δh, where Δh is included in r', r'' :

$$\Delta p = B + ((H - \Delta h)^2/\cos^2\Omega'' - H_2^2)^{1/2} - ((H - \Delta h)^2/\cos^2\Omega' - H^2)^{1/2} \qquad (3.42)$$

This expression will be used to compute the exaggeration factors of radar stereo.

3.4 STEREO QUALITY MEASURE WITH VERTICAL EXAGGERATION FACTOR

IA PRADE (1970) and LA PRADE et al.(1980) describe a concept for the evaluation of stereo viewability and quality using a vertical exaggeration factor, q. This is related to central perspective geometry which in turn is the model used to explain human vision. For ease of reference we present this concept of LA PRADE. Figure 3.5 describes the central perspective image collection geometry for a pair of cameras, and an observer looking at a stereoscopic image pair through the lenses of a stereoscope, both illustrated for a pyramid-shaped object. The exaggeration factor that is of relevance results from the ratio $\Delta h/w$ of the pyramid as it is in object space ($\Delta h_n / w_n$) and as it appears from the stereo observation, $\Delta h_s / w_s$. This is thus a measure of the flatness of the subjectively observed models.

In addition to the ratio in nature, $\Delta h_n / w_n$, and in the stereo-observation, $\Delta h_s / w_s$, there is a corresponding ratio in the image, $\Delta p_i / w_i$ according to Figure 3.6. This ratio also exists in the object reference plane $\Delta p_n / w_n$.

We find :

$$\Delta p_n / w_n = \Delta p_i / w_i \qquad (3.43)$$

$$\Delta p_n / \Delta h_n = B_n / H_n \qquad (3.44)$$

B_n is the equivalent camera stereo base and H_n the equivalent camera flying height. Thus :

$$\Delta p_i / w_i = (B_n / H_n) . \Delta h_n / w_n \qquad (3.45)$$

The stereoscopic observation has a stereo base, B_s, and distance

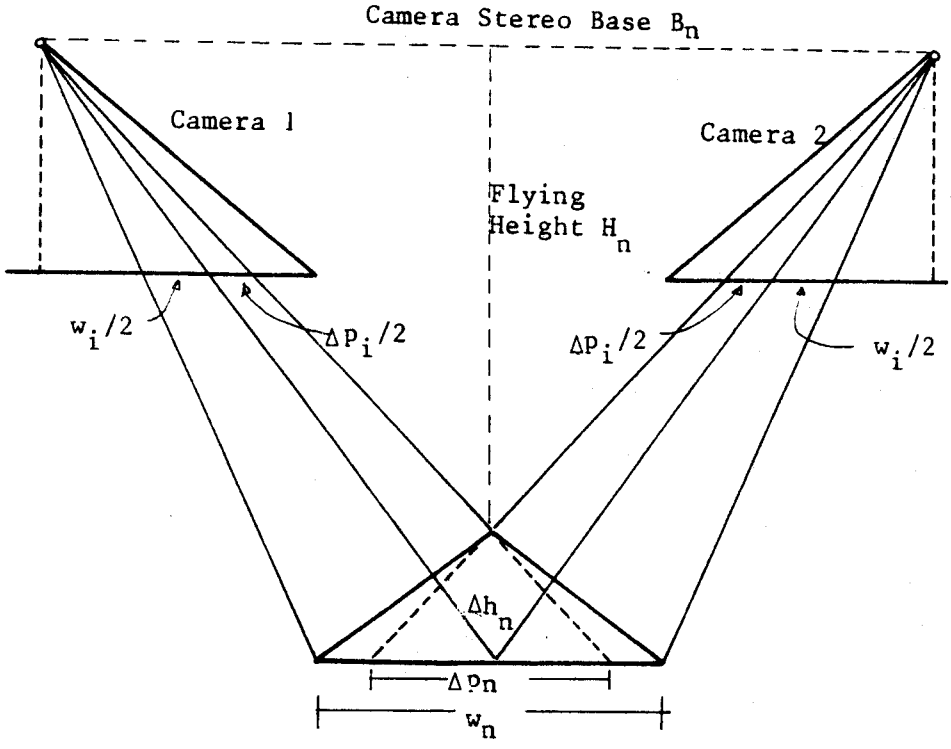

Figure 3.5 Definitions in object space for the vertical exaggeration factor after LA PRADE et al.(1980)

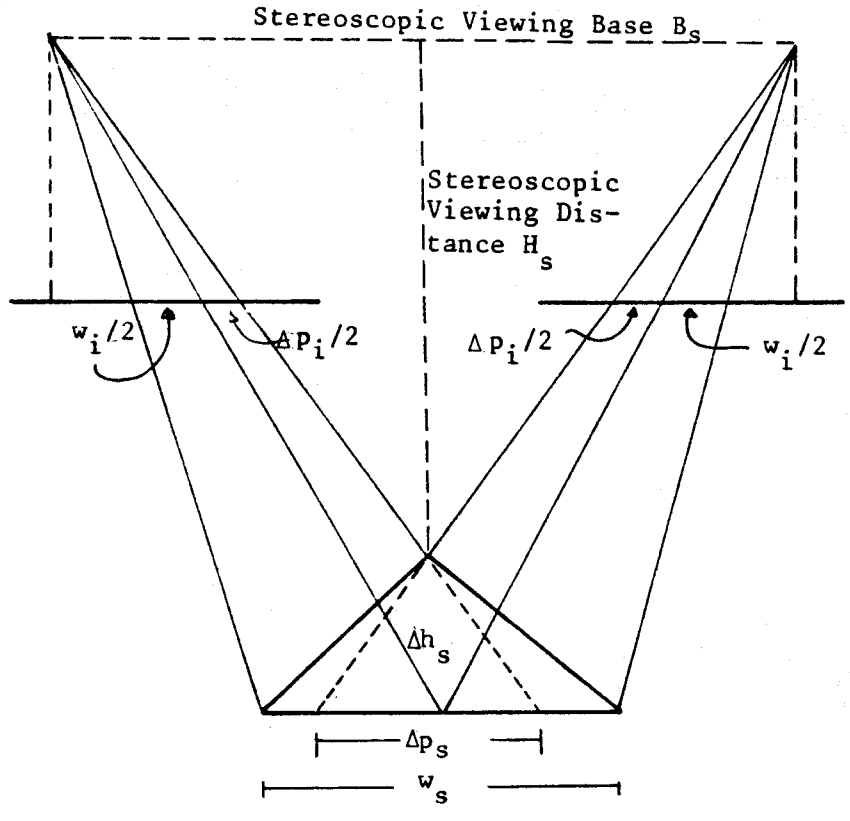

Figure 3.6 Definitions in image space for vertical exaggeration

to the virtual image, H_s. We find again from Figure 3.6 :

$$\Delta h_s / \Delta p_s = H_s / B_s$$
$$\Delta p_s / w_s = \Delta p_i / w_i \qquad (3.46)$$

Thus

$$\Delta h_s / w_s = (H_s / B_s).(\Delta p_i / w_i)$$

and

$$\Delta h_s / w_s = (H_s / B_s).(B_n / H_n).(\Delta h_n / w_n) \qquad (3.47)$$

The vertical exaggeration, q, is then :

$$q = (\Delta h_s / w_s)/(\Delta h_n / w_n) \qquad (3.48)$$

This is, for equivalent central perspective imaging :

$$q = (H_s / B_s).(B_n / H_n) \qquad (3.49)$$

According to IA PRADE et al.(1980) optimum stereo viewing with a stereoscope requires the ratio

$$H_s/B_s \approx 5$$

and therefore

$$q \approx 5.\Delta p_n / \Delta h_n . \qquad (3.50)$$

The ratio $\Delta p/\Delta h$ needs to be related to radar. Using equations (3.39) and (3.40) we obtain a value q′:

$$q' \approx 5.(\cos \Omega'' \pm \cos \Omega')$$

or

$$q' \approx 5.(\cot \Omega'' \pm \cot \Omega')$$

for slant- and ground range presentations, respectively. But for small angles Ω', Ω'', such as those in satellite radar, these equations represent merely an approximation. It would thus be appropriate to employ equation (3.42) to avoid neglections due to approximations.

C H A P T E R 4

RESULTS WITH SINGLE SATELLITE RADAR IMAGES

4.1. INTRODUCTION

At the time of this study, the only available satellite radar images of the Earth were those of the SEASAT-SAR experiment. In October 1981, the Space Shuttle's second flight resulted in SAR-images of selected areas (Figure 4.1). However, these data are not yet available for radargrammetric research.

Therefore this report will be limited to an analysis of SEASAT-data. The SAR-imaging configuration will be described in the next section, followed by a radargrammetric analysis of images presented on film, both generated optically and digitally. No results have been generated thus far on actual digital SAR-images.

4.2. THE SEASAT - SAR EXPERIMENT

The SEASAT satellite was launched as an oceanographic satellite on 4 July 1978 and operated successfully for three months until 11 October. It stopped functioning due to an electrical short circuit. A summary of the parameters of this experiment is given in Table 4.1 and Figure 4.2 presents the geometrical arrangement of the SEASAT-SAR.

Figure 4.1 The second flight of the Space Shuttle resulted in 25 cm wavelength SAR-images, taken with a back-up SEASAT-SAR, but imaging at 45° off nadir

Mission duration	28 June - 11 October 1978
Orbit height	790 - 820 km
Orbit inclination	108° retrograde
Orbit period	100 minutes
Radar wave length	25 cm, L-band
Radar look angle off-nadir	17° to 23°
Swath width	100 km
Ground resolution	25m x 25 m nominal

Table 4.1 SEASAT satellite orbit and parameters of the synthetic aperture radar.

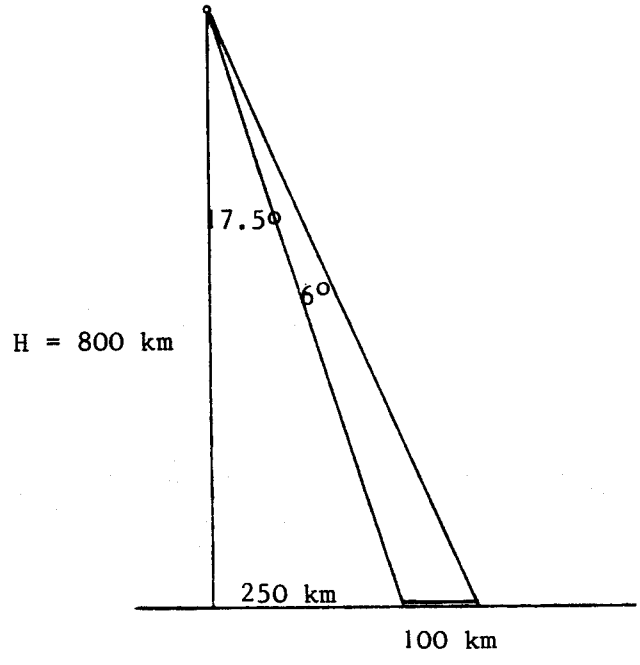

Figure 4.2 Imaging arrangement of SEASAT

The satellite carried a synthetic aperture radar imaging system on board and was the first one to produce satellite radar images of the Earth. Previously such satellite radar images only existed of portions of the Moon and resulted from the APOLLO-17 mission in 1972 (LEBERL,1976).

Radar is an active imaging system providing its own illumination and penetrates rain,fog and clouds. For this reason radar has some advantages over other imaging systems,

especially for imaging polar regions and for ocean monitoring, which were the main goals of the SEASAT mission.

Furthermore it was expected that satellite radar should have some advantages over traditional airborne radar (LEBERL,1978) :

....large swath (100 km) with small variation of angle of illumination
....reduced geometric deformation due to small variation of look-angle
....higher accuracy due to stable satellite orbits
....comparatively small variable cost for repeated coverage of quickly changing phenomena.

The SEASAT imaging radar system produced images at a scale of about 1 : 500 000, which may be generated either with optical or with digital correlation. In the optically generated image time marks for each second of imaging serve as references for the 'sensor events' or imaging times and the slant range. Also the position of the SEASAT-sensor is known (in geographic coordinates) for the corresponding times.

4.3. RADARGRAMMETRIC MAPPING METHOD

The orbit of the sensor is given by some measured sensor positions. Smoothing of this measurements is done by interpolating a spatial polygon with the method of moving averages (see chapter 2.2).

The cartesian image coordinates x and y (compare Figure 2.3) are converted to time of imaging t and slant range r :

$$r = y.f + c$$
$$t = t_i + (x - x_i).(t_{i+1} - t_i)/(x_{i+1} - x_i) \qquad (4.1)$$

x_i , x_{i+1} .....x-coordinates of tick-marks i,i+1

t_i , t_{i+1} .....times for tick-marks i,i+1 , where t defines the sensor position $\underline{s}$ and the velocity vector $\dot{\underline{s}}$ of the sensor, when image point (x,y) was imaged.

With the assumptions that the reference surface is a sphere and that the squint angle τ is zero, the geocentric coordinates of an imaged point can be computed with the direct algorithm described in chapter 2 (see formulas 2.11).

Available ground control points with known geocentric coordinates are used to calibrate the radar sensor and orbit data. Therefore the parametric method described in chapter 2.2.3 is used with the following correction polynomials for Δr and Δt :

$$\Delta t = a_{10} + a_{20}x + a_{30}x^2 + a_{40}x^3 + a_{01}y + a_{02}xy + a_{03}x^2y + a_{04}xy^2 + a_{05}x^2y^2 + a_{06}x^3y$$
$$\Delta r = b_{10} + b_{20}x + b_{30}x^2 + b_{40}x^3 + b_{50}x^4 + b_{01}y + b_{02}xy + b_{03}x^2y + b_{04}xy^2 + b_{05}x^2y^2 \qquad (4.2)$$

Depending on the number of ground control points a selected number of i + j polynomial coefficients a_{ij}, b_{ij}, is used to compute corrections Δr and Δt for time and slant range for each image point. With these corrected values for t and r the geocentric coordinates for new points are computed with equations (2.11)

4.4. ACCURACY EVALUTION IN THE CONTEXT OF ICE MOTION AND ICE DEFORMATION MEASUREMENTS

4.4.1 Data Set

Since SEASET was launched as an oceanographic satellite, about one fourth of all its observations are of the arctic Beaufort-Sea to the north-west of Canada. For the determination of the motion of sea-ice the (optically correlated) data of seven sequential orbits were selected, which covered also parts of Banks Island and Victoria Island. These seven images are listed in Table 4.2; their geographical location is shown in Figure 4.3.

Orbit nr.	Day of Year	Equator Crossing	Time on	Time off	Highest Latitude
1038	250	$297^{o}77$	14:02:12	14:05:52	$71^{o}66$
1081	253	$297^{o}84$	14:16:30	14:18:30	$71^{o}78$
1296	268	$297^{o}85$	15:19:10	15:23:10	$71^{o}97$
1339	271	$297^{o}84$	15:32:53	15:34:53	$71^{o}71$
1382	274	$297^{o}82$	15:45:36	15:47:36	$71^{o}80$
1425	277	$297^{o}85$	15:55:43	16:03:57	
1468	280	$297^{o}85$	16:08:25	16:16:39	

Table 4.2 SEASAT-SAR arctic ice images for sea-ice motion studies

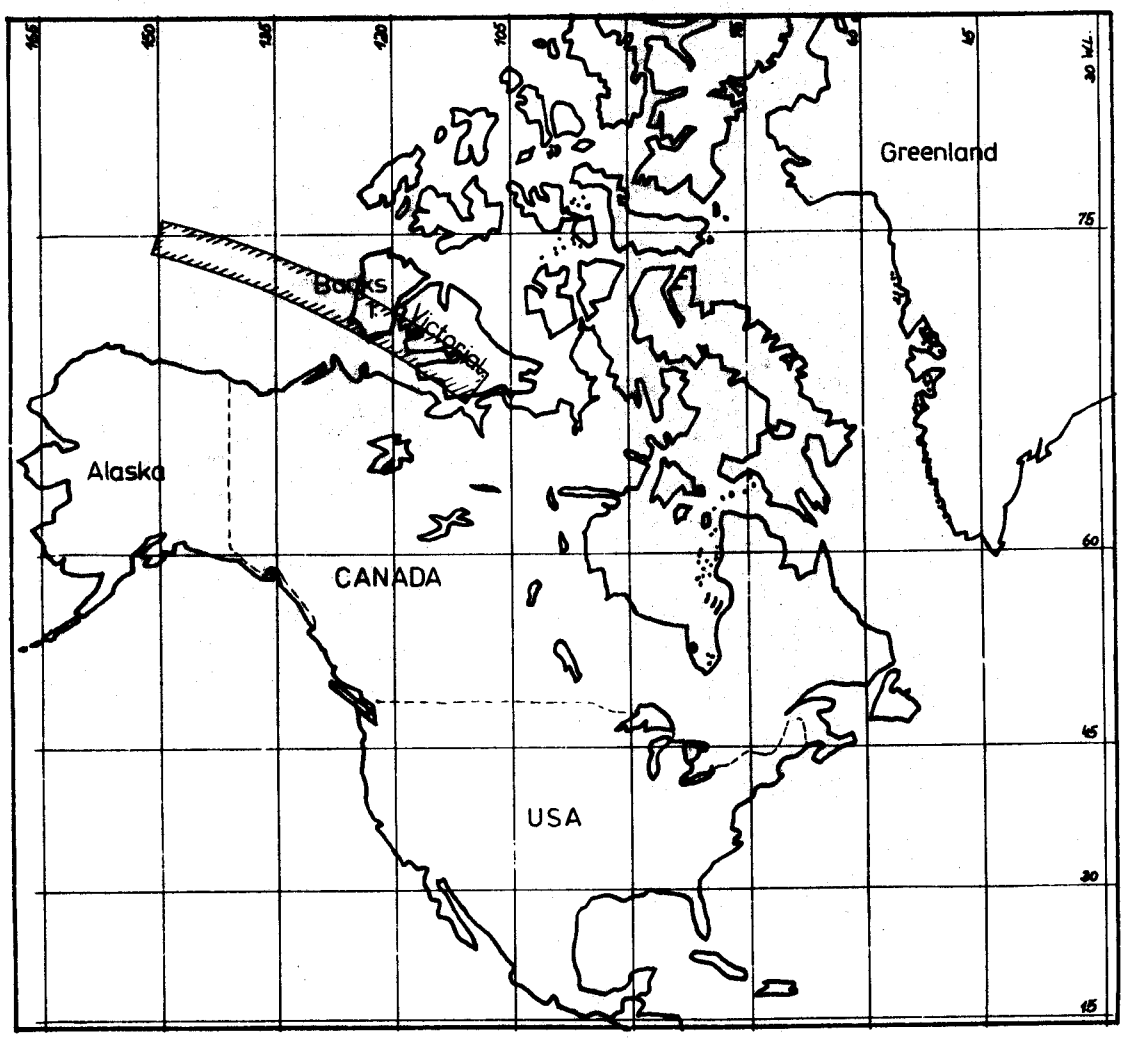

Figure 4.3 Geographical location of the area covered by the seven SEASAT images

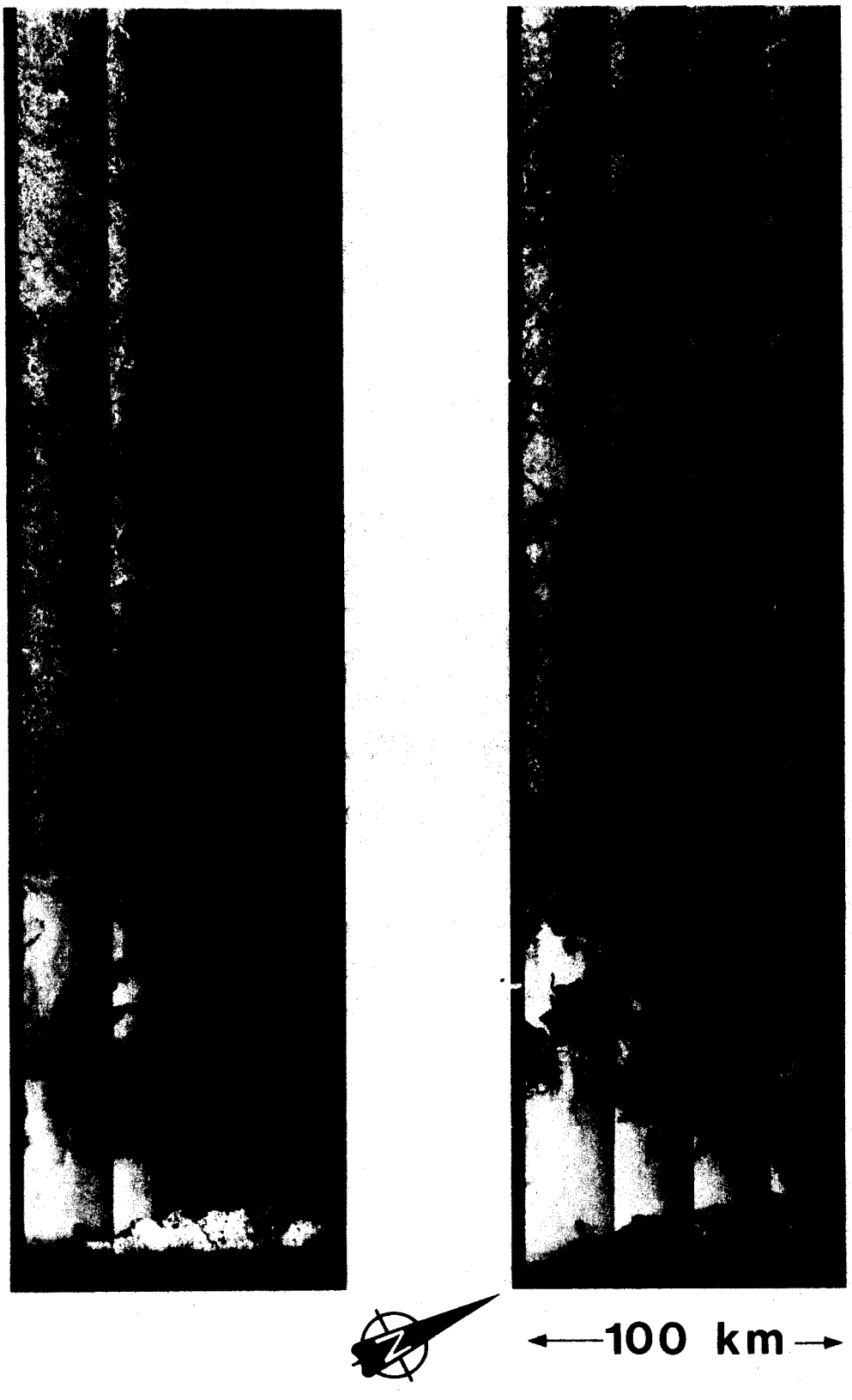

Figure 4.4 SeaSAT-images of orbits 1339 and 1382

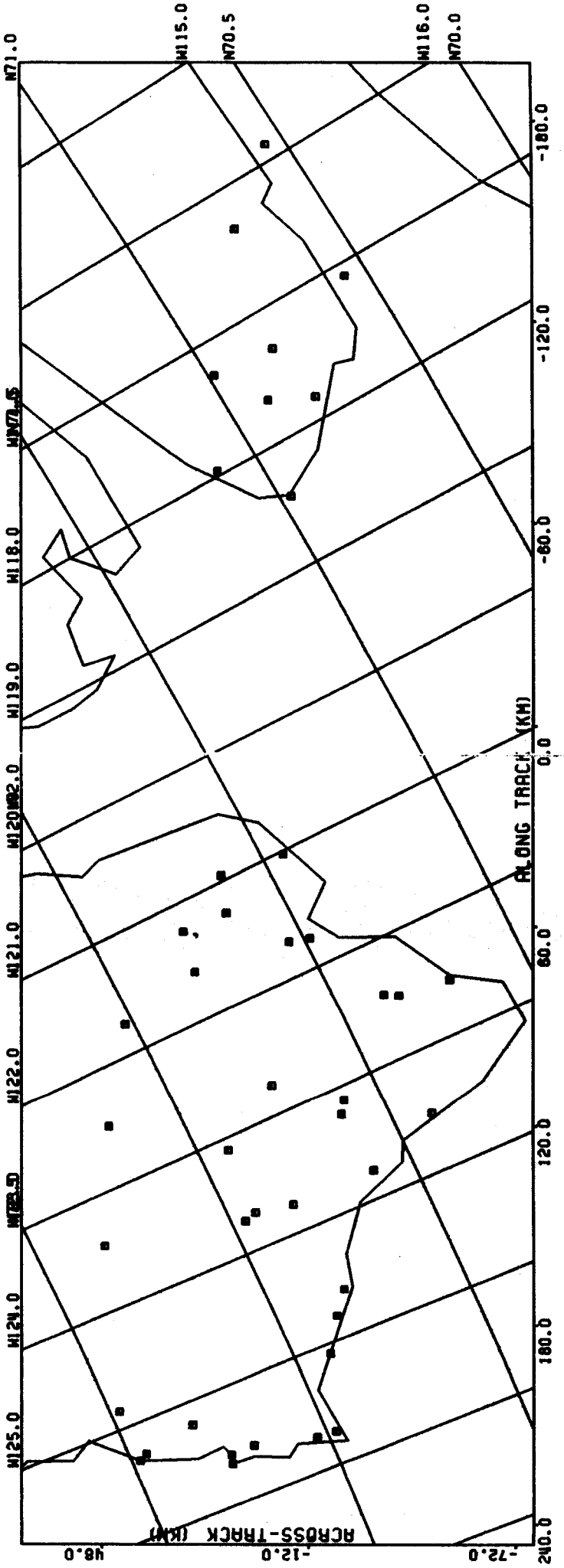

Figure 4.5 Distribution of ground control points over Banks and Victoria Island

Figure 4.4 shows the images which correspond to orbit numbers 1339 and 1382. It is to be noted that one optically correlated SEASAT pass consists of four separate image strips. The ground control is given by 44 identified ground control points over Banks and Victoria Island. Their geographic "true" coordinates were taken from maps 1 : 500 000; larger scale maps were not available. The distribution of these control points is shown in Figure 4.5. It is with these images, ground control points and SEASAT orbit data, that an accuracy evaluation was performed with respect to ice motion measurements.

4.4.2 Ice Motion and Ice Deformation

For the measurement of sea-ice motion the same set of sea ice features was identified on all seven SEASAT passes. The image coordinates of the homologue features, of the ground control points and also of some tick marks were measured on a coordinatograph.

Then the geocentric coordinates of each point were computed separately from each of the seven images as described in Table 4.2. The changes in the coordinates of ice features derived from sequential orbit passes were then interpreted as "ice-motion". This motion can be presented graphically in a tangential projection. Figure 4.6 shows this motion for ice features between two sequential orbits. Figure 4.6 (d) for example shows the ice motion of the image pair of Figure 4.4, that means between orbits 1339 and 1382.

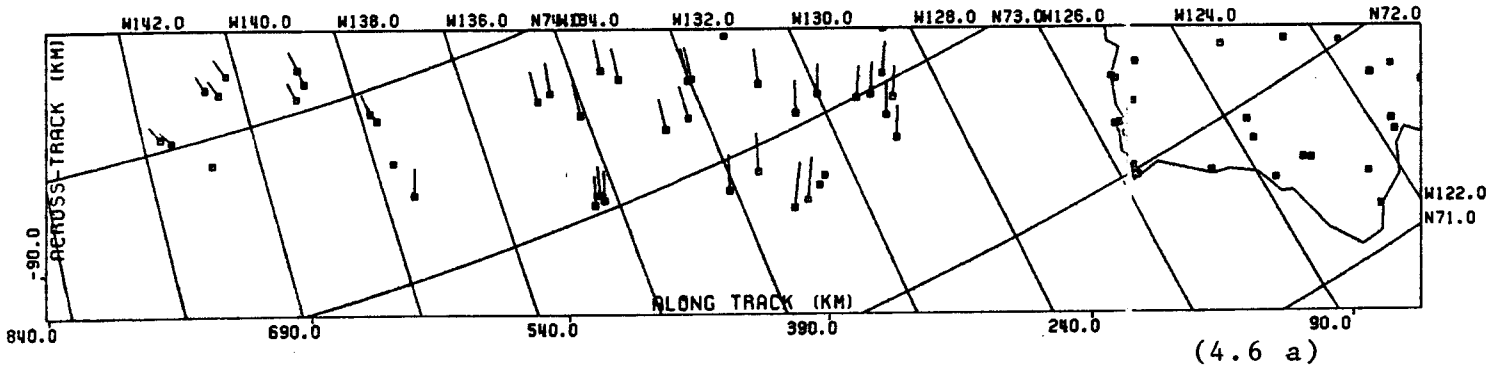
W142.0
W140.0
W138.0
W136.0
W132.0
W130.0
W128.0
W126.0
W124.0
N72.0
W122.0
N71.0
ACROSS-TRACK (KM)
-90.0
ALONG TRACK (KM)
840.0
690.0
540.0
390.0
240.0
90.0

(4.6 a)

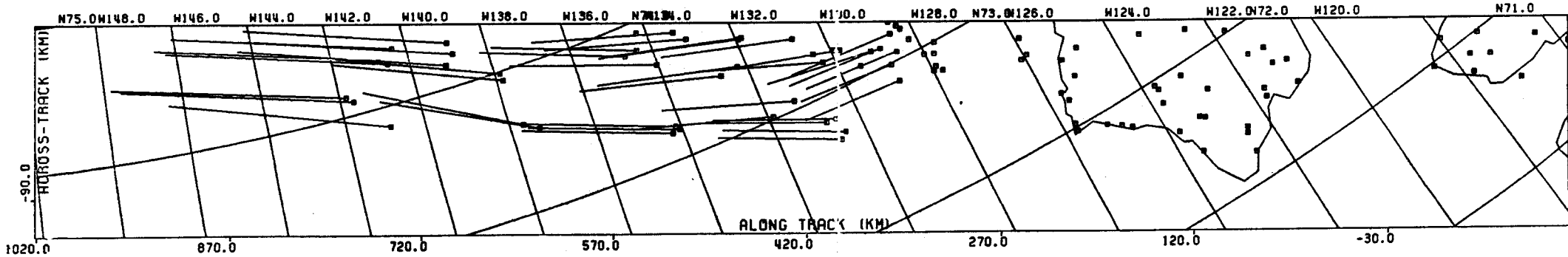
N75.0
W148.0
W146.0
W144.0
W142.0
W140.0
W138.0
W136.0
W132.0
W128.0
W126.0
W124.0
W122.0
N72.0
W120.0
N71.0
ACROSS-TRACK (KM)
-90.0
ALONG TRACK (KM)
1020.0
870.0
720.0
570.0
420.0
270.0
120.0
-30.0

(4.6 b)

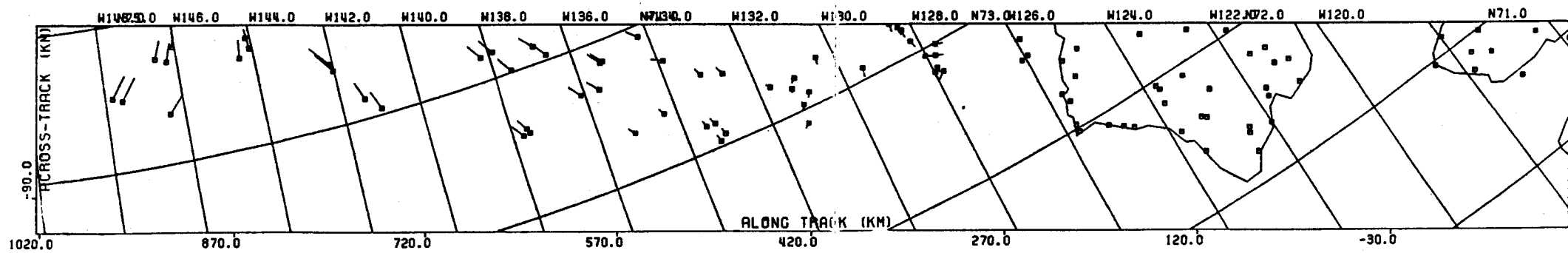
W146.0
W144.0
W142.0
W140.0
W138.0
W136.0
W132.0
W128.0
W126.0
W124.0
W120.0
N71.0
ACROSS-TRACK (KM)
-90.0
ALONG TRACK (KM)
1020.0
870.0
720.0
570.0
420.0
270.0
120.0
-30.0

(4.6 c)

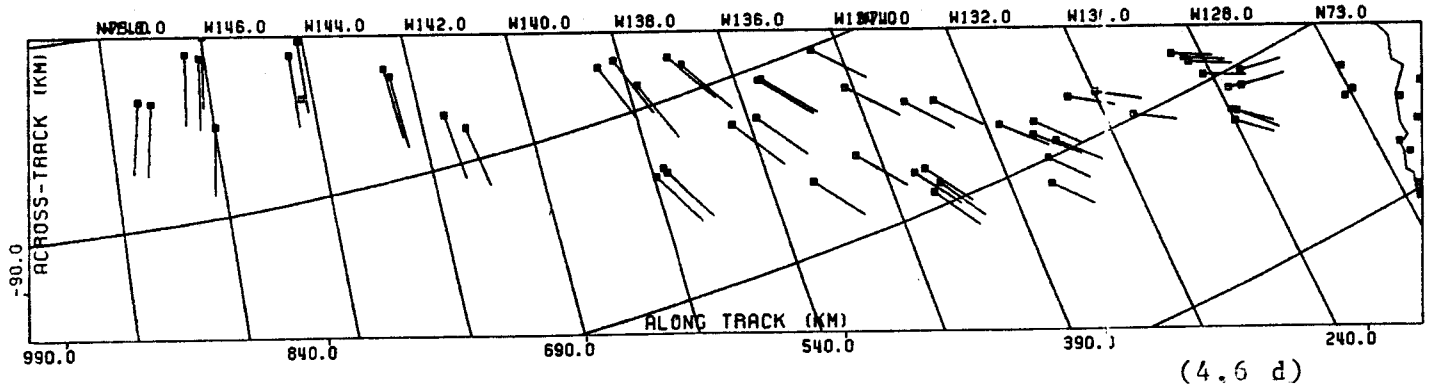

(4.6 d)

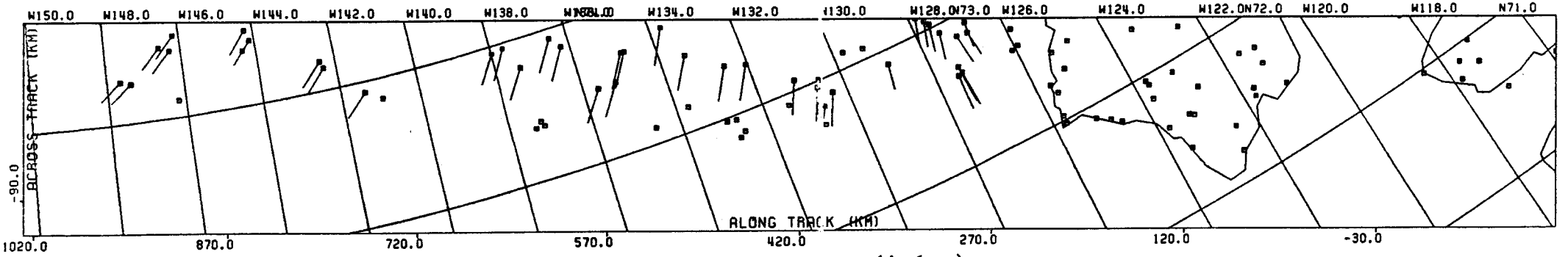

(4.6 e)

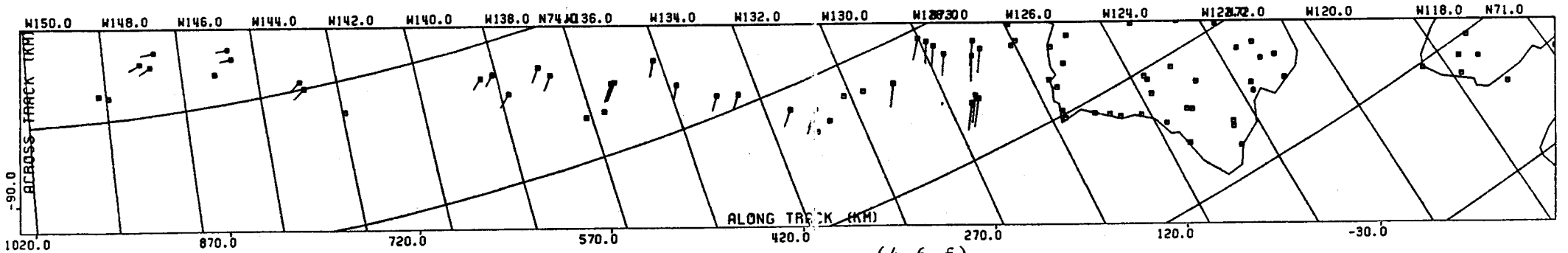

(4.6 f)

Figure 4.6 (a)-(f) Ice motion between two respectively sequent SEASAT passes

The rather large ice motion of Figure 4.6.b between orbit 1081 and orbit 1296 refers to the 15-day interval between these orbits, while the other intervals amount to 3 days.

The total ice motion of all seven SEASAT passes is shown in Figure 4.7 as a synopsis of Figures 4.6 (a) to (f). The root mean square values of the ice motions according to Figures 4.6 (a) to (f) are summarized in Table 4.3 and the mean value for the ice motion for one day of the observational period was computed with 6.4 kilometers per day.

As a simplified method for the computation of the coordinates of ice features one may consider to use the ground control points on the land areas for a linear conformal transformation between image coordinates and geocentric coordinates. It will be shown in the following section, that this would lead to grossly erroneous results.

Figure 4.8 illustrates the results for the total ice motion obtained with this simplified method. Orbit 1081 could not be used because no land areas and therefore no ground control points were on the radar image. A comparision of figures 4.7 and 4.8 shows clearly different motions of ice features in the radargrammetric and simplified method, especially in regions far away from the islands.

Important for the study of ice dynamics is the ice deformation, which means the relative motion of ice features with respect to one another. The results for this ice deformation were obtained from a linear conformal transformation

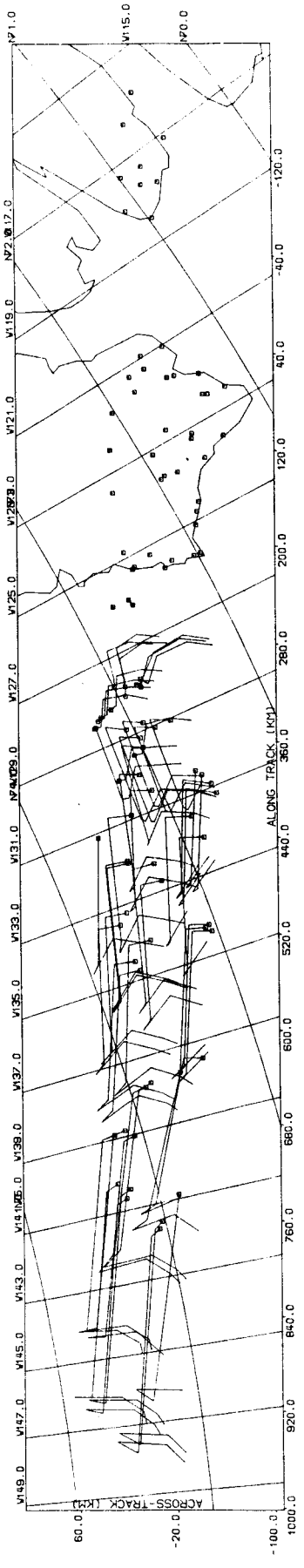

Figure 4.7 Overall ice motion of the observational period between days 250 and 280 of 1978, measured with radargrammetric mapping method

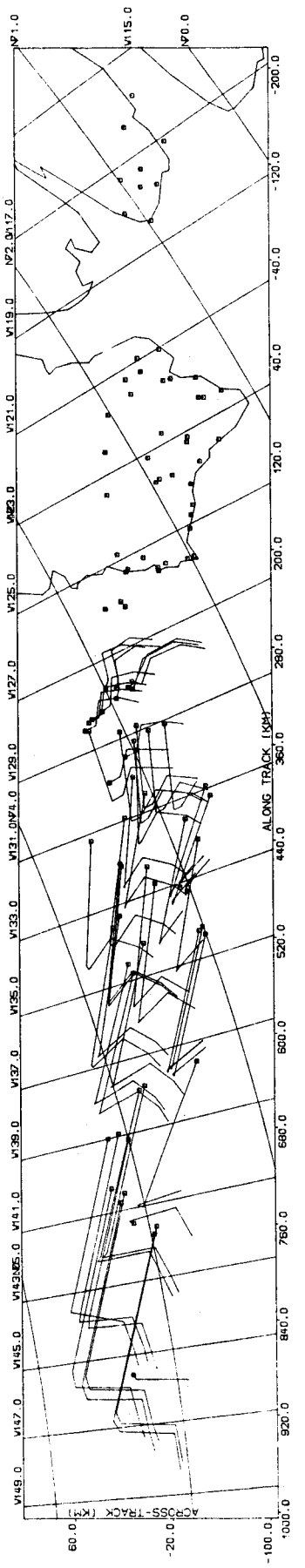

Figure 4.8 Overall ice motion measured with a simple linear conformal transformation

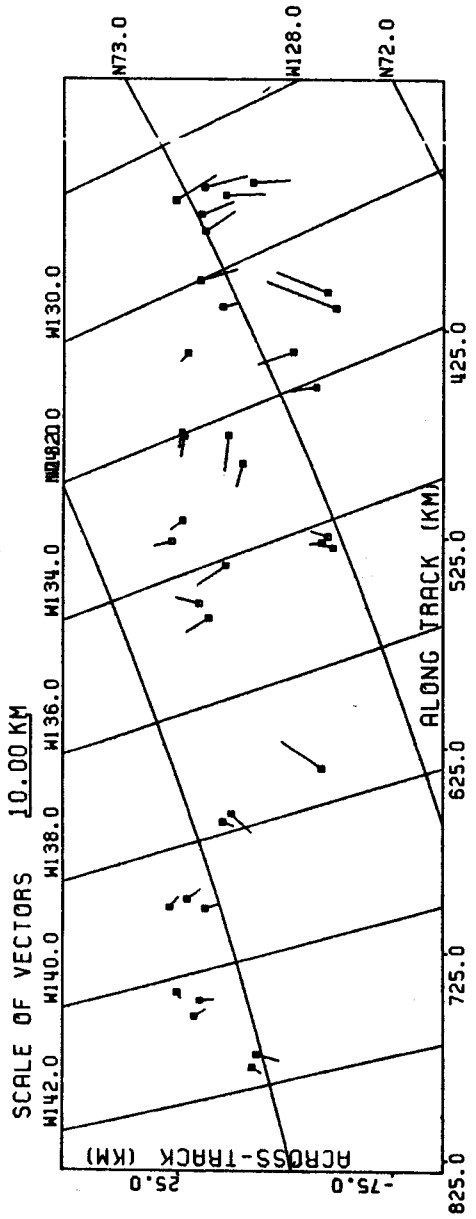

Figure 4.9 (a)

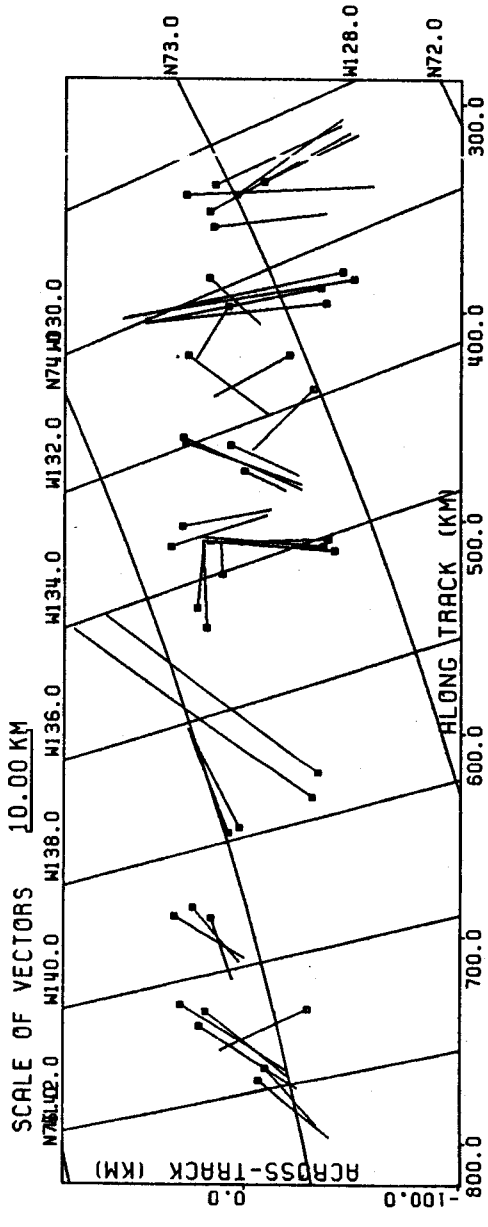

Figure 4.9 (b)

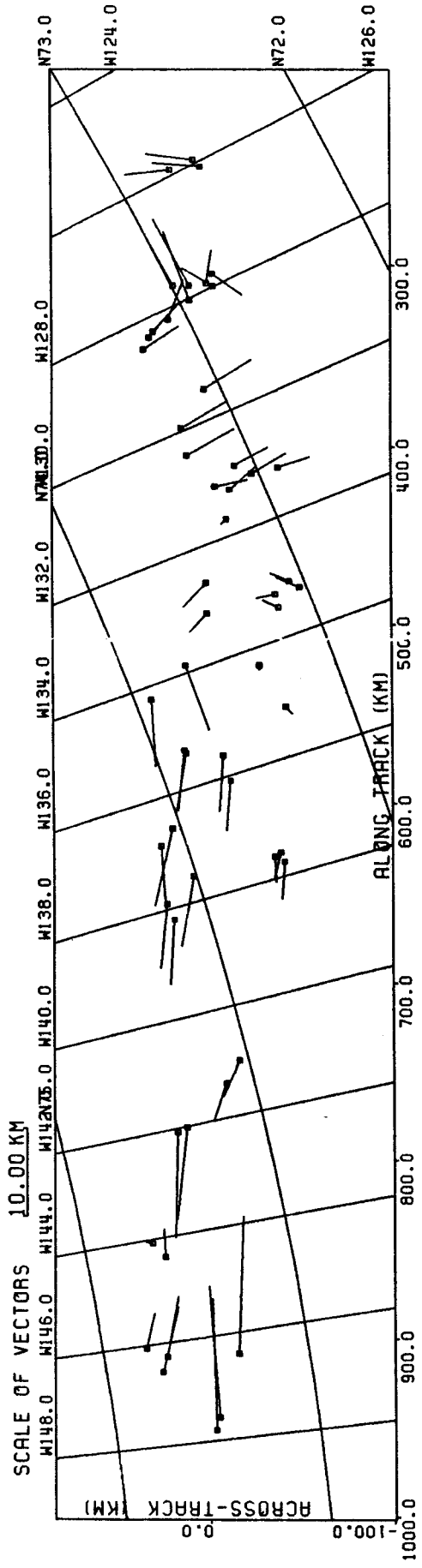

Figure 4.9 (c)

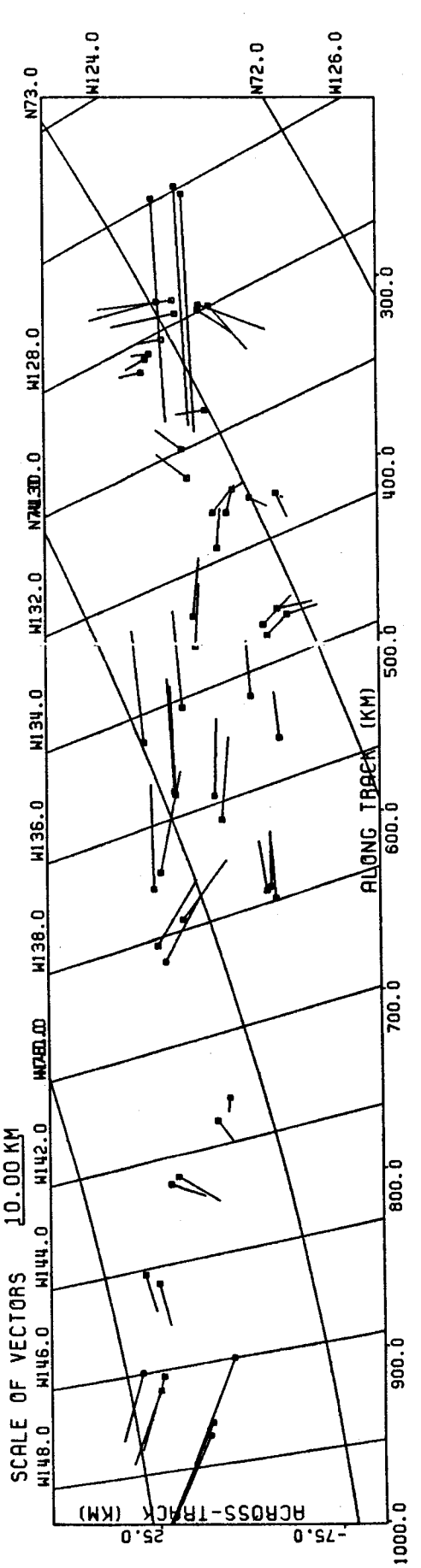

Figure 4.9 (d)

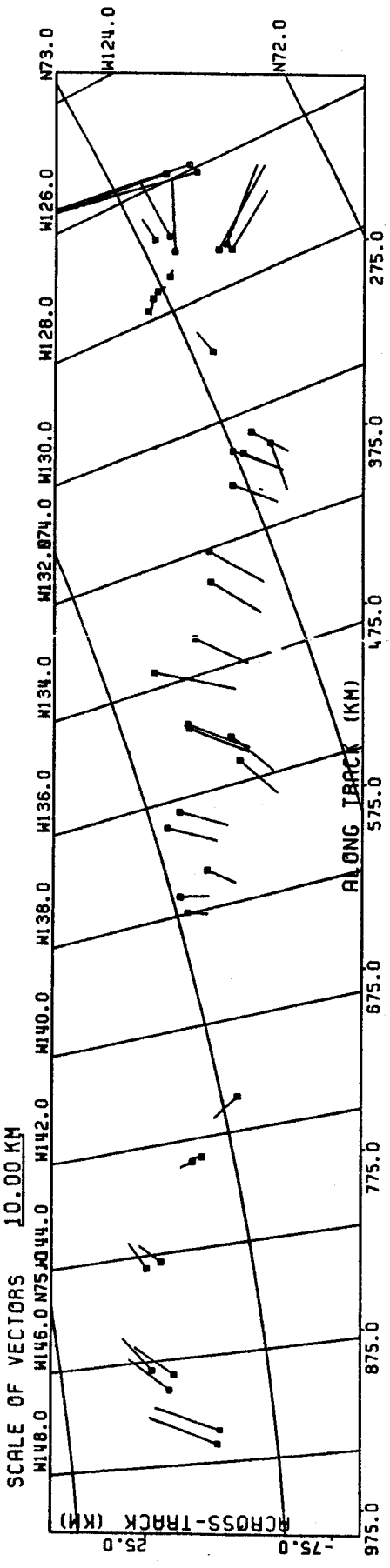

Figure 4.9 (e)

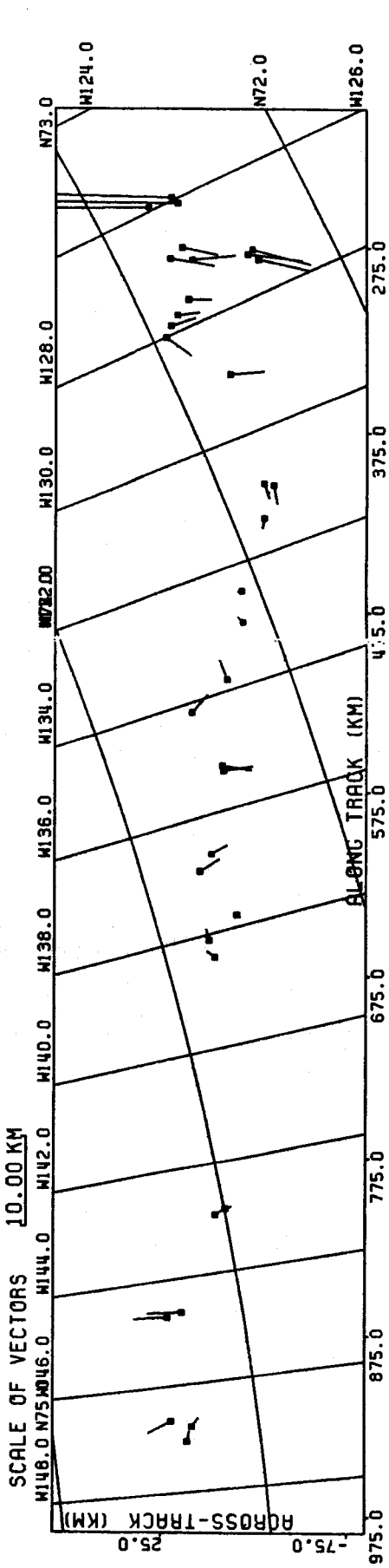

Figure 4.9 (f)

Figure 4.9 (a)-(f) Sea ice deformations according to the ice motions of Figures 4.6 (a)-(f)

between the coordinates of two sequential orbit passes. Figures 4.9 (a) to (f) shows the deformations of the 6 image pairs; this relates to Figure 4.6 (a) to (f) illustrating displacement vectors after the transformation. Their RMS-values are summarized in Table 4.3 and amount to as much as several kilometers.

Orbits	Ice motion		Ice deformation	
	x	y	x	y
1038 - 1081	8.04	14.57	1.78	2.24
1081 - 1296	101.33	71.08	8.89	9.07
1296 - 1339	5.60	8.84	4.97	4.12
1339 - 1382	15.65	28.51	7.18	5.94
1382 - 1425	15.78	17.54	4.32	6.15
1425 - 1468	10.21	9.71	3.09	4.49

Table 4.3 RMS-values for ice motions and ice deformations

4.4.3 Accuracy Evaluation With Arctic Land Data

Since the selected SEASAT passes also cover parts of Banks and Victoria Island, this ground information can be used for accuracy evaluation of the radargrammetric mapping method.

Furthermore the error propagation on one end in a SAR strip should be determined for both the radargrammetric and the simplified method with linear transformation under the assumption that there is only ground control on one end of the strip. This can be a relevant limitation in satellite radar mapping particularly with sea ice images. For this evaluation

only one of four parts of an optically correlated SEASAT image is used and any number of known ground points can be selected as control, while the remaining points serve for comparision.

Ground control	Polynomial (equ. 4.2)	Radargrammetric method		Simple scale fit	
		x	y	x	y
0	- - - -	15.12	12.88	--	--
1	1-0-1-0	.35	.28	--	--
2 at both ends	1-0-1-0	.33	.22	.37	.35
	1-1-1-1	.34	.47	--	--
	2-0-2-0	.33	.21	--	--
2 at one end	1-0-1-0	.33	.25	2.00	4.85
	1-1-1-1	.26	.44	--	--
	2-0-2-0	16.77	18.50	--	--
5 at one end	1-0-1-0	.31	.31	.86	1.47
	1-1-1-1	.34	.36	--	--
	2-0-2-0	.34	.91	--	--
	2-1-2-1	.40	1.15	--	--
17	1-0-1-0	.33	.24	.30	.20
	2-1-2-1	.28	.21	--	--
	3-4-3-4	.24	.21	--	--
	4-6-5-5	.19	17	--	--

Table 4.4 Coordinate errors in km with different ground control distribution

The results of these investigations are summarized in Table 4.4. Theoretically the radargrammetric mapping method works also without using any control point. But as one can see from Table 4.4 this would lead to large errors in computed

coordinates. The reason for this fact is that time marks sometimes are off for several seconds of time in the images. For example the time mark offset in the used image strip was 0.0008 hours corresponding to 3 seconds of time. This value corresponds to a displacement of about 20 kilometers on the ground.

Therefore at least one ground control point must be used to eliminate the obvious set-off of time-marks. This would reduce the errors in the check points to about 400 meters on ground (see Table 4.4). Figure 4.10 shows the distribution of used control points and their residuals when using one single ground control point at one end of the pass.

In Figure 4.11 (a) the results of the radargrammetric method are illustrated when using two ground control points, one at each end of the strip. In this case the errors of coordinates would be of the same order of magnitude as seen from Table 4.4.

With two ground control points also the mentioned simplified method of a linear conformal transformation can be used to compute the coordinates of comparision points. The results for this method are shown graphically in Figure 4.11 (b). It can be seen that the amount of residual vectors is of the same order of magnitude than those of Figure 4.11 (a). One must thus conclude that with 2 or more well distributed ground control points there is no reason to employ proper radargrammetry.

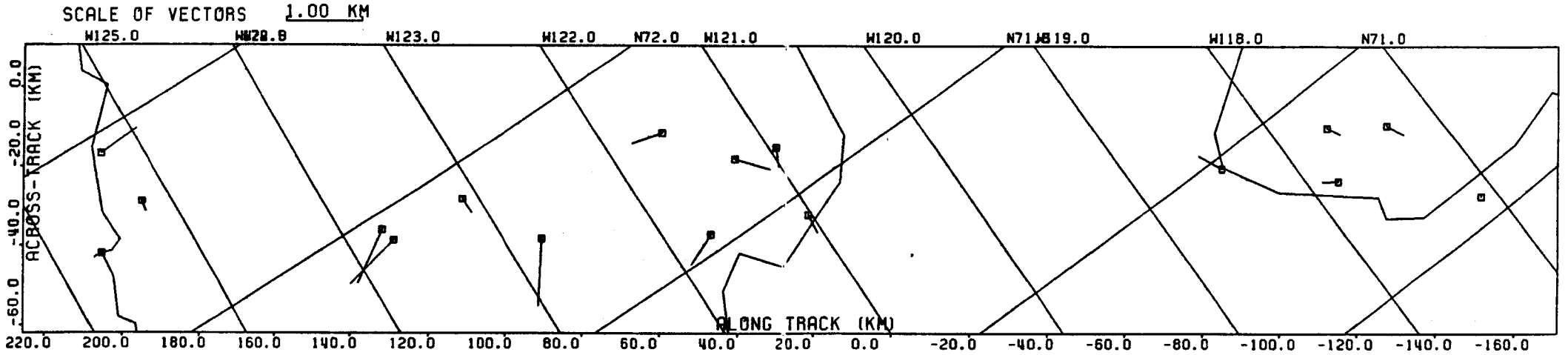

Figure 4.10 Error vectors after radargrammetric computation of coordinates with only one ground control point

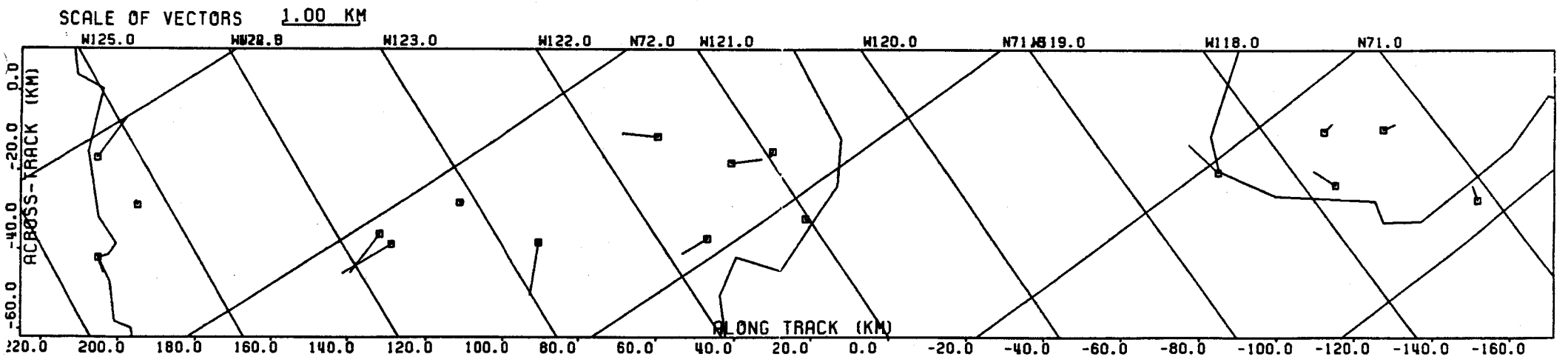

Figure 4.11 (a) Same as Figure 4.10 but using two ground control points, one at each end of the strip

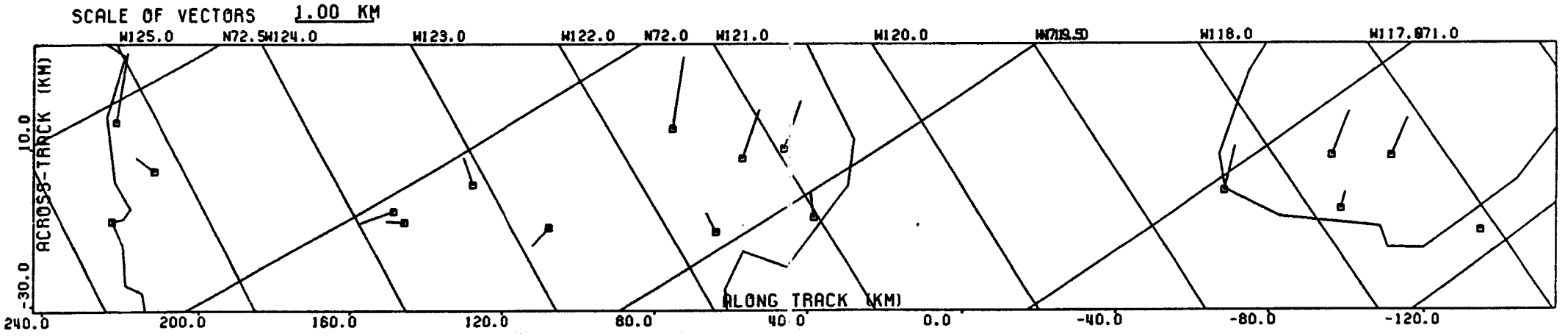

Figure 4.11 (b) Error vectors after coordinate computation with simplified transformation using the same ground control as in Figure 4.11 (a)

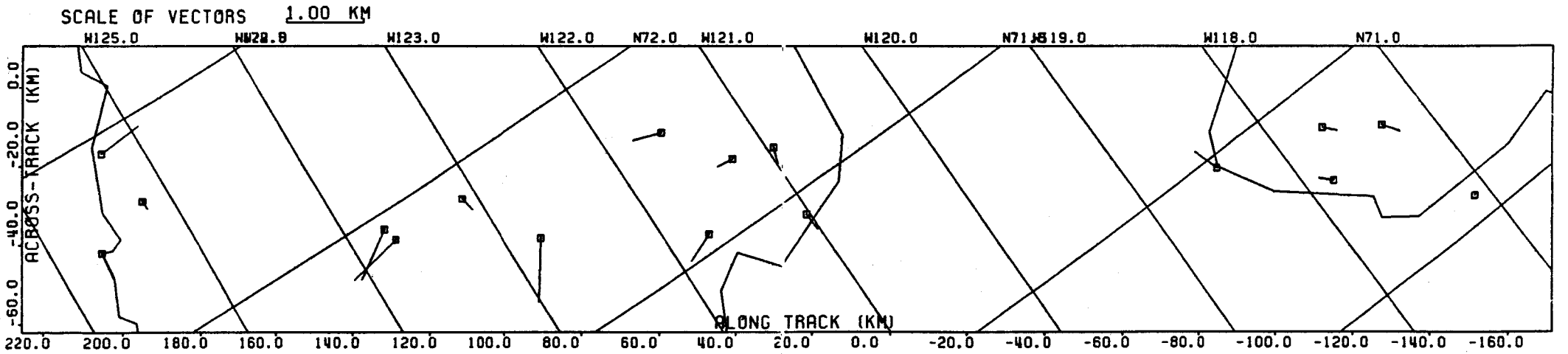

Figure 4.12 (a) Same as Figure 4.11 (a) but using the two ground control points at the same end of the strip

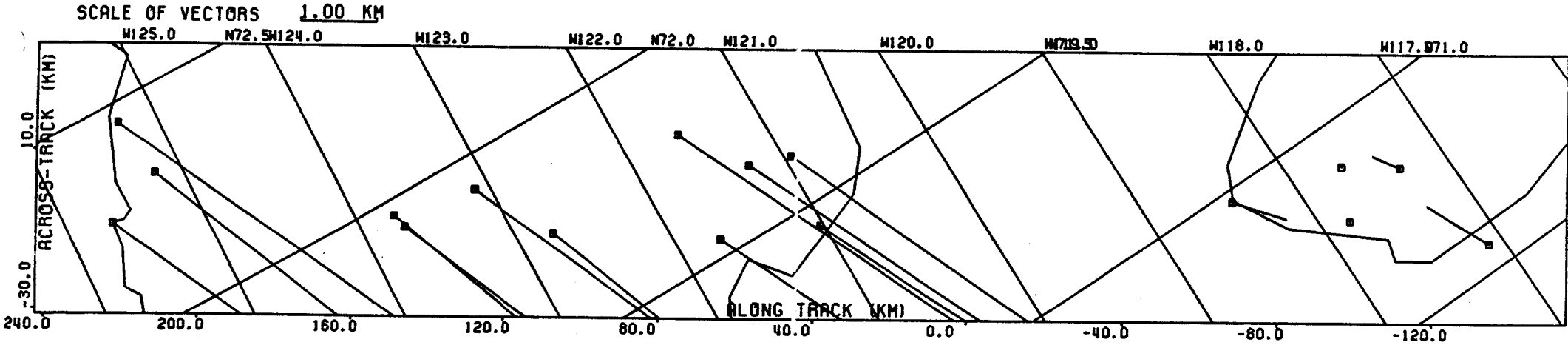

Figure 4.12 (b) Same as Figure 4.11 (b) with the two ground control points at the same end of the strip

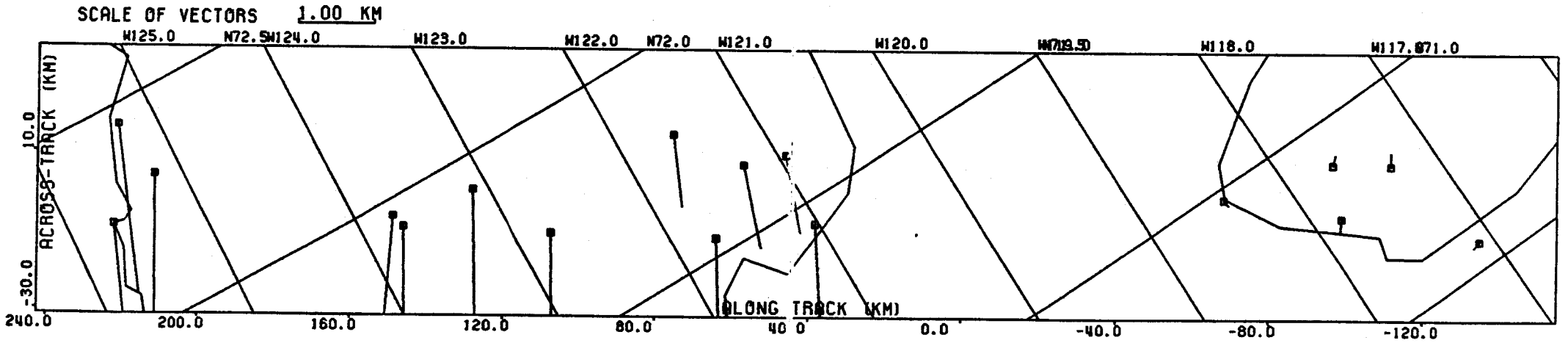

Figure 4.12 (c) Same as Figure 4.12 (b) but with five ground control points at the same end of the strip

However, the advantage of the radargrammetric method versus the simple one is clear if two ground control points are used at the same end of an image strip. The result is illustrated in Figures 4.12 (a) and (b); while for the radargrammetric method the residuals do not change drastically they increase to about 5 kilometers on the ground when using merely a conformal transformation of the images to ground control. Even when using five control points at the one end of the strip there remain coordinate residuals of 1.5 km on the ground as shown in Figure 4.12 (c).

From Table 4.4 it also can be seen that it is not useful to employ a polynomial of higher order for the calibration of orbit data, if only ground control on one end of the strip is available. This only would lead to an extrapolation of the coordinates at the other end and therefore to erroneous results.

Extrapolation must be avoided. For the radargrammetric method and a low order correction polynomial, the use of all available ground points predictably results in no significant improvement compared to the results obtained when using only two control points at both ends of the strip. Only when polynomials of higher order are employed can we reduce the residuals in the check points to about + 150 to + 200 meters.

The cause of this accuracy limitation to + 150 meters may be the difficulty of identifying homologue ground points on the map and in the images. The ground control points were taken from a map at scale 1 : 500 000; small identification errors of 0.25 mm on the map represent an error of 125 meters on the

Figure 4.13 (a)

Figure 4.13 (b)

Figure 4.13 (c)

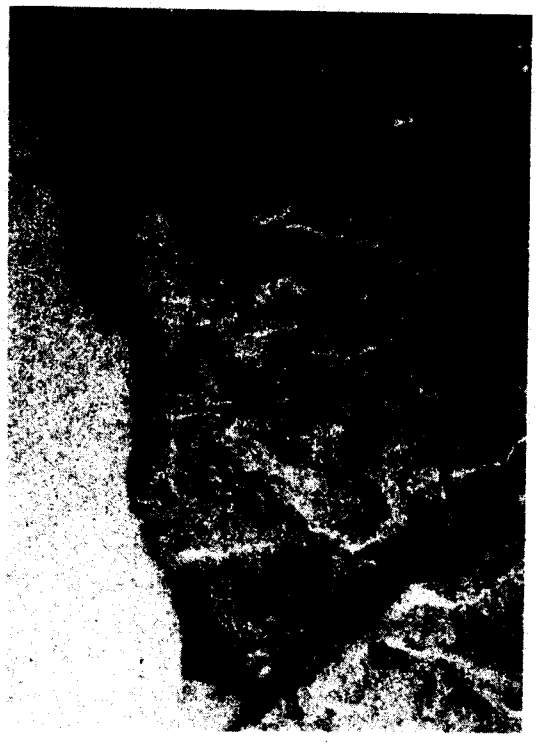

Figure 4.13 (d)

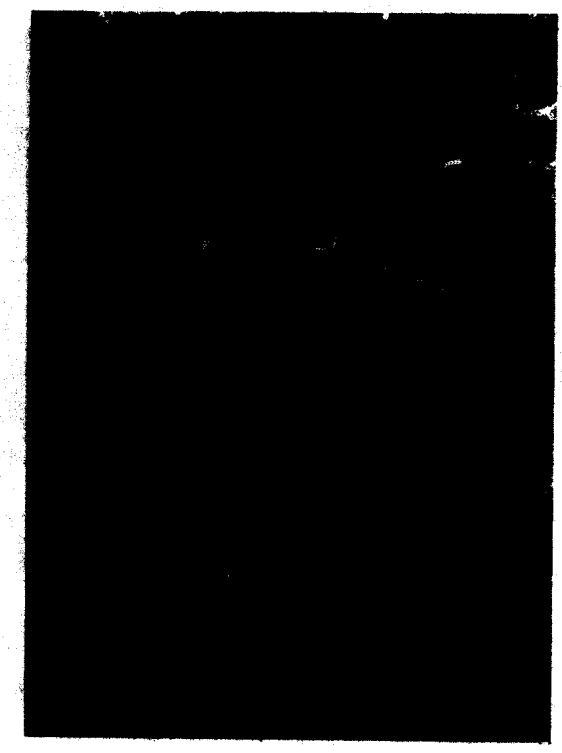

Figure 4.13 (e)

Figure 4.13 (f)

Figure 4.13 (g)

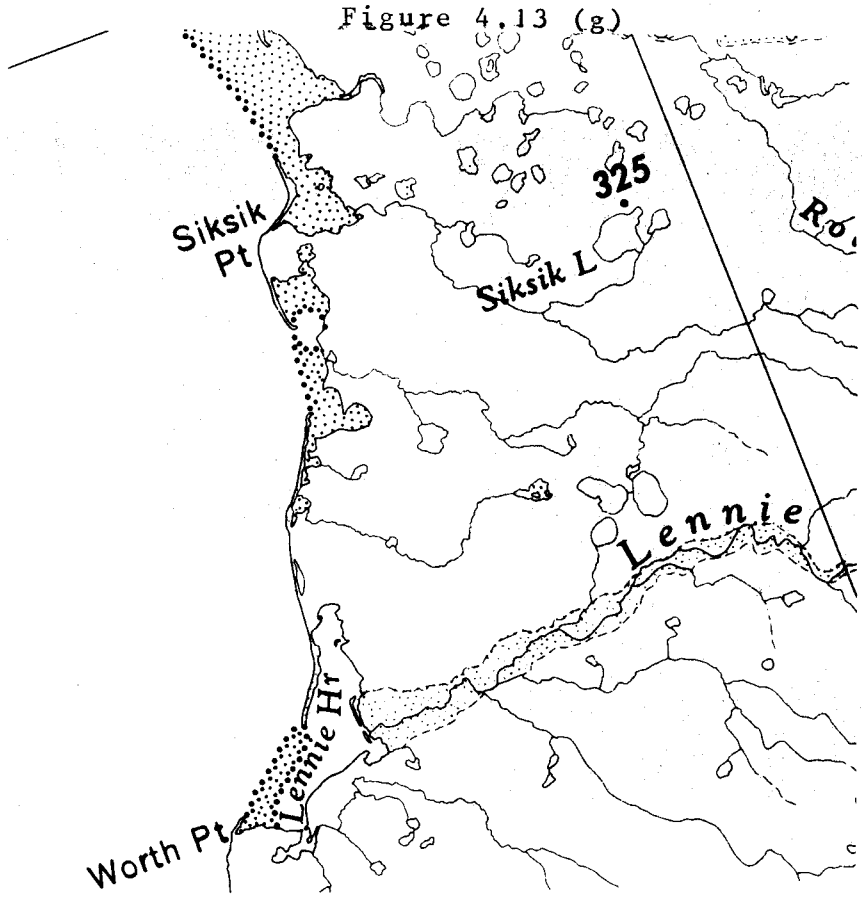

Figure 4.13 (a)-(f) Comparision of SEASAT SAR images of Banks Island from different times
(g) Map segment of Banks Island taken from the map 1 : 500 000

ground. The same is valid for identification errors in the images, which are also of a scale of about 1 : 500 000. The difficulty is appreciated when juxtaposing a SAR-image and a map (see Figure 4.13).

Another cause for accuracy limitations might be the lack of precision in the time marks, which serve for the computation of times of imaging. Table 4.5 shows that these time marks are not equidistant and therefore lead to errors in imaging or senser events times.

Image coordinate x (time) (in mm)	Deviations dy of time marks from range reference line (in mm)	Differences dx between time marks (in mm)
22.600	-0.072	
410.200	-0.184	
503.500	-0.274	13.400
516.900	-0.029	13.600
530.500	-0.035	13.500
544.200	-0.041	13.450
557.450	-0.004	13.350
570.800	-0.002	13.650
584.450	-0.207	13.550
598.000	0.087	13.400
611.400	0.281	12.100
623.500	0.276	13.650
637.450	0.070	13.500
650.650	0.115	14.750
665.400	0.109	13.800
679.200	0.153	13.200
692.400	0.147	13.150
705.550	0.142	13.150
718.700	0.136	13.600
732.300	0.137	11.800
744.100	0.126	13.350
757.450	0.120	
1305.118	-0.057	
1572.752	-0.194	
2240.976	-0.209	
St. Dev.	0.174	0.607

Table 4.5 Deviations of time marks from range reference line and equidistance

Also the use of a spatial polygon for the satellite orbit (compare equations 2.9) did not seem to be the best solution for this problem. The length of a linear polygon piece is defined

by a chosen value Δt for the corresponding time interval. In our case the value for Δt was 0.0002 hours, which corresponds to about 5 kilometers on the ground. Attempts with smaller time intervals also did not lead to an improvement of the accuracy.

But an experiment was made using a polynomial of third order to approximate the orbit as described in chapter 2 by equations (2.10). This led to significantly smaller errors in check points especially when using calibration polynomials for range and time of higher order. A comparision of the results of this methods for the approximation of the satellite orbit is shown in Table 4.6.

Correction polynomial (equ. 4.2)	Use of a spatial polygon with Δt = 0.0002 hours (equation 2.9)		Use of polynomials according to equation (2.10)	
	x	y	x	y
1-0-1-0	.33	.24	.28	.17
2-2-2-2	.28	.18	.17	.13
3-4-3-4	.24	.21	.15	.09

Table 4.6 RMS-values in km for errors in control points when using a polygon respectively a polynomial for representation of the orbit.

4.5.RESULTS WITH A WELL-MAPPED URBAN SCENE

As shown in the example of sea ice mapping the accuracy of computed ground coordinates can be limited by the accuracy of the identification of ground points. Therefore an optically and digitally correlated image of Los Angeles was used to evaluate the accuracy of the radargrammetric mapping method if well-defined ground points exist.

Figure 4.14 shows the optically correlated and Figure 4.15 the digitally correlated image. The optical image has time and range references for the conversion of image coordinates into slant range and sensor events (imaging times), while the digitally correlated image has no such references. In this case these unknown entities were defined using ground control points according to equations (4.2). Ground coordinates were read off maps of a scale 1 : 24 000 and therefore the identification errors could be expected to be an order of magnitude smaller than from the 1 : 500 000 maps of Banks and Victoria Islands.

As can be seen from Figures 4.14 and 4.15 there is no difficulty to find well defined ground control points, especially in the form of street crossings. Figure 4.16 shows an enlargement of a section of both the optically and digitally correlated image of Los Angeles together with a section of a street map of this area. One may conclude from this illustration, that digitally processed images have a better resolution than optically correlated images.

Fifty ground points were identified both in the optically

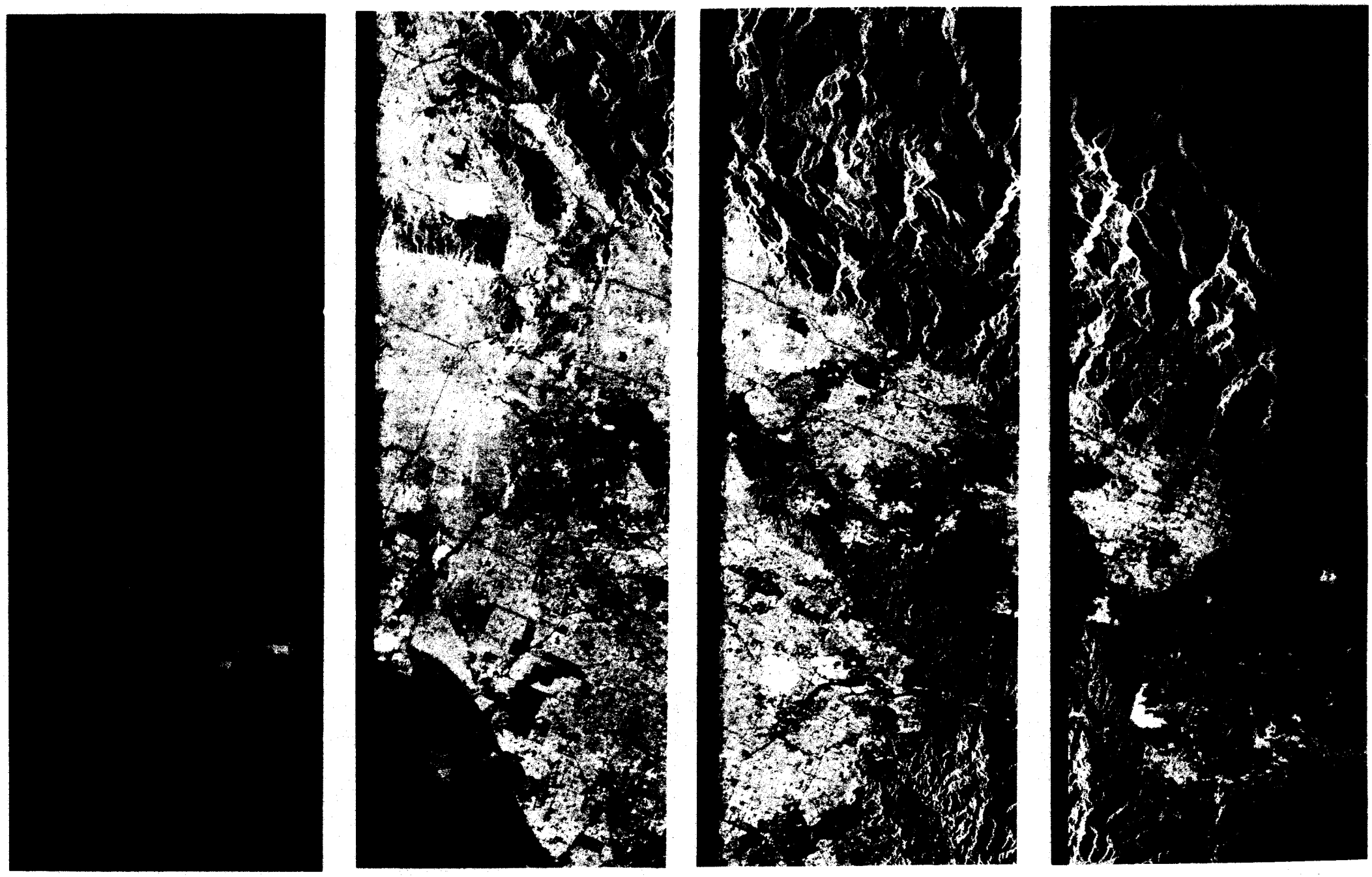

Figure 4.14 Optically correlated SEASAT-SAR image of Los Angeles (orbit 351) 10 km

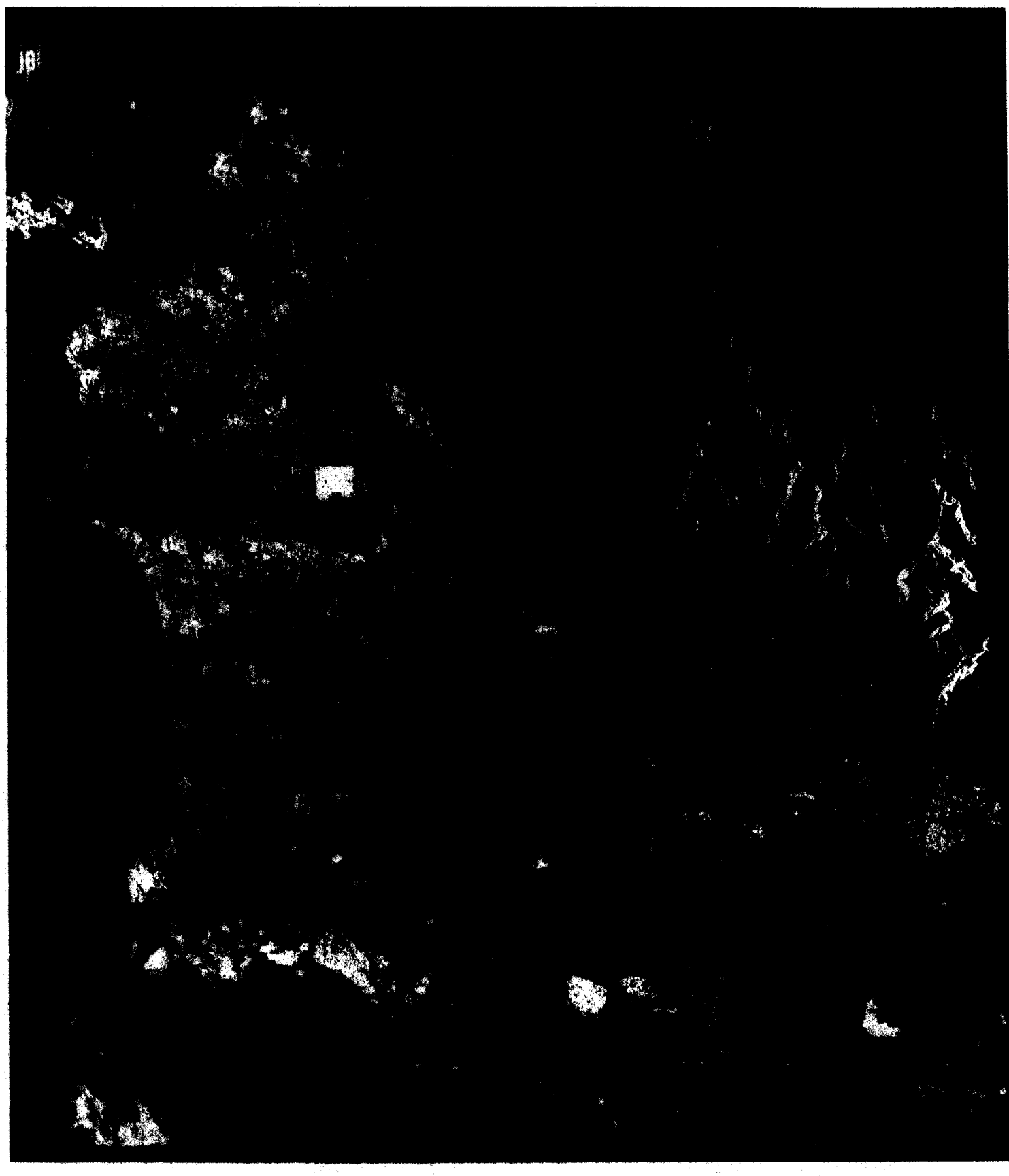

Figure 4.15 Digitally correlated SEASAT-SAR image of Los Angeles (orbit 351)

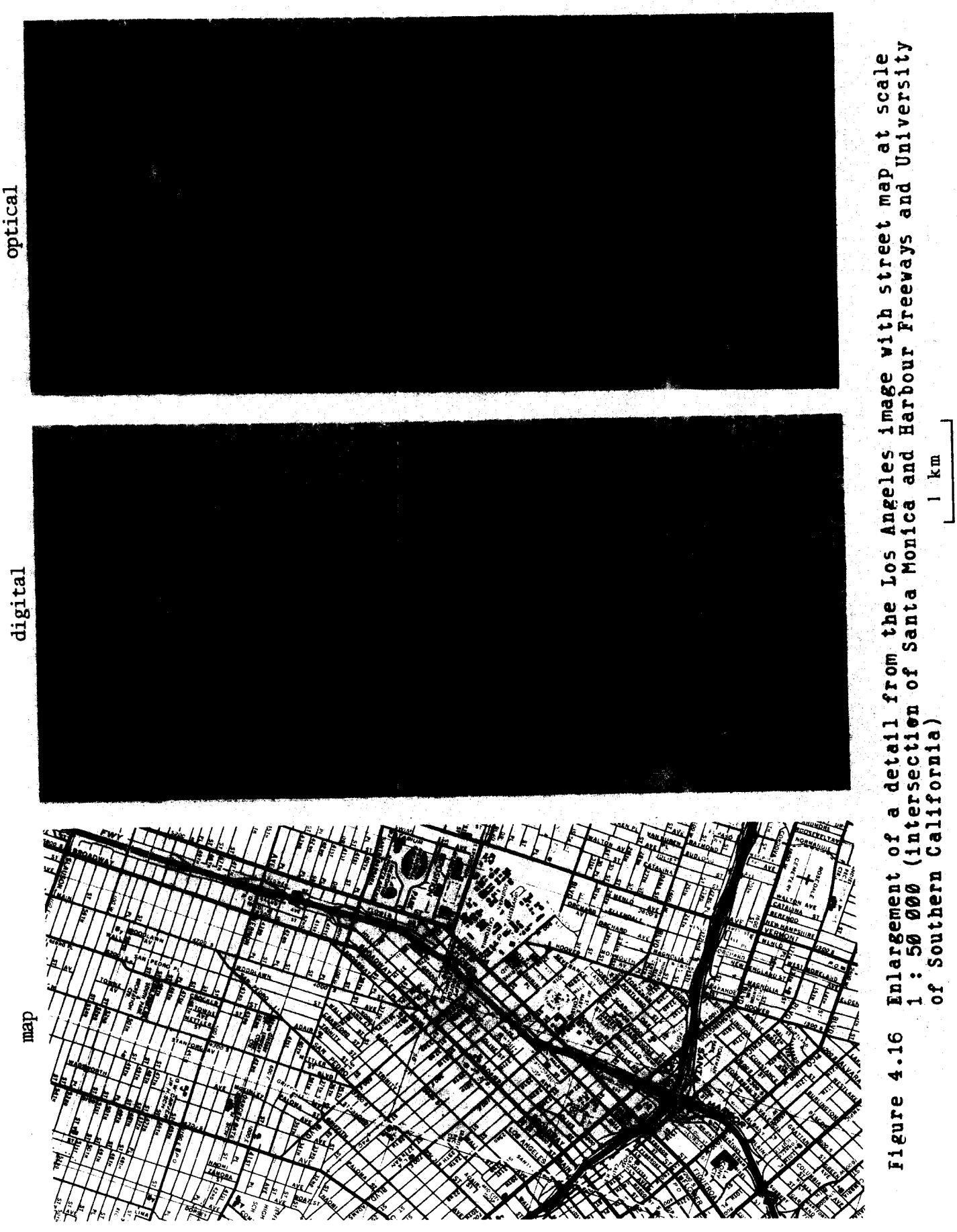

Figure 4.16 Enlargement of a detail from the Los Angeles image with street map at scale 1 : 50 000 (intersection of Santa Monica and Harbour Freeways and University of Southern California)

and the digitally correlated image distributed over the whole area of interest; their image coordinates were measured on a monocomparator. Because no measurements of sensor positions of the satellite were made when imaging this area, the orbit was assumed to be a straight line defined by two basic points and was corrected with polynomials of higher order.

For the purpose of comparision the points of the digitally correlated image were also separated in four parts, each correponding to one strip of the optical image. The errors of the radargrammetically computed coordinates of the ground control points are summarized for several correction polynomials in Table 4.7 (grossly erroneous points are eliminated). Figures 4.17 and 4.18 show the residual vectors for the optical and the digital image.

Polynomial	Optically correlated image		Digitally correlated image (four parts)		Digitally correlated image	
	x	y	x	y	x	y
2-1-2-1	0.056	0.034	0.069	0.028	0.185	0.075
3-1-3-1	0.029	0.023	0.057	0.023	0.147	0.062
3-4-3-4	0.024	0.017	0.022	0.012	0.078	0.034

Table 4.7 RMS-values of radargrammetric mapping errors of optically and digitally correlated SEASAT-SAR images of Los Angeles.The digitally correlated image once was evaluated in one way and once after separating it into four parts.

As can be seen from Table 4.7 the achievable accuracy with the radargrammetric mapping method is near the ground resolution of ± 25 meters if a high density of 7 control points is used per

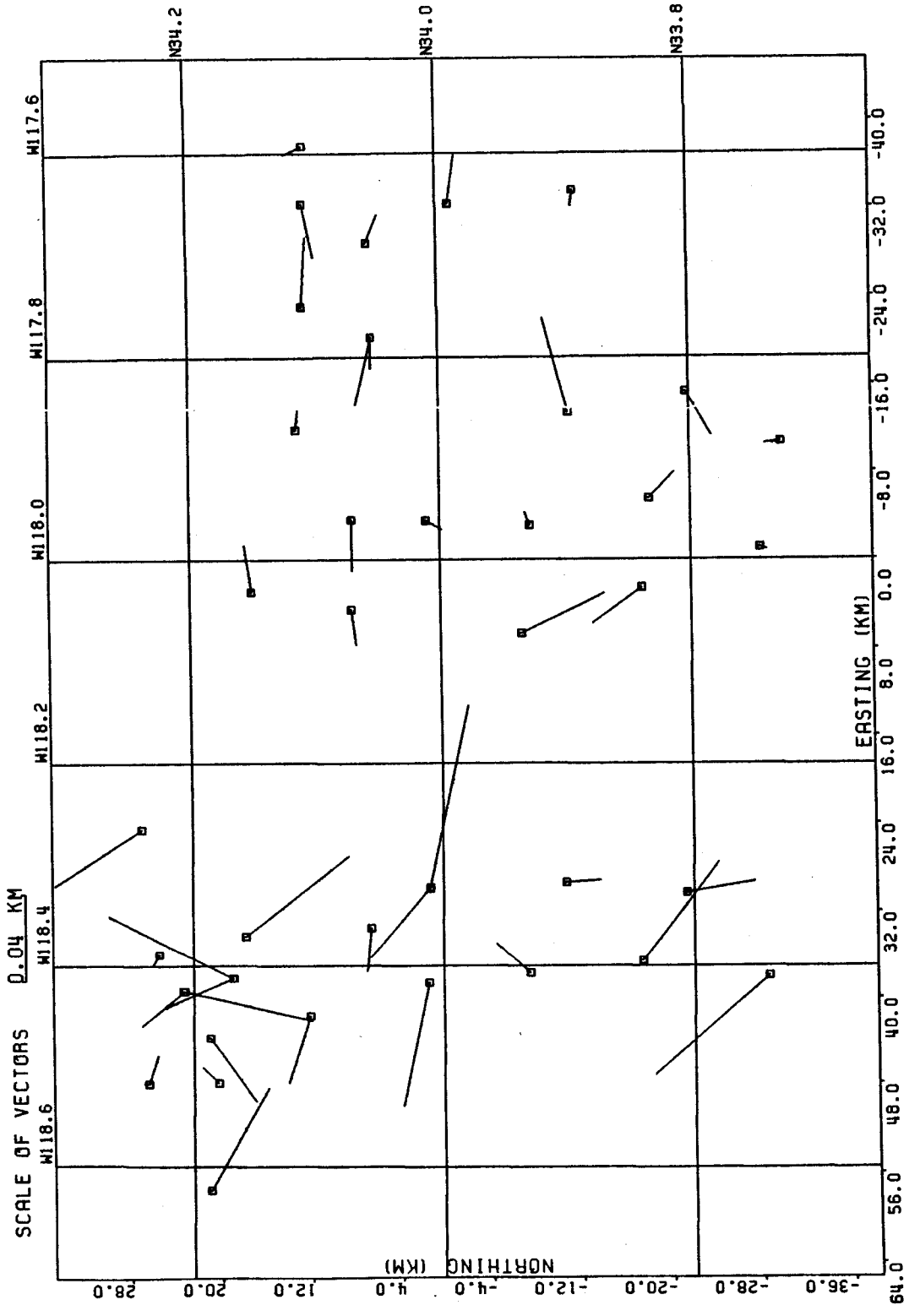

Figure 4.17 Residual vectors in ground control points after radargrammetric evaluation for the optical data of Los Angeles

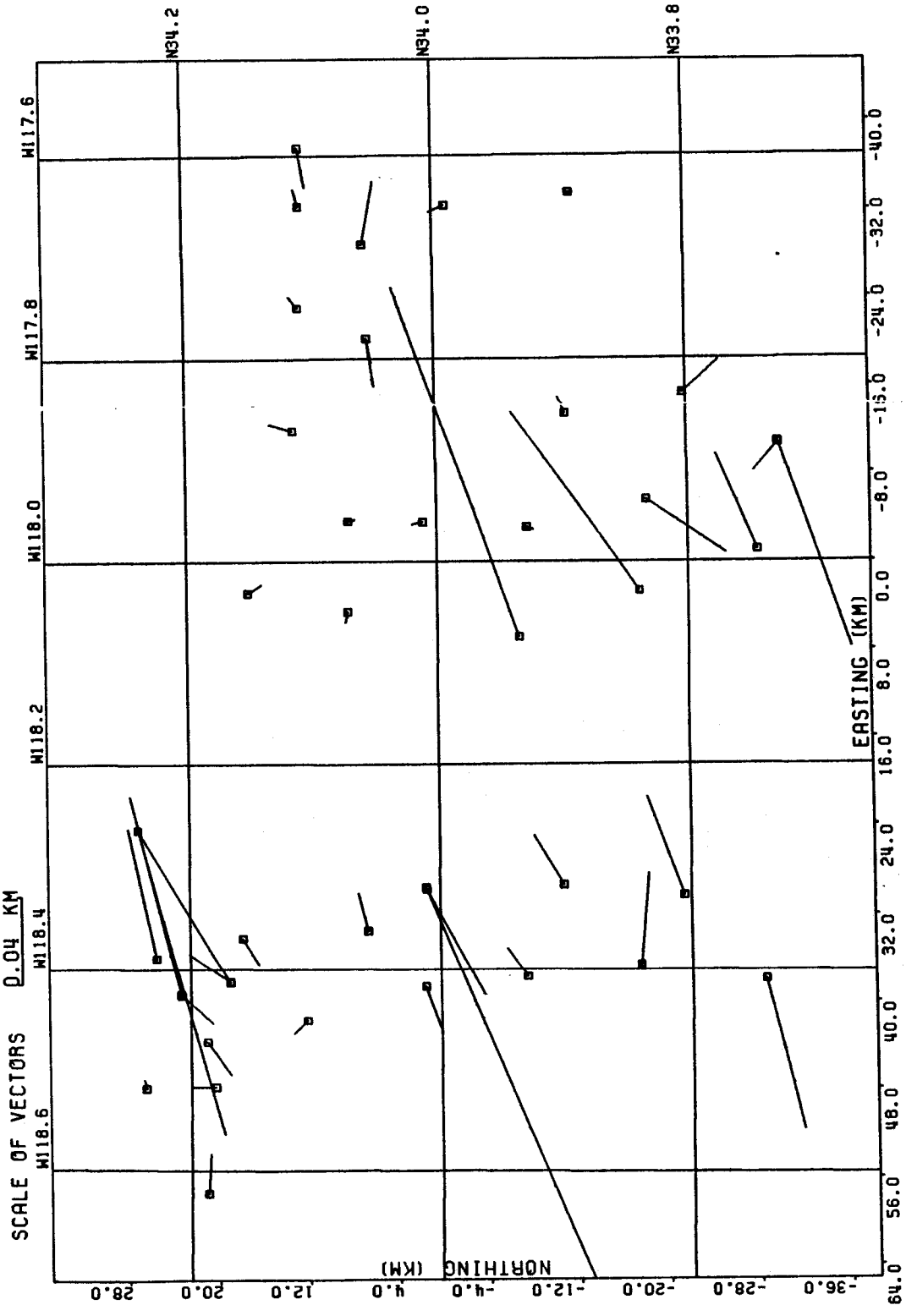

Figure 4.18 Residual vectors in ground control points for the digitally correlated image, which was separated into four parts in this case

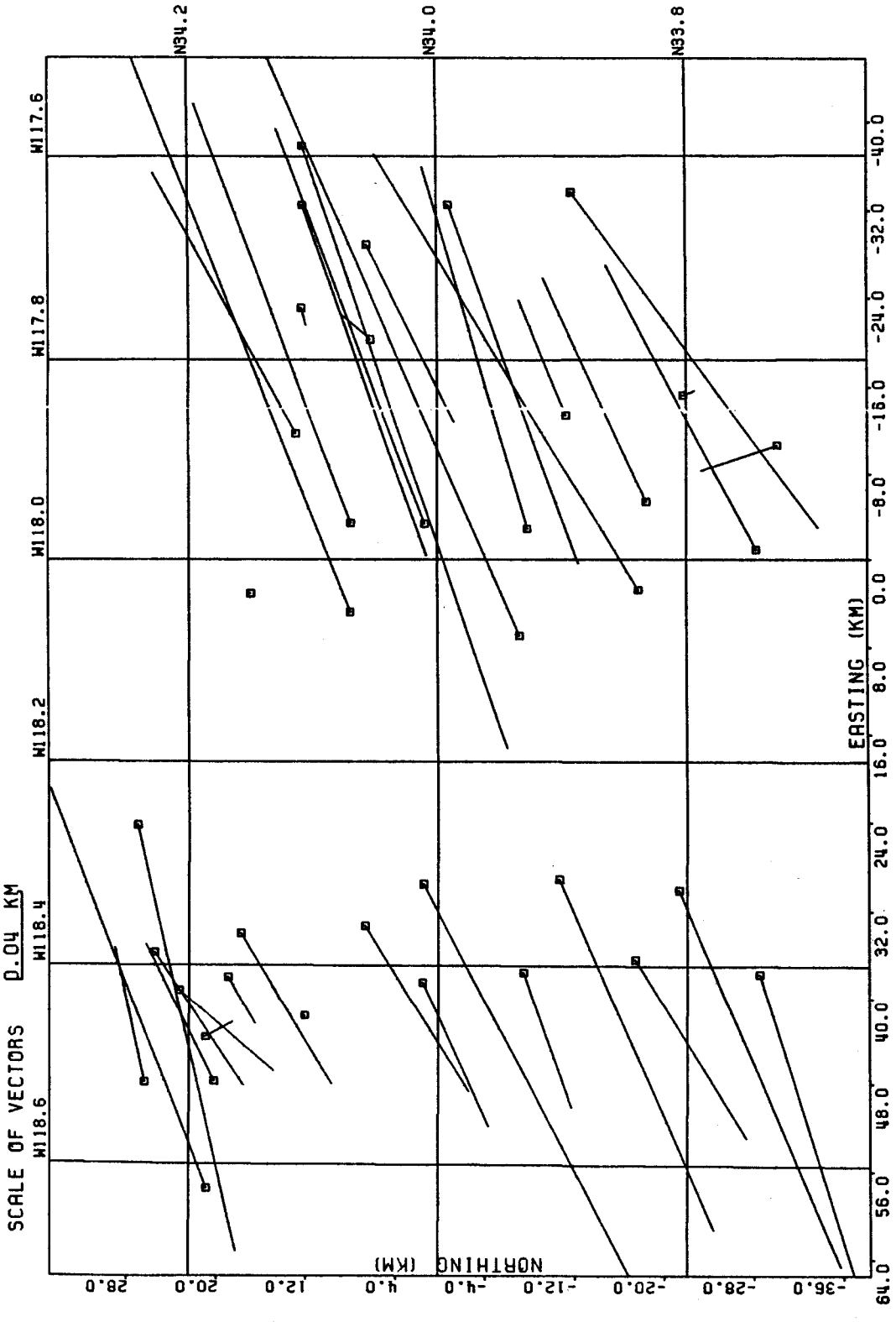

Figure 4.19 Residual vectors in ground control points for the digitally correlated image, in this case evaluated in one single transformation

1000 square kilometers.

The digital image was also evaluated without separating it into four parts in one single transformation. The residual errors obtained in this case are shown in Figure 4.19. As can be noted from this illustration the digital image has several distinct image deformation zones and the residual vectors amount up to about 200 meters. Therefore it seems that there are some parts with different image geometry in the digital image.

4.6. AN EXPERIMENT TO DETERMINE THE EFFECT OF RESOLUTION AND MULTIPLE LOOKS ON THE RADARGRAMMETRIC SINGLE IMAGE ACCURACY

For a section of the digital image of Los Angeles twelve images produced with various ground resolution and multiple looks at JPL were available. Table 4.8 gives a summary of these images with the mentioned parameters. The effect of various ground resolutions distinctly can be seen from Figures 4.20 and 4.21 which shows version 3 with a ground resolution of 25 meters and version 6 with a ground resolution of 100 meters.

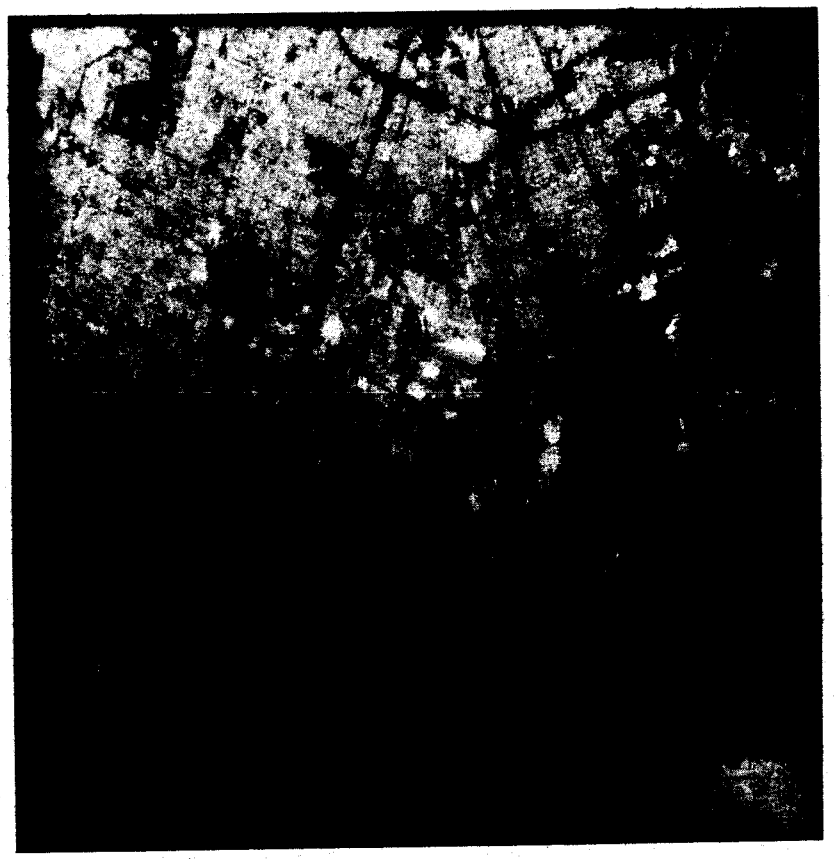

3 km

Figure 4.20 Digitally correlated radar image of a section of Los Angeles with a ground resolution of 25 meters

3 km

Figure 4.21 Digitally correlated radar image of a section of Los Angeles with a ground resolution of 100 meters

Version	Ground resolutions in meters	Looks	
A - 1	25 x 25	1	4-bit
B - 2	25 x 25	2	4-bit
C - 3	25 x 25	4	4-bit
D - 4	50 x 50	4	4-bit
E - 5	50 x 50	16	4-bit
F - 6	100 x 100	16	4-bit
G - 7	100 x 100	64	4-bit
H - 8	25 x 25	2	2-bit
I - 9	25 x 25	4	2-bit
J -10	50 x 50	8	2-bit
K -11	50 x 50	16	2-bit
L -12	100 x 100	32	2-bit

Table 4.8 Parameters of twelve versions of a section of the image of Los Angeles

For the evaluation 26 ground control points distributed over the whole imaged area were identified and their image coordinates measured for all twelve images. It is evident from the visual impression of Figures 4.20 and 4.21 that the ease of point identification depends on ground resolution. For example it was even difficult to identify only 26 relatively well defined homologue image points in all twelve images.

The coordinates of these points were computed in a geocentric coordinate system with the algorithm described in chapter 4.3 using calibration polynomials for time and range to determine sweep delay, time offset and image scales in x- and y-direction, which are unknown entities for this image.

The root mean square values of the discrepancies between given and radargrammetric computed coordinates are summarized in Table 4.9 which also contains the result after additional linear conformal transformation and of only a simple linear transformation with six parameters.

Version	Linear transformation $X=a_0+a_1 .x+a_2 .y$ $Y=b_0+b_1 .x+b_2 .y$		Radargrammetric method		Linear transformation after radargrammetric method		
	x	y	x	y	x	y	
1	49	34	29	46	26	30	
2	46	29	24	41	19	21	
3	41	27	23	40	18	18	(a)
4	43	37	25	48	21	33	
5	41	36	25	42	20	22	
6	45	37	32	50	30	36	
7	43	26	35	48	32	34	
8	55	41	30	47	27	31	
9	43	25	25	42	21	22	
10	44	39	32	48	29	34	
11	40	24	25	39	21	16	
12	56	47	35	55	33	44	(b)

Table 4.9 RMS-values in meters of residuals in ground control points: (a) - best image
(b) - poorest image

All results show the tendency that the accuracy of single radar image evaluations depends on ground resolution and the number of looks: the higher the resolution and the number of looks, the higher is the accuracy in the coordinates.

However,,as can be seen from Table 4.9, the difference of the coordinate errors between the best and the poorest image is not as large as one might have expected. For example for a simple linear transformation the errors for the poorest image (version 12 with a ground resolution of 100 meters) amount to about 70 meters while for the best image (version 3 with a ground resolution of 25 meters) the coordinate errors are at about 50 meters.

The relatively high accuracies for the images with a poor ground resolution refer to the fact, that the control points were identified in images with a large scale of about 1 : 85 000. For this image scale a length of 100 meters on ground corresponds to 1.2 mm in the image, and therefore identification errors can be assumed to be rather small.

4.7. SUMMARY

The single radar image evaluations presented in this chapter are based on a rigorous radargrammetric mapping method, which was previously described in chapter 2. The obtained results give some useful information about the capability of this method.

Since the SEASAT satellite performed a considerable part of its observations in arctic regions, these data can be used for the determination of the sea ice motion and deformation. For this purpose we used a set of seven sequential SEASAT passes over the Beaufort-Sea. The ice motion for the appropriate

observational period of thirty days was about 6.4 kilometers per day.

It was shown, that the mentioned radargrammetric mapping method, which uses the information of measurements of sensor positions, is superior to simpler methods, such as linear conformal transformation. This relates to the fact, that for the ice motion measurement ground control was available only on the islands on the one end of the imaged areas.

As shown in an error analysis, the simplified method would lead to strongly erroneous results in this case. But also the accuracy of the radargrammetric method was limited to about ± 150 meters on the ground. This fact may be caused by the low density of ground control with one point per 10 000 square kilometers, by the difficulty and accuracy of point identification and by the used technique for modelling the satellite orbit.

A radargrammetric analysis was also performed with an optically and digitally correlated SEASAT satellite image of Los Angeles. For this urban area it is not difficult to find well defined homologue points and identification errors are smaller than for the arctic scene.

With a ground control density of about 7 points per 1000 square kilometers the accuracy is of the order of magnitude of the ground resolution of about ± 25 meters on the ground for both the optically and the digitally correlated image.

C H A P T E R 5

RESULTS WITH STEREO RADAR IMAGES

5.1. THE POSSIBILITY OF STEREO RADAR VIEWING

As known from traditional photogrammetry two overlapping aerial photographs can be used for stereo viewing. Thus one obtains a three-dimensional replica of the imaged object, the stereo model, which serves the interpretation and geometric measurement of the image contents.

In the same manner a radargrammetric stereo model is obtained by viewing two overlapping radar images. Aerial photographs are based on central projections, whereas the projection rays for radar imaging are circles (range projection). The two types of stereo models have quite a different geometry. Theoretical analyses of radar stereo have been performed by numerous authors, such as by LA PRADE (1963), ROSENFIELD (1968), GRACIE (1970) or LEBERL (1979).

The most common radar stereo arrangements are obtained from two separate flight paths. Depending on the relative position of the overlapping area with respect to the flight lines or orbits one has same-side or opposite-side stereo (see Figure 5.1); in the first case the overlap area is to the same side, in the second case it is between the two orbits.

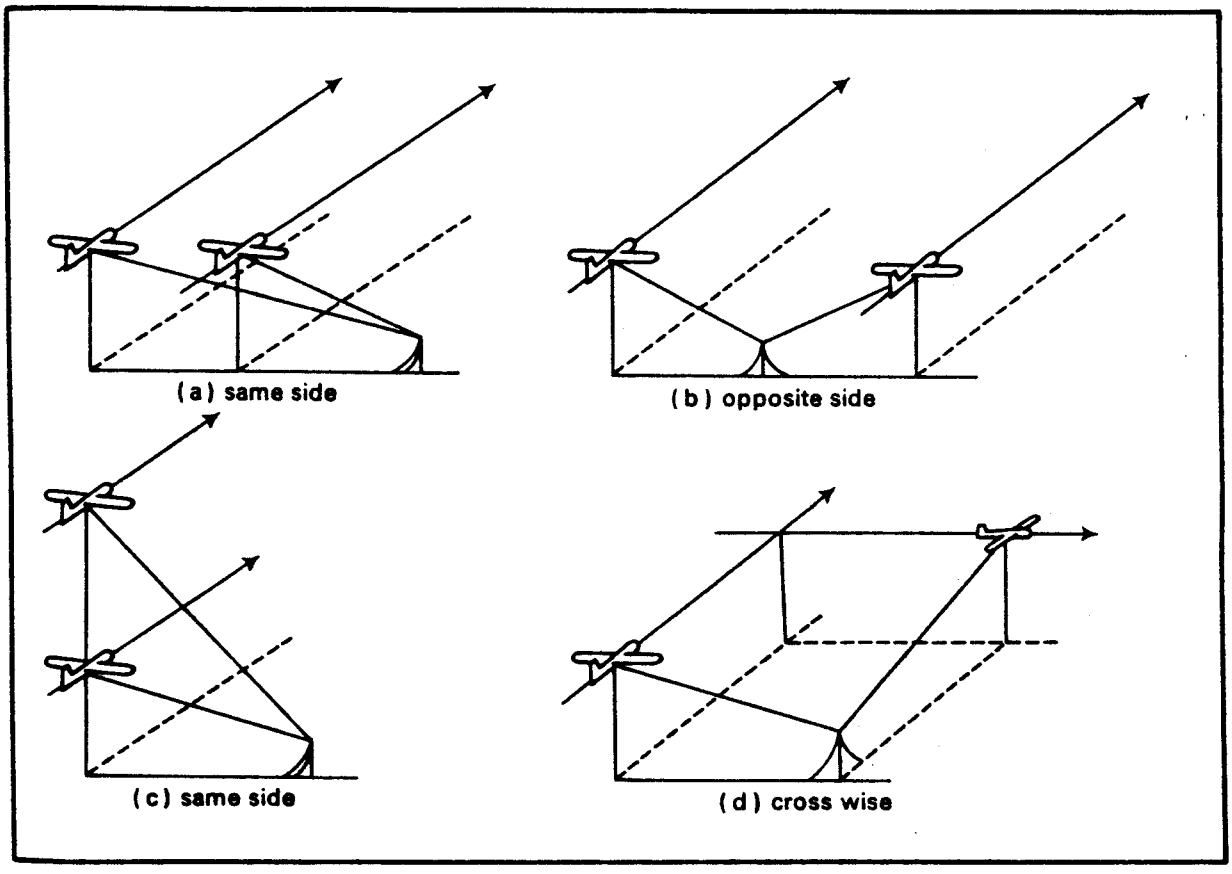

Figure 5.1 Flight configurations to obtain overlapping images with two flight lines

Other stereo arrangements using two flight paths are cross-wise or at different altitudes. As shown in Figure 5.2 overlapping images also can be obtained from single flight lines, but only with real aperture radar, when tilting the radar antennas around horizontal or vertical axes (BAIR and CARLSON,1975).

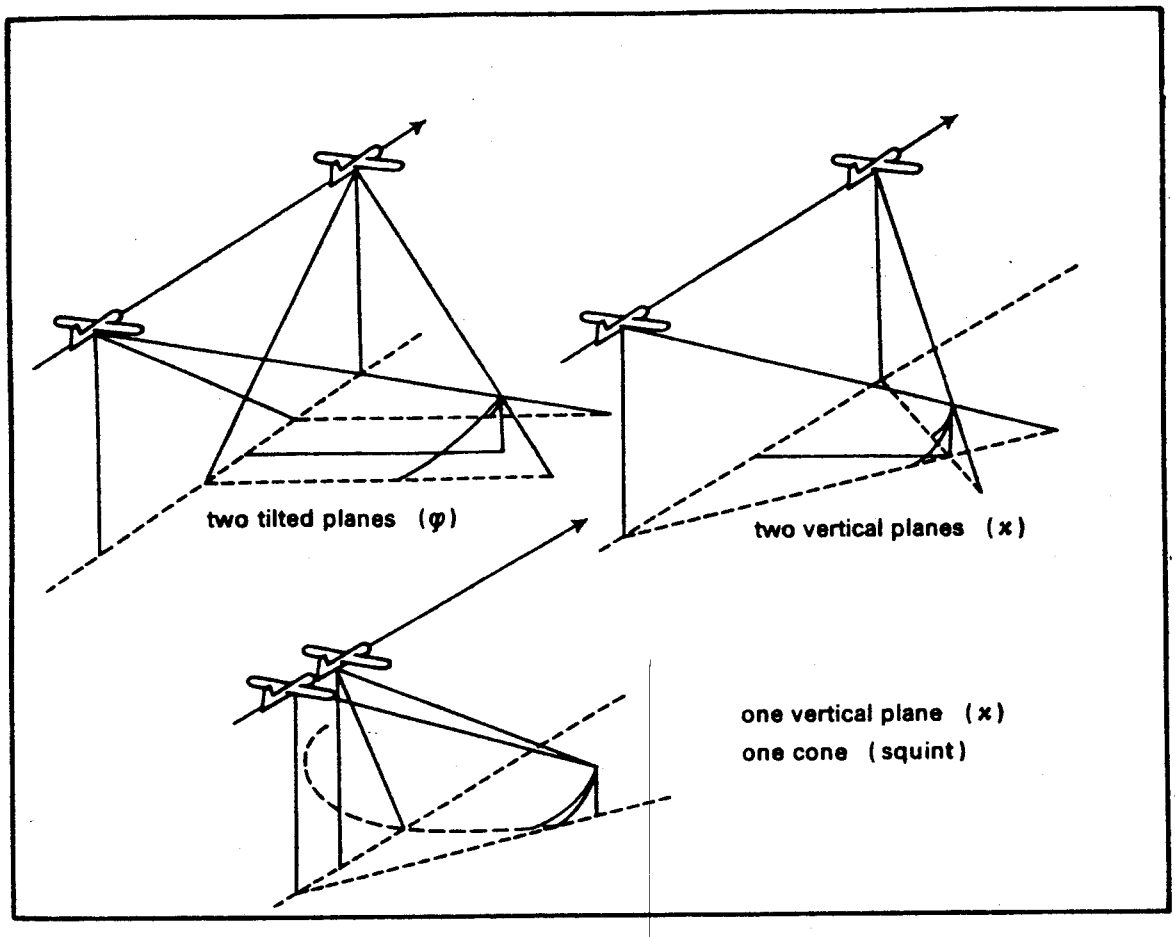

Figure 5.2 Stereo arrangements for a single flight line

To get a three-dimensional impression, the two images of a stereo pair must be sufficiently similar with respect to image quality, object illumination and geometric differences. This is no problem in aerial photography, because sun angles do not change drastically. But in radargrammetry the illumination of the objects depends on the sensor position and therefore especially in the opposite-side case the stereo impression becomes impossible for rugged areas both for ground range and slant range presentation, as argued and shown in some examples by LEBERL (1979). In this case the images can only be used for monocular identification and measurement of homologue features.

But if the images are in slant range presentation also for

same-side arrangements stereo-vision might become impossible if look angles are steep. Then larger relief displacements are obtained and even for small stereo bases the image geometry becomes rather different for rugged regions.

Therefore radar stereo viewing depends on (LEBERL, 1979)

... the stereo arrangement,
... the look angles off-nadir,
... the stereo intersection angles,
... the ruggedness of the terrain.

In the Appendix a set of radar stereo models is compiled and a discussion of these parameters and of the feasibility of stereo viewing is given in this chapter.

5.2. SIMPLIFIED COMPUTATION OF HEIGHTS FROM ACTUAL STEREO MODELS

5.2.1. The Used Radar Stereo Models

As mentioned in chapter 3, the height difference between two terrain points can be derived by measuring the parallax difference between these points and using the simplified formulas (3.39) for ground range presentation or (3.40) for slant range presentation. For this purpose some same-side radar stereo image pairs were selected with considerable terrain elevations, which are listed in Table 5.1.

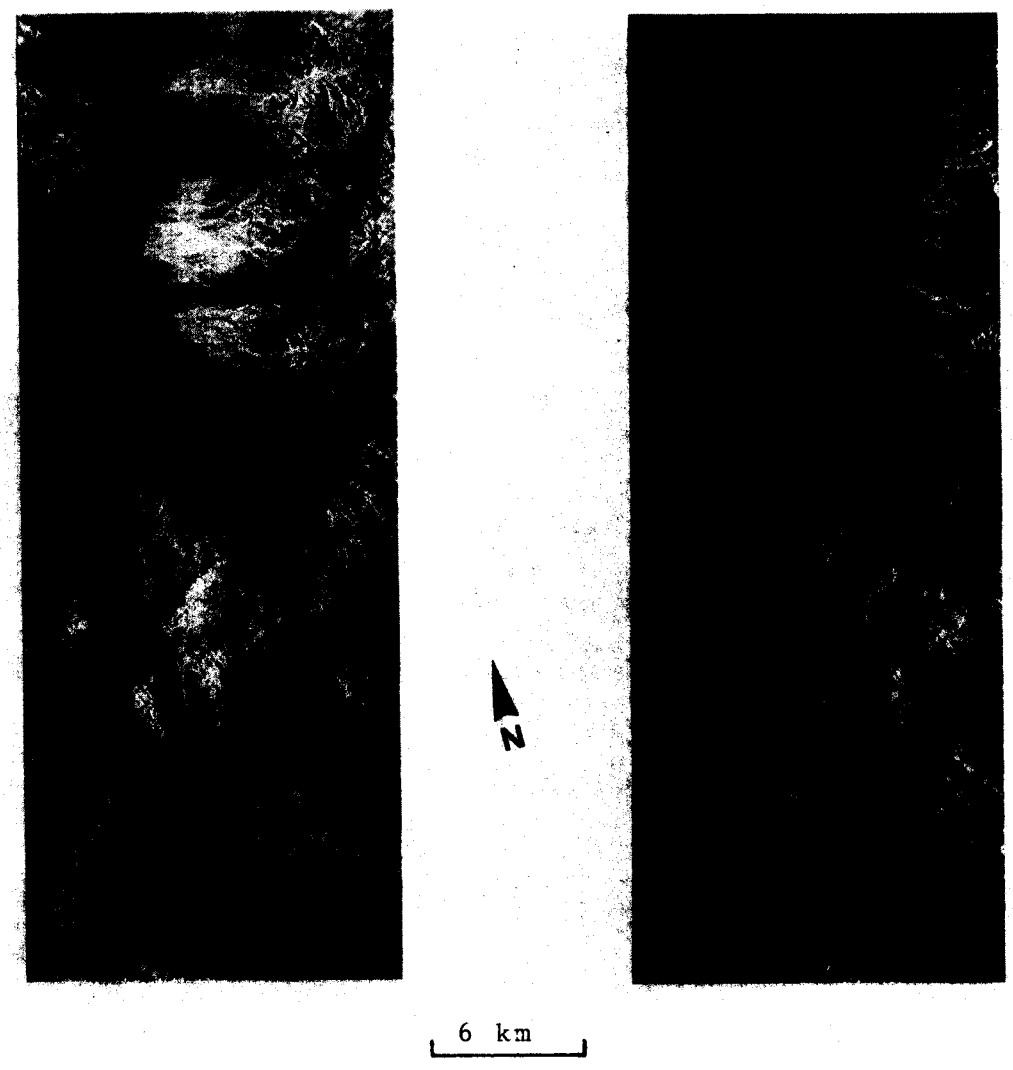

Figure 5.3 Stereo model of Granite Mountain, aircraft radar

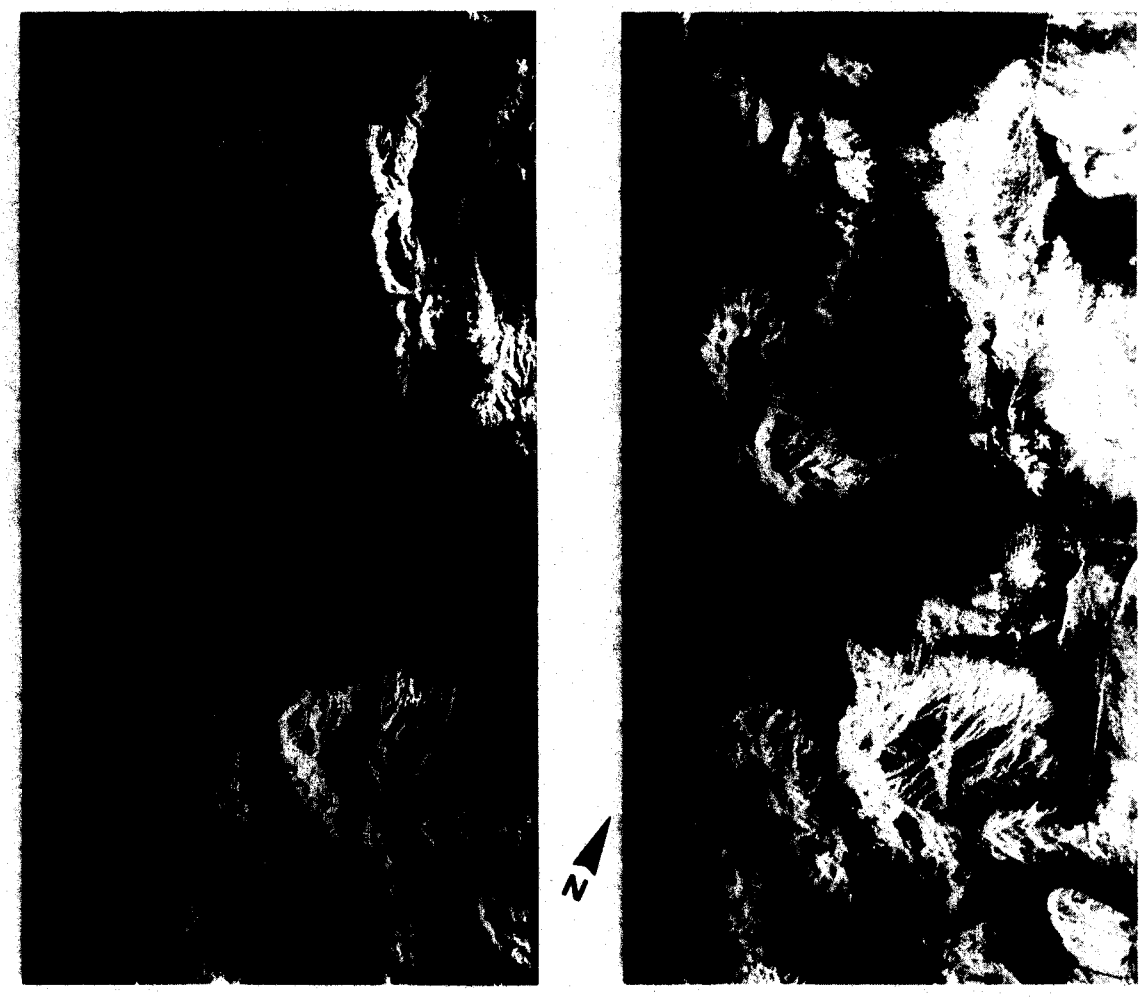

Figure 5.4 Stereo model of Granite Mountain, satellite radar

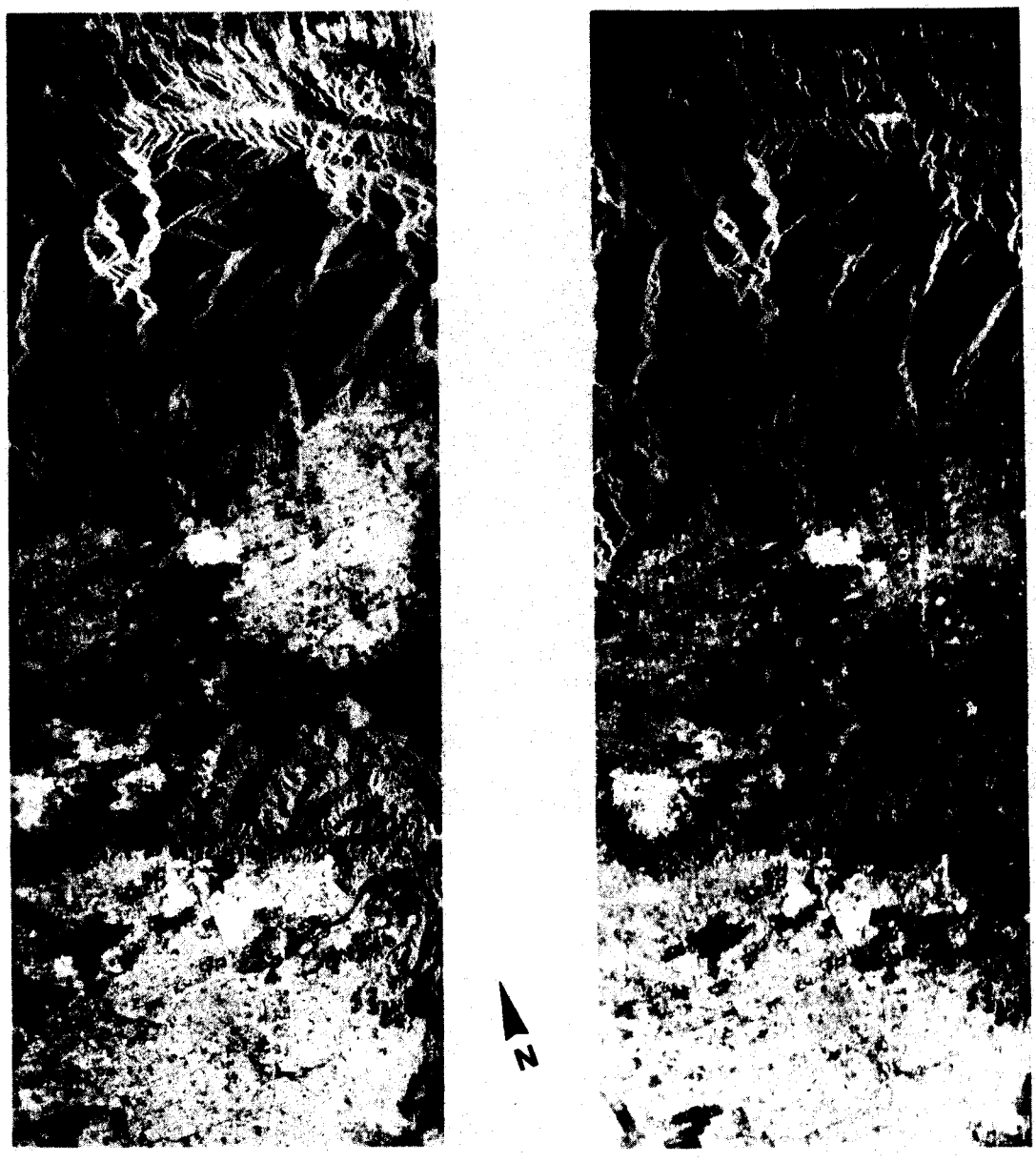

Figure 5.5 Stereo model of Los Angeles, satellite radar, with optical correlation

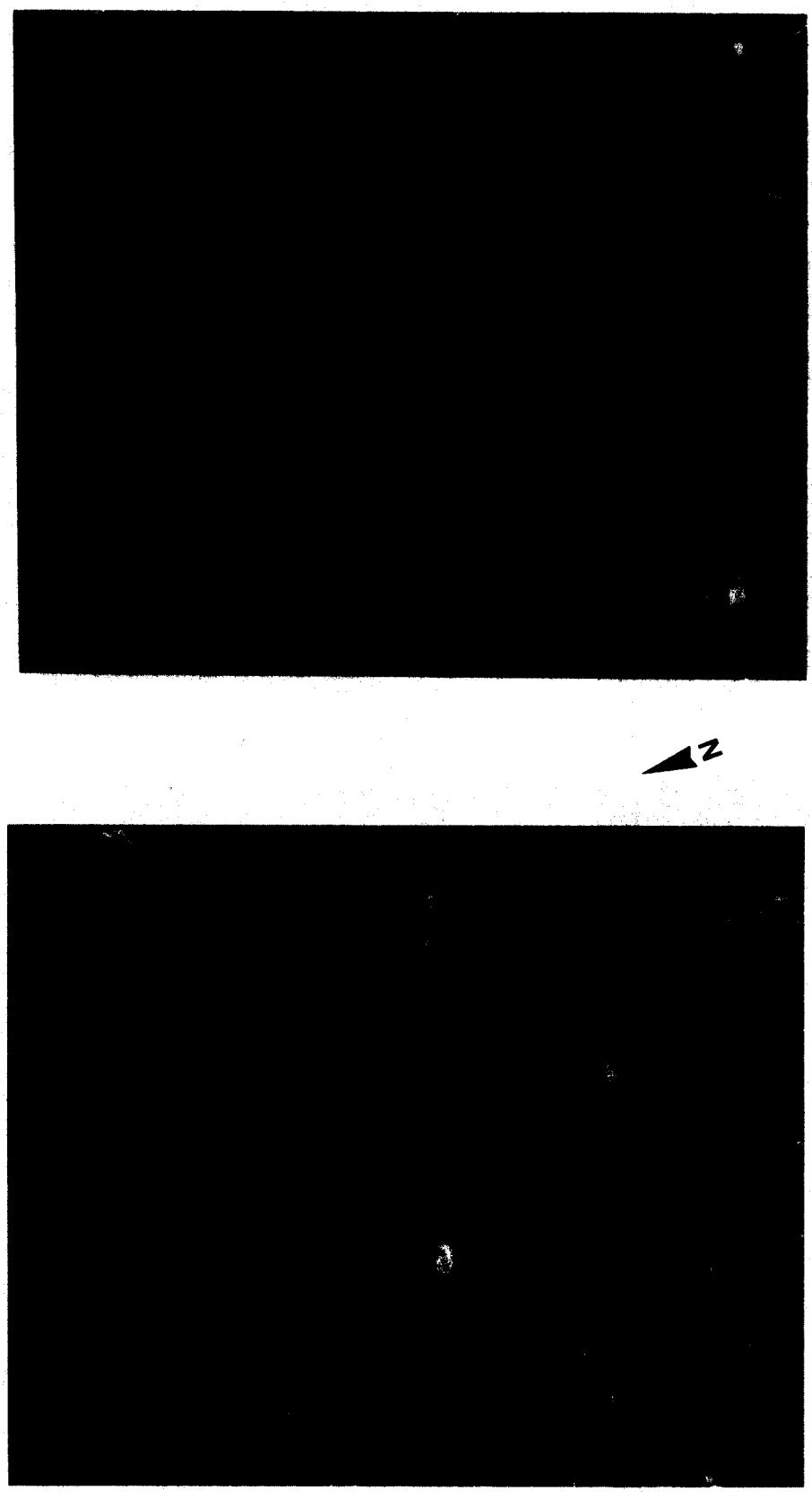

Figure 5.5 Stereo model of Los Angeles, satellite radar, with digital correlation

(a) Aircraft radar image pair of Granite Mountain (Arizona, USA) in ground range presentation. This image pair is shown in Figure 5.3. and originates from Goodyear-Aero Service.

(b) Satellite radar image pair of Granite Mountain (SEASAT-orbits 1140 and 193) in slant range presentation and with optical correlation. This image pair is shown in Figure 5.4.

(c) Satellite radar image pair of Los Angeles, California (SEASAT-orbits 1291 and 416) in slant range presentation and with optical correlation. This image pair is shown in Figure 5.5.

(d) Satellite radar image pair of Los Angeles (SEASAT-orbits 1291 and 416) in slant range presentation and with digital correlation. This image pair is shown in Figure 5.6.

Table 5.1 Same side stereo models

The imaging arrangements for these stereo models are shown in Figure 5.7. For the models of Granite Mountain the heights of ground points were read off maps with a scale 1 : 62 500 and with contour intervals of 40 feet. The heights of the ground points of the Los Angeles models were taken from maps with a scale 1 : 250 000 and contour intervals of 200 feet and (for

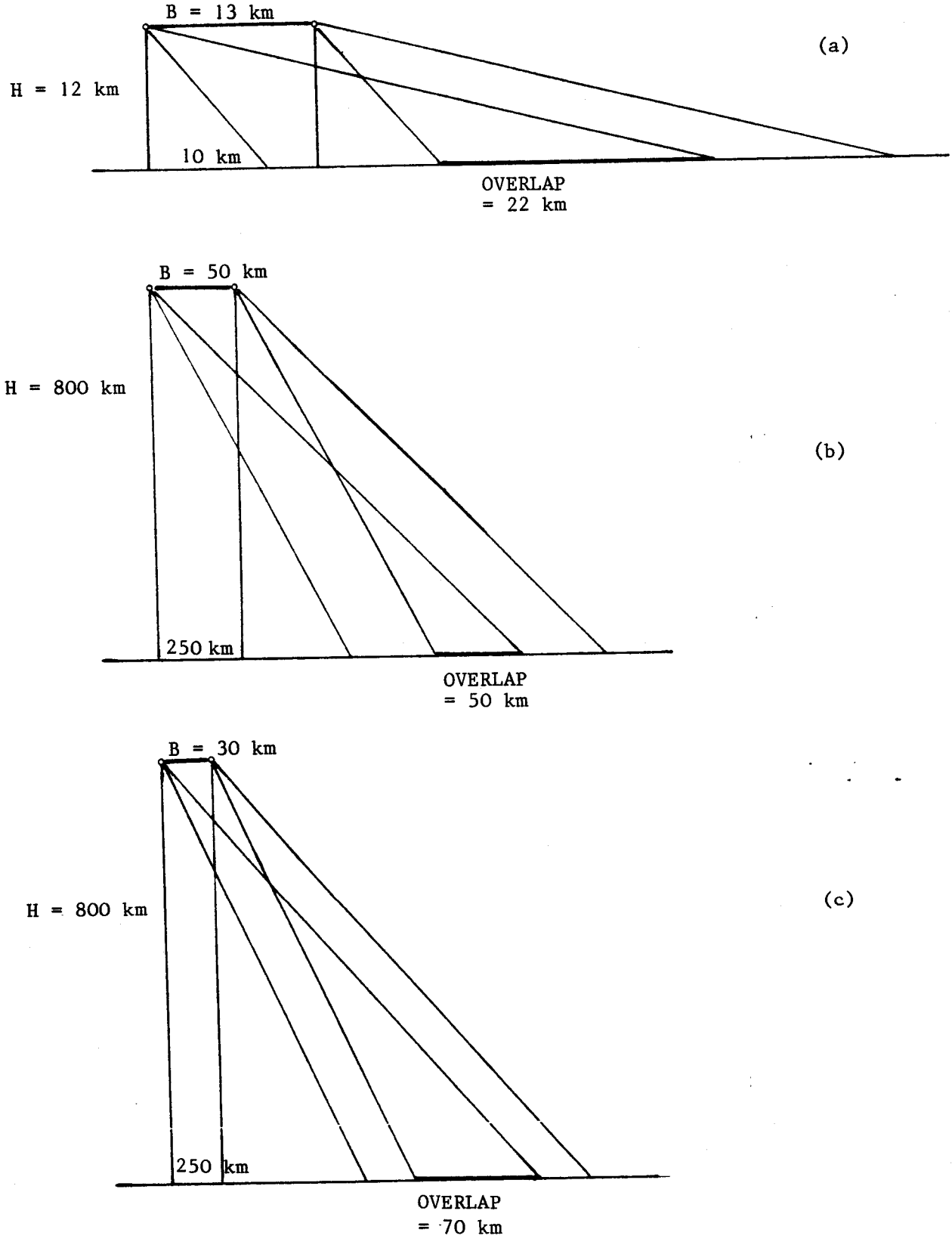

Figure 5.7 Geometric arrangements of the stereo models of
(a) Granite Mountain, aircraft radar
(b) Granite Mountain, satellite radar
(c) Los Angeles, satellite radar

the urban areas) from maps 1 : 24 000 with 20 feet contour intervals.

5.2.2 Definition of Parallaxes in the Radargrammetric Stereo Model

(a) Ground range presentation

In the case of ground range presentation the absolute parallax is defined as the difference between the ground ranges of a homologue point in the two stereo images. Parallax differences are differences of absolute parallaxes of points with different terrain heights and therefore are defined as the difference of relief displacements in the two radar images (compare Fig. 3.3). The height difference between two points can be computed with formula 3.39. For ease of reference this is noted here again:

$$\Delta h = \Delta p/(\cot \Omega'' - \cot \Omega') \qquad (3.39)$$

(b) Slant range presentation

For slant range presentations the absolute parallax is defined as the difference between slant ranges to an object point. This situation is more complex, because in this case points with the same terrain heights (points in a datum plane) have various absolute parallaxes in contrast to ground range presentation. LEBERL (1978) has shown, that the absolute parallaxes of a slant range stereo model leads to a model

deformation similar to a hyperbolic cylinder with the axis parallel to the flight line. The absolute parallaxes increase in across-track direction according to a hyperbolic function.

The difference of the absolute parallax of two points with different terrain heights is again defined as the difference of relief displacements in the radar images (compare Figure 3.4). With formula 3.40 (see chapter 3) the height difference Δh of two points can be computed:

$$\Delta h = \Delta p/(\cos \Omega'' - \cos \Omega') \qquad (3.40)$$

5.2.3 Simplified Height Evaluation

With the aid of the formulas mentioned above height differences should be computed for the stereo models cited in chapter 5.2.1. For this purpose one must know:

a) the parallax difference Δp of two points. Usually this parallax differences are measured using a stereoscope and a parallax bar. This effort was done with the available images. We also attempted to derive parallax differences in a more precise way, namely with a photogrammetric stereo plotter Zeiss-Planimat for stereo viewing and measuring model coordinates.

According to Figure 5.8 Δp can be computed with formula (5.1)

$$\lambda \Delta p = B.(z_i - z_l)/(z_o - z_i) \qquad (5.1)$$

equivalent to the photogrammetric parallax formula

$$\Delta h = \Delta p.H/B$$

λ is the scale factor between image and model coordinates and Z are the Z-coordinates of the model.

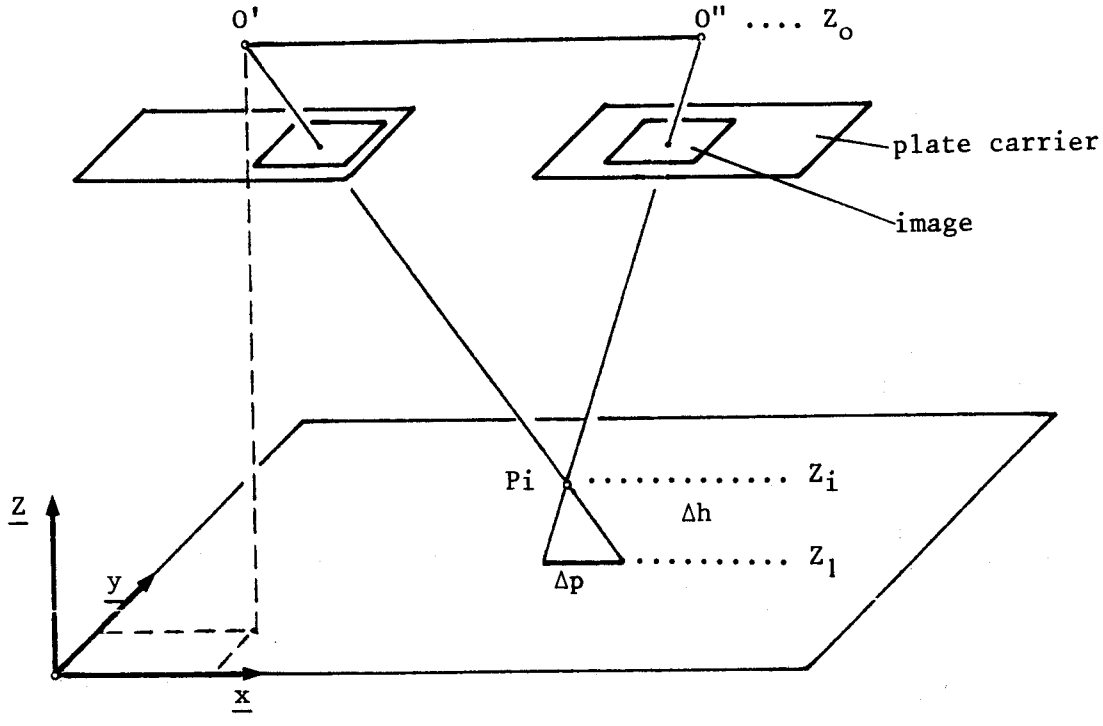

Figure 5.8 Deviation of parallax differences Δp using a stereoplotter with the projection centers O' and O"

b) the two elevation angles Ω' and Ω''. These are computed using a simplified imaging geometry as shown in Figure 5.7. With the approximately known y-image coordinate ground ranges r_g (in the case of ground range presentation) or slant ranges r_s (for slant range presentation) are computed as follows:

$$r_g = y.f + c_g$$
$$\text{or} \quad r_s = y.f + c_s \qquad (5.2)$$

f is the image scale in across-track direction and c_g respectively c_s are the sweep delays for ground and slant range presentation. The elevation angles are then computed with equations (5.3):

$$\text{Ground ranges:} \quad \tan\Omega = r_g / H$$

$$\text{Slant ranges:} \quad \cos\Omega = H / r_s \qquad (5.3)$$

To get height differences Δh in meters, the measured parallax differences Δp must be multiplied with the scale factor f.

For the discussion of the errors in height differences Δh caused by approximately known flight parameters the following error equations can be used, which partly were published in previous papers, e.g. in LEBERL (1978):

a) Ground range presentation:

$$\begin{aligned}
d\Delta h &= [\, f/(\cot\Omega'' - \cot\Omega')\,].d\Delta p &&= a_1.d\Delta p \\
d\Delta h &= [\, f.\Delta p/(\cot\Omega'' - \cot\Omega')\sin^2\Omega'\,].d\Omega' &&= a_2.d\Omega' \\
d\Delta h &= [\, f.\Delta p/(\cot\Omega'' - \cot\Omega')\sin^2\Omega''\,].d\Omega'' &&= a_3.d\Omega'' \qquad (5.4) \\
d\Delta h &= [\, 1/(\cot\Omega'' - \cot\Omega')\,].dB &&= a_4.dB \\
d\Delta h &= [\, 1/(1 - \tan\Omega'.\cot\Omega'')\,].dH &&= a_5.dH
\end{aligned}$$

b) Slant range presentation:

$$
\begin{aligned}
d\Delta h &= [\, f/(\cos\Omega'' - \cos\Omega')\,].d\Delta p && = b_1.d\Delta p \\
d\Delta h &= [\, f.\Delta p/(\cos\Omega'' - \cos\Omega').\sin\Omega'\,].d\Omega' && = b_2.d\Omega' \\
d\Delta h &= [\, f.\Delta p/(\cos\Omega'' - \cos\Omega').\sin\Omega''\,].d\Omega'' && = b_3.d\Omega'' \qquad (5.5) \\
d\Delta h &= [\, 1/(\cot\Omega'' - \cot\Omega')\,].dB && = b_4.dB \\
d\Delta h &= [\, 1/(1 - \tan\Omega'.\cot\Omega'')\,].dH && = b_5.dH
\end{aligned}
$$

The error coefficients $a_1 \ldots a_5$ or $b_1 \ldots b_5$ are presented in Table 5.2 for the three stereo arrangements of Figure 5.7. for near (A), mid (B) and far (C) range positions.

Granite Mountain Aircraft radar				Granite Mountain Satellite radar				Los Angeles Satellite radar			
	(A)	(B)	(C)		(A)	(B)	(C)		(A)	(B)	(C)
a1 =	0.58	1.65	3.21	b1 =	11.00	10.53	10.15	b1 =	19.16	17.18	16.50
a2 =	0.05	0.13	0.48	b2 =	3.72	3.64	3.60	b2 =	10.59	9.44	9.51
a3 =	0.04	0.16	0.52	b3 =	3.16	3.15	3.17	b3 =	9.58	8.64	8.82
a4 =	1.45	4.12	8.03	b4 =	1.88	2.26	2.69	b4 =	2.98	3.71	4.73
a5 =	0.74	1.48	2.21	b5 =	5.01	5.58	6.16	b5 =	8.51	9.41	10.83

Table 5.2 Error coefficients of the used stereo models

A graphical presentation of these error coefficients is shown in Figures 5.9, 5.10, 5.11 and 5.12. It can be seen that for the models of Granite Mountain the error curves for the satellite stereo model are considerable poorer than for the aircraft stereo model. Otherwise the coefficients for the satellite stereo model are somewhat better than for the one of

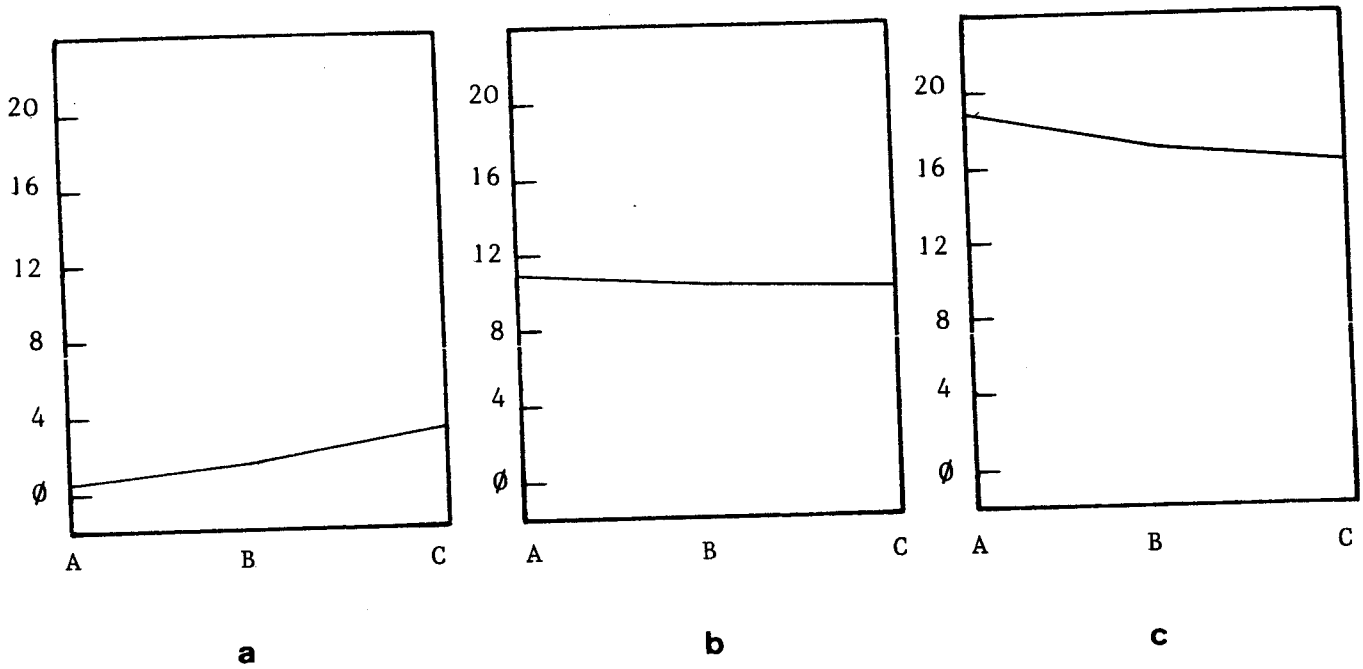

Figure 5.9 Error coefficients $d\Delta h/d\Delta p$ for the stereo models of Figure 5.7 for near (A), mid (B) and far (C) range positions

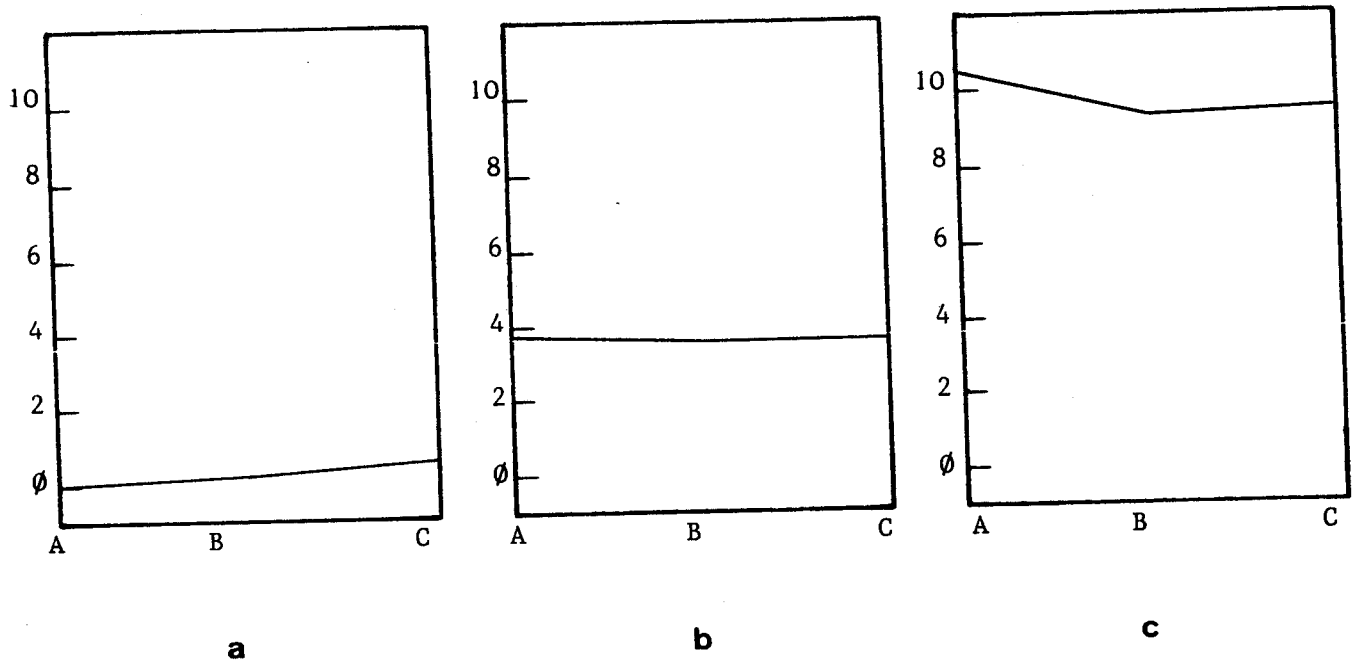

Figure 5.10 Error coefficients $d\Delta h/d\Omega'$ for the stereo models of Figure 5.7 for near (A), mid (B) and far (C) range positions

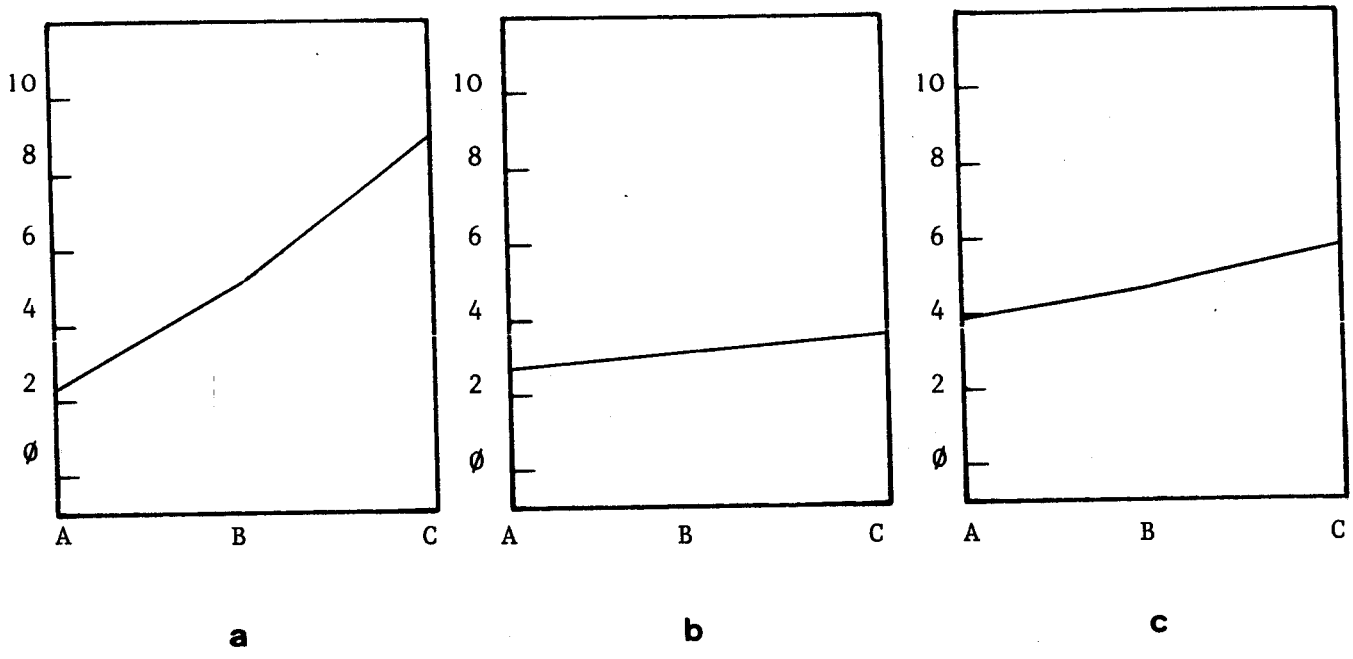

Figure 5.11 Error coefficients $d\Delta h/dB$ for the stereo models of Figure 5.7 for near (A), mid (B) and far (C) range positions

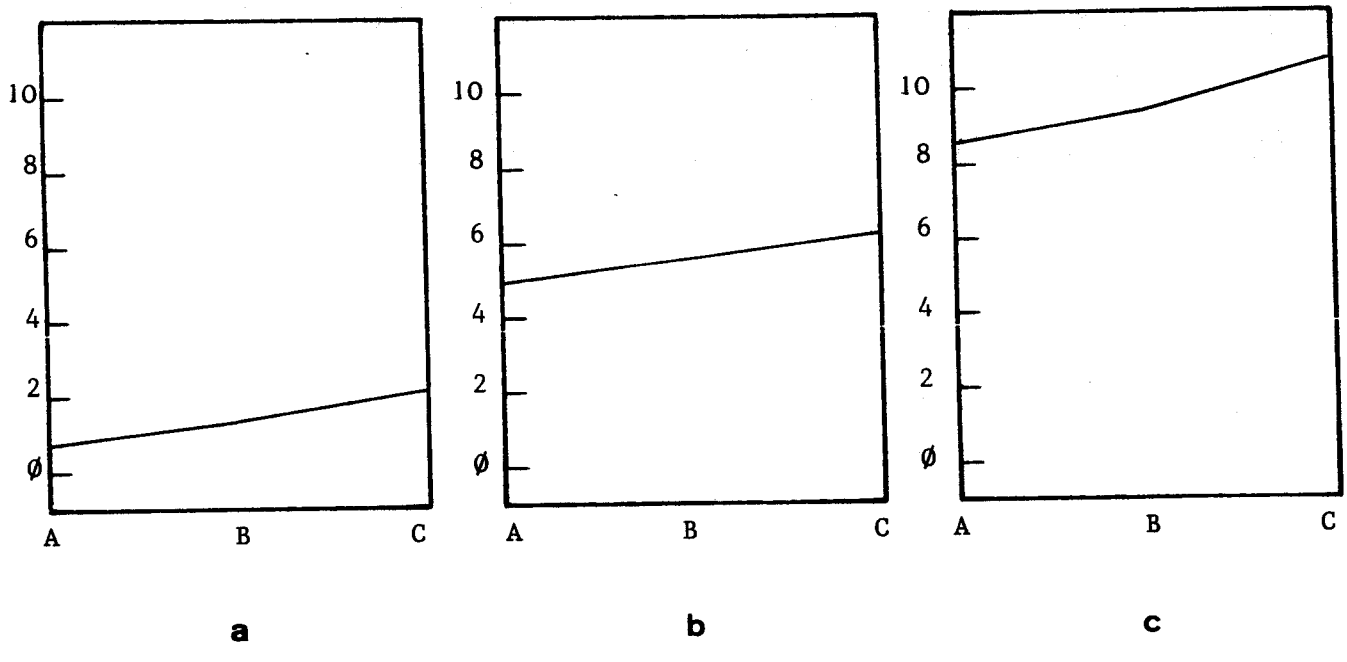

Figure 5.12 Error coefficients $d\Delta h/dH$ for the stereo models of Figure 5.7 for near (A), mid (B) and far (C) range positions

Los Angeles. This refers to the fact, that the satellite model of Granite Mountain at the one hand has a better stereo configuration than the model of Los Angeles and at the other hand a poorer one than the aircraft stereo model.

Parallax differences were measured for the four radar stereo models mentioned in chapter 5.2.1 using a stereoscope and a parallax bar and for the two models of Granite Mountain also using a photogrammetric stereo plotter. Height differences were computed with the formulas (3.39) and/or (3.40). For slant range presentations (equation 3.40) the radar stereo models are deformed similar to a hyperbolic cylinder; computed height differences and therefore also the errors of these values are increasing in across track direction. This is shown in Figure 5.13, which is a contour line presentation of differences between given and computed height differences for the satellite radar model of Granite Mountain, obtained after evaluating the parallax measurements with stereoscope and parallax bar. The model deformation is distinctly systematic.

For the reason of the hyperbolic cylinder model deformation the measured parallaxes in across track direction are increasing and therefore also parallax differences related to a reference point in the near (or far) range are increasing (or decreasing). The errors in height differences Δh caused by this fact are corrected with a polynomial as follows:

$$\Delta h = \sum_{i=1}^{I+1} \cdot \sum_{j=1}^{J+1} \cdot \sum_{k=1}^{K+1} \cdot c_{ijk} \cdot x^{(i-1)} \cdot y^{(j-1)} \cdot z^{(k-1)} \qquad (5.6)$$

with the condition : $i+j+k \leq 3$.

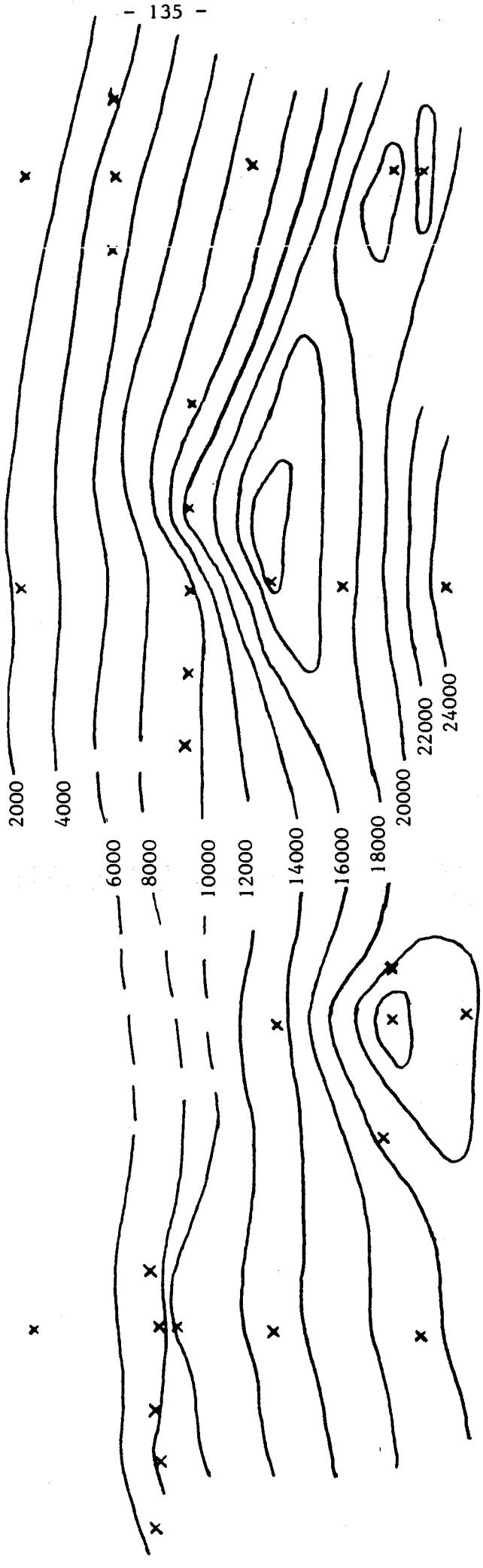

Figure 5.13 Contour line presentation of height errors before correction

The polynomial coefficients c_{ijk} are computed by a least squares adjustment with the observations Δh, which are the height differences related to a reference point. x and y are the image coordinates of the points and z are the computed height differences. A set of such polynomials was used for the four (respectively six measured) stereo models to correct the computed values for Δh. The root mean square values for remaining errors are summarized in Table 5.3.

Polynomial	Number of polynomial coefficients	I	II	III	IV	V	VI
I J K		30 points	30 points	23 points	23 points	30 points	30 points
1 - 1 - 0	4	350	352	365	365	474	456
1 - 0 - 1	4	363	364	219	231	375	427
2 - 1 - 1	4	177	147	189	169	347	669
1 - 1 - 1	8	140	139	138	134	274	262
2 - 1 - 1	11	135	130	78	106	199	236
1 - 2 - 1	11	121	134	133	128	256	207
1 - 1 - 2	11	136	124	124	120	217	218
2 - 2 - 1	14	102	127	68	89	186	169
1 - 2 - 2	14	99	122	99	70	180	141
2 - 2 - 2	17	96	121	49	48	143	121

I ... Granite Mountain , satellite radar , parallax bar measurements
II ... Granite Mountain , satellite radar , stereoplotter measurements
III ... Granite Mountain , aircraft radar , parallax bar measurements
IV ... Granite mountain , aircraft radar , stereoplotter measurements
V ... Los Angeles , optically correlated , parallax bar measurements
VI ... Los Angeles , digitally correlated , parallax bar measurements

Table 5.3 Root mean square errors in meters of the used stereo models after correction with polynomials according to equations (5.6)

With these results it seems to be useful to take a polynomial with the three variables x,y and z, because this

leads generally to better results than the use of a polynomial with only two (or one) variable(s). Furthermore we can say that with the available data the use of a photogrammetric stereo plotter for parallax measurements did not lead to better results than the simple measurement with stereoscope and parallax bar.

One might expect that with the use of a flexible polynomial systematic errors caused by the approximate values for the base B and the flying height H and by the hyperbolic model deformation can be eliminated for the most part and that the remaining errors chiefly are caused by measurement errors.

This is also shown in Figure 5.14, which shows the distribution of remaining errors in the height differences after correction with a 1-1-1 polynomial for the satellite radar model of Granite Mountain. The effect of correcting the height errors with a polynomial is shown in Figure 5.15 for points arranged in across track direction. This illustration distinctly shows the increasing values for the height differences Δh in across track direction caused by the cylindric model deformation.

With the values of Table 5.3. one can conclude:

...the results for the aircraft stereo model of Granite Mountain are somewhat better than those for the satellite radar stereo model. This refers to the fact that the aircraft stereo model has a better stereo configuration, which is expressed by the relationship of stereo base and flying height. Therefore also the error coefficients of Table 5.2 are somewhat better

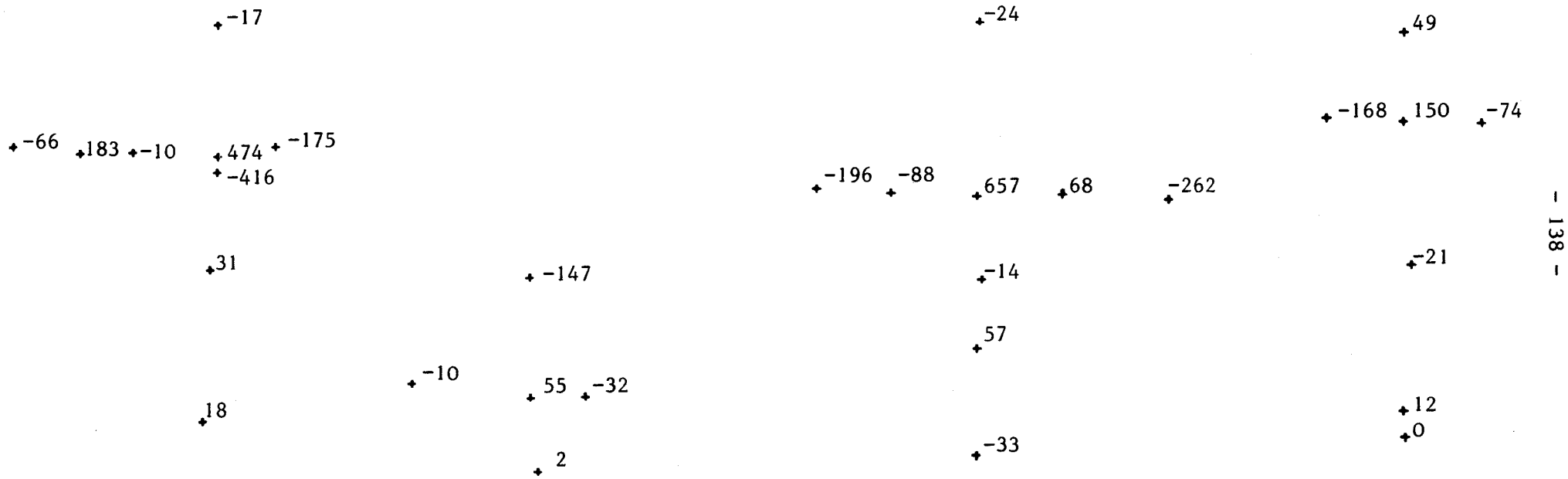

Figure 5.14 Remaining height errors after correction

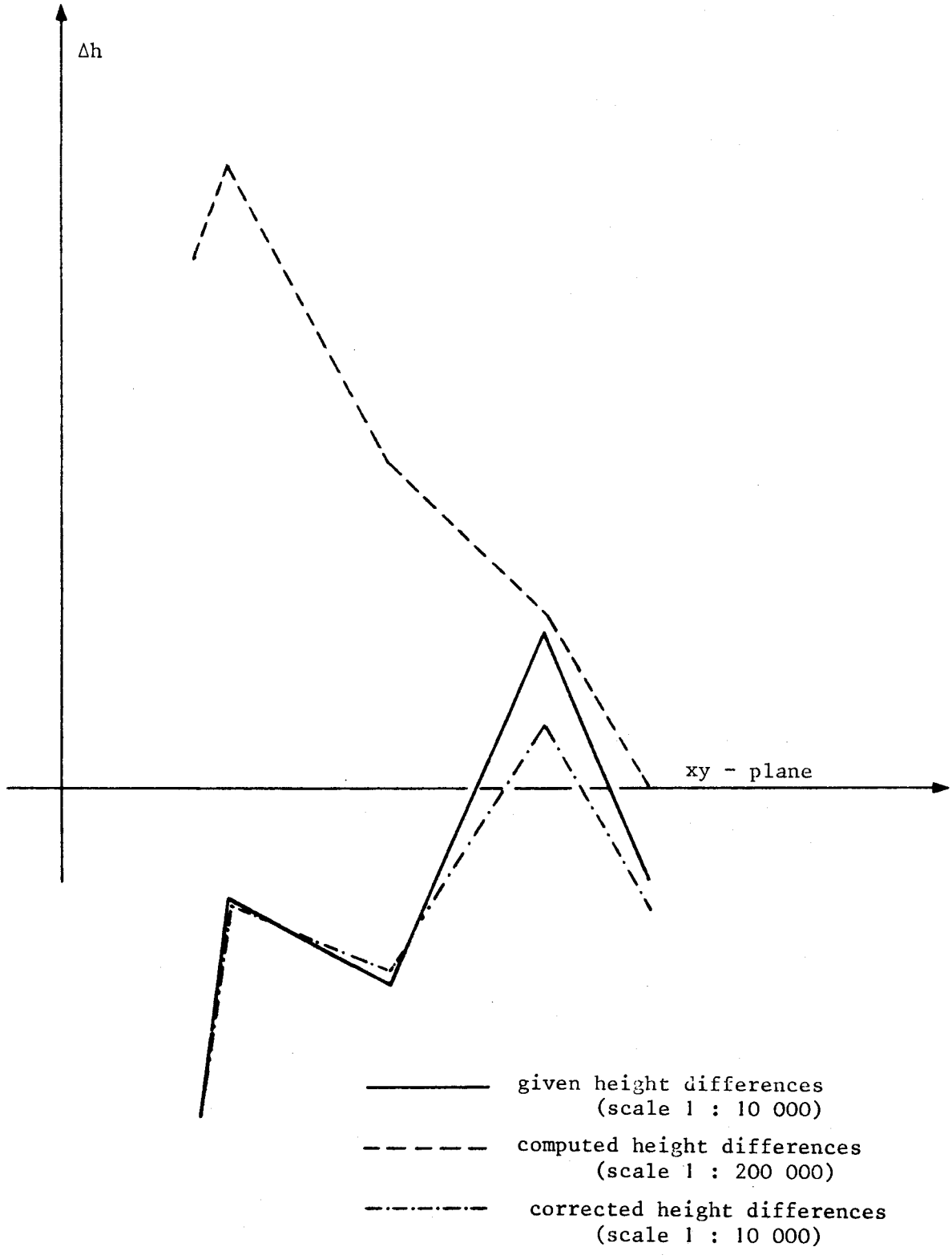

Figure 5.15 Correction of height errors in across track direction

for the aircraft stereo model than for the satellite stereo model.

...the results for the models of Los Angeles are somewhat poorer than for the satellite stereo model of Granite Mountain. This could be expected, because the error coefficients of Table 5.2 are also somewhat poorer for the Los Angeles case, due to the better stereo configuration of the Granite Mountain satellite radar stereo model.

...there is no significant difference between the accuracies of the optical and the digital radar stereo model of Los Angeles. Therefore we can say, that for the purpose of simple parallax measurement evaluations the resolution of the images does not affect the accuracy significantly.

5.3. RIGOROUS STEREO EVALUATIONS

For the SEASAT radar stereo model of Granite Mountain also attempts were made for rigorous stereo intersections according to formulations 3.1 or 3.5. These methods both need for input the orbit positions and the sensor velocity vectors when imaging a homologue pair of points in the left and the right image of the radar stereo model. These entities can be evaluated with any single image mapping method, for example with the algorithm described in chapter 4.3 as we did.

But since there were obviously time offsets in the single images, the single image evaluations led to strongly erroneous sensor positions, for a time error of 3 seconds in a SEASAT image leads to a position error of about 20 km as shown in chapter 4.4. It is evident that also the stereointersection with one of the two mentioned methods would lead to erronecus coordinates for the intersected point.

To get correct results with this method one should have ground control points to introduce time and range calibration polynomials for the single images and therefore to eliminate the effect of time offsets. This should be done in ongoing efforts.

5.4. ERRORS OF RADAR STEREO MODELS

Error equations for radar stereo models were derived by LEBERL (1978) for a simplified flight arrangement as shown in Figure 3.4. In this local coordinate system the vectors of sensor positions ($\underline{s}'$ and $\underline{s}''$) and the velocity vectors of the sensor ($\dot{\underline{s}}'$ and $\dot{\underline{s}}''$) are given as follows:

$$\underline{s}' = (x_s' \ , y_s' \ , z_s' \ ) = (0 \ , 0 \ , H \ )$$
$$\underline{s}'' = (x_s'' \ , y_s'' \ , z_s'' \ ) = (0 \ , B \ , H \ )$$
$$\dot{\underline{s}}' = (\dot{x}_s' \ , 0 \ , 0 \ )$$
$$\dot{\underline{s}}'' = (\dot{x}_s'' \ , 0 \ , 0 \ )$$

The error equations (coefficients) in this local system are summarized in Table 5.4.

	Error in x	Error in y	Error in z
dx_s'	$dx_s'/2$	0	0
dy_s'	0	$dy_s'/(1 - \cot\Omega'.\tan\Omega'')$	$dy_s'/(\cot\Omega'' - \cot\Omega')$
dz_s'	0	$dz_s'/(\tan\Omega'' - \tan\Omega')$	$dz_s'/(1 - \tan\Omega'.\cot\Omega'')$
$d\dot{x}_s'$	0	0	0
$d\dot{y}_s'$	$-d\dot{y}_s'.H.\tan\Omega'/2$	0	0
$d\dot{z}_s'$	$d\dot{z}_s'.H/2$	0	0
dr_s'	0	$dr_s'.\cos\Omega''/\sin(\Omega' - \Omega'')$	$dr_s'.\sin\Omega''/\sin(\Omega' - \Omega'')$
dx_s''	$dx_s''/2$	0	0
dy_s''	0	$dy_s''/(\tan\Omega'.\cot\Omega'' - 1)$	$-dy_s''/(\cot\Omega'' - \cot\Omega')$
dz_s''	0	$-dz_s''/(\tan\Omega'' - \tan\Omega')$	$dz_s''/(1 - \cot\Omega'.\tan\Omega'')$
$d\dot{x}_s''$	0	0	0
$d\dot{y}_s''$	$-d\dot{y}_s''.H.\tan\Omega''/2$	0	0
$d\dot{z}_s''$	$d\dot{z}_s''.H/2$	0	0
dr_s''	0	$-dr_s''.\cos\Omega'/\sin(\Omega' - \Omega'')$	$-dr_s''.\sin\Omega'/\sin(\Omega' - \Omega'')$

Table 5.4 Error equations of the radar stereo model

An error dy_s' for the sensor position for example leads to model deformations

$$d\underline{x} = \begin{bmatrix} c_x \\ c_y \\ c_z \end{bmatrix} . dy_s' = \begin{bmatrix} 0 \\ 1 - \cot\Omega'.\tan\Omega'' \\ \cot\Omega'' - \cot\Omega' \end{bmatrix} . dy_s' \qquad (5.7)$$

To get this model deformation in a planeto(geo-)centric coordinate system ($d\underline{X}$), the displacement vectors $d\underline{x}$ must be multiplied with the transformation matrix $\underline{A}$ between the two coordinate systems:

$$d\underline{X} = \underline{A}.d\underline{x} \qquad (5.8)$$

Assumed errors	Error equations of Table 5.4			Errors with algorithm (3.1)			Errors with algorithm (3.2)		
	x	y	z	x	y	z	x	y	z
$dx_s' = 100$ m	50	0	0	49	0	0	50	0	0
$dy_s' = 100$ m	0	520	136	0	520	136	0	520	137
$dz_s' = 100$ m	0	-1600	-420	0	-1602	-421	0	-1602	-419
$d\dot{x}_s' = .001$	0	0	0	0	0	0	0	0	0
$d\dot{y}_s' = .001$	-130	0	0	-128	0	0	-130	-73	-21
$d\dot{z}_s' = .001$	400	0	0	393	0	0	400	64	19
$dr_s' = 100$ m	0	1682	442	0	1682	443	0	1682	443
$dx_s'' = 100$ m	50	0	0	51	0	0	50	0	0
$dy_s'' = 100$ m	0	420	-136	0	420	-136	0	420	-136
$dz_s'' = 100$ m	0	1600	520	0	1592	519	0	1598	521
$d\dot{x}_s'' = .001$	0	0	0	0	0	0	0	0	0
$d\dot{y}_s'' = .001$	-105	0	0	-107	0	0	-105	-59	-17
$d\dot{z}_s'' = .001$	400	0	0	407	0	0	400	64	19
$dr_s'' = 100$ m	0	-1654	-538	0	-1655	-538	0	-1655	-536

Base : 50 km ; Flying height : 800 km

Table 5.5 Model errors of an assumed SEASAT stereo arrangement with error equations and rigorous mathematical formulations

Table 5.5 contains model errors for the arrangement of the satellite radar stereo model of Granite Mountain in a local system for near range. At the left side of the Table these errors were computed with the error formulas of Table 5.4. Furthermore these errors were computed using the rigorous mathematical formulations for radar-stereo intersections defined by equations (3.1) and (3.2) in chapter 3. The results are summarized in the middle and at the right hand side of Table 5.5. We see that there is nearly no difference between the two rigorous formulations. Only the effect of errors $d\dot{y}_s'$, $d\dot{z}_s'$, $d\dot{y}_s''$, $d\dot{z}_s''$ in the sensor velocity vectors is somewhat different. Also there is hardly a difference between approximate computation with the equations of Table 5.4 and a rigorous mathematical solution.

It can be seen that the accuracy is strongly affected by errors in the height of the senor position (dz_s) and in the slant ranges (dr_s). Also errors in the velocity vector of the sensor in z-direction cause large position errors in flight direction. As mentioned above, these errors can be computed for a global (planetocentric) coordinate system with equation 5.8.

5.5 THE VIEWABILITY OF RADAR STEREO MODELS

As mentioned in section 5.1 we have compiled a set of stereo models which are presented in the Appendix. Critical parameters for the quality of a radar stereo model are the stereo arrangement, the look angles off-nadir, the intersection angles and the ruggedness of the terrain. These parameters are summarized for all stereo models (also for the models of Granite Mountain and Los Angeles, which were discussed in previous sections) in tabular form in Table 5.6, which will serve as the basis of the following discussion.

One can see from Table 5.6, that there is no difficulty in stereo viewing for same-side stereo arrangements of the SEASAT models. Independent of the base lengths, which amount from 20 up to 75 kilometers, always a stereo impression is obtained. The intersection angles for these models vary approximately between 1° and 5°. From a geometric point of view intersection angles should be large. This was also shown when evaluating the SEASAT models of Granite Mountain and Los Angeles. The results for the Granite Mountain stereo model were superior in this case, due to the better stereo configuration and larger

Figure	Type of Stereo	Area	Type of Radar	H	B	Ω' (degrees)	ΔΩ (degrees)	Δh	Stereo Viewability
5.5	SEASAT	Los Angeles	(*)	800 km	30 km	20	2.1 - 2.2	2000m	yes
A1	-"-	-"-	(*)	-"-	50 km	20	3.1 - 3.2	-"-	-"-
A2	-"-	-"-	(*)	-"-	20 km	20	1.2 - 1.3	-"-	-"-
A3	-"-	-"-	(*)	-"-	35 km	20	2.1 - 2.3	-"-	-"-
A4	-"-	-"-	(*)	-"-	20 km	20	1.2 - 1.3	-"-	-"-
A5	-"-	-"-	(**)	-"-	550 km	20	40	-"-	no
A6	-"-	Utah	(*)	-"-	55 km	20	3.4 - 3.5	1500m	yes
A7	-"-	-"-	(*)	-"-	-"-	20	-"-	500m	-"-
A8	-"-	-"-	(*)	-"-	75 km	20	4.7 - 4.8	-"-	-"-
A9	-"-	Granite Mtn.	(*)	-"-	55 km	20	3.4 - 3.5	1300m	-"-
5.4	-"-	-"-	(*)	-"-	50 km	20	3.1 - 3.2	-"-	-"-
5.3	GOODYEAR	-"-	(*)	12 km	13 km	63 - 75	5.9 -23.1	-"-	-"-
A10	-"-	Fremont	(*)	-"-	0.7 km	42 - 75	0.2 - 1.9	600m	-"-
A11	-"-	Estrella Mtn.	(*)	-"-	10 km	59 - 75	10.1 -19.2	1000m	-"-
A12	-"-	-"-	(**)	-"-	30 km	40 - 59	100	-"-	only when flat
A13	MOTOROLA	Sierrita	(*)	4 km	10 km	78 - 83	3.5 -12.1	hilly	yes
A14	-"-	-"-	(**)	-"-	48 km	74 - 83	160	-"-	only when flat
A15	APOLLO 17	Hevelius	(*)	112 km	10.1 km	5.2 - 22	4.5 - 5.2	1600m	no
A16	-"-	Reiner	(*)	-"-	9.6 km	4.9 - 22	4.4 - 4.9	900m	-"-
A17	-"-	Carpatus	(*)	-"-	6.9 km	3.5 - 22	3.0 - 3.5	1700m	locally
A18	-"-	Appenninus	(*)	-"-	3.5 km	1.8 - 22	1.5 - 1.8	2000m	yes
A19	-"-	Mons Haemus	(*)	-"-	1.9 km	0.9 - 22	0.8 - 0.9	1800m	-"-
A20	-"-	Mare Serenitatis	(*)	-"-	1.3 km	0.7 - 22	0.6 - 0.9	500m	-"-
A21	-"-	Mons Maraldi	(*)	-"-	3.2 km	1.6 - 22	1.4 - 1.6	1600m	-"-
A22	-"-	Mare Crisium	(*)	-"-	6.9 km	3.5 - 22	3.0 - 3.5	100m	-"-
A23	-"-	Condorcet	(*)	-"-	7.8 km	4.0 - 22	3.4 - 4.0	4700m	no
A24	-"-	Neper	(*)	-"-	9.5 km	4.8 - 22	4.2 - 4.8	-	-"-
A25	-"-	Erro	(*)	-"-	10.0 km	5.1 - 22	4.4 - 5.1	-	-"-
A26	-"-	Bussior	(*)	-"-	10.3 km	5.3 - 22	4.6 - 5.3	-	-"-
A27	-"-	Aitken	(*)	-"-	4.4 km	2.2 - 22	1.9 - 2.2	6700m	-"-
A28	-"-	De Vries	(*)	-"-	2.8 km	1.4 - 22	1.2 - 1.4	6000m	yes
A29	-"-	Mohorovicic	(*)	-"-	0.7 km	0.4 - 22	0.3 - 0.4	-	-"-
A30	-"-	Unnamed	(*)	-"-	1.0 km	0.5 - 22	0.4 - 0.5	-	-"-
A31	-"-	Belopolsky	(*)	-"-	4.9 km	2.5 - 22	2.1 - 2.5	-	locally
A32	-"-	Lowell	(*)	-"-	8.4 km	4.3 - 22	3.7 - 4.3	-	no
A33	-"-	Schlueter	(*)	-"-	9.8 km	5.0 - 22	4.3 - 5.0	-	no
A34	JPL	Flagstaff	(*)	10 km	0.8 km	59 - 69	0.6 - 1.2	800m	yes
A35	-"-	-"-	(*)	-"-	7.8 km	58 - 67	9.4 -19.3	-"-	yes
A36	-"-	-"-	(*)	-"-	1.8 km	10 - 58	3.2 -10.2	-"-	yes
A37	-"-	-"-	(**)	-"-	41 km	58 - 68	128	-"-	no
A38	-"-	-"-	(**)	-"-	32 km	31 - 58	110	-"-	no
A39	-"-	-"-	(**)	-"-	20 km	22 - 58	65	-"-	no
A40	-"-	Grand Canyon	(*)	-"-	0.9 km	5.1 - 58	1.5 - 5.1	2000m	yes
A41	-"-	-"-	(*)	-"-	2.2 km	12.4 - 58	3.9 -12.4	-"-	yes
A42	-"-	-"-	(**)	-"-	22 km	11.3 - 58	69 - 95	-"-	no
A43	-"-	-"-	(*)	-"-	1.8 km	10.2 - 58	3.2 -10.2	-"-	yes
A44	-"-	-"-	(**)	-"-	24 km	39 - 58	100	-"-	no

(*) ... Same-side stereo; (**) ... Opposite side stereo; H ... Flying height
B ... Stereo base; Ω' ... Elevation angle; ΔΩ ... Intersection angle;
Δh ... Terrain elevations

Table 5.6 Summary of viewability test for radar stereo with actual imagery

intersection angles.

However, for the cross-wise stereo arrangement of Los Angeles no stereo impression can be obtained. The objects are illuminated in this case from different directions and especially but not only rugged regions therefore look quite different in the two radar images. Since this stereo model is formed with small elevation angles, there are considerable geometric image distortions in rugged areas and mountains lay over towards the satellite. For cross-wise or opposite-side stereo arrangements therefore the geometric differences in the images are too large to permit a stereo percertion.

As with same-side SEASAT stereo models also the stereo models with aircraft radar of GOODYEAR and MOTOROLA (see Table 5.6) with same-side imaging arrangement permit stereo viewing. Due to the relationship between flying height and stereo base these stereo models generally have a better stereo configuration than the SEASAT stereo models with intersection angles of more than 20°.

But again for the opposite-side arrangements it can be seen that hardly a three-dimensional impression will be obtained for rugged regions of the stereo model. Regions which are strongly reflecting in one image, are in the radar shadow in the other image, because slopes are illuminated from opposite sides. As can be seen from the stereo models of Estrella Mountain or Sierrita (Figures A12 and A14 in the Appendix) terrain elevations look very different in this case and stereo viewing only might be possible in flat areas.

For the radar stereo models of the Moon (Apollo-17 mission) the look angles off-nadir are steeper than for the SEASAT models and therefore stereo viewing also becomes more difficult, although the intersection angles are similar to those of the SEASAT models. But steep look angles cause large relief displacements so that homologue features may look quite different in the two images. As can be seen from Table 5.6 there seems to be distinctly a limit in the intersection angle for the possibilty of stereo viewing for the Appolo-17 stereo models.

This limit is at about 2^{o} for rugged terrain, while it may be naturally larger for flat terrain.

Also for the same-side stereo models of JPL-aircraft radar the stereo viewability is rather convenient, especially if elevation angles Ω' are large. But for steep look angles (near range regions) it might be impossible to get a stereo impression because of the relief displacements in the images. Distinctly this is shown in Figure A35 in the Appendix.

Stereo viewing is also impossible for the opposite-side stereo models. As can be seen from the models of Grand Canyon (Figures A42 and A43), the image contents are not similar enough for rugged regions and therefore permit no three-dimensional impression. But also rather flat areas in near range regions (see Figure A39) may look quite different in the images, due to the relief displacements caused by steep look angles.

Now we discuss separately each of the parameters affecting

the quality of a radar stereo model.

(a) the stereo arrangement: Generally we can say that only same-side stereo arrangements are suitable to permit a stereo impression. With other arrangements, such as with cross-wise or with opposite-side stereo, only in flat areas a stereo impression can be obtained. But if there are terrain elevations, these would "produce" different radar shadows and the images would not be sufficiently similar for stereo viewing. Especially if the images are in slant range presentations, there occur large relief displacements and the images miss any geometric similarity in rugged regions and probably also for flat areas (if look angles are steep) for cross-wise or opposite-side arrangements.

(b) the look angles off-nadir: If the terrain is rather flat and the stereo base is small there is almost no indication for the optimum look angle off-nadir. In this case both for the steep look angles of the Apollo-17 mission as for the shallower look angles of the GOODYEAR imaging system a good stereo impression is obtained. But the ruggedness of the terrain is a factor that affects the viewability of a radar stereo model depending on the look angles considerably. This especially was shown with the images of the Moon. For these stereo models no three-dimensional impression was obtained for rugged terrain, if the intersection angles were larger than about 2°. This also refers to the fact, that relief displacements are large for steep look angles. LA PRAIE (1975) reported optimum stereo viewing if look angles are between 37° and 67° off nadir. This is valid for aircraft radar with small

flying heights. But from Table 5.6 it can be seen that for the SEASAT satellite radar configuration also a good stereo impression can be obtained, where the look angles amount to about 20^{o} off nadir.

(c) the intersection angles: From a geometric point of view intersection angles should be large while they should be small to permit stereo viewing. As can be seen from Table 5.6 stereo viewing is possible with intersection angles of various orders of magnitude which depends on the stereo configuration (flying height, stereo base) and amounts up to more than 20^{o} . Evaluations with some stereo radar models performed in this chapter have shown, that the results for stereo models with larger intersection angles are superior.

(d) the ruggedness of the terrain: The stereo models of the Apollo-17 mission show, that the ruggedness of the terrain has a considerable effect on stereo viewing, especially in connection with steep look angles. In this case the relief displacements are rather large, so that stereo viewing may be difficult even for a stereo pair with small stereo base. For example for the stereo models of the Moon only for intersection angles of about 2^{o} a three-dimensional impression could be obtained. For larger intersection angles this only was possible for a few models where the terrain elevations were rather small.

It can be seen from this conclusion that there is a very difficult interaction between stero arrangement, look angles, intersection angles and ruggedness of the terrain. To recieve an image pair suitable for stereo viewing obviously a same-side

stereo arrangement should be used. Furthermore the condition of the terrain can be viewed as a given parameter. For rugged terrain the look angles off-nadir should not be too steep to avoid large differences of image appearence or thematic content.

The maximum intersection angles were about 20°. Since no larger intersection angles occurred in all the stereo models summarized in Table 5.6 there is no indication if stereo viewing is possible with larger intersection angles.

5.6 AN EVALUATION OF STEREO RADAR WITH THE EXAGGERATION FACTOR

Table 5.7 presents computed values of Δp for various stereo cases and the corresponding exaggeration factor q as obtained with equation (3.42) for $\Delta p/\Delta h$.

Type of Radar	Stereo Base km	Look Angle Ω' (°)	Intersection Angle $\Delta\Omega'$ (°)	Flying Height H (km)	Parallax Diff. due to h= 1km Ground ranges	Exaggeration Factors If Ground Ranges		if Slant Ranges	
						Rigourous q	Approximate q'	q	q'
SEASAT	25	20°	1°.6	800	0.263	1.3	1.3	0.05	0.05
	75	22°	4°.8	800	0.761	3.8	3.8	0.14	0.14
Aircraft SAR Goodyear	0.7	68°	0°.5	12	0.011	0.06	0.05	0.04	0.04
	13.5	65°	23°	12	0.720	3.6	3.2	1.60	1.60
Aircraft RAR Motorola	10	81°	10°	4	0.215	1.1	0.9	0.95	0.85
	48	80°	160°	4	0.414	2.1	1.8	2.01	1.74
Apollo 17 ALSE Moon	0.7	10°	0°.3	116	0.383	1.9	0.9	0.00	0.00
	3.9	10°	1°.9	116	3.422	17.1	6.8	0.03	0.03
	10.0	13°	4°.7	116	2.584	12.9	6.4	0.07	0.07
	10.0	13°	4°.8	116	5.220	26.1	10.6	0.08	0.08

Table 5.7 Exaggeration factors for radar stereo models, all related to ground range presentations

The values of q' due to equations (3.39) or (3.40) can be different from q. To quantify these differences due to effects of neglections, Table 5.7 also contains the values of q'.

We see that the exaggeration factors and thus the stereo parallaxes that are obtained with radar in a ground range presentation, can compare well with photographic stereo: as look angles become steeper, one has a more accertuated stereo-effect in spite of small stereointersection angles. The effect assumes extreme values for a case such as Apollo 17-ALSE, where very small intersection angles create parallaxes that are multiples of the object height. In camera photogrammetry, the largest parallaxes are of the order of an observed height difference, and q-values amount to 3 - 5.

It must be emphasised that the exaggeration factor is not a promise of high accuracy: for radar it can well be that errors propagate strongly into parallaxes and are magnified with the parallaxes themselves.

An interesting fact is the difference of observed parallaxes in slant and ground range presentation: in the latter the parallax differences are magnified particularly with steep look angles.

5.7 SUMMARY

In this chapter some evaluations were performed to compute height differences for some same-side stereo radar images using the simplified method based on parallax measurements.

The parallax differences were measured in two ways : with a stereoscope and a parallax bar, and with a convertional

photogrammetric plotter used as a comparator. Since for this simplified method there are considerable systematic errors in computed height differences, they need to be corrected with control points and correction polynomials.

The obtained results confirmed the dependency of the accuracy on the stereo configuration. For example the accuracy for a SEASAT stereo model with a base of 50 kilometers was about ± 150 meters after correction with an 8 parameter polynomial, while it amounted to about ± 300 meters for a stereo model with a base of 30 kilometers.

A large set of almost 50 stereo models was compiled with regard to their stereo viewability. It was shown, that there is no difficulty in stereo viewing for same-side radar stereo geometry if the look angles off-nadir are large. This was confirmed for aircraft radar with look angles of up to 80° as for satellite radar (SEASAT) with look angles of about 20°. Only for very steep look angles, such as for the Apollo 17 ALSE-radar images or for near range regions of the JPL aircraft radar, same-side stereo of rugged areas became impossible. For the Apollo 17 radar images this was at a limit in the intersection angles of about 2°.

Vertical exaggeration factors were between 0.06 and 3.6 for aircraft, between 1.3 and 3.8 for SEASAT and between 1.9 and 26 for Apollo 17 data. This compares with a value of q 3 to 5 for standard aircraft wide-angle photography. We see for the very small intersection angles of satellite radar that the vertical exaggeration factors are rather large. This, however,

is valid due to the small look angles off-nadir where small intersection angles still create large parallaxes in ground range presentations. The large exaggeration factors are not existent in slant range presentations.

C H A P T E R 6

CONCLUSIONS AND OUTLOOK

This report presents methods of single image and stereo radar mapping and some practical applications on radar images. The single radar image evaluations were performed with SEASAT-SAR images, which were the only available satellite radar data at the time of this study. They were based on a rigorous radargrammetric mapping method using the orbit information for the imaging sensor.

The capability of this method was shown by an evaluation of an optically and digitally correlated SEASAT image of Los Angeles. For this area the accuracy in ground coordinates was at the order of magnitude of the ground resolution of ± 25 meters. The ground control density was at about 7 points per 1000 square kilometers.

An application for satellite radar images is also the study of rapidly changing phenomena on Earth. This was done for the measurement of the motion and deformation of sea ice using images of the arctic Beaufort-sea to the north-west of Canada. For an observational period of 30 days the evaluation of the sea-ice motion resulted in 6.4 kilometers per day.

An error analysis for this arctic scene has shown, that the accuracy of the radargrammetric mapping method in this case was limited to about ± 500 meters, because ground control was available only at one end of the imaged area. If ground control

points were distributed over the whole imaged area, the errors would reduce to about ± 150 meters. These comparatively large errors may be caused by the low ground control density with one point per 10 000 square kilometers and by the fact, that point identificatior is more difficult than for the scene of Los Angeles.

The main goals of the evaluations with stereo radar images were the determination of the effect of the stereo configuration on stereo viewing, accuracy and vertical exaggeration.

About 50 radar stereo models were evaluated with respect to their viewability. It was shown, that a stereo impression is ensured for same-side stereo arrangements and shallow look angles off-nadir. For steeper look angles it might become impossible to get a three-dimensional impression especially for mountainous areas. In this case relief displacements are rather large and the images miss any geometric similarity. Therefore steep look angles together with considerable terrain elevations may prevent any stereo impression. This was shown with the Apollo 17 radar images, where no stereo impression could be obtained for intersection angles larger than 2°. The maximum intersection angles of all the compiled stereo models were at about 20°. Therefore there is no indication for the possibility of stereo viewing with larger intersection angles.

Analytical evaluations confirmed the geometrical point of view, that intersection angles and stereo bases should be large. For stereo models with a better stereo configuration, which is defined by the relationship between stereo base and flying

height, the results were more accurate than for those with a poorer one.

The difficult interaction between the critical parameters for stereo viewing (stereo arrangement, look angles off-nadir, intersection angles, ruggedness of the terrain) cannot be sufficiently determined with only the used five different types of radar imaging systems (SEASAT, GOODYEAR, MOTOROLA, APOLLO 17, JPL). Further investigations therefore will require a larger set of images with a larger variety of cases. Image simulation techniques might be useful to produce various simulated radar images with subjective selected parameters for stereo viewing.

The ongoing work needs to be directed towards three areas :

- the use of photogrammetric stereoplotting devices for radar stereo mapping;
- the development of image simulation techniques to study various radargrammetric problems with operator-selected image parameters; a typical problem is the question of stereo viewability;
- the processing of digital radar images in a digital image processing environment.

It is thus neccesary to use precision photogrammetric techniques for analog radar recordings. This requires a novel, previously hardly feasible application of recent computer-controlled stereoplotting devices. A KERN - DSR - 1 analytical plotter was recently installed at the Graz Research Center. Its use for stereoradar will require a sizeable

software development effort that must be performed, should the widely publicized promise of this new photogrammetric equipment technology be materialized.

The image simulation capability is of urgent importance for radargrammetry, in particular with questions relating to stereo. Appropriate real test radar data cannot be expected to ever be available to study the impact of sensor-geometries on single image and stereo radargrammetry. Digital terrain models and orbit geometries together must be used to generate simulated images, so that various effects on image evaluation, viewability, identifiability etc. can succesfully be studied.

Future radar sensors will be all digital devices. Their output will be digital. This leads to the requirement to establish capabilities to digitally process the digital radar images. Based on existing image processing work, new efforts need to be spent to study the rectification of single images, image - image correspondence for mosaicking, image registration and stereo parallax detection. A modest image signal history correlation capability should be installed so that trade-offs between multiple looks and geometric resolution, and image generation with various parameters can be evaluated in their effect on radargrammetric results.

From these described current problems it is apparent that satellite radar, and in particular a VENUS radar mapping mission, will still require considerable work to fully develop the capabilities and understanding for successful, operational radargrammetry.

BIBLIOGRAPHY ON RADARGRAMMETRY

AKOWETZKY W.I. (1968): "On the Transformation of Radar Coordinates into the Geodetic System". Geodezia i Aerofotosjomka (in Russian).

AMBROSE W. (1967): "A Radar Image Correlation Viewer". Photogramm. Eng., Vol. XXXIII.

AZEVEDO L. DE (1971): "Radar in the Amazon". Proc. 7th Int.Symp. Remote Sensing of the Environment, Ann Arbor, Michigan.

BAIR G.L. and G.E. CARLSON (1975): "Height Measurement with Stereo Radar". Photogramm. Eng. and Remote Sensing, Vol. XLI.

BAIR G.L. and G.E. CARLSON (1974): "Performance Comparison of Techniques for Obtaining Stereo Radar Images". IEEE Trans. on Geoscience Electronics, GE-11.

BERLIN L.G. and G.E.CARLSON (1974): "Radar Mosaics". The Professional Geographer, Vol. XXIII, No. 1.

BICKNELL T. et al. (1975): "A Study to Determine the Feasibility of Using Radar Techniques for Public Land Surveying". Jet Propulsion Laboratory Report under Contract to the Bureau of Land Management, Contract No. 5300-PH-995, Pasadena, California.

BOSMAN E. et al. (1971): "Project Karaka - The Transformation of Points from Side Looking Radar Images into the Map System". Final Report, Part 1, Netherlands Interdepartmental Working Community for the Application and Research of Remote Sensing Techniques (NIWARS), Delft.

BOSMAN E.R., E. CLERICI, D. ECKHART, K. KUBIK (undated): "Project BEBLOKA - The Transformation of Points from Overlapping Images Obtained with Different Sensors into the Map System". Final Report, Netherlands Interdepartmental Working-Community for the Application and Research of Remote Sensing Techniques (NIRWARS), Delft.

BOSMAN E. R., E. CLERICI, D. ECKHART, K. KUBIK (1972): "Information of Points from Side-Looking-Radar Images into the Map System". Bildmessung und Luftbildwesen, Vol. 42, No. 2.

BOSMAN E. R., E. CLERICI, D. ECKHART, K. KUBIK (1972): "KARIN-A Program system for the Mapping of Remote Sensing Information". Pres. Paper, 12th Congress, Int. Soc. Photogrammetry, Ottawa, Canada; and Final Report, Netherlands, Interdepartmental Working Community for the Application and Research of Remote Sensing Techniques (NIRWARS), Delft.

BROWN W. et al. (1981): "Application of Seasat SAR Digitally Correlated Imagery for Sea Ice Dynamics". Invited Paper, 1981 AGU-Meeting, Baltimore, USA.

BRYAN M. L, W. STROMBERG, T. FARR (1977): "Computer Processing of SAR L-band Imagery". Photo. Eng. and Remote Sensing, Vol. 43, No. 10, pp 1283 - 1294.

CARLSON G.E. (1973): "An Improved Single Flight Technique for Radar Stereo". IEEE Trans. on Geoscience Electronics, GE-11, No. 4.

CLAVELOUX B.A. (1960): "Sketching Projector for Side Looking Radar Photography". Photogramm. Eng., Vol. XXVI.

CRANDALL C.J. (1963): "Advanced Radar Map Compilation Equipment". Photogramm. Eng., Vol. XXIX.

CRANDALL C.J. (1969): ""Radar Mapping in Panama". Photogramm. Eng. Vol. XXXV.

CURLANDER J. (1981): "Geometric and Radiometric Distortion in Spaceborne SAR Imagery". Invited Paper, NASA Workshop on Registration - Rectification for Terrestrial Applications. November 17 -19. Jet Propulsion Laboratory, Pasadena, USA.

CURLANDER J. (1981): "Sensor to Target Range Determination". IPL-Interoffice Memorandum 334.7-80-056. Jet Propulsion Laboratory, Pasadena, USA.

DAILY, M. et al. (1978): "Application of Multispectral Radar and Landsat Imagery of Gelogic Mapping in Death Vally". JPL-Publication, 78-19, Pasadena, USA 47 pp.

DALKE G. et al. (1968): "Regional Slopes with Non Stereo Radar". Photogramm. Eng., Vol. XXIV.

DBA SYSTEMS (1974): "Research Studies and Investigastions for Radar Control Extensions". DBA Systems, Inc., P.O. Drawer 550, Melbourne, Florida, Defense Documentation Center Report No. 530784L.

DELLWIG L.F. (1980): "A New Look at Togo through the Eyes of a SLAR". In Radar Geology, An Assessment, JPL-Publication 80 - 61, Jet Propulsion Laboratory, Pasadena, USA.

DERENYI E.E. (1970): "An Exploratory Investigation into the Relative Orientation of Continuous Strip Imagery". Ph.D. Thesis and Research Report No. 8, Univ. of New Brunswick, Canada.

DERENYI E.E. (1972): "Geometric Consideration in Remote Sensing". Proc. First Canadian Symp. on Remote Sensing, Ottawa.

DERENYI E.E. (1974): "SLAR Geometric Test". Photogramm. Eng., Vol. XL.

DERENYI E.E. (1974): "Metric Evaluation of Radar and Infrared Imageries". Second Canadian Symp. on Remote Sensing, Univ. of Guelph, Guelph, Ontario.

DERENYI E.E. (1975): "Topographic Accuracy of Side Looking Radar Imagery". Bildmessung und Luftwesen, 1975, No. 1.

DERENYI E.E. (1975): "Terrain Heights from SLAR Imagery". Pres. at the 41st Annual Conv. Am. Soc. Photogramm., Washington, D.C., March.

DICARLO C. et al.(1968): "All Weather Mapping". Pesented Paper, International Congress of Surveyors (FIG), London, England.

DICARLO C. et al. (1971): "DoD Data Processing Equipment for Radar Imagery". Pres. Paper, Int. Congress of Surveyors, Wiesbaden.

DOWIDEIT G. (1975): "A Simulation System for Theoretical Analysis of Radar Restitution and a Test by Adjustment". Proc. Symp. Comm. III, Int. Soc. Photogramm., Stuttgart, W. Germany, in Deutsche Geodaetische Kommission, Reihe B., Heft No. 214.

DOWIDEIT, G. (1977): "Eine Blockausgleichung fuer Abbildungen des seitwaertschauenden Radar (SLAR)". Wissensch. Arbeiten der Lehrstuehle fuer Geodaesie etc., Nr. 75, Technische Universitaet Hannover, FRG, 185 pp.

DOWIDEIT, G. (1977): "Eine Blockausgleichung fuer Aufzeichnungen des Seitwaerts-Radar (SLAR)". Bildmessung und Luftbildwesen Vol. 45, No. 1, pp 17 - 23.

EGBERT E. (1969): "Calculation of Ground Street Lenghts and Area from Radar Measurements". Simonnett, D.S., (ed.), "The Utility of Radar and Other Remote Sensors in Thematic Land Use Mapping from Spacecraft". Annual Report, U.S. Geolog. Survey Interagency Report-NASA 140.

ESA (1981): "ERS-1 Announcement of Opportunity for Participation in the Proposed ERS-1 Mission". APP (81) 1, Part B.

ESTEN R.D. (1953): "Radar Relief Displacement and Radar Parallax". USAERDL-Report No. 1294, Ft. Belvoir, Virginia.

FIORE C. (1967): "Side Looking Radar Restitution". Photogramm. Eng., Vol. XXXIII.

FROIDEVAUX C.M. (1980): "Radar, an Optimum Remote Sensing Tool for detailed Plate Teetonic Analysis and its Application to Hydrocarbon Exploration". (An Example in Irian Jaya, Indonesia). In Radar Geology, An Assessment, JPL-Publication 80 - 61, Jet Propulsion Laboratory, Pasadena, USA.

GEIER F. (1971): "Beitrag zur Geometrie des Radarbildes". Diss., Techn. Univ., Graz.

GEIER F. (1972): "Fundamentals of Orientation for Radar PPI Images with approximated Horizontal Distances". Pres. Paper, 12th Congress, Int. Soc. Photogramm., Ottawa, Canada.

GLUSHKOV W.M. et al. (1972): "Toros-Side Looking Radar Sytems and its Application for Sea Ice Condition Study and for Geologic Explorations". Pres. Paper, 12th Congress, Int. Soc. Photogramm., Ottawa, Canada.

GOODYEAR (1972): "Flight Test Report All-Weather Topographic Mapping System AN/ASQ-142". Contract No. F 33657-70-0769, Goodyear Aerospace Corp., Litchfield Park, Arizona.

GOODYEAR (1974): "Preliminary Imagery Data Analysis Goodyear Electronic Mapping System (GEMS)". Goodyear Aerospace Corp., Report GIB-9342, Code 99696.

GRACIE G. et al. (1970): "Stereo Radar Analysis". U.S. Engineer Topographic Laboratory, Ft. Belvoir, Virginia. Report No. FTR-1339-1.

GRACIE G.and E.D. SEWELL (1972): "The Metric Quality of Stereo Radar". Proc. of the Techn. Program, Electro-Optical Systems Design Conference, New York, 12-14 Sept.

GRAHAM L.C. (1970): "Cartographic Applications of Synthetic Aperture Radar". Proc. Am. Soc. Photogramm., 37th annual Meeting; and Goodyear Aerospace Corp., Report GERA-1626.

GRAHAM L. (1972): "An Improved Orthographic Radar Restitutor". Presented Paper, 12th Congress, Int. Soc. Photogramm., Ottawa Canada, and Goodyear Aerospace Corp., Report GERA-1831.

GRAHAM L. and H.O. RYDSTROM (1974): "Synthetic Aperture Radar Applications to Earth Resources Development". Goodyear Aerospace Corp., Report GERA-2010, Code 99696.

GRAHAM L.C. (1975): "Geometric Problems in Side-Looking Radar Imaging". Proc. Symp. Comm. III. Int. Soc. Photogramm.; Stuttgart, W. Germany, in Deutsche Geodaetische Kommission, Reihe B, Heft No. 214.

GRAHAM L. (1975): "Flight Planning for Stereo Radar Mapping". Proc. Am. Soc. Photogramm., 41 st Meeting, Washington, D.C.

GRAHAM L. (1976): "Earth Resources Radar Stereo Considerations". Goodyear Aerospace Corp., Arizona Div., AEEM-550, 13p.

GREVE C. and W. COONEY (1974): "The Digital Rectification of Side Looking Radar". Proc. Am. Soc. Photogramm., Annual Convention, Wash., D.C.

HIRSCH TH. and J. VAN KUILENBURG (1976): "Preliminary Tests of the EMI-SLAR Mapping Quality". Netherlands Interdepartmental Working Community for the Appli. and Res. of Remote Sensing (NIWARS), Internal Report No. 39, Delft.

HOCKEBORN H.A. (1971): "Extraction of Positional Information from Side Looking Radar". Bildmessung und Luftbildwesen, Vol. 39, No. 1.

HOFFMANN P. (1958): "Photogrammetric Applications of Radar Scope Photographs". Photogramm. Eng., Vol. XXIV.

HOHENBERG F. (1950): "Zur Geometrie des Funkmessbildes". Austrian academy of Sciences, Math.-Naturwissenschaftliche Klasse, Vienna, Vol. 2-3.

HOLTZMAN,I.C. et al. (1977): "Radar Image Simulation: Validitation of the Point Scattering Method". Report ETL-0017 (Vol.1), USA Engineer Topographie Laboratory, Fort Belvoir, USA.

IEEE-CONFERENCE (1981): "IGARSS 81". International Geoscience and Remote Sensing Symposium. IEEE Catalog No. 81 CH 1656-8.

INNES, R.B. (1964): "Principles of SLAR Measurement of the Third Coordinate of Target Position". Report of Project Michigan No. 2900-474-T.

ITO N. (1981): "SAR Digital Processing System". Presented Paper ISPRS-SAR Working Group II 15 , 3. - 4. Dec. Frascati, Hobs.

JENSEN H. (1972): "Mapping with Coherent-Radiation Focused Synthetic Aperture Side-Looking Radar". In "Operational Remote Sensing: An Interactive Seminar to Evaluate Current Capabilities". Am. Soc., Photogramm.

JENSEN H. (1975): "Deformations of SLAR Imagery-Results from actual Surveys". Proc. Symp. Comm. III, Int. Soc. Photogramm., Stuttgart, W.Germany, in Deutsche Geodaetische Kommission, Reihe B, Heft No. 214.

KOBER C.L. et al. (1950): "Determination of Target Height from Radar PPI-Photographs". Air Force Techn. Report No. 6500, Wright Air Development Center, Ohio.

KONECNY G. and E.E. DERENYI (1966): "Geometric Consideration for Mapping from Scan Imagery". Proc. 4th Symp. Remote Sensing of the Environment, Ann Arbor, Michigan.

KONECNY G. (1970): "Metric Problems in Remote Sensing". Publications of the International Institute for Aerial Surveying and Earth Sciences (ITC), Series A, No. 50, Delft.

KONECNY G. (1971): "Orientierungsfragen bei Streifenbildern und Aufnahmen der Infrarotabtastung". Bildmessung und Luftbildwesen, Vol. 41, No. 1.

KONECNY G. (1972): "Geometrical Aspects of Remote Sensing". Arch. Int. Soc. Photogramm., Invited Paper, 12th Congress, Ottawa, Canada.

KONECNY G. (1972): "Geometrische Probleme der Fernerkundung". Bildmessung und Luftbildwesen, Vol. 42. No. 2.

KONECNY G. (1975): "Approach and Status of Geometric Restitution for Remote Sensing Imagery". Pro. Symp. Comm. III, Int. Soc. Photogramm., Stuttgart, W.Germany, in Deutsche Geodaetische Kommission, Reihe B, Heft No. 214.

KOOPMANS B. (1974): "Should Stereo SLAR Imagery be Preferred to Single Strip Imagery for Thematic Mapping?". ITC-Journal 1974-3, Enschede.

KOOPMANS B. (1974): "Drainage Analysis on Radar Images". ITC-Journal, 1973-3, Enschede, Netherlands.

KORNEEV IU. N. (197-): "Analytical Method for Photogrammetric Processing of a Single Radar Photograph". Geodezia i Aerofotosjomka, No. 2.

KRATKY, V. (1979): "SEASAT Orbit Effects on Imaging Geometry of Synthetic Aperture Radar". 3rd GDTA Symposium, Toulouse.

LA PRADE G.L. (1963): "An Analytical and Experimental Study of Stereo for Radar". Photogramm. Eng., Vol. XXIX.

LA PRADE G.L. (1969): "Elevations from Radar Imagery". Photogramm. Eng., Vol. XXXV.

LA PRADE G.L. (1970): "Subjective Considerations for Stereo Radar". Goodyear Aerospace Corp., Report GIB-9169, and Photogramm. Eng.

LA PRADE G. (1972): "Stereoscopy - A More General Theory". Photogrammetric Engineering, Vol. 38, pp. 1177 - 1187.

LA PRADE G. (1973): "Stereoscopy - Will Facts or Dogma Prevail?". Photogrammetric Engineering, Vol. 39, pp. 1271 - 1275.

LA PRADE G. (1973): "A More General Theory of Stereoscopy". Goodyear Aeorspace Corp., Arizona Div., GiB-9268, Rev. A, 58 p.

LA PRADE G. (1975): Addendum to GiB-9169, "Subjective Considerations for Stereo Radar". Goodyear Aerospace Corp., Arizona Division.

LA PRADE G. (1975): "Stereoscopy". Goodyear Aerospace Corp., Arizona Div., GERA-2120, Code 99696; 57 p.

LA PRADE G.L. (1975): "Radar Signature of Inverted Catenary with Equilateral Triangular Cross Section (St. Louis Gateway Arch)". Arizona Electronics Eng. Memo. No. 525, Goodyear Aerospace Coop., Arizona Div., Litchfield Park, Arizona.

LA PRADE G. et al. (1980): "Stereoscopy". Chapter X, Manual of Photogrammetry, 4th Edition.

LEBERL F. (1970): "Metric Properties of Imagery Produced by Side Looking Airborne Radar and Infrared Line Scan Systems". Publications of the International Institute for Aerial Survey and Earth Sciences (ITC), series A, No. 50, Delft.

LEBERL F. (1971): "Vorschlaege zur instrumentellen Entzerrung von Abbildungen mit Seitwaerts Radar (SLAR) und Infrarotabtastsystemen". Bildmessung und Luftbildwesen, Vol. 39.

LEBERL F. (1971): "Remote Sensing - Neue Methoden zur Wahrnehmung auf Abstand". Oesterreichische Zeitschrift fuer Vermessungswesen, No. 6.

LEBERL F. (1971): "Untersuchungen ueber die Geometrie und Einzelbildauswertung von Radarschraegaufnahmen". Diss., Techn. Univ., Wien.

LEBERL F. (1972): "On Model Formation with Remote Sensing Imagery". Oesterr. Zeitschrift fuer Vermessungswesen, Vol. 60, pp. 93 - 61.

LEBERL F. (1972): "Evaluation of Single Strips of Side Looking Radar Imagery". Arch. Int. Soc. Photogrammetry, Invited Paper, 12th Congress, Ottawa, Canada.

LEBERL F. (1972): "On Model Formation with Remote Sensing Imagery". Oesterreichische Zeitschrift fuer Vermessungswesen und Photogrammetrie, No. 2.

LEBERL F. (1972): "Radargrammetria para los Interpretes de Imagenes". Centro Interamericano de Fotointerpretacion, (CIAF), Bogota, Colombia.

LEBERL F. (1974): "Evaluation of SLAR Image Quality and Geometry for PRODRADAM". ITC-Journal, Vol. 2, No. 4, Enschede.

LEBERL F. (1975): "The Geometry of, and Plotting from, Single Strips of Side Looking Airborne Radar Imagery". Int. Institute for Aerial Survey and Earth Sciences (ITC) Techn. Report No. 1, Enschede.

LEBERL F. (1975): "Radargrammetry for Image Interpreters". ITC Technical Report No. 2, Enschede.

LEBERL F. (1975): "Radargrammetric Point Determination PRORADAM". Bildmessung und Luftbildwesen, Vol. 45, No. 1.

LEBERL F. (1975): "Sequential and Simultaneous SLAR Block Adjustment". Photogrammetria, Vol. 31. No. 1.

LEBERL F. (1975): "Lunar Radargrammetry with ALSE-VHF Imagery". Proc. Am. Soc. Photogramm., Fall Tech. Meeting, Phoenix, Arizona.

LEBERL F., T. FARR, L. BRYAN, C. ELACHI (1976): "Study of Arctic Sea Ice Drift form L-Band Side Looking Radar Imagery". Proc. Am. Soc. Photogramm., 42nd Annual Conv., Washington, D.C.

LEBERL F. (1976): "Mapping of Lunar Surface from Side Looking Orbital Radar Images". The Moon, Vol. 15, No. 3/4.

LEBERL F. (1976): "Imaging Radar Applications to Mapping and Charting". Photogrammetria, Vol. 32.

LEBERL F., J. JENSEN and J. KAPLAN (1976): "Side-Looking Radar Mosaicking Experiment". Photogramm. Eng. and Remote Sensing, Vol. XLII.

LEBERL F. (1977): "Radar Mapping Applications using Single Images, Stereo Pairs, and Image Blocks: Methods and Applications". Revista Brasileira de Cartographia, No. 20, pp. 16 - 26.

LEBERL F., C. ELACHI (1977): "Mapping with Satellite Side-Looking Radar". Proceedings, 2nd GDTA Symposium, St. Mande, France, pp. 451 - 465.

LEBERL F. (1978): "Satellitenradargrammetrie". Deutsche Geodaetische Kommission, Series C, No. 239, Munich, 156 p.

LEBERL F., H. FUCHS (1978): "Photogrammetic Differential Rectification of Radar Images". Pres. Paper Symp. of Comm. III of the Intl. Soc. Photogrammetry, Moscow and Mittl. d. geod. Inst. No. 33, TU-Graz, 8010 Graz, Austria.

LEBERL F. (1978) "Current Status and Perspectives of Active Microwave Imaging for Geoscience Application". ITC-Journal 1978 - 1.

LEBERL F. et al. (1979): "Mapping of Sea-ice and Measurement of its Drifts Using Aircraft Synthetic Aperture Radar Images". J. Geophysical Research, Vol. 84, No. C4, pp 1827 - 1935.

LEBERL F. (1979): "Accuracy Aspects of Stereo-Side-Looking Radar". JPL-Publication 1979 - 17, Jet Propulsion. Laboratory Pasadena, USA.

LEBERL F. (1980): "Preliminary Radargrammetric Assessment of SEASAT-SAR Images". Mitteilungen der geodaetischen Institute, NO. 33, Tech. Univ., A-8010 Graz, pp. 59-80.

LEBERL F., E. CLERICI (1980): "Current Status of Metric Reduction of Active Sensor Data". Archives of the Intl. Soc. of Photogrammetry, Vol. 23/B.3, pp. 435-450.

LEBERL F. (1981): "The Venus Orbital Imaging Radar, (VOIR) Mission". Proceedings, Alpbach summer School, 29. July - 7. August. ESA SP - 164.

LEBERL F., J. RAGGAM, C. ELACHI, W. CAMPBELL (1981): "Measuring Sea Ice Motion from Seasat SAR Images". Invited Paper, 1981 AGU-Meeting, Baltimore, USA. Submitted Journal of Geophysical Research.

LEBERL F., H. FUCHS, J. FORD (1981): "A Radar Image Time Series". International Journal of Remote Sensing, Vol. 2, No. 2.

LEONARDO E. (1959): "An Application of Photogrammetry to Radar Research". Photogramm. Eng., Vol. XXV.

LEONARDO E. (1963): "Comparison of Imaging Geometry for Radar and Photographs". Photogramm. Eng., Vol. XXXIX.

LEONARDO E. (1964): "Capabilities and Limitations of Remote Sensors". Photogramm. Eng., Vol. XXX.

LEVINE D. (1960): "Radargrammetry". Mac Graw-Hill Book Company, New York.

LEVINE D. (1963): "Principles of Stereoscopic Instrumentation for PPI-Photographs". Photogramm. Eng., Vol. XXX.

LEVINE D. (1965): "Automatic Production of Contour Maps from Radar Interferometric Data". Pres. Paper, Fall Tech. Meeting, Am. Soc. Photogramm., Dayton, Ohio.

LEWIS A.J. and H.C. MacDonald (1970): " Interpretive and Mosaicking Problems of SLAR Imagery". Remote Sensing of Environment, Vol. 1, No. 4.

LING C., RASMUSSEN L., W. CAMPBELL (1978): "Flight Path Curvature Distortion in Side-Looking Airborne Radar Imagery". Photogramm. Eng. and Remote Sensing, Vo. No. 44, No. 10, pp 1255 - 1260.

LOELKES G.L. (1965): "Radar Mapping Imagery-Its Enhancements and Extraction for Map Construction". Pres. Paper, Fall Tech. Meeting, Am. Soc. Photogramm., Dayton, Ohio.

LOSHCHILOV, U.S., U.A. VOYEVODIN (1972): "Determining Elements of Drift of the Ice Cover and Movement of the Ice-Edge by the Aid of the TOROS Aircraft Lateral Scan Radar Station". Problemi Ariki, Antartiki, No. 40, pp 23 - 30.

LUCHININOV V.S. (1975): "Contactless Radar Mapping of Warm Valley Glaciers-Transformation of Radar Coordinates". Transl. from Russian in Soviet Physics-Technical Physics, Vol. 20, No. 4, 1976.

MACCHIA R.P. (1957): "Radar Presentation Restitutor". Photogramm. Eng., Vol. XXIII.

MANUAL OF PHOTOGRAMMETRY (1966): "Photogrammetric and Radargrammetric Techniques". Vol. II, 3rd Ed.

MARTIN-KAYE P.H.A. et al. (1980): "Fracture Trace Expression and Analysis in Radar Imagery of Rain Forest Terrain (Peru)". In Radar Geology. An Assessment, JPL-Publication 80 - 61, Jet Propulsion Laboratory, Pasadena, USA.

MASRY S.E., E.E. DERENYI, B.G. CRAWLEY (1976): "Photomaps from Non-Conventinal Imagery". Photogramm. Eng. and Remote Sensing, Vol. XLII, No. 4.

MC KEON, J.B. (1979): "Remote Sensing of the Resources of Los Andes Region". Venezuela, Final Report - Vol. I. Environemental Research Institute of Michigan. Report 305 200-7-F, Ann Arbor, Michigan.

MOORE R.K. (1969): "Heights from Simultaneous Radar and Infrared". Photogramm. Eng., vol. XXXV.

MOREIRA H.F. (1973): "Project RADAM-Remote Sensing Application to Environement Analysis of Amazon Region". 2nd Annual Remote Sensing of Earth Resources Conference, Univ. of Tennessee Space Inst., Tullahoma, Tennessee.

NARAGHI M., W. STROMBERG, M. DAILY (1981): "Geometric Rectification of Radar Imagery Using Digital Elevation Models". Image Processing Laboratory of the Jet Propulsion Laboratory, Pasadena, U.S.A.

NORVELLE F.R. (1972): "AS-11-A Radar Program". Photogramm. Eng., Vol. XXXVIII.

PETERSON R.K. (1976): "Radar Correlator Geometric Control". Goodyear Aerospace Report GIB 9397, Litchfield Park, Arizona; Pres. Paper, 13th Cong. Int. Soc. Photogramm., Helsinki, Finland.

PROTHERSE W.M. et al. (1950): "The Geometry of the Radarscope". Techn. paper, No. 107, Mapping and Charting Laboratory Ohio State Univ. , Ohio.

RADAR GEOLOGY (1980): "Radar Geology". An Assessement, JPL-Publication 80 - 61, Jet Propulsion Laboratory, Pasadena, USA.

RANEY K. (1981): "Radarsat Programme". Pesented Paper, ISPRS-SAR Processing Working Group II 15, Frascati, Italy, 3. - 4. Dec.

RAYTHEON CO. (1973): "Digital Rectification of Side-Looking Radar (DRESLAR)". Final Report, Raytheon Co., Autometric Operation, Proep. for U.S.Army Engineer Topographic Laboratories, Fort Belvoir, Virginia 22060, Report No. ETL-CR-73-18.

RINNER K. (1948): "Die Geometrie des Funkbildes". Austrian Academy of Sciences, Math. Naturwiss. Klasse, also in "Handbuch der Vermessungskunde", Jordan-Eggert-Kneissl, Vol. VI, Metzlersche Verlagsbuchhandlung, Stuttgart.

ROESSL J. VAN and R. DE GODOY (1974): "SLAR Mosaics for Project RADAM". Photogramm. Eng., Vol. XL.

ROSENFIELD G.H. (1968): "Stereo Radar Techniques". Photogramm. Eng., Vol. XXXIV.

RYDSTROM H.C. (1968): "Radargrammetric Applications of the Right Angle Solution Nomogram". Goodyear Aerospace Corp., Report GIB 9124, Litchfield Park, Arizona.

SCHEPS B.B. (1960): "To Measure is to Know-Geometric Fidelity and Interpretation in Radar Mapping". Photogramm. eng., Vol. XXVI.

SCHERTLER R.J. et al. (1975): "Great Lakes All-Weather Ice Information System". Proc, 10th Symp. Remote Sensing of the Environment", Ann Arbor, Michigan.

SCHREITER J.B. (1950): "Strip Projection for Radar Charting". Techn. Paper No. 130, Mapping and Charting Laboratory, Ohio state Univ., Ohio.

SHAKINE A., T. LE TOAN (1978): "A Study of Digitized Radar Images". Intl. Symp. of Remote Sensing of Environment, Ann Arbor, USA.

SMITH H.P. (1948): "Mapping by Radar - The Procedures and Possibilities of a New and Revolutionary Method of Mapping and Charting". U.S. Air Force, Randolph Field, Texas.

STILWELL J.E. (1963): "Radar Network Adjustment". Photogramm. Eng., Vol. XXI

SUPER A.D. et al. (1975): "Remote Sensing Applied to the International Ice Patrol". Proc. 10th Symp. on Remote Sensing of the Environment, Ann Arbor, Michigan.

TIERNAN M. et al. (1976): "Lunar Cartography with the Apollo 17 Radar Imagery". the Moon, Vol. 15, Nos. 1/2.

THOMAN G. (1969): "Distance Computation on Radar Film". Simonnett, D.G. (ed.), "The Utility of Radar and Other Remote Sensors in Thematic Land Use Mapping from Spacecrft", Annual Report, NASA-140.

THOMPSON T.W. et al. (1972): "Progress Report on 25 cm Radar Observations of the 1971 AIDJEX Studies". Arctic Ice Dynamics Joint Experiment (AIDJEX) Bulletin, No. 12, Univ. of Wash., Seattle, Wash.

YORITOMO K. (1965): "All Weather Mapping". Presented Paper, Fall Technical Meeting, Soc. Photogramm, Dayton, Ohio.

YORITOMO K. (1972): "Methods and Instruments for the Restitution of Radar Pictures". Arch. Int. soc. Photogramm., Inv. Paper, 12th Congress, Ottawa, Canada.

ZHURKIN I.G., N.KORNEYEV (1974): "Relationship between the Coordinates of Terrain Points and the Coordinates of Image Points in Side-looking Radar Systems with an Antennna along the Fuselage". Goodesy, Mapping, Photogrammetry, Vol. 16, No. 3, pp 140 - 146.

REFERENCES ON VENUS RADAR RESAERCH

BROWN W.E. et al. (1972): "Planetary Imaging Radar Study". Jet Propulsion Laboratory, Publication Nr. 701-145, Pasadena, Cal. 91103, USA.

CAMPBELL D.B. et al. (1972): "Venus Topography Revealed by Radar Data". Science, 175, 514-516.

CAMPBELL D.B. et al. (1976): "New Radar Image of Venus". Science, 193, pp 1123-1124.

CAMPBELL D.B. et al. (1979): "Venus: Further Evidence for Impace Cratering and Tectonic Activity from Radar Observations". Science, 204, 1424-1427.

CAMPBELL D.B. , B. BURNS (1980) "Earth-Based Radar Imagery of Venus". J. Geophysical Research, A13, 8271-8281.

FLORENSKY C.P. et al. (1977): "The Surface of Venus as Revealed by Soviet Venera 9 and 10". Geol. Soc. of America Bull., 88, 1537-1545.

FRIEDMAN L., J. ROSE (1973): "Venus Orbital Imaging Radar Study (VOIR)". Jet Propulsion Laboratory, Report 760-89, Pasadena, Cal 91103, USA.

GOLDSTEIN R.M. (1965): "Preliminary Venus Radar Results". Radio Science, 70, 1623-1625.

GOLDSTEIN R.M., et al. (1972): "A Radar Image of Venus". Icarus, 17, 699-703.

GOLDSTEIN R.M. et al. (1976): "Venus Radar Images". J. Geophysical Research, 81, 4807-4818.

GOLDSTEIN R.M. et al. (1978) "Venus Brightness and Altitude Images". Icarus, 36, 334-352.

HAGFORS T., D.B. CAMPBELL (1974): "Radar Backscattering from Venus at Oblique Incidence at a Wavelength of 70 cm". Astronomical J., 79 (4), 493-502.

JURGENS R.F. (1970): "Some Preliminary Results of the 70 cm Radar Studies of Venus". Radio Science, 5, 435-442.

JURGENS R.F. (1980): "Images of Venus by Three Station Interferometry - 1977 Results". J. Geophysical Research, 85(A13(, 8282-8299.

MALIN M., S.R. SAUNDERS (1977): "Surface of Venus, Evidence of Diverse Landforms from Radar Observations". Science, 196, 987-990.

MARTIN-MARIETTA CORP. (1974): "Venus Orbital Imaging Radar Trade-Off Study". Martin-Marietta Aerospace Corp., Denver Div., Colorado, Contract JPL 753-766.

MASURSKY H. et al. (1980): "Pioneer Venus Radar Results: Geology from Images and Altimeters". J. Geophysical Research, 85 (A13), 8231-8260.

PETTENGILL G. (1977): "Orbiter Radar Mapper Instrument. Pioneer Venus Experiment Descriptions". Space Science Reviews, 20, 512-515.

PETTENGILL G. et al. (1979b): "Venus: Preliminary Topographic and Surface Imaging Results from the Pioneer Orbiter". Science, 205, 91-93.

PETTENGILL G. et al. (1980b): "Pioneer Venus Radar Results: Altimetry and Surface Properties". J. Geophysical Research, 85 (A13), 8261-8270.

PHILLIPS R. et al. (1973): "Apollo Lunar Sounder Experiment". Apollo 17 Preliminary Science Report, NASA SP-330, Washington D.c.

RUMSEY H.C. et al. (1974): "A Radar Brightness and Altitude Image of Portion of Venus". Icarus, 23, 1.

ROGERS A.E.E., R.P.INGALLS (1969): "Mapping the Venus Surface Reflectivity by Radar Interferometry". Science, 165, 797-799.

ROGERS A.E.E.,R.P. INGALLS (1970): "Radar Mapping of Venus with Interferometric Resolution of the Range Doppler Ambiguity". Radio Science, 5, 425-433.

SAUNDERS R.S., MALIN (1977): "Venus: Geological Analysis of Radar Images". Geol. Romana, 15, 507-515.

SAUNDERS R.S. et al. (1973): "Mission Planning for Remote Exploration of the Surface of Venus". Am. Inst. of Aeronautics and Astronautics, AIAA-Paper 73-580.

WESTINGHOUSE (1974): "Spaceborne Sythetic Aperture Radar Pilot Study". Final Report, Contract NAS 5-2/951, Westinghouse Electric Corp., Systems Development Div., Baltimore, Maryland, USA.

ADDITIONAL REFERENCES

BAKER J., E.M. MIKKAIL (1975): "Geometric Analysis and Restitution of Digital Multispectral Scanner Data Arrays". LARS Information Note 05 28 75, Purdue Univ., USA.

EBNER H., R. HOESSLER (1978): "The Use of Gauss-Markov Processes in Digital Rectification of Remote Sensing Proceedings Data". of the LSP-Comm. III Symposium, Moscow, pp. 258 - 265.

GRAHAM L.C. (1974): "Synthetic Interferometer Radar for Topographic Mapping". Proc. IEEE, Vol. 62, No. 6.

KRAUS K. (1976): "Anwendungsmoeglichkeiten eines digital gesteuerten Differentialumbildegeraetes". Geowissenschaftliche Mitteilungen, No. 8, pp 1-22. Technical University Vienna, Austria.

LEBERL F. (1975f): "Photogrammetric Interpolation". Photogramm. Eng., Vol. XLI.

LA PRADE G., J. BRIGGS, R. FARREL, E. LEONARDO (1980) "Stereoscopy". Manual of Photogrammetry, 4 th Edition, Am. Soc. of Photogr., Falls Church, U S A.

MAKAROVIC B. (1973): "Digital Mono Plotters". ITC-Journal, 1973-4, Enschede, The Netherlands.

MANNING B.N. and D.D. HANN (1967): "Some Simple Equations of Satellite Motion". Arizona Electronics Eng. Memo No. 267, Goodyear Aerospace Corp., AAP-26297, Litchfield Park Arizona.

MATTEWS R.E. (ed.) (1975): "Active Microwave Workshop Report". NASA Special Report SP-376, Washington, C.D.

MORIZ H. (1973): "Least Squares Collocation". Deutsche Geodaetische Kommission, Serie A, Nr. 75, Muenchen, W.-Deutschland.

PHILLIPS R.J. u.a. (1973): "Apollo Lunar Sounder Experiment". Apollo 17 Preliminary Science Report, NASA Special Publ. SP-330, Washington, D.C.

RINNER K., W. BURKHARDT (1972): "Photogrammetry". Vol. III a of Handbuch des Vermessungswesens. Jordan - Eggert-Kneissl (Ed.), 10th Edition. Metzler-Stuttgart, 2371 pages.

SCHUT G. (1970): "External Block Adjustment of Planimetry". Photogrammetric Eng., Vol. XXXVI.

TELEKI P., R. RAMSEIER (1978): "The Seasat-A Synthetic Aperture Radar Experiment". Proc. Intl. Symp. Comm. VII of Intl. Soc. of Photogrammetry, July 2-8, Univ. of Freiburg, Vol. 1, 93 - 114.

A P P E N D I X

Catalogue of Radar Stereo Image Pairs

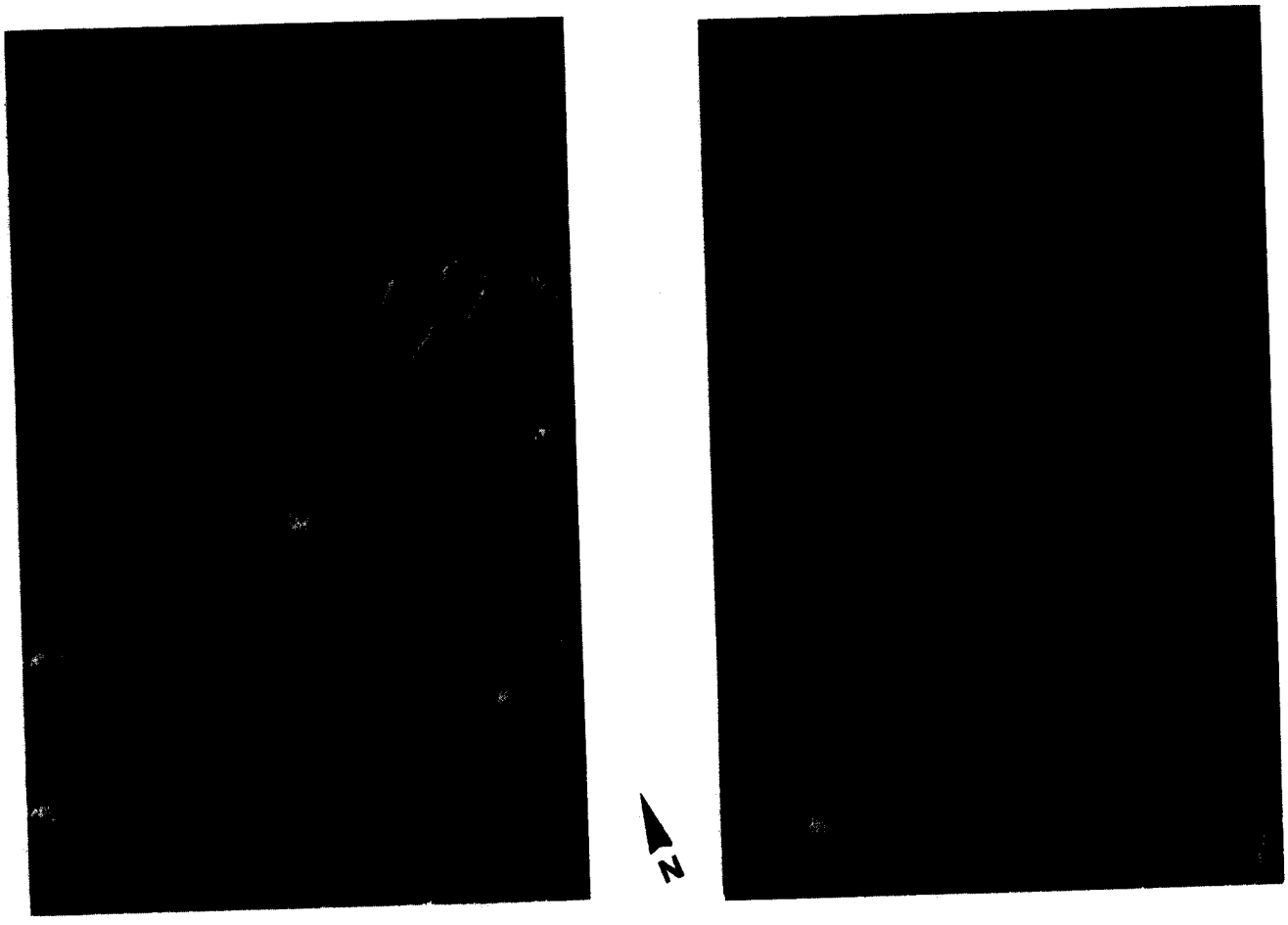

Figure A1 : SEASAT stereo model, same-side geometry

Area : Los Angeles, California

Altitude : 800 km

Stereo Base : 50 km

Stereo Viewability : very convenient

Figure A2 : SEASAT stereo model, same-side geometry

Area : Los Angeles, California

Altitude : 800 km

Stereo Base : 20 km

Stereo Viewability : very convenient

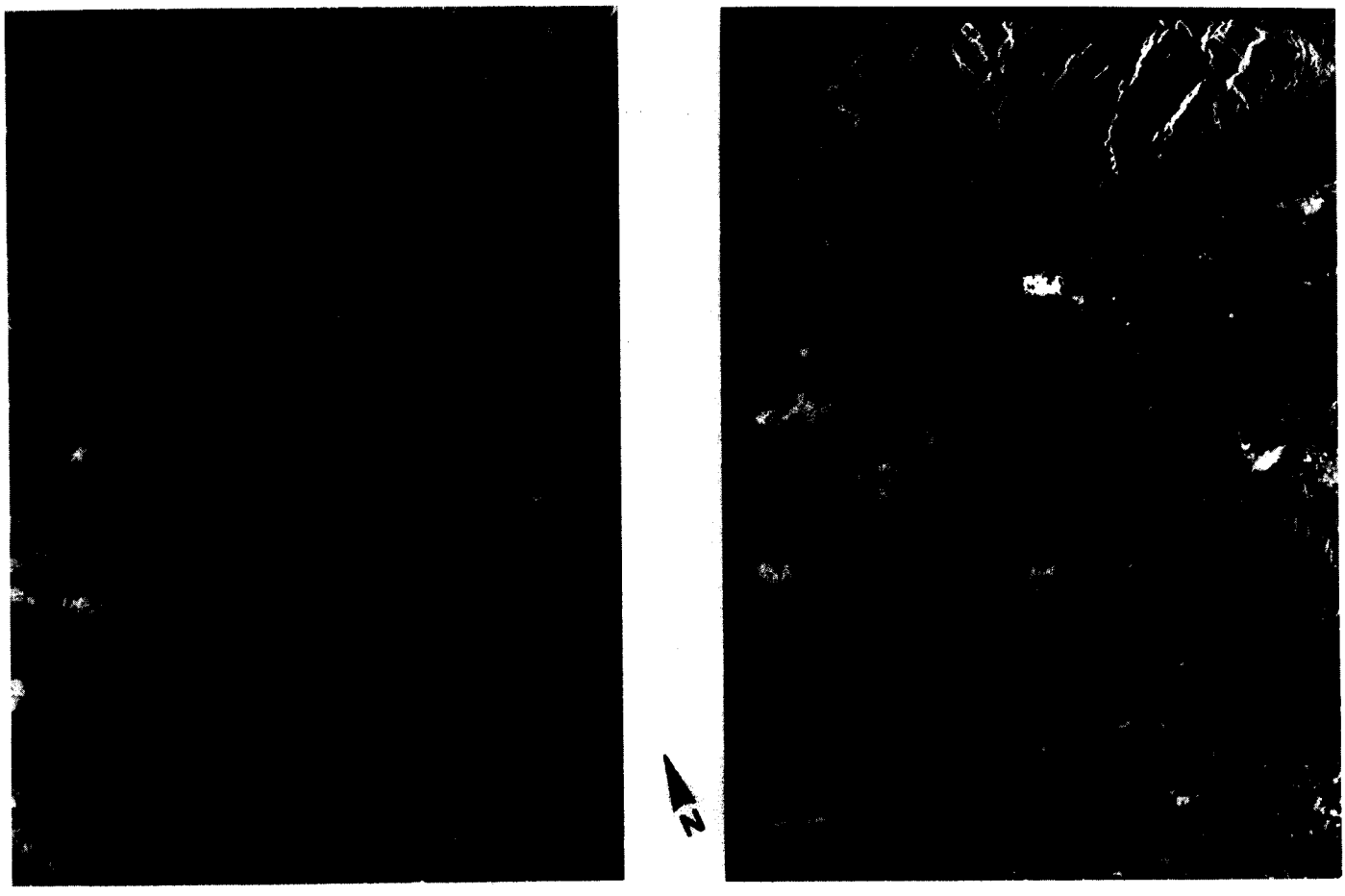

Figure A3 : SEASAT stereo model, same-side geometry

Area : Los Angeles, California

Altitude : 800 km

Stereo Base : 35 km

Stereo Viewability : very convenient

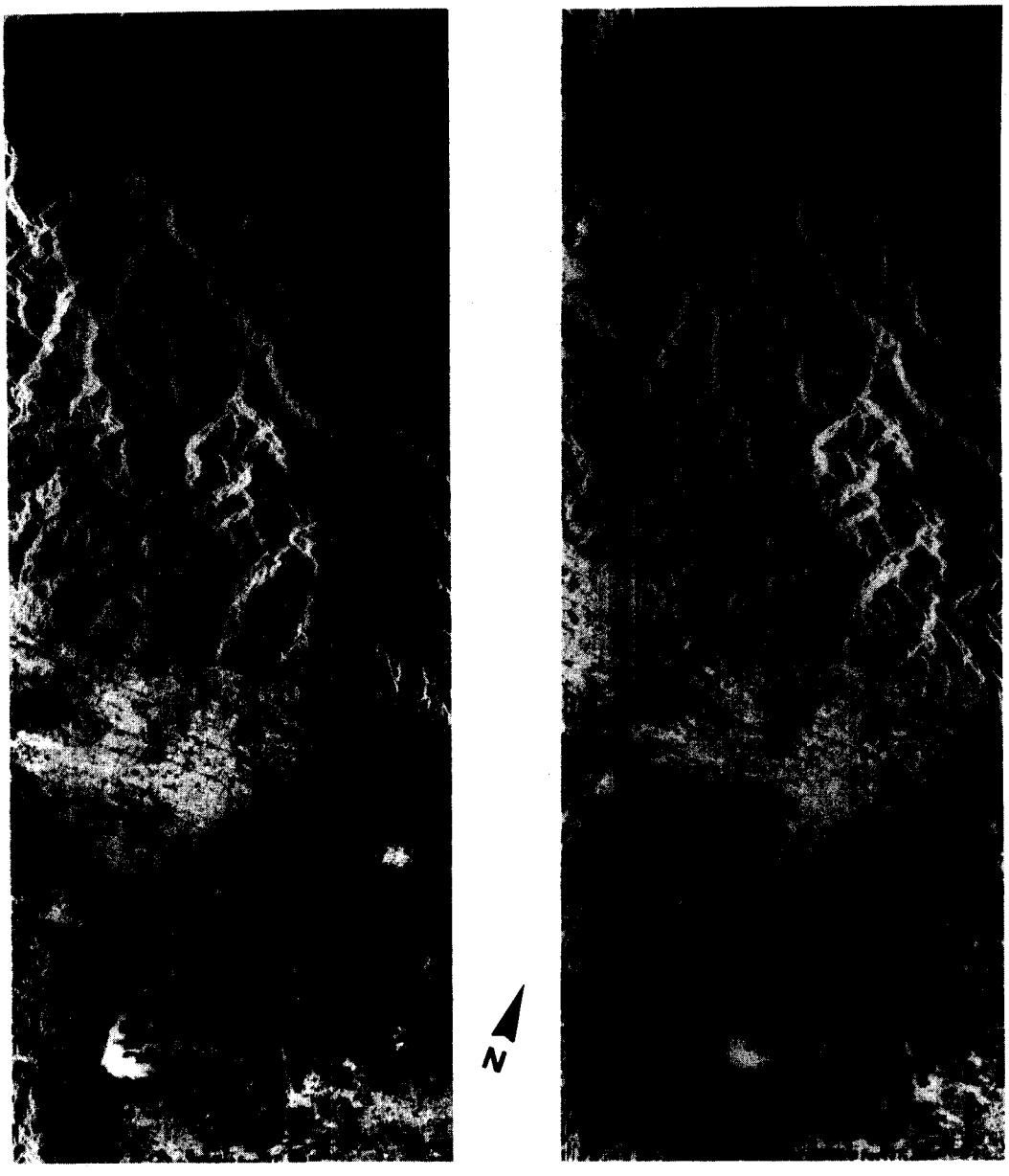

Figure A4 : SEASAT stereo model, same-side geometry

Area : Los Angeles, California

Altitude : 800 km

Stereo Base : 20 km

Stereo Viewability : convenient

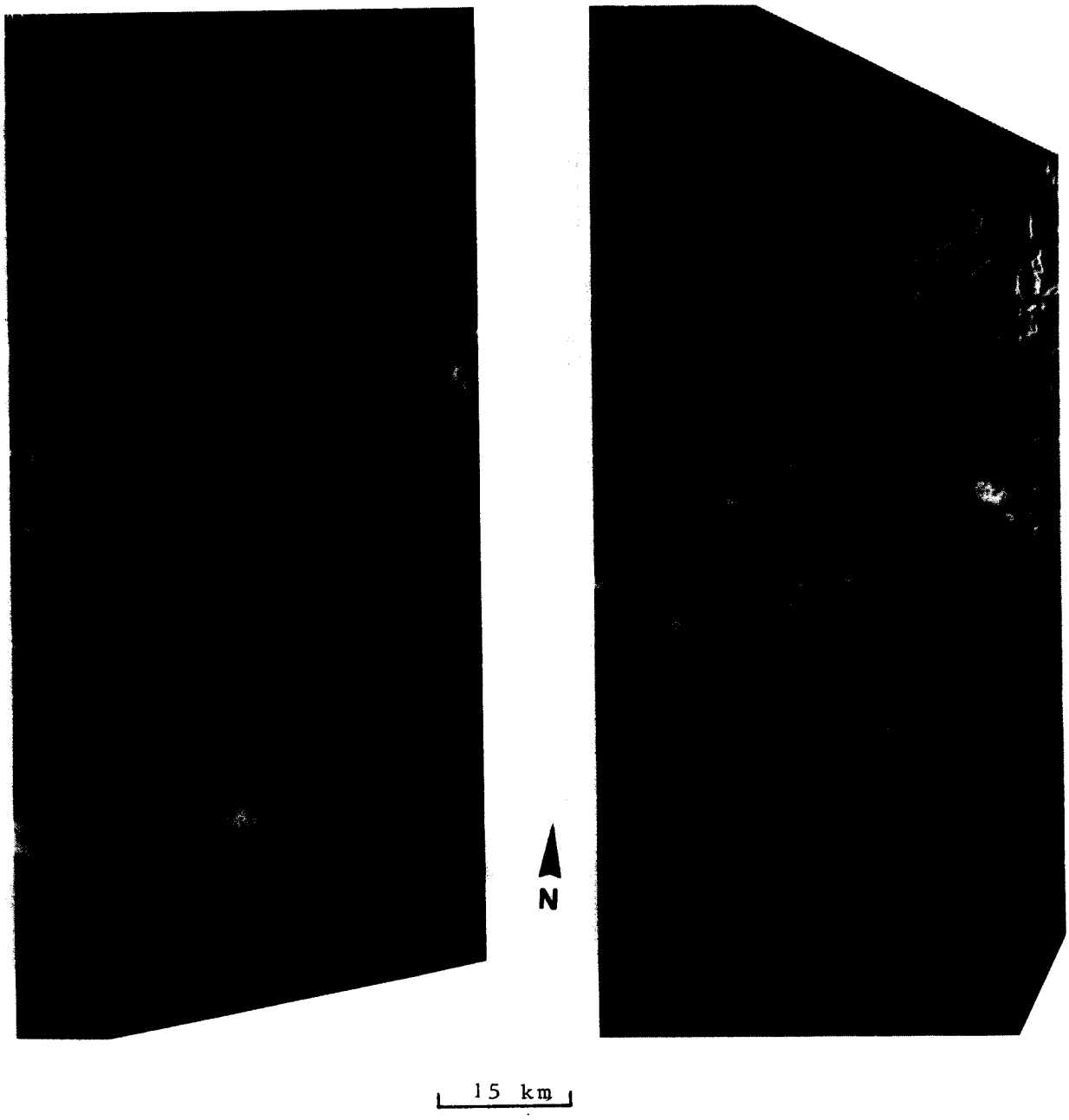

Figure A5 : SEASAT stereo model, opposite-side geometry

Area : Los Angeles, California

Altitude : 800 km

Stereo Base : 550 km

Stereo Viewability : not possible

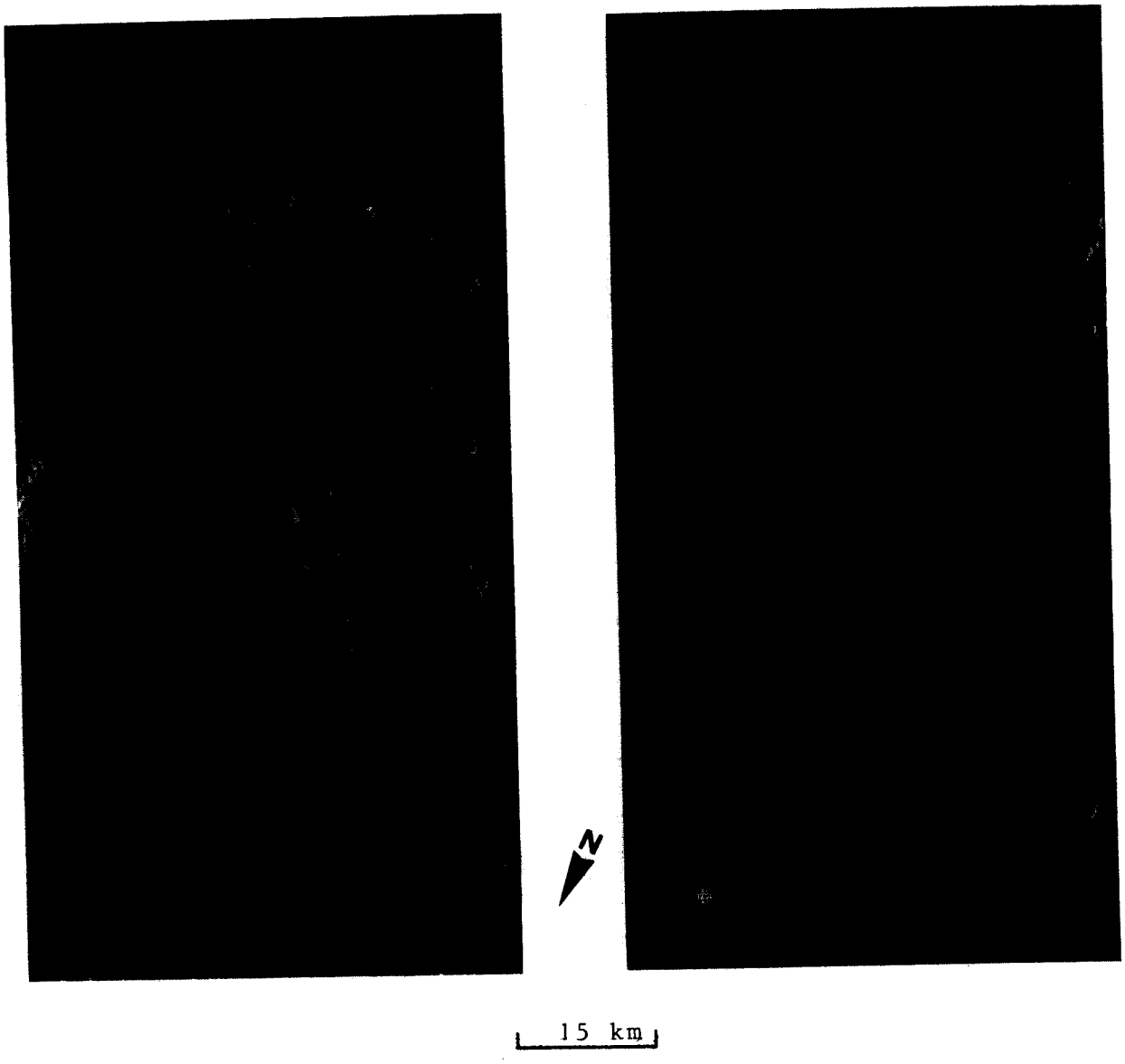

Figure A6 : SEASAT stereo model, same-side geometry

Area : Tushar Mountains, Utah

Altitude : 800 km

Stereo Base : 55 km

Stereo Viewability : convenient

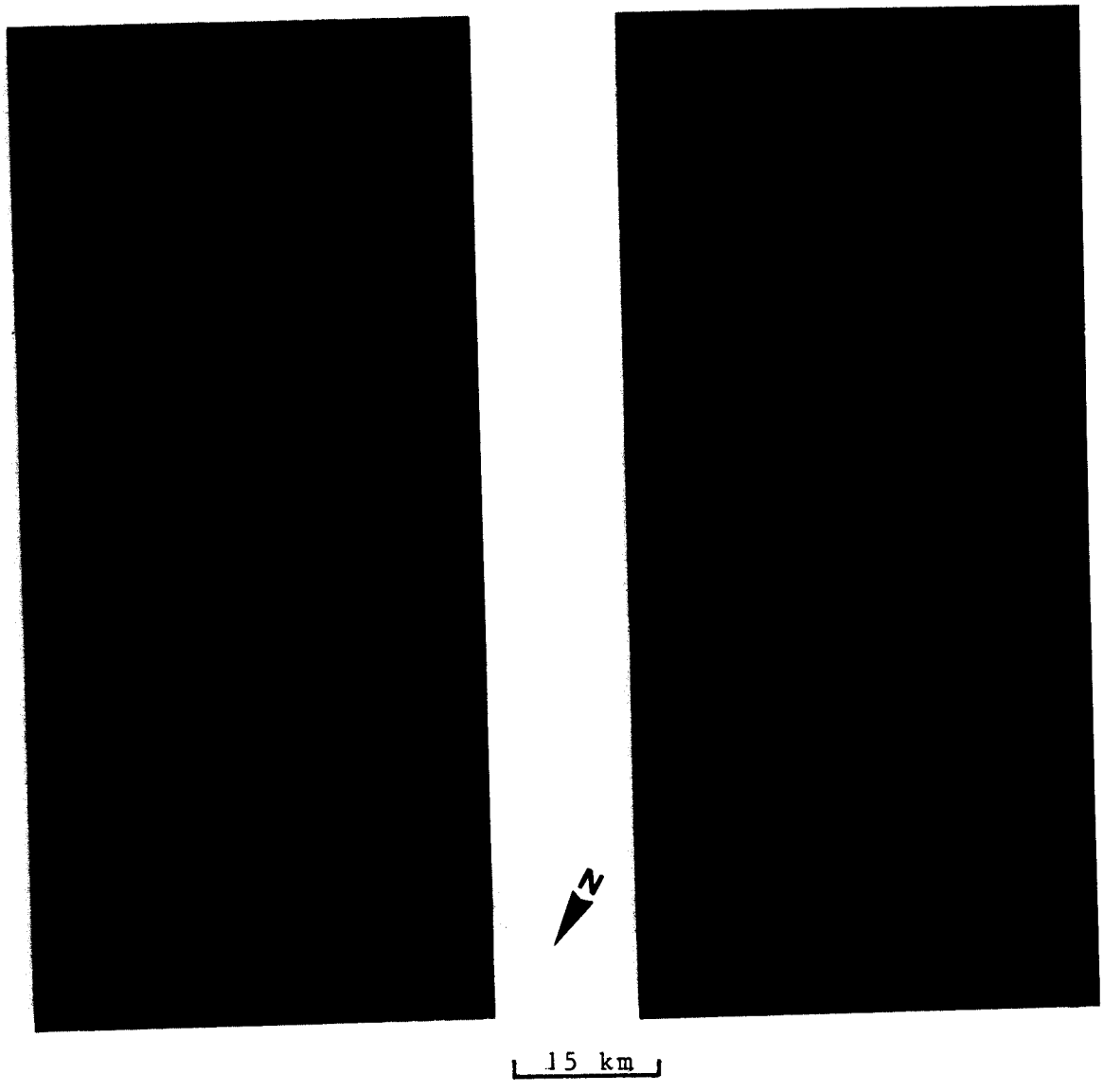

Figure A7 : SEASAT stereo model, same-side geometry

Area : Canyonlands, Utah

Altitude : 800 km

Stereo Base : 55 km

Stereo Viewability : convenient

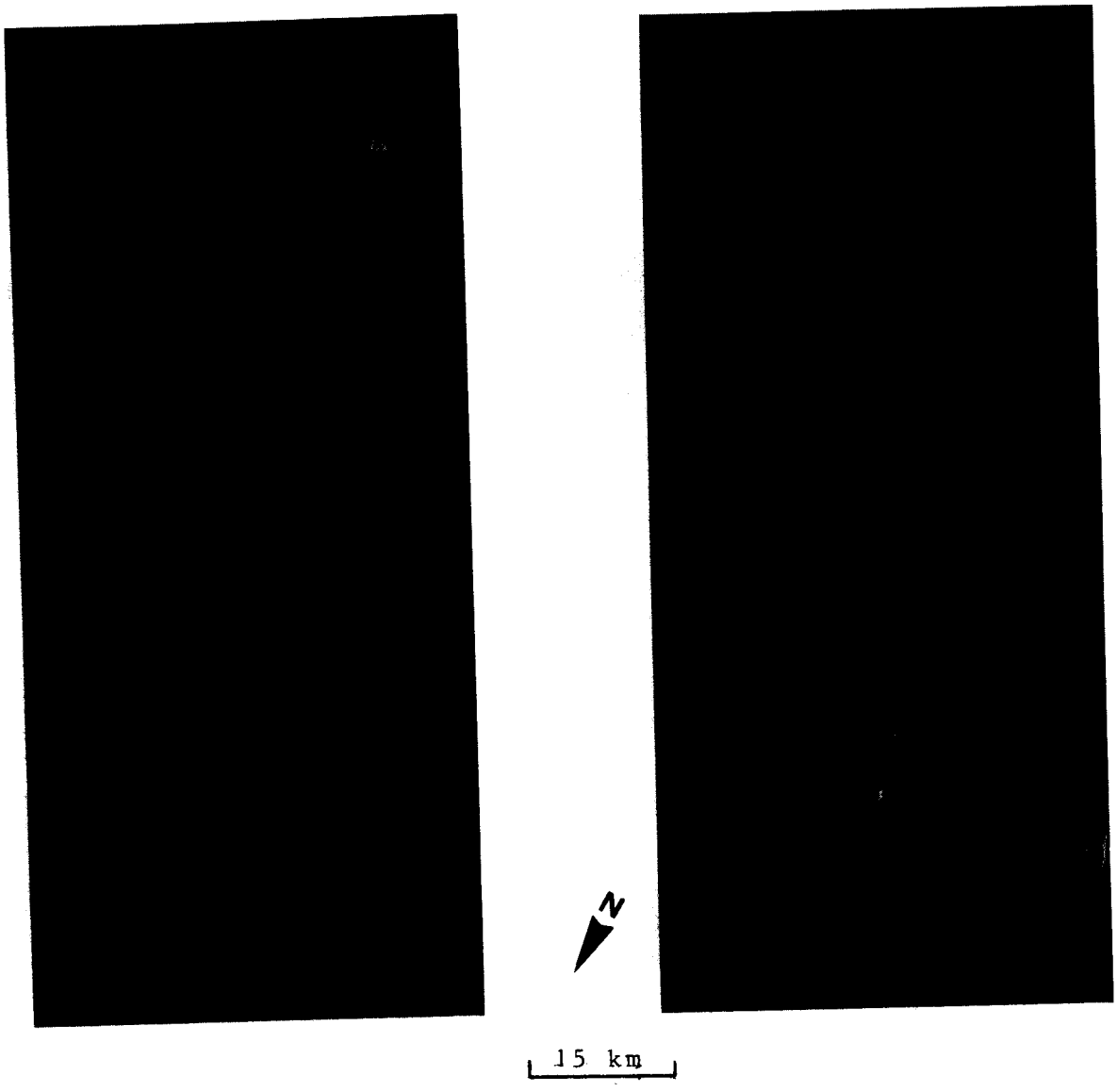

Figure A8 : SEASAT stereo model, same-side geometry

Area : Sevier Lake, Utah

Altitude : 800 km

Stereo Base : 75 km

Stereo Viewability : convenient, but poor image quality

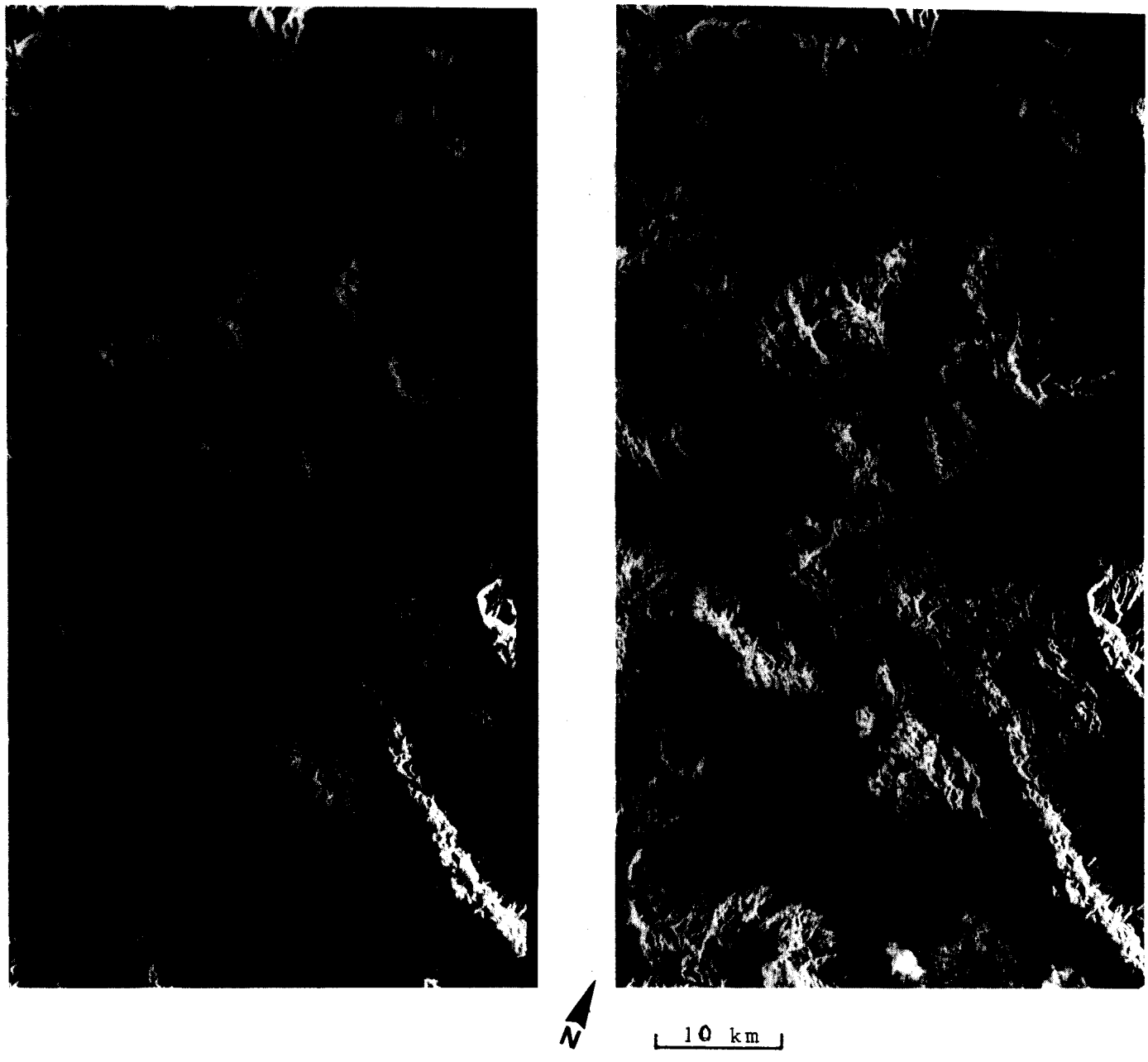

Figure A9 : SEASAT stereo model, same-side geometry

Area : Granite Mountain, Arizona

Altitude : 800 km

Stereo Base : 55 km

Stereo Viewability : convenient

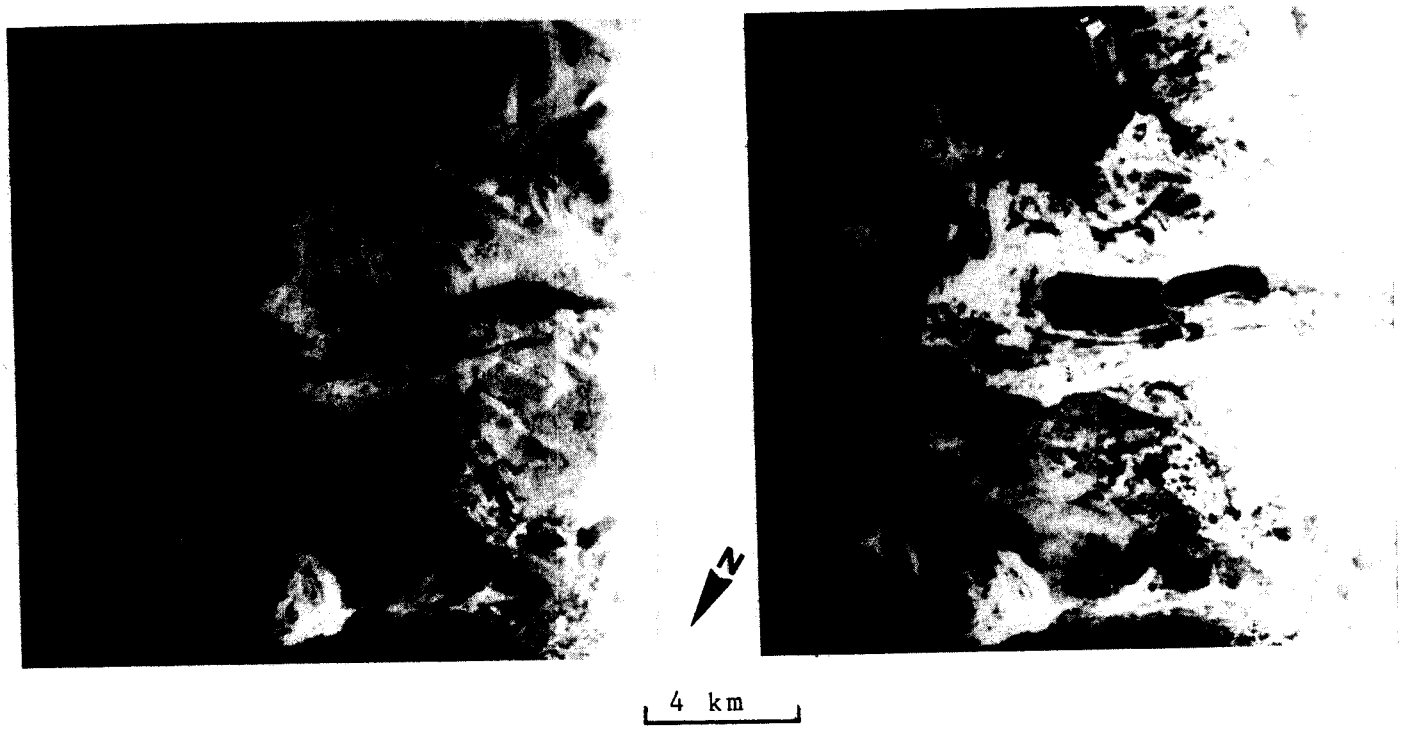

Figure A10 : GOODYEAR stereo model, same-side geometry

Area : Fremont, Wyoming

Altitude : 12 km

Stereo Base : 0.7 km

Stereo Viewability : convenient

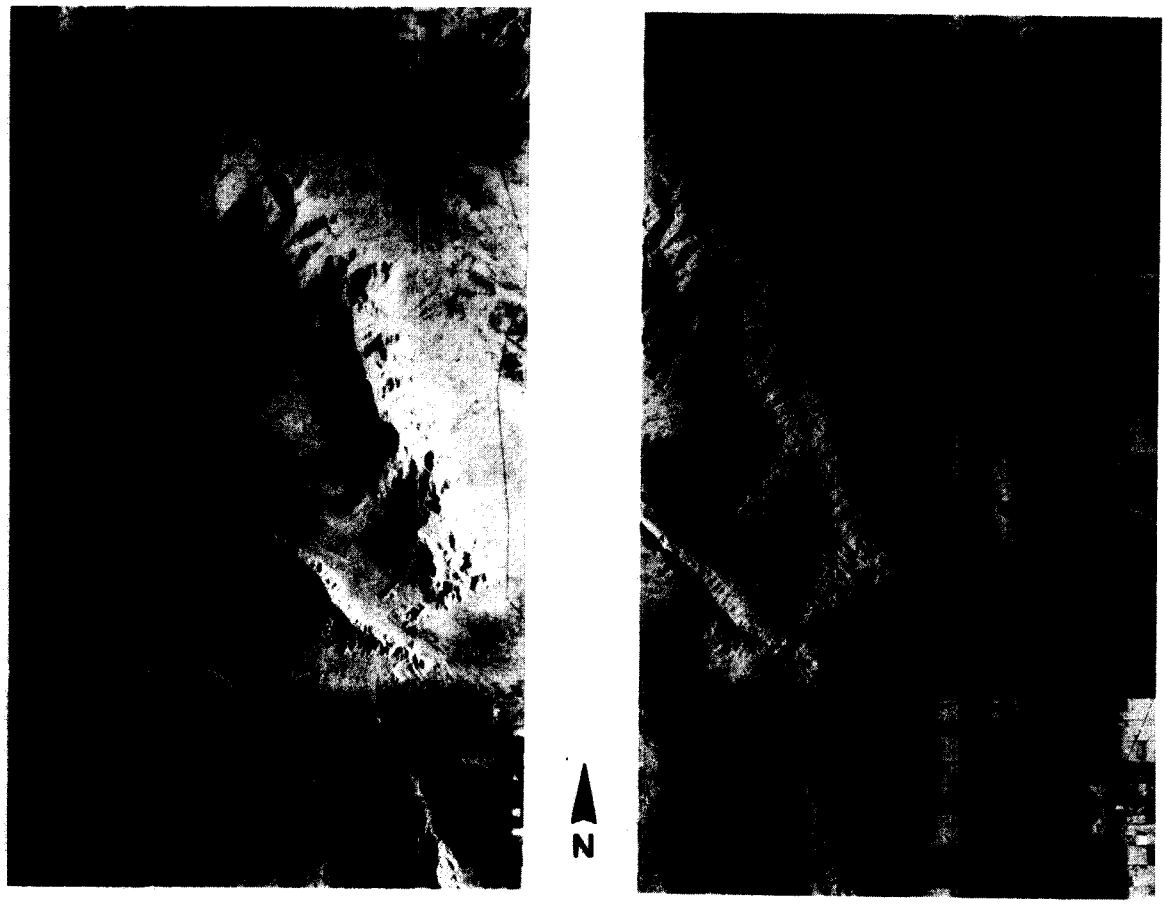

Figure All : GOODYEAR stereo model, same-side geometry

Area : Estrella Mountain, Arizona

Altitude : 12 km

Stereo Base : 10 km

Stereo Viewability : very convenient

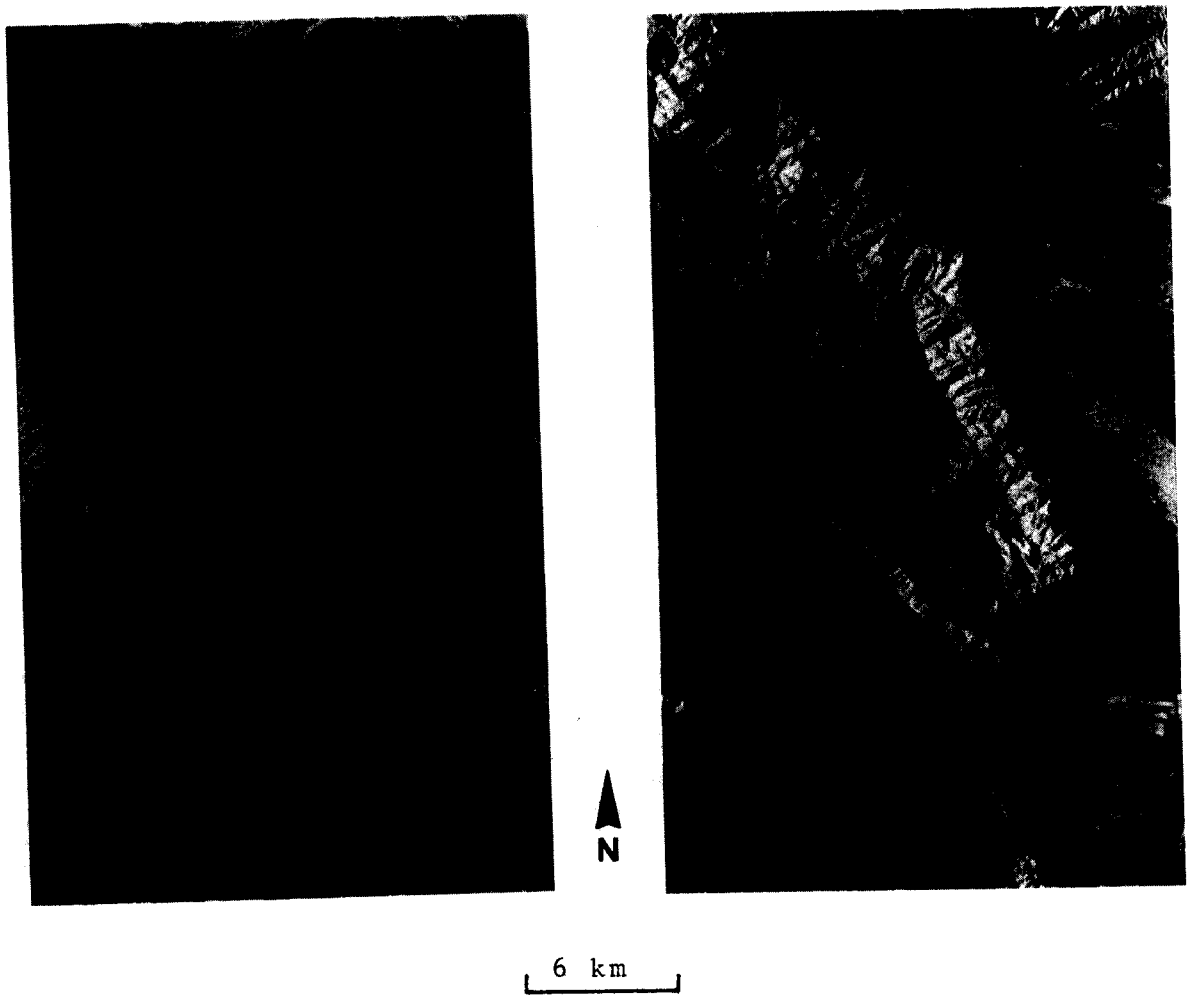

Figure A12 : GOODYEAR stereo model, opposite-side geometry

Area : Estrella Mountain, Arizona

Altitude : 12 km

Stereo Base : 10 km

Stereo Viewability : only for flat terrain

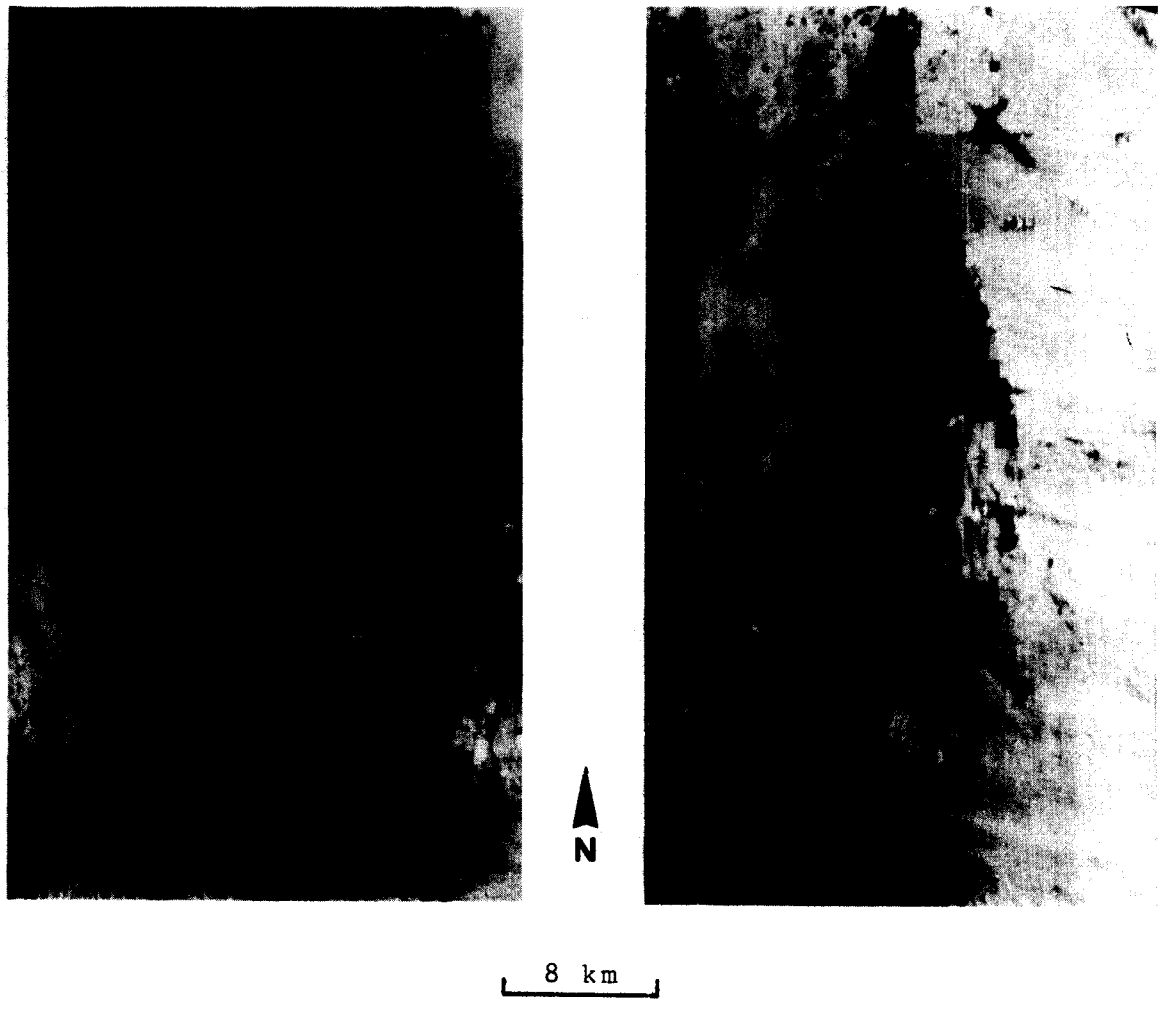

Figure A13 : MOTOROLA stereo model, same-side geometry

Area : Sierrita, Arizona

Altitude : 4 km

Stereo Base : 10 km

Stereo Viewability : convenient

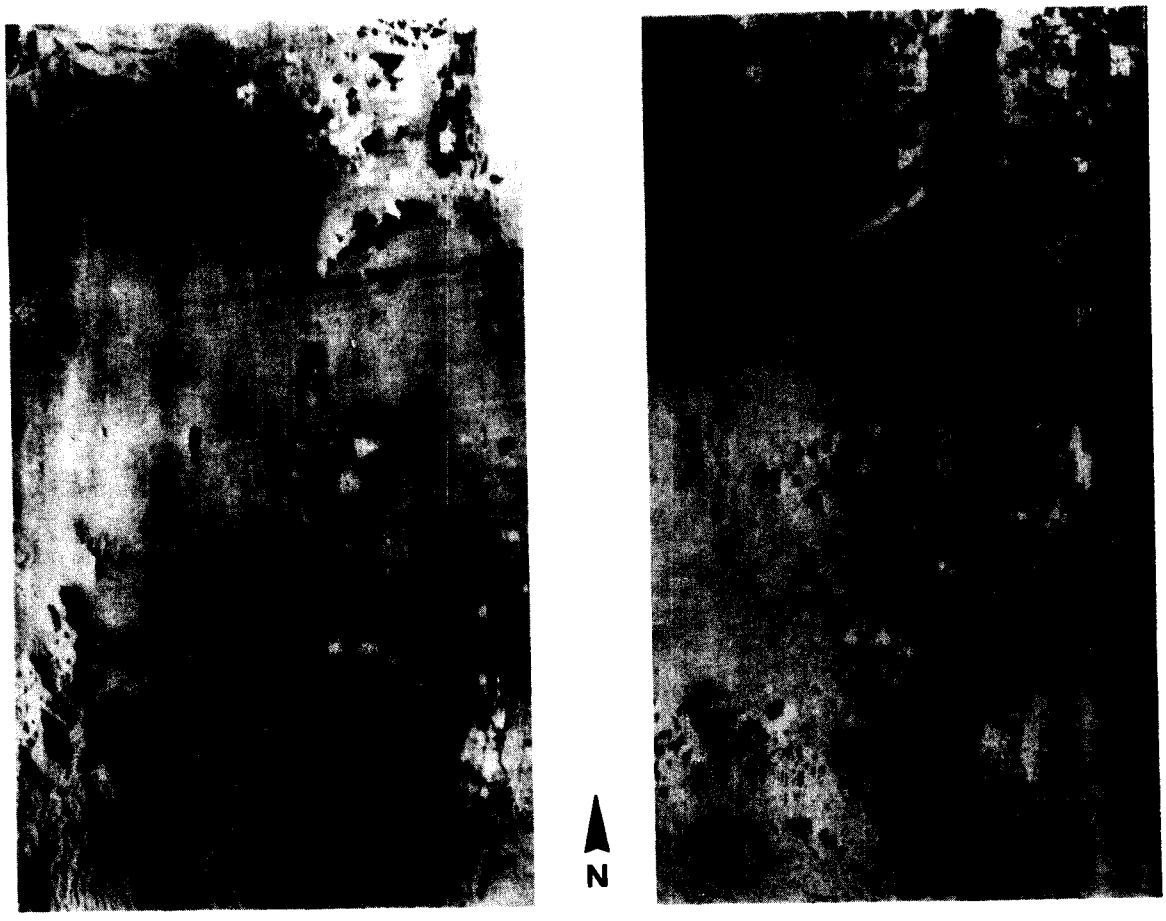

Figure A14 : MOTOROLA stereo model, opposite-side geometry

Area : Sierrita, Arizona

Altitude : 4 km

Stereo Base : 48 km

Stereo Viewability : only for flat terrain

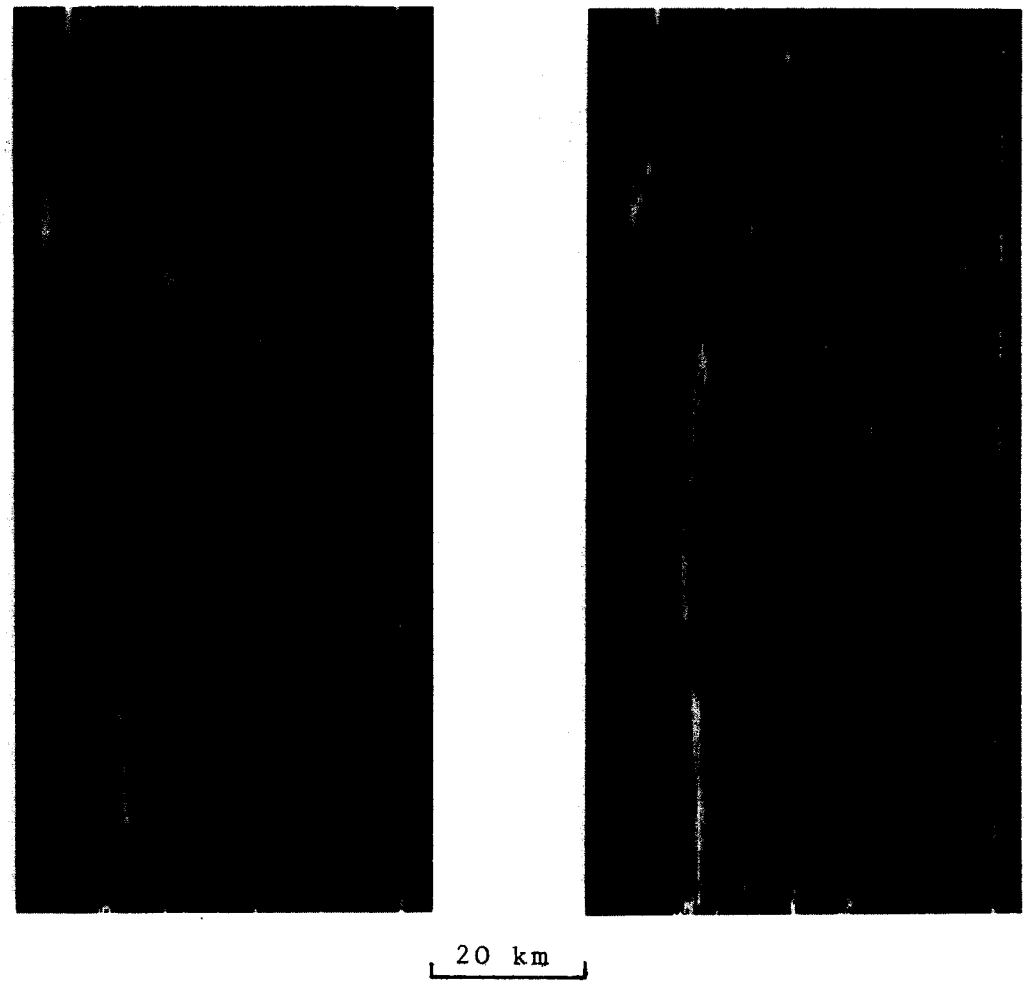

Figure A15 : APOLLO 17 stereo model, same-side geometry

Area : Hevelius, Moon

Altitude : 112 km

Stereo Base : 10.1 km

Stereo Viewability : not possible

Figure A16 : APOLLO 17 stereo model, same-side geometry

Area : Reiner, Moon

Altitude : 112 km

Stereo Base : 9.6 km

Stereo Viewability : not possible

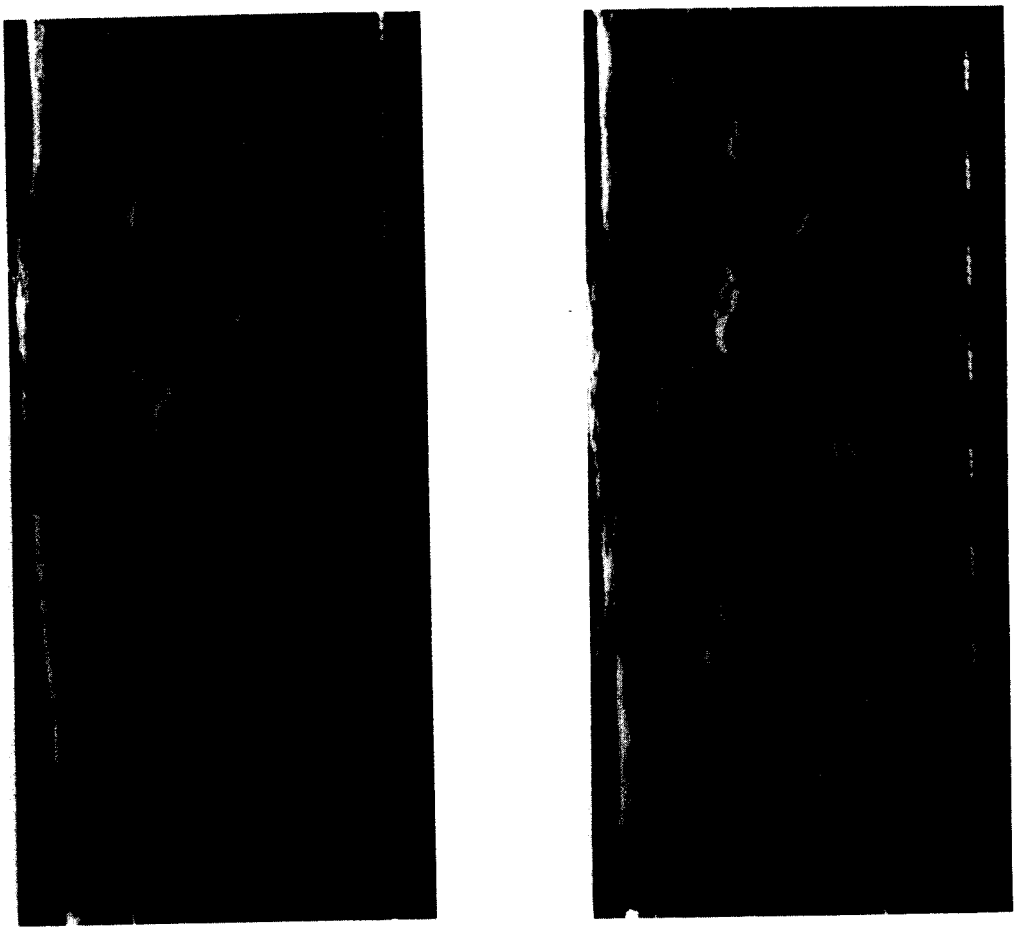

Figure A17 : APOLLO 17 stereo model, same-side geometry

Area : Montes Carpatus, Moon

Altitude : 112 km

Stereo Base : 6.9 km

Stereo Viewability : only for some local areas

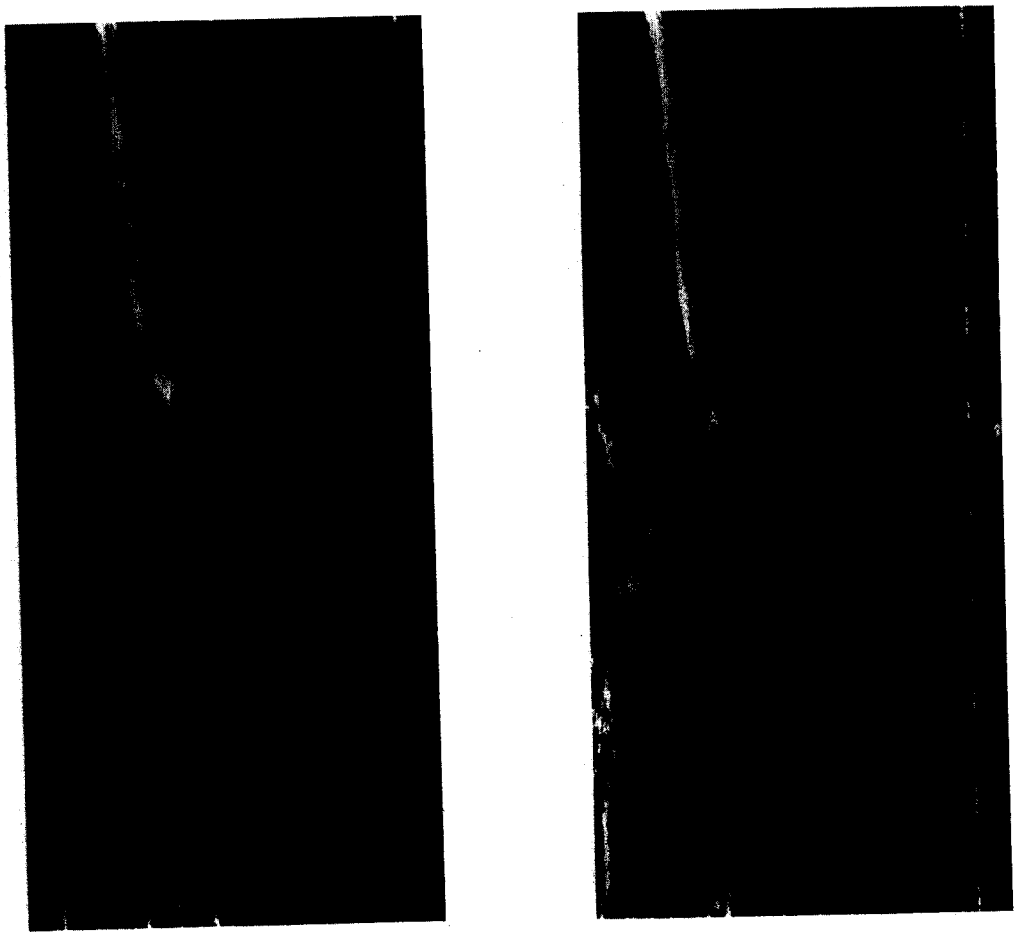

Figure A18 : APOLLO 17 stereo model, same-side geometry

Area : Montes Appenninus, Moon

Altitude : 112 km

Stereo Base : 3.5 km

Stereo Viewability : possible

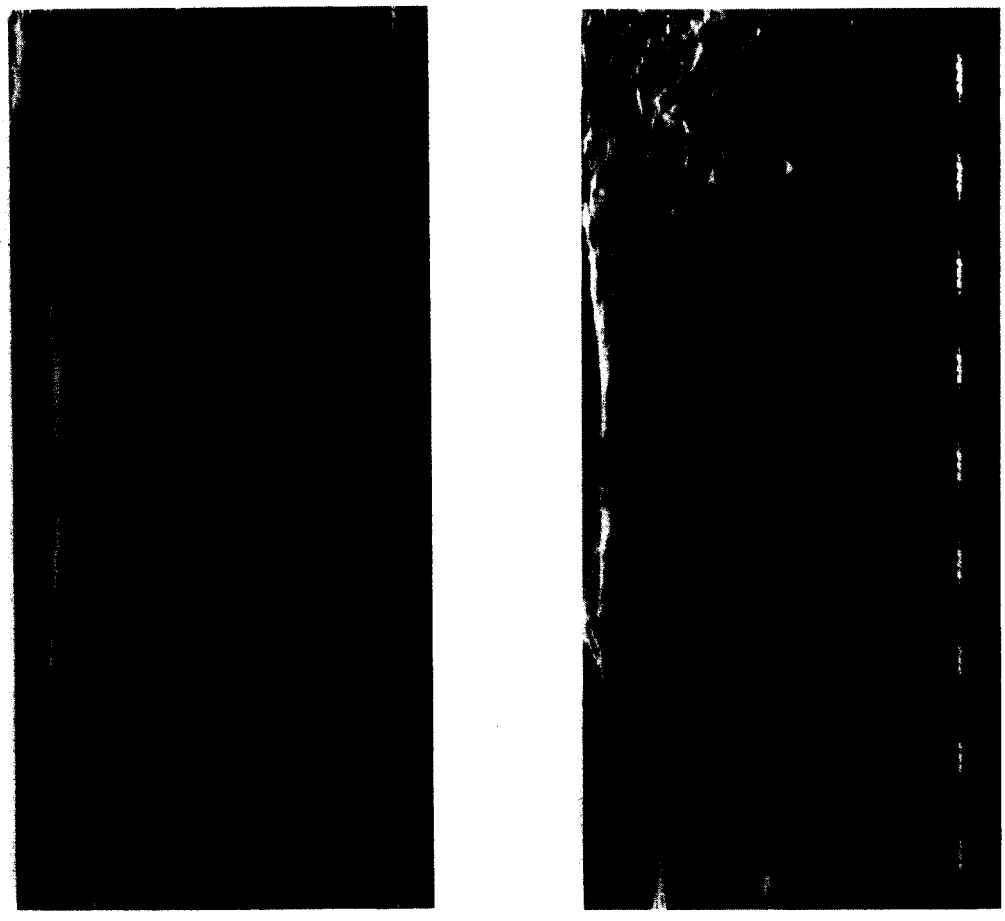

Figure A19 : APOLLO 17 stereo model, same-side geometry

Area : Mons Haemus, Moon

Altitude : 112 km

Stereo Base : 1.8 km

Stereo Viewability : possible

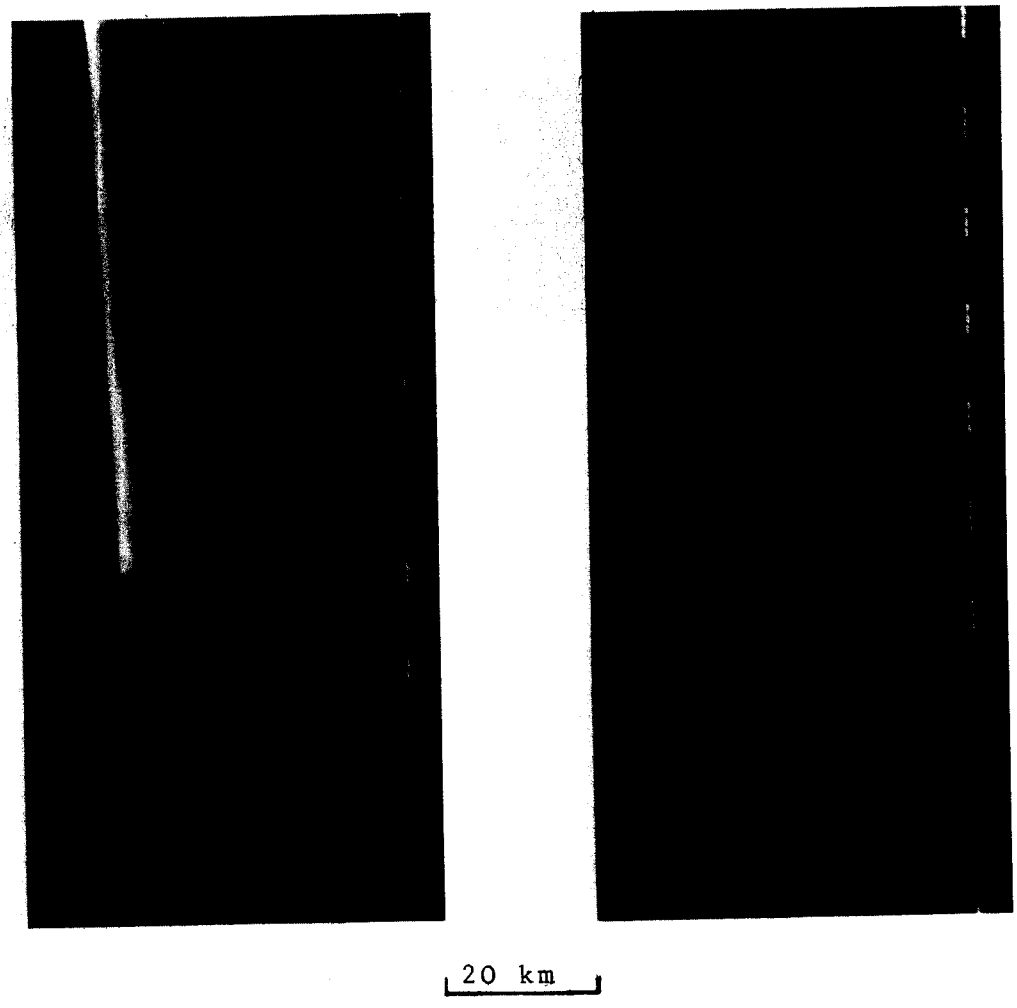

Figure A20 : APOLLO 17 stereo model, same-side geometry

Area : Mare Serenitatis, Moon

Altitude : 112 km

Stereo Base : 1.3 km

Stereo Viewability : possible, but flat terrain

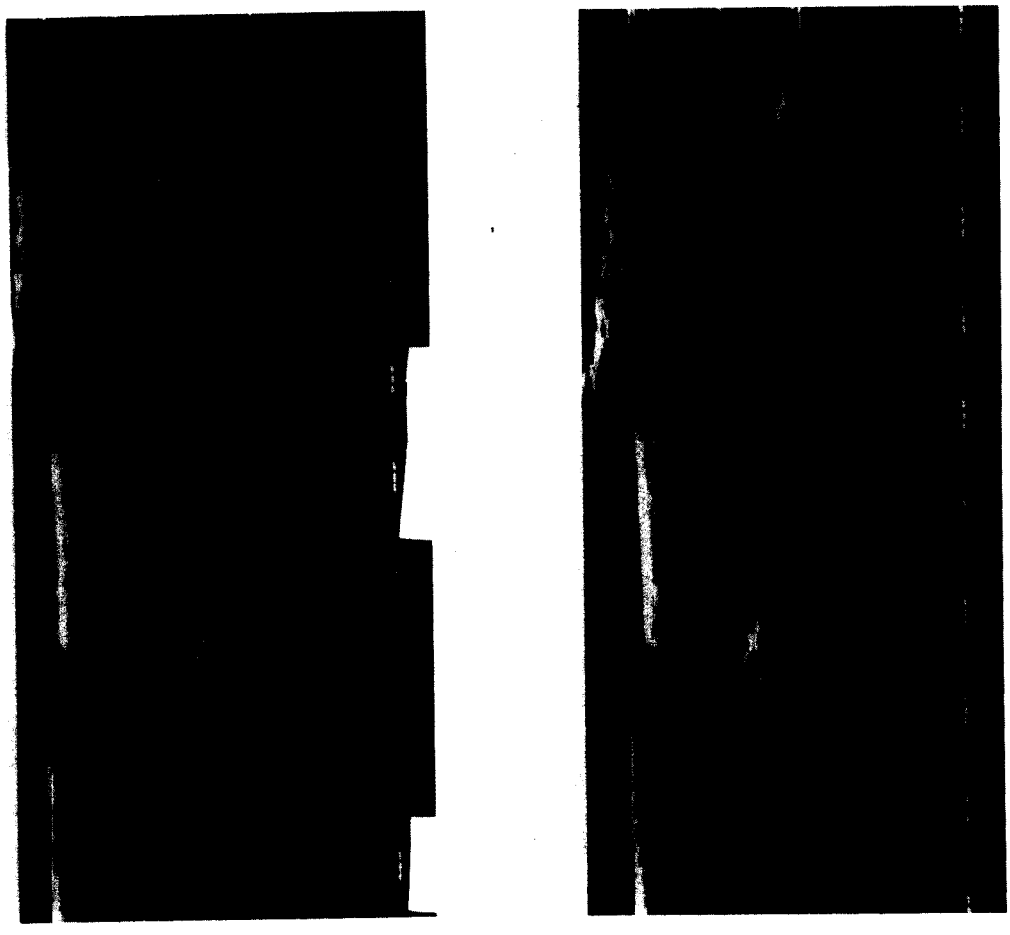

Figure A21 : APOLLO 17 stereo model, same-side geometry

Area : Mons Maraldi, Moon

Altitude : 112 km

Stereo Base : 3.2 km

Stereo Viewability : possible

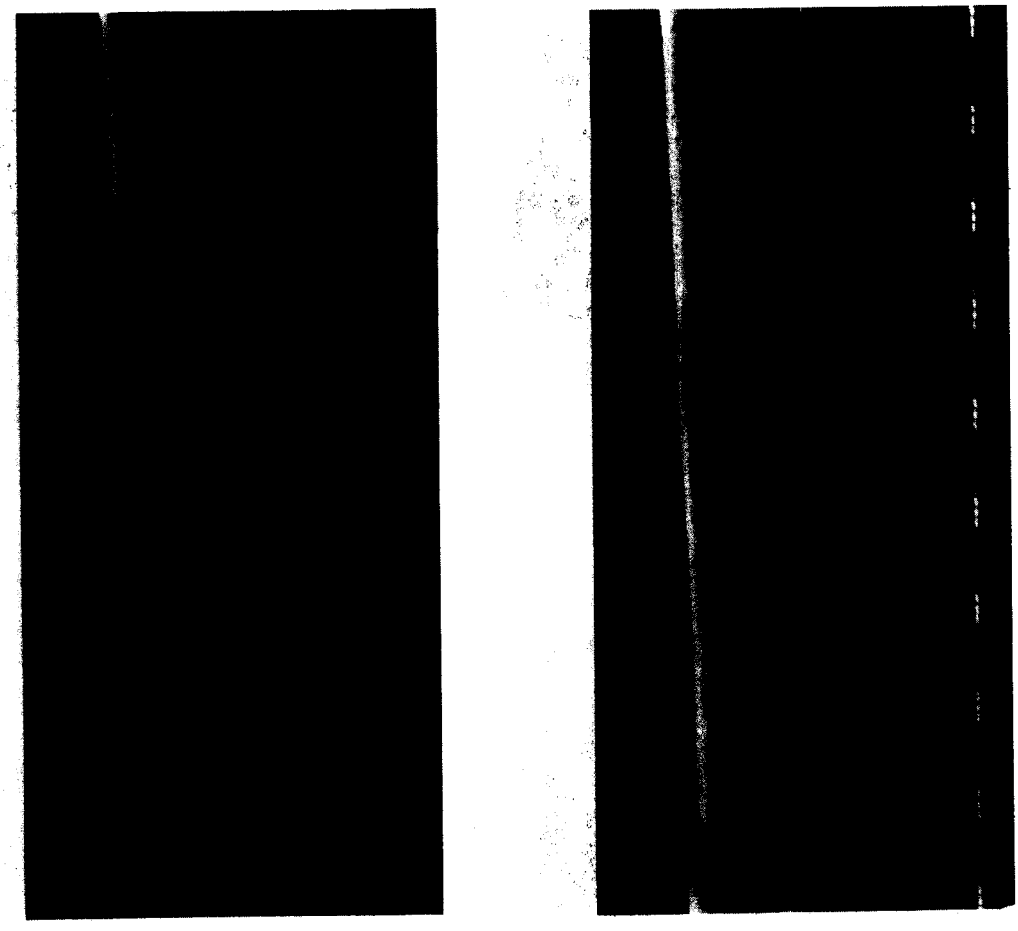

Figure A22 : APOLLO 17 stereo model, same-side geometry

Area : Mare Crisium, Moon

Altitude : 112 km

Stereo Base : 6.9 km

Stereo Viewability : possible, but flat terrain

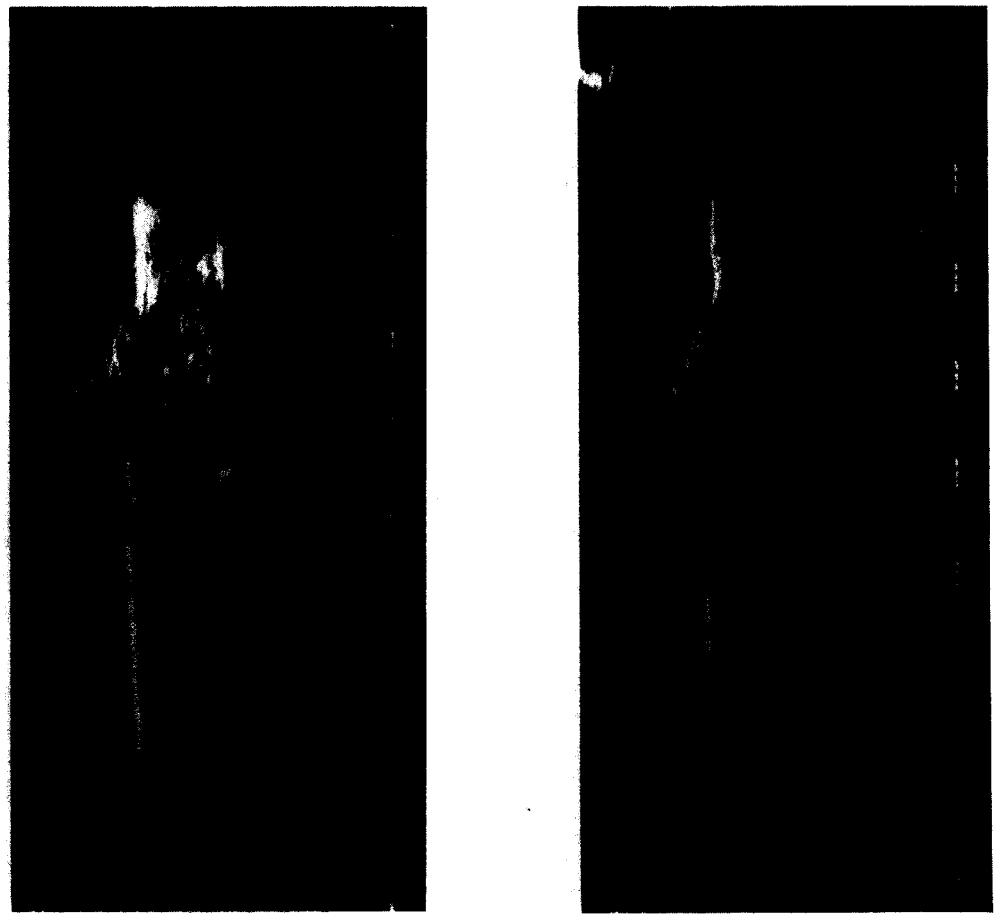

Figure A23 : APOLLO 17 stereo model, same-side geometry

Area : Condorcet, Moon

Altitude : 112 km

Stereo Base : 7.8 km

Stereo Viewability : not possible

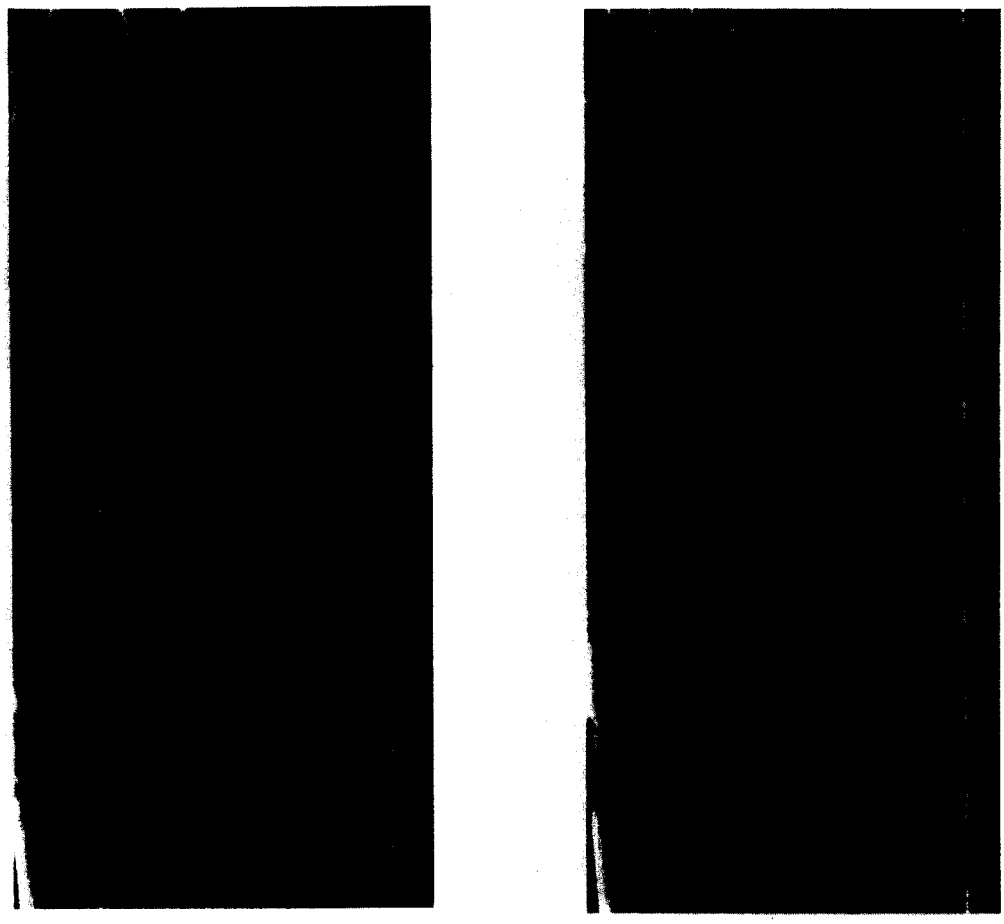

Figure A24 : APOLLO 17 stereo model, same-side geometry

Area : Neper, Moon

Altitude : 112 km

Stereo Base : 9.5 km

Stereo Viewability : not possible

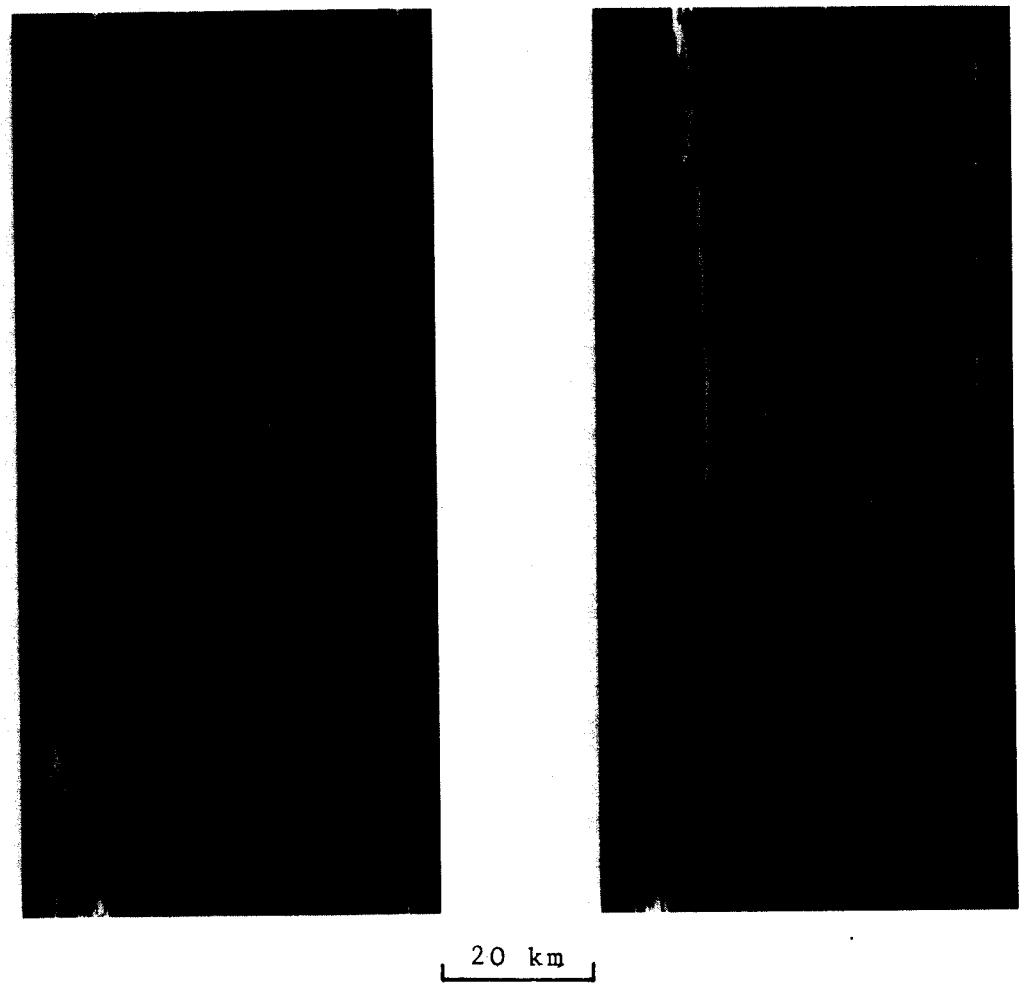

Figure A25 : APOLLO 17 stereo model, same-side geometry

Area : Craters south of Erro, Moon

Altitude : 112 km

Stereo Base : 10.0 km

Stereo Viewability : not possible

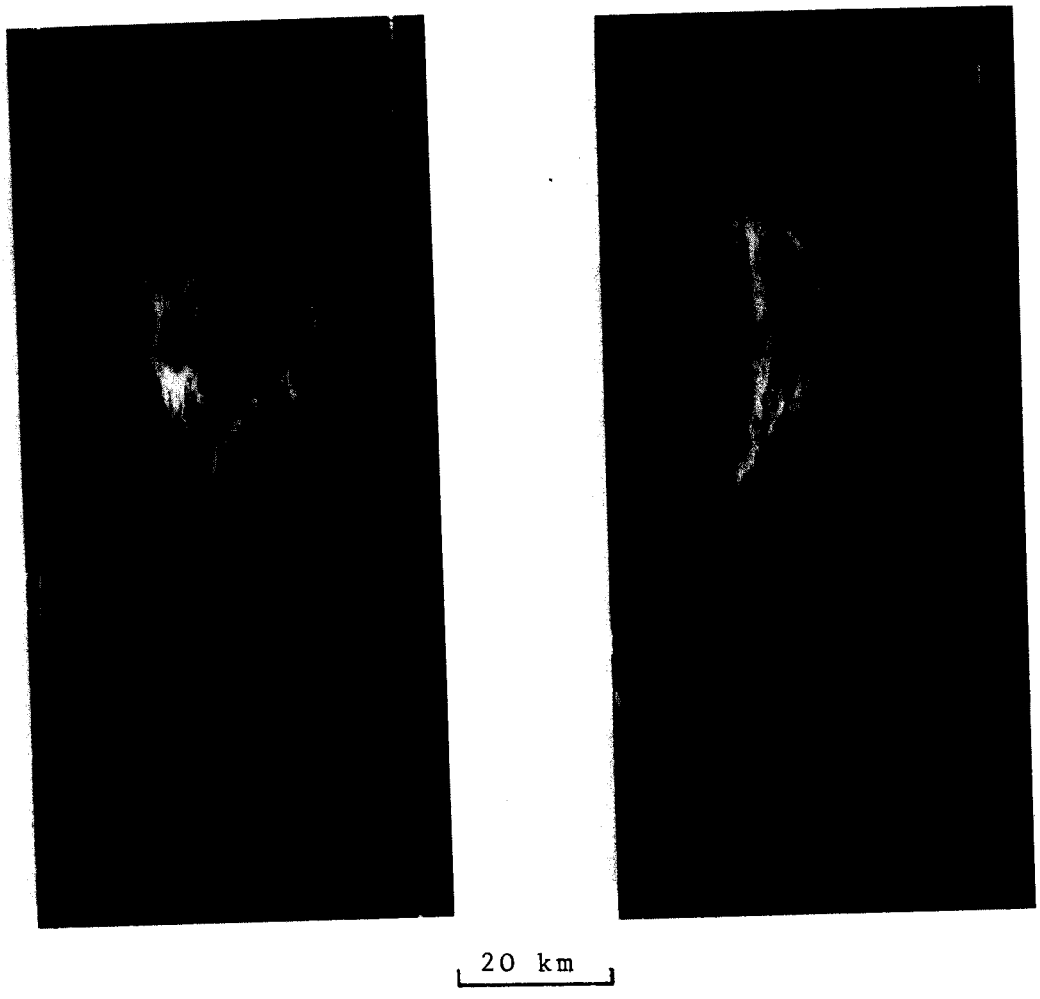

Figure A26 : APOLLO 17 stereo model, same-side geometry

Area : Buisson, Moon

Altitude : 112 km

Stereo Base : 10.3 km

Stereo Viewability : not possible

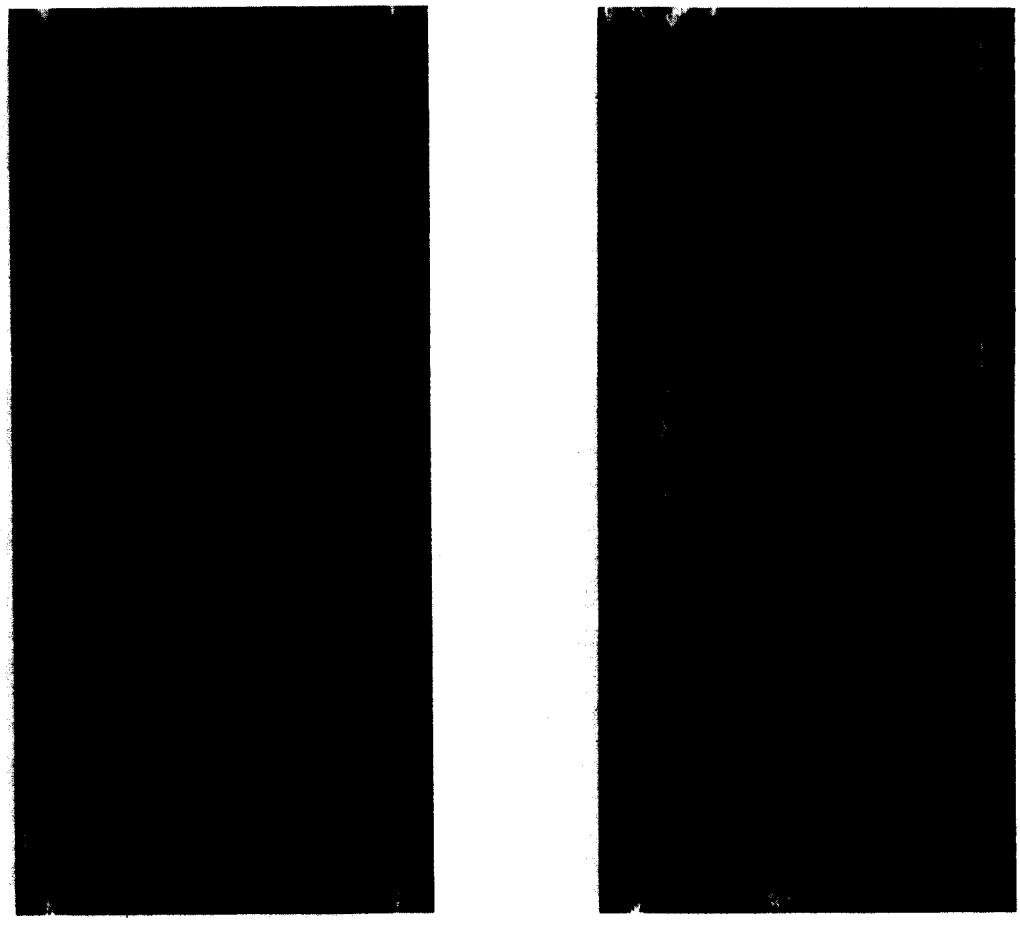

Figure A27 : APOLLO 17 stereo model, same-side geometry

Area : Aitken, Moon

Altitude : 112 km

Stereo Base : 4.4 km

Stereo Viewability : not possible

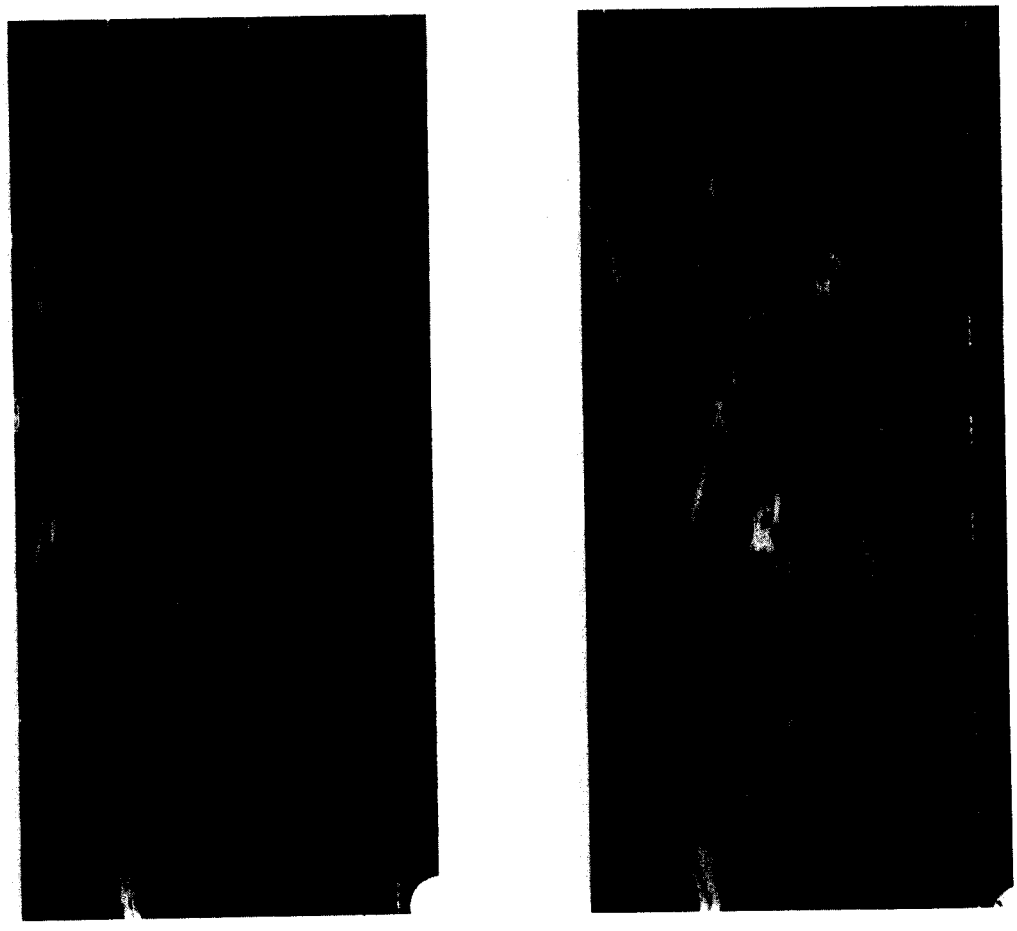

Figure A28 : APOLLO 17 stereo model, same-side geometry

Area : De Vries, Moon

Altitude : 112 km

Stereo Base : 2.8 km

Stereo Viewability : possible

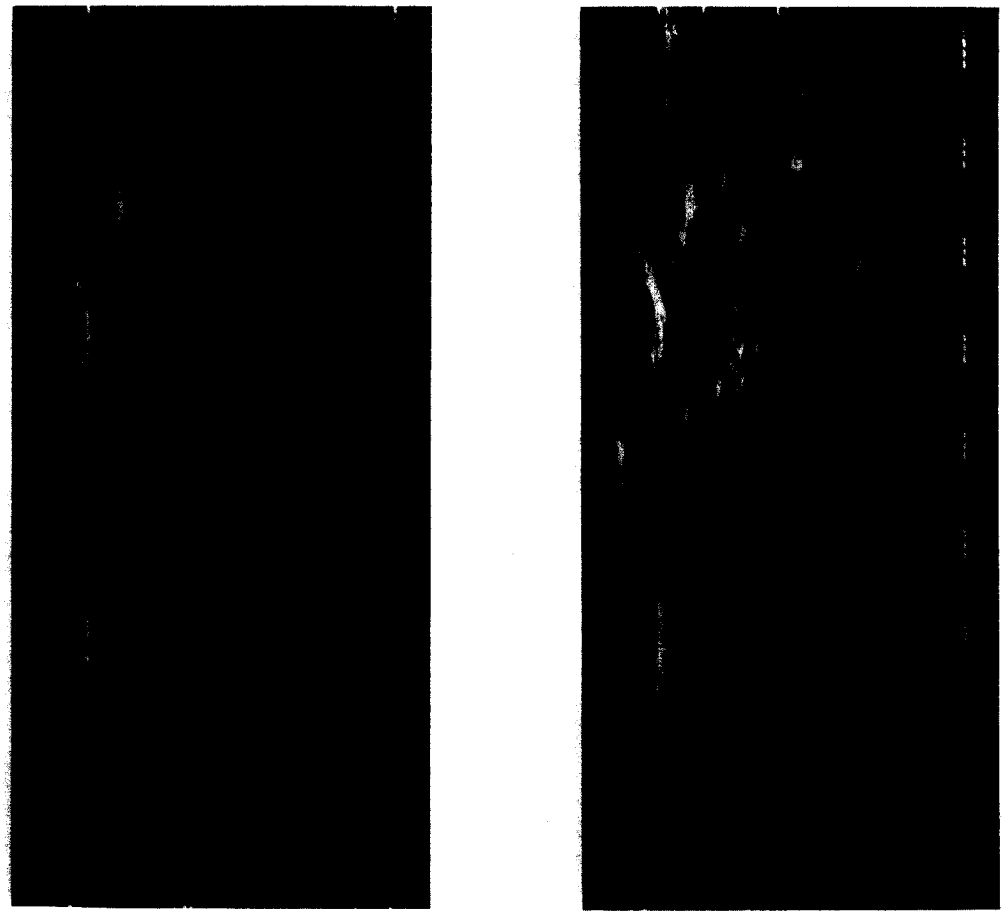

Figure A29 : APOLLO 17 stereo model, same-side geometry

Area : Mohorovicic, Moon

Altitude : 112 km

Stereo Base : 0.7 km

Stereo Viewability : convenient

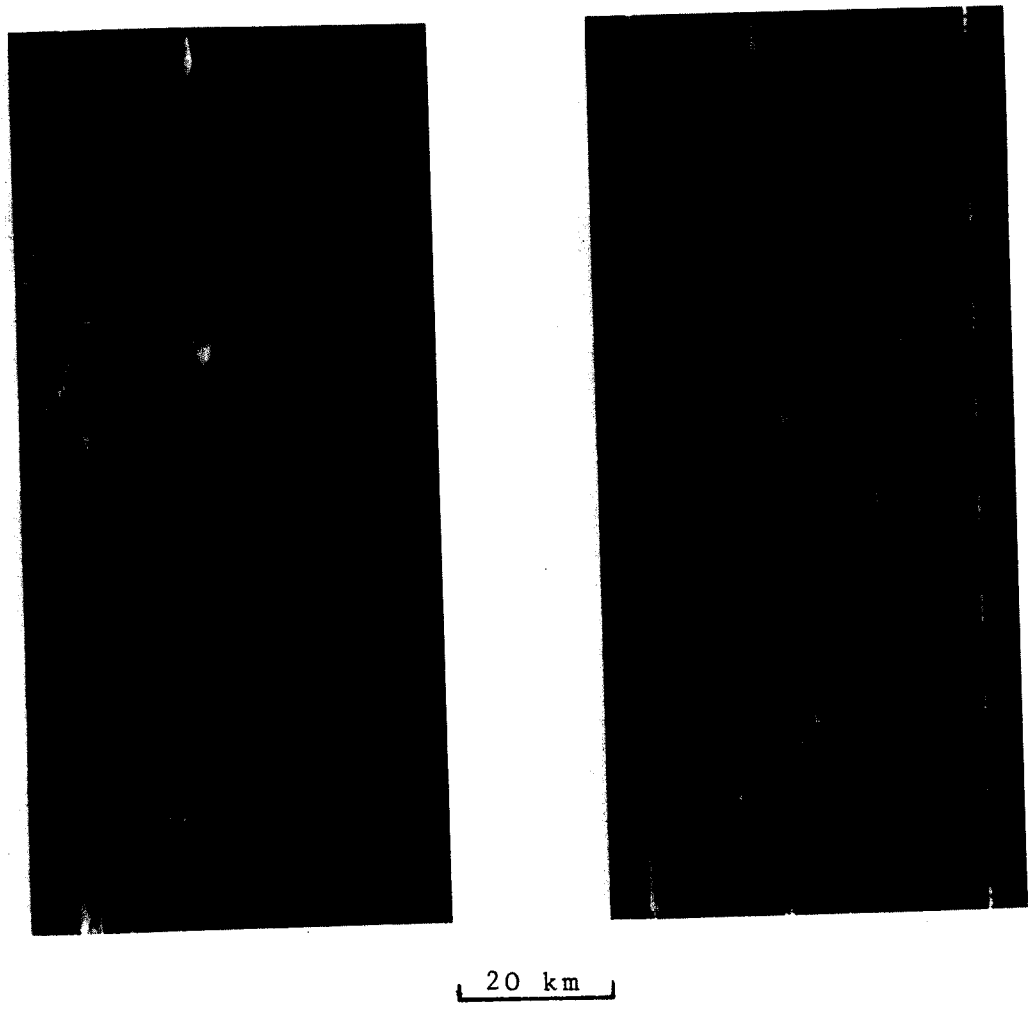

Figure A30 : APOLLO 17 stereo model, same-side geometry

Area : Unnamed area, Moon

Altitude : 112 km

Stereo Base : 1.0 km

Stereo Viewability : possible

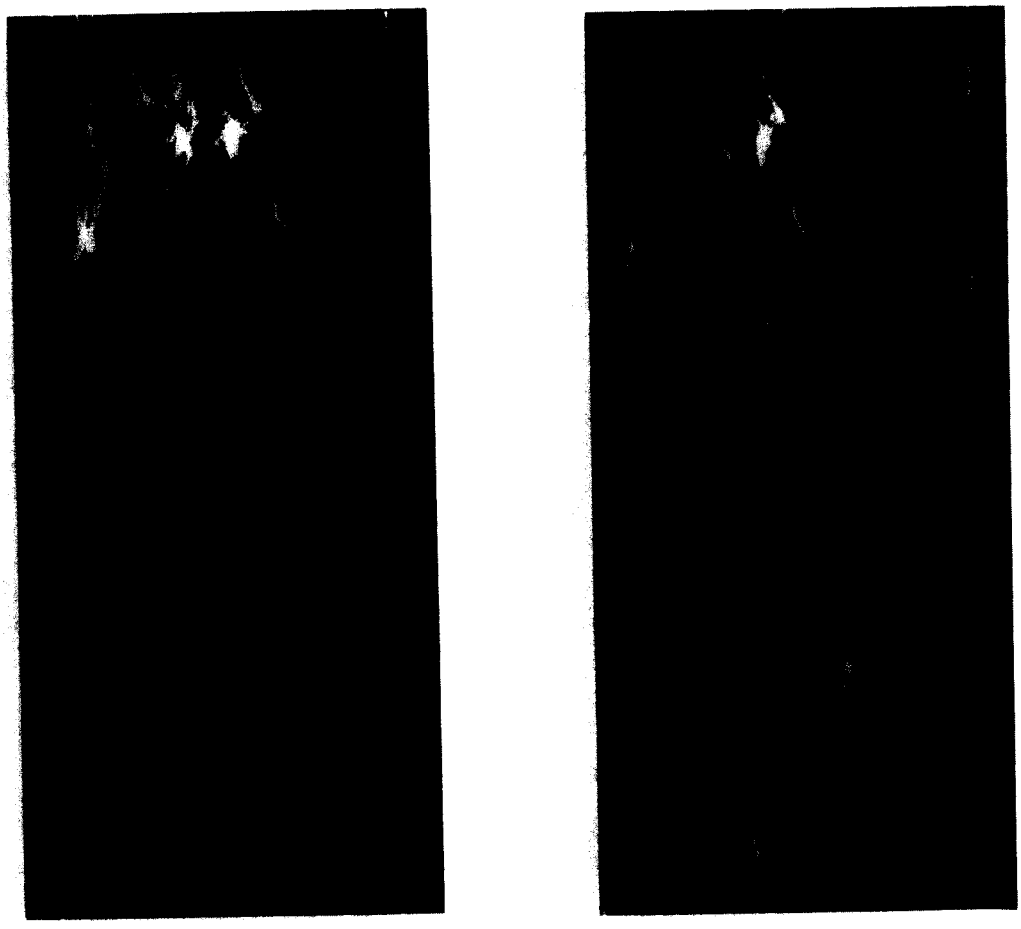

Figure A31 : APOLLO 17 stereo model, same-side geometry

Area : Belopolsky, Moon

Altitude : 112 km

Stereo Base : 4.9 km

Stereo Viewability : only for local areas

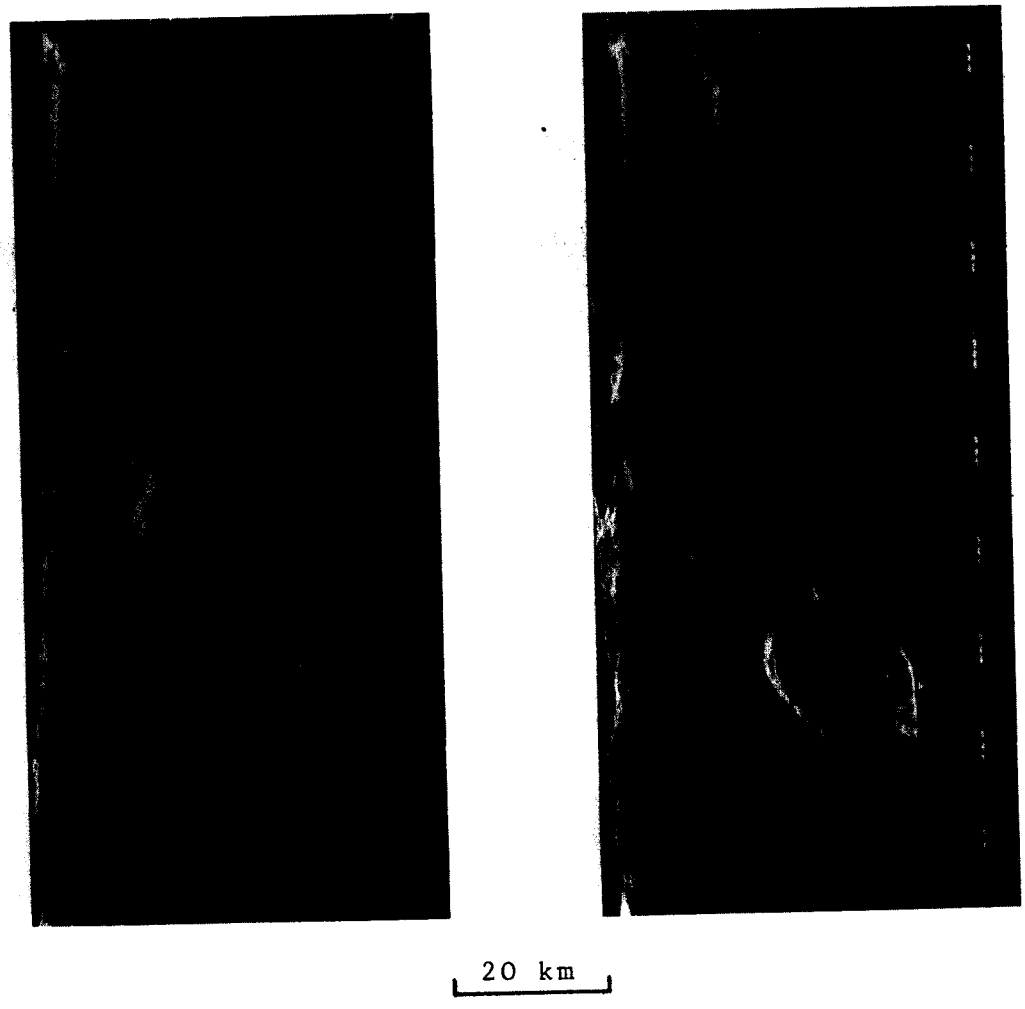

Figure A32 : APOLLO 17 stereo model, same-side geometry

Area : Lowell, Moon

Altitude : 112 km

Stereo Base : 8.4 km

Stereo Viewability : not possible

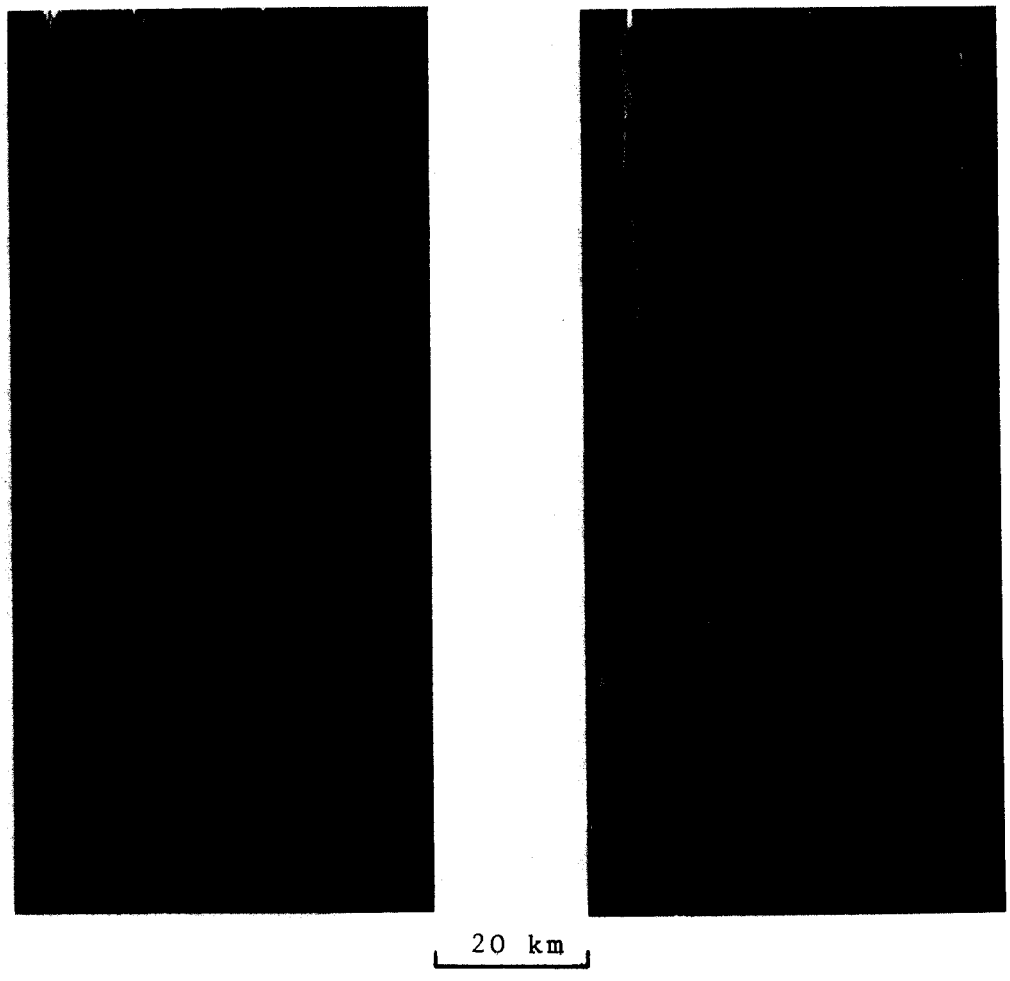

Figure A33 : APOLLO 17 stereo model, same-side geometry

Area : Schlueter, Moon

Altitude : 112 km

Stereo Base : 9.8 km

Stereo Viewability : not possible

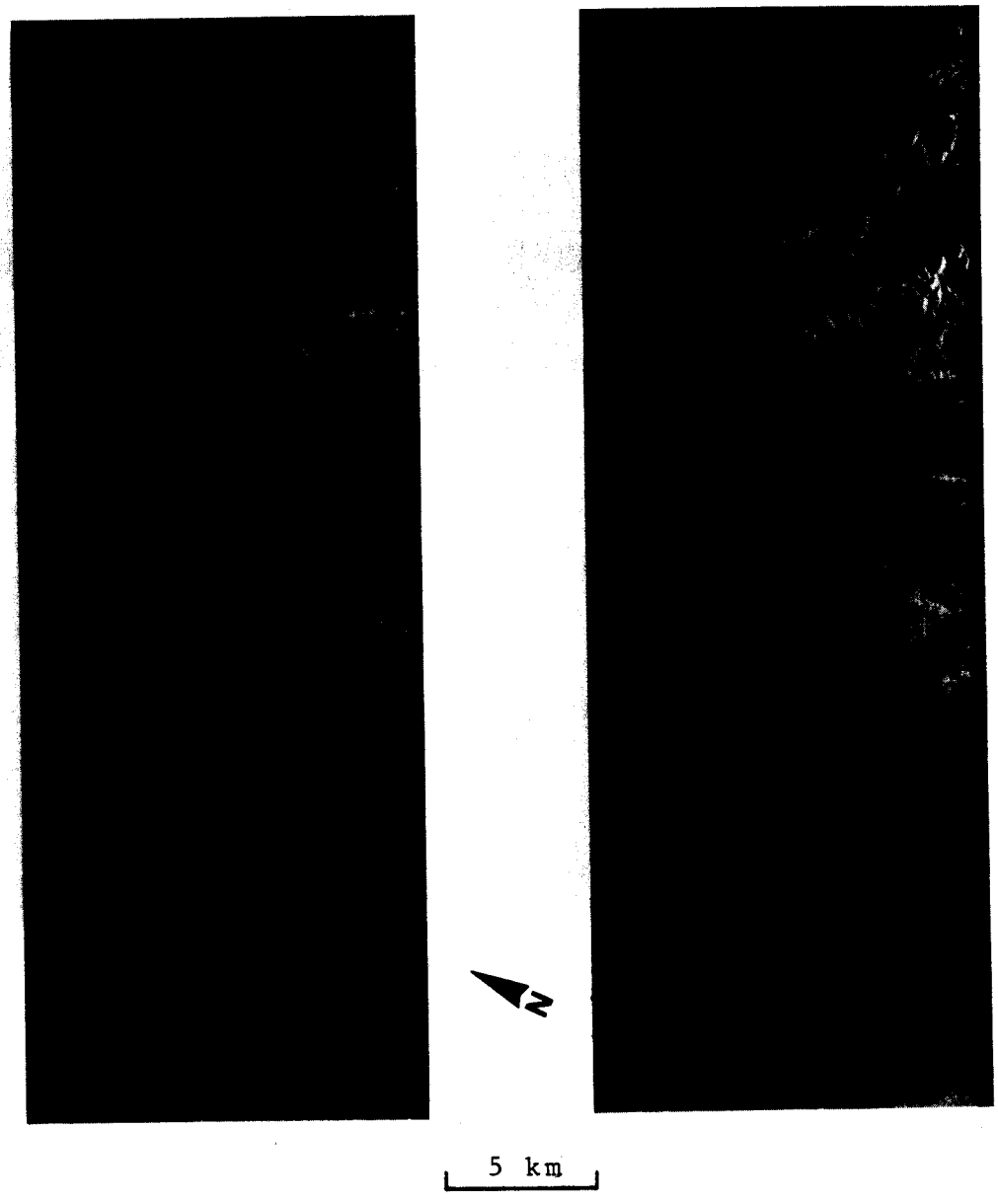

Figure A34 : JPL stereo model, same-side geometry

Area : Flagstaff, Arizona

Altitude : 10 km

Stereo Base : 0.8 km

Stereo Viewability : convenient

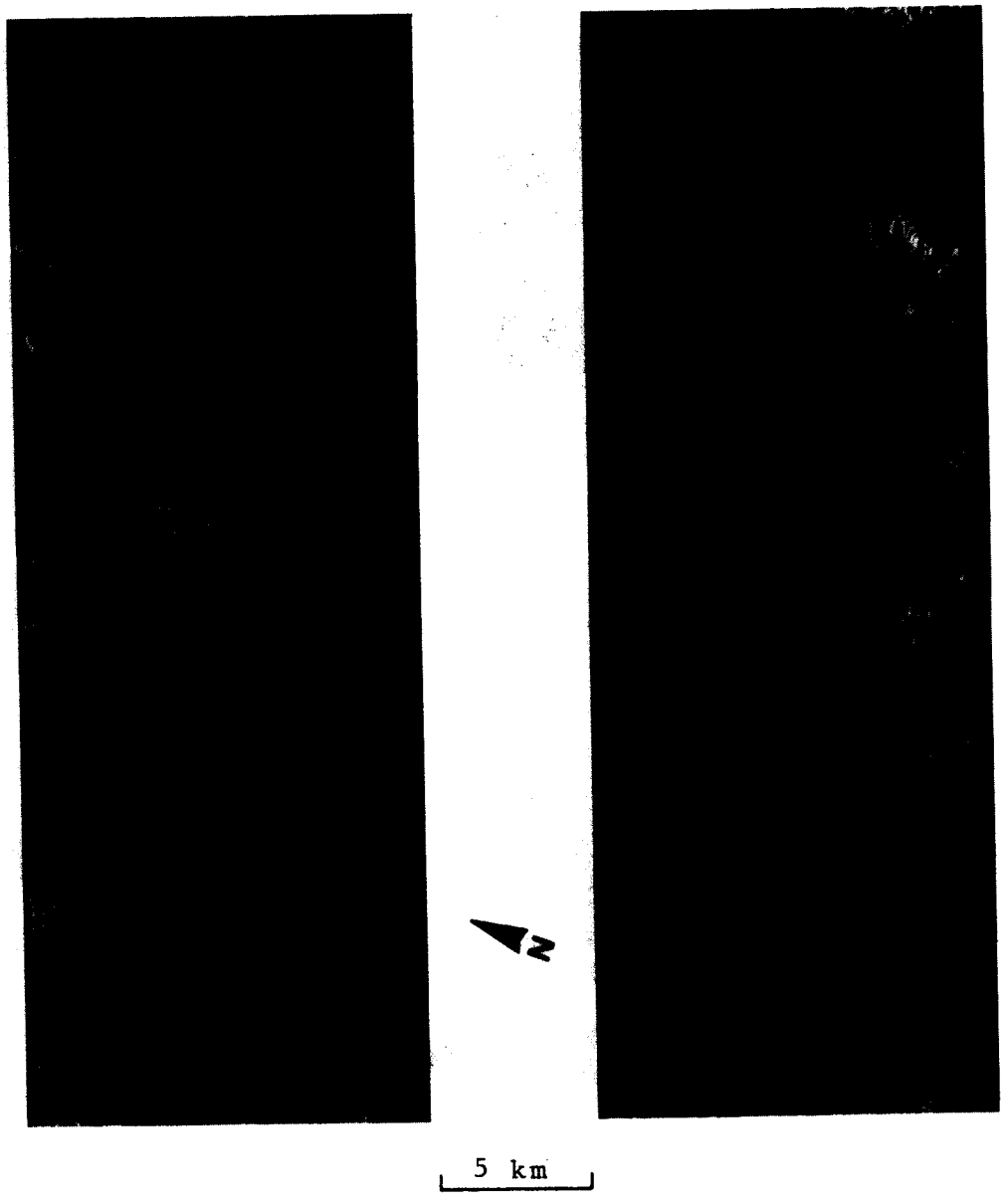

Figure A35 : JPL stereo model, same-side geometry

Area : Flagstaff, Arizona

Altitude : 10 km

Stereo Base : 7.8 km

Stereo Viewability : possible except for near range regions

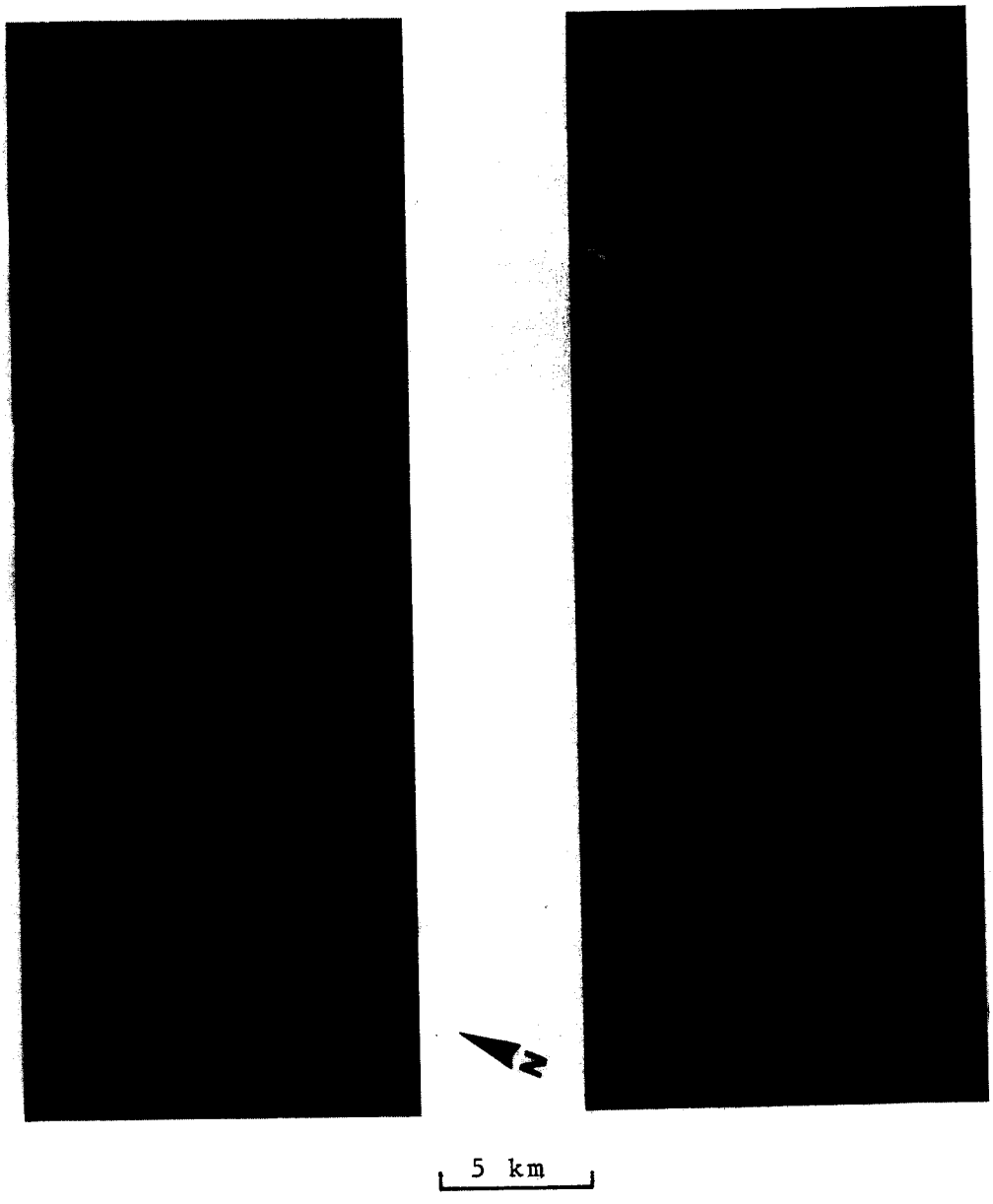

Figure A36 : JPL stereo model, same-side geometry

Area : Flagstaff, Arizona

Altitude : 10 km

Stereo Base : 1.8 km

Stereo Viewability : convenient

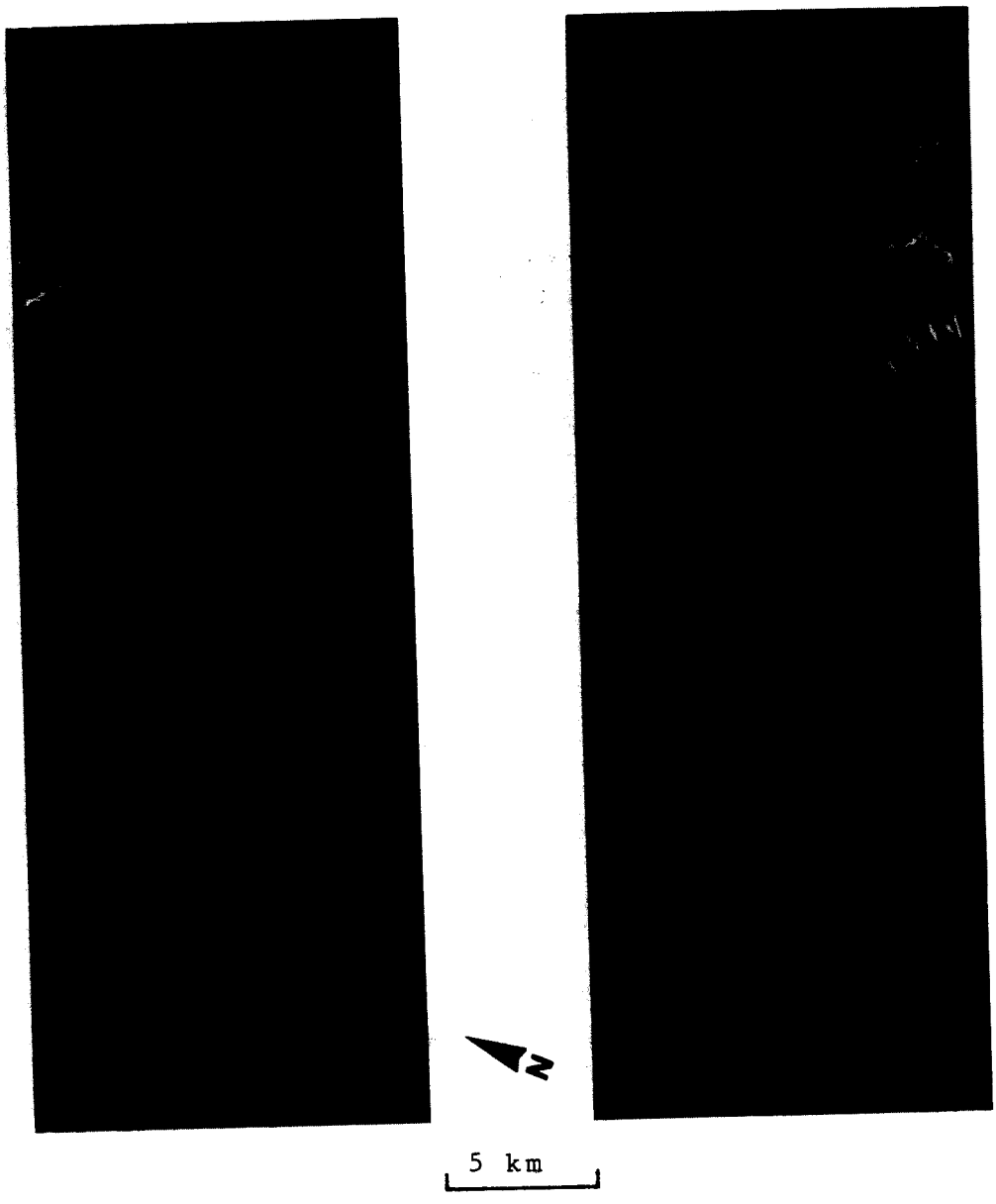

Figure A37 : JPL stereo model, opposite-side geometry

Area : Flagstaff, Arizona

Altitude : 10 km

Stereo Base : 41 km

Stereo Viewability : not possible

(except for flat areas)

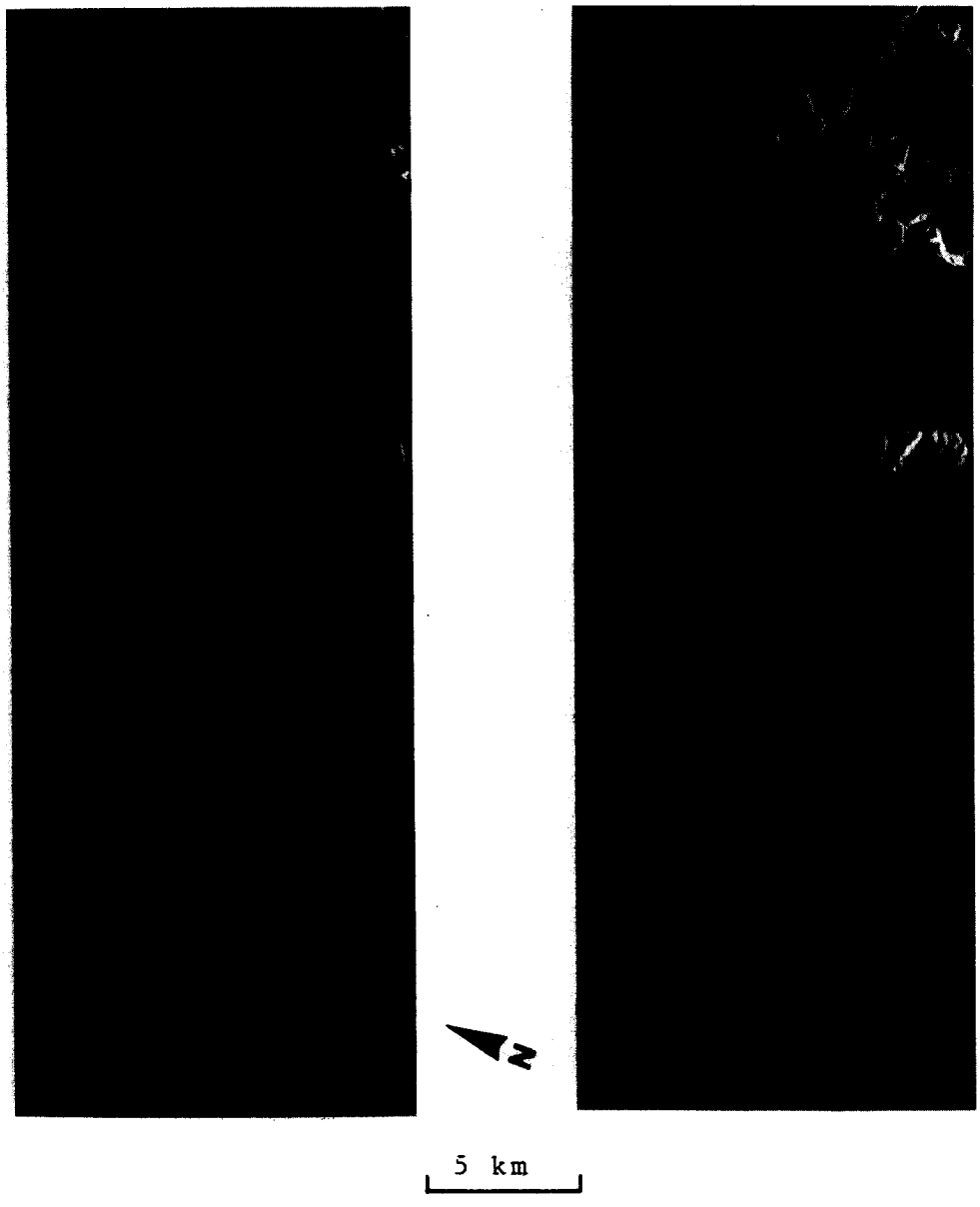

Figure A38 : JPL stereo model, opposite-side geometry

Area : Flagstaff, Arizona

Altitude : 10 km

Stereo Base : 32 km

Stereo Viewability : not possible

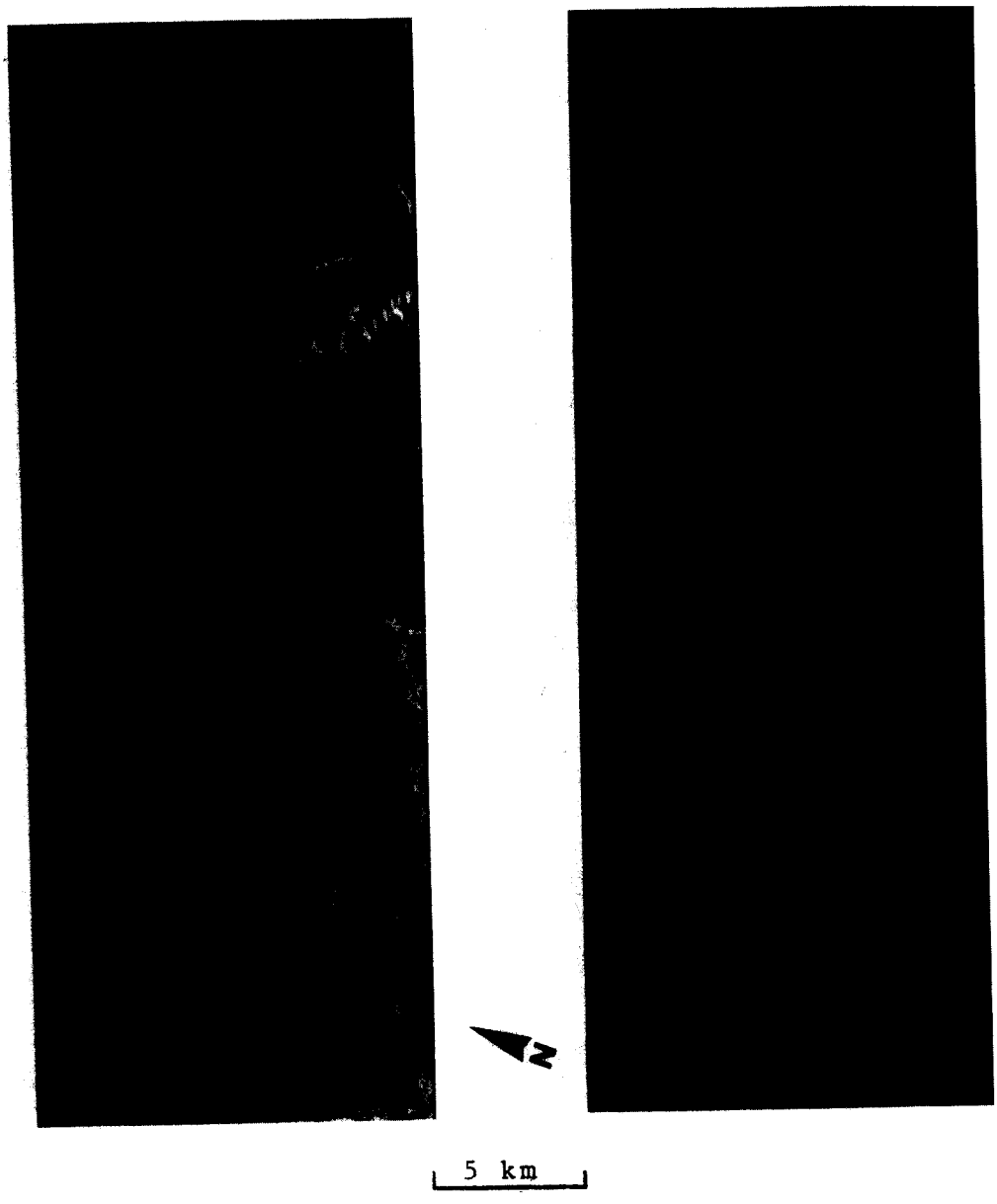

Figure A39 : JPL stereo model, opposite-side geometry

Area : Flagstaff, Arizona

Altitude : 10 km

Stereo Base : 20 km

Stereo Viewability : not possible

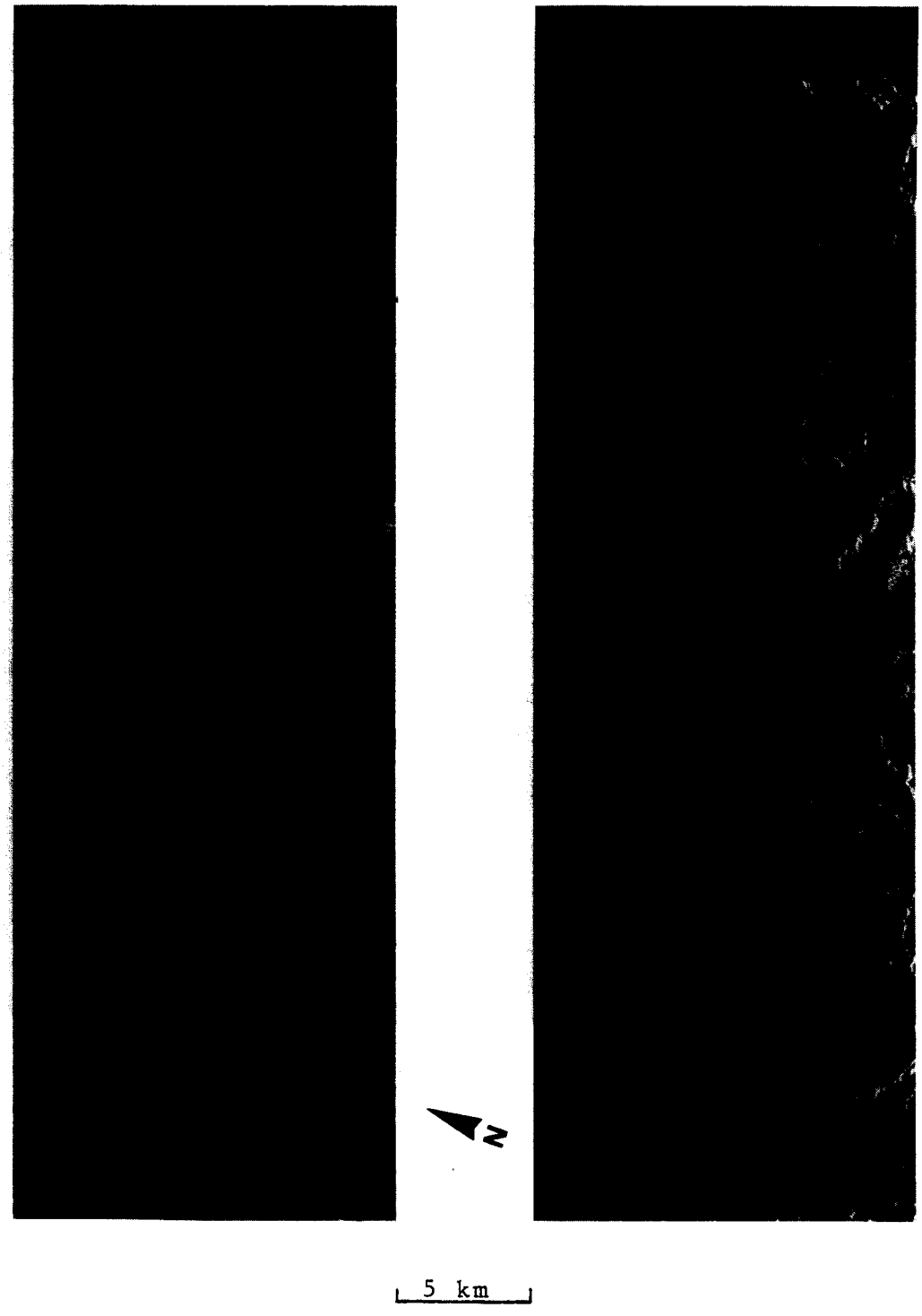

Figure A40 : JPL stereo model, same-side geometry

Area : Grand Canyon, Arizona

Altitude : 10 km

Stereo Base : 0.9 km

Stereo Viewability : convenient

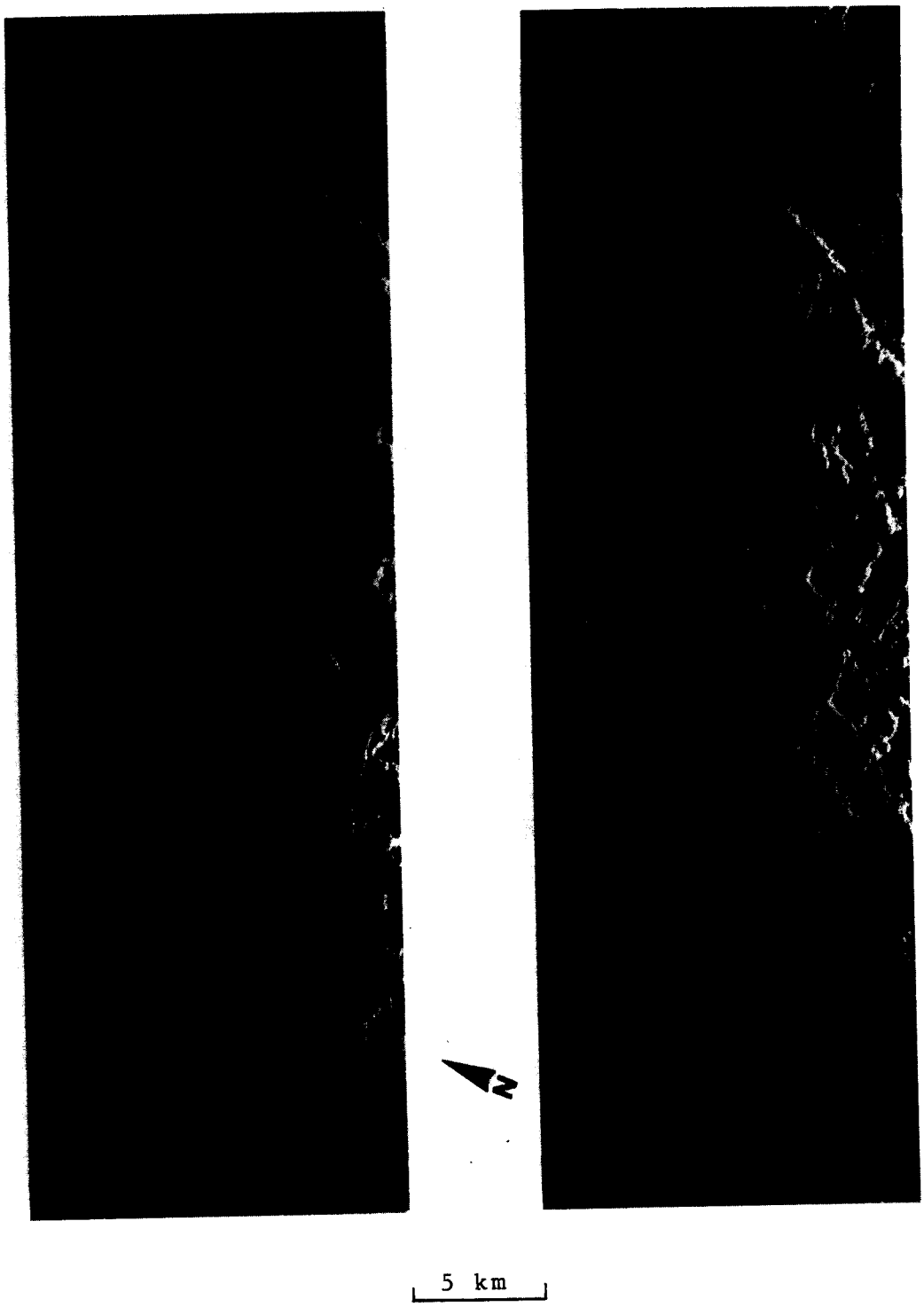

Figure A41 : JPL stereo model, same-side geometry

Area : Grand Canyon, Arizona

Altitude : 10 km

Stereo Base : 2.2 km

Stereo Viewability : possible

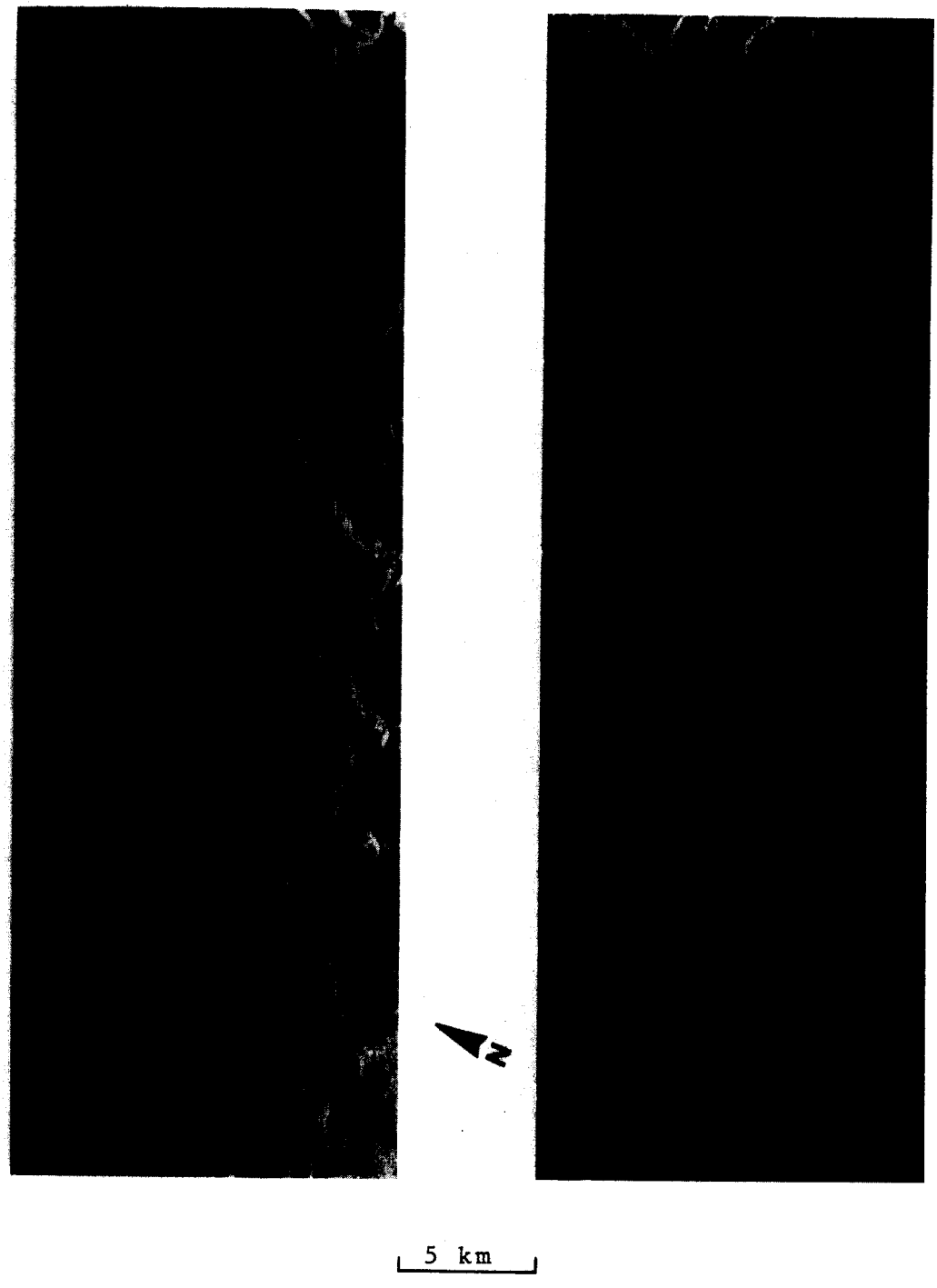

Figure A42 : JPL stereo model, opposite-side geometry

Area : Grand Canyon, Arizona

Altitude : 10 km

Stereo Base : 22 km

Stereo Viewability : not possible

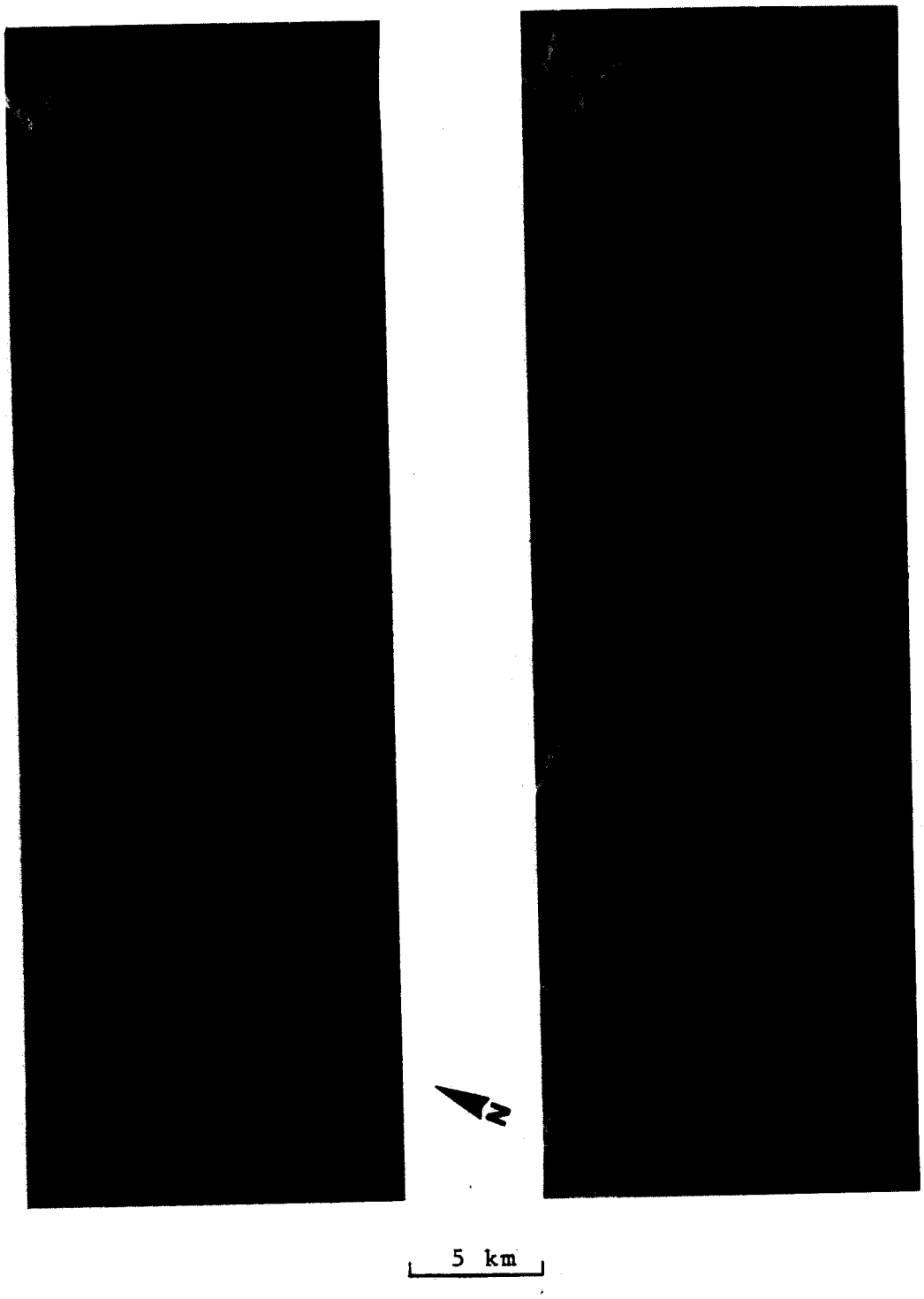

Figure A43 : JPL stereo model, same-side geometry

Area : Grand Canyon, Arizona

Altitude : 10 km

Stereo Base : 1.8 km

Stereo Viewability : very convenient

Figure A44 : JPL stereo model, opposite-side geometry

Area : Grand Canyon, Arizona

Altitude : 10 km

Stereo Base : 24 km

Stereo Viewability : not possible